DOE/OR/00033--T421

DE89 010609

UNIVERSITY OF CALIFORNIA

Los Angeles

Thermal Convection Loop Experiments and Analysis of Mass Transport Processes in Lithium/Fe-12Cr-1MoVW Systems

A dissertation submitted in partial satisfaction of the requirements for the degree Doctor of Philosophy in Nuclear Engineering

by

Graham Edgar Carlsen Bell

1988

The dissertation of Graham Edgar Carlsen Bell is approved.

N. M. Ghoniem

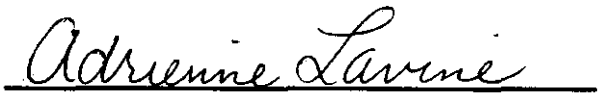

A. G. Lavine

G. Melnick

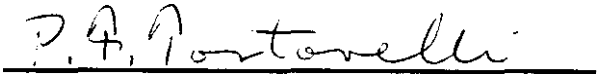

P. F. Tortorelli

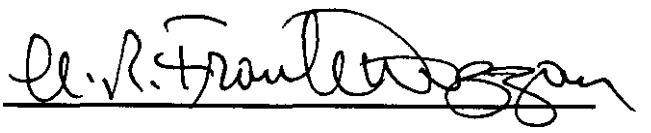

A. R. Wazzan

M. A. Abdou, Committee Chair

University of California, Los Angeles

1988

DEDICATION

To my parents: Graham Bernat Bell Ph.D. (deceased 23 October 1968), whose name and legacy as a teacher of life have been my inspiration; my mother, Carol Agnes Gramer, whose loving spirit has nurtured my soul; and Melvin Julian Schiff, my stepfather, whose friendship and appreciation of my scientific aspirations have been my sustenance, this dissertation is dedicated with love and respect.

TABLE OF CONTENTS

LIST OF FIGURES

LIST OF TABLES

ACKNOWLEDGEMENTS

I have been fortunate in my scholastic career to have encountered many people who in a variety of ways have helped in the production of this dissertation. There are those whose names do not appear in this acknowledgement not for lack of assistance or effort, but due to my lapse of memory.

First, I would like to thank the members of my certifying committee. My advisor, Professor M. A. Abdou has supported me in every way possible and has helped me through the maze of learning from ignorance to enlightenment. I would like to thank the rest of the UCLA members, Professors N. M. Ghoniem, A. G. Lavine, G. Melnick and A. R. Wazzan, for their careful review of this dissertation and critique of the research. In particular, Dean Wazzan was responsible for convincing me to attend and continue graduate school. For this guidance, I am forever grateful. Dr. P. F. Tortorelli served as an outside member on the certifying committee and as my mentor during my experimental sojourn at Oak Ridge National Laboratory (ORNL). His professional guidance and personal friendship made my first experimental effort both successful and enjoyable.

Dr. Dai Kai Sze of Argonne National Laboratory and Mr. Jack H. DeVan of ORNL were responsible for the the conception of the experiments and their efforts and concerns are gratefully acknowledged. Dr. Lee Berry of ORNL provided a pathway for funding my experiments. Dr. Everett Bloom of ORNL fiscally bailed

me out when I over spent my construction budget. It is safe to say that with out the help of these men, my dissertation would never have started or finished.

Southern hospitality is alive and well. Many of the people in the Metals and Ceramics Division of Oak Ridge National Laboratory helped me through the experimental experience. In particular, Gene Lawrence was my teacher in liquid metal handling technology. His labors and friendship are debts which I can never hope to repay. I only hope I was as good of a student as he was a teacher. Mike Howell, Jim Hendricks, Pat Bishop, Tim Kirkland and Ron Baldwin all provided assistance to me in many ways. Sometimes they served as a third hand, or helped to expedite matters about which I was ignorant or, at other times, acted as morale counselors. Karen Perry was my pseudo-secretary, travel agent, part-time sister and social coordinator. Her lilting East Tennessee accent is dearly missed. Jim DiStefano put up with me and my temper. Jim Keiser introduced me to Oak Ridge High School sports. Dane Wilson and Dick Pawel kept the coffee pot full from sunrise to sunset. Summer students Don Dobbs, Jr. and Mark Daniel helped with specimen polishing. Playing volleyball and softball and learning to row with the people of Oak Ridge provided the necessary amount of distraction from the drudgery of lab work. East Tennessee will always be my second home.

I have been blessed with a large family who have served as a tremendous source of emotional support. My brother Geoff and his family, sisters Karla and her family, Patricia, Victoria and Debra Ann,

my Aunt Margie and Uncle Mickey and their family and, of course, my parents Carol and Mel have always been there for me.

I have made many good friends in my academic life. Drs. David Yeh, Charles Kessel, Gregor Campbell and Dean Sanzo led the way. Rene Raffray, Kathy McCarthy, Gianfranco Federici, Myungdahl Song, Chang Kim and all the other fusion graduate students and staff were and are my close friends at UCLA. Special thanks to Sue Ehrlich for her help in the preparation of the dissertation and administrative assistance during the past several years. Steven and Cherie Kasakitis were always there for me. Tim Thomas spent many hot summer afternoons and weekends helping me conceive, design and draw my experiments Tim did all of it for our friendship and a few lousy Domino's pizzas. Robert, Kathy, Dave, Scott, Dr. Kathy, Mort, Buzz, Chip, Brad, Mark, Ranger George, Jen, Nat and many others are also deserving of thanks. These people have helped me carry the emotional burden. They celebrated my victories, consoled me in defeat and assured me of the eventual rewards of my labors. Little do they know that their friendship has been reward enough.

Kelly Clark deserves special thanks. I nicknamed her "mom" when we first met because of her caring soul and genuine concern for people. She and her sons, Todd and Scott, have served as my surrogate family for the past five years. Her house was always open to me as a waystation between Westwood and Claremont for a hot meal, a cold beer and good conversation with a close friend. The world would be a whole lot better off if there were more people like Kelly. Thanks, "mom".

To my Julie, who has had to suffer through the last portion of this work with all of my mood swings and frustrations, I love you and look forward to our life together.

To all my teachers, from Mrs. Forcenelli in kindergarten at Condit Elementary School who taught me to tie my shoes to Dr. Pomraning in college at UCLA who taught me neutron transport theory, my deepest thanks for educating me.

THIS PUBLICATION IS BASED, IN PART, ON WORK PERFORMED IN THE LABORATORY GRADUATE PARTICIPATION PROGRAM UNDER CONTRACT DE-AC05-76OR00033 BETWEEN THE U. S. DEPARTMENT OF ENERGY AND OAK RIDGE ASSOCIATED UNIVERISTIES.

VITA

1981	Bachelor of Science, Engineering University of California, Los Angeles
1983	Master of Science, Engineering University of California, Los Angeles

PUBLICATIONS AND PRESENTATIONS

G. E. Bell, G. H. Gelb and F. R. Furnace, "A Combined Geothermal/Ocean Thermal Conversion (GEOTEC) System for Adak Island, Alaska," presented at the Pacific Congress on Marine Technology, Honolulu, Hawaii, April 23-27, 1984.

G. E. Bell and A. R. Wazzan, "Thermal Hydraulic Performance of a Moisture Separator Reheater at Saint Laurent Unit B1," presented at International Nuclear Power Plant Thermal Hydraulic and Operations Topical Meeting, Taipei, Taiwan, October 22 - 25, 1984.

G. E. Bell and A. R. Wazzan, "Thermal Hydraulic Performance of a Moisture Separator Reheater at Saint Laurent Unit B1," Nuclear Engineering and Design, 85 (1985).

G. E. Bell, "Recent Experimental and Analytical Results of Corrosion and Mass Transfer in Lithium/12Cr-1MoVW Steel System," presented at the International Workshop on Lithium and Lithium/Lead Corrosion and Chemistry, Sceaux, France, October 1987.

G. E. Bell, "Lithium Purification Chemistry and Technology," presented at the Workshop on Lithium Purification for the SP-100 Program, Rocketdyne International, Canoga Park, California, January 26, 1988.

PUBLICATIONS AND PRESENTATIONS (continued)

G. E. Bell, M. A. Abdou and P. F. Tortorelli, "Experimental and Analytical Investigations of Mass Transport Processes of 12Cr-1MoVW Steel in Thermally-Convected Lithium Systems," presented at the International Symposium on Fusion Nuclear Technology, Tokyo, Japan, April 11-15, 1988.

G. E. Bell, M. A. Abdou and P. F. Tortorelli, "Experimental and Analytical Investigations of Mass Transport Processes of 12Cr-1MoVW Steel in Thermally-Convected Lithium Systems," submitted for publication to Fusion Engineering and Design (1989).

G. E. Bell and M. A. Abdou, "The Role of Carbides in the Corrosion Behavior of 12Cr-1MoVW Steels in Liquid Lithium," presented at the ANS Eighth Topical Meeting on the Technology of Fusion Energy, Salt Lake City, Utah, October 9-13, 1988.

G. E. Bell and M. A. Abdou, "The Role of Carbides in the Corrosion Behavior of 12Cr-1MoVW Steels in Liquid Lithium," accepted for publication in Fusion Nuclear Technology, (1989).

ABSTRACT OF THE DISSERTATION

Thermal Convection Loop Experiments and Analysis of Mass Transport Processes in Lithium/Fe-12Cr-1MoVW Systems

by

Graham Edgar Carlsen Bell
Doctor of Philosophy in Nuclear Engineering
University of California, Los Angeles, 1988
Professor M. A. Abdou, Chair

Lithium is an attractive coolant and breeder material for first-generation fusion reactor blankets. The compatibility of lithium with structural alloys, in the form of mass transport and deposition, may impose restrictions on blanket operating parameters such as temperature and lithium purity. A ferritic steel, such as Fe-12Cr1MoVW, is a candidate for use as a structural alloy in a self-cooled lithium blanket design.

Experimental data on mass transport in lithium/Fe-12Cr1MoVW were obtained from two thermal convection loops which spanned the fusion relevant temperature range; one operated from 360 to 505 °C for 3040 hours and the other from 525 to 655 °C for 2510 hours. The experimental effort was supported by analysis of the mechanisms and processes of mass transport and deposition.

It was found that mass transport and deposition, as measured by specimen weight change, were not simple functions of temperature for the entire temperature range investigated.

The mass transfer behavior and surface morphology at low temperatures were dominated by impurity reactions of nitrogen and carbon in the lithium with the steel. In the experiment between 360 and 505 °C, nitrogen levels were sufficient below 450 °C to allow the formation of the adherent, protective corrosion product Li_9CrN_5. Weight losses in the 360 to 505 °C experiment were insensitive to temperature below 450 °C. Between 450 and 505 °C, the precipitation of carbon in the form of chromium-rich $M_{23}C_6$ (M= Fe or Cr) carbides, due to the formation of Li_9CrN_5 and corresponding release of carbon, resulted in weight gains for the highest temperature specimens in the experiment.

In the 525 to 655 °C experiment, the nitrogen content of the lithium was insufficient to allow formation of protective Li_9CrN_5 corrosion product and weight changes were strongly dependent on temperature. The corrosion process at the highest temperatures (580 to 655 °C) was exponentially related to temperature with an activation energy of dissolution of 63.7 kJ/mole. Deposition was, again, dominated by carbon (precipitation of $M_{23}C_6$ carbides).

Physical models and descriptions of the processes were developed and limitations on carbon in lithium to prevent carbide precipitation were determined. Recommendations for the development of an alloy more resistant to attack by lithium were made.

CHAPTER 1 INTRODUCTION AND BACKGROUND

1.1 Fusion Energy Systems

The first generation of fusion power reactors will operate on a deuterium-tritium (D-T) fuel cycle. The D-T fusion reaction has characteristics which make achievement of nuclear fusion technologically easier in the near term. The D-T reaction is given below.

$$ {}^{2}_{1}D + {}^{3}_{1}T \Longrightarrow {}^{4}_{2}He\ (3.5\ MeV) + {}^{1}_{0}n\ (14.1\ MeV) $$

The numbers in parentheses represent the kinetic energies of the respective particles in units of million electron-volts (MeV). It is estimated that a typical 1000 megawatt-electric fusion power reactor will consume about 350 grams and 500 grams of deuterium and tritium, respectively, per full-power day. It will, therefore, be necessary to provide copious amounts of both deuterium and tritium on a continuous basis.

Deuterium is a stable isotope of hydrogen with a natural abundance of 0.0153 atomic % (a/o) and can be obtained from ordinary sea water. Tritium is a radioactive isotope of hydrogen with a half-life of 12.3 years. Because of its short half-life, tritium has essentially zero natural abundance. In order to close the D-T fuel cycle, it will be necessary to produce, or breed, tritium by some nuclear means. The most efficient and preferred method is to breed

tritium from neutron interactions with naturally-occurring isotopes of lithium. The ^{6}Li and ^{7}Li tritium breeding reactions and their corresponding energy yields (Q-values) are:

$$^{6}_{3}Li + {}^{1}_{0}n \Longrightarrow {}^{4}_{2}He + {}^{3}_{1}T \ (Q = 4.8 \text{ MeV})$$

$$^{7}_{3}Li + {}^{1}_{0}n \Longrightarrow {}^{4}_{2}He + {}^{3}_{1}T + {}^{1}_{0}n \ (Q = -2.5 \text{ MeV})$$

Positive Q-values indicate energy is released in the reaction and, conversely, a negative Q-value reaction indicates conversion of kinetic energy into mass. The neutron produced by the D-T fusion reaction can be utilized to breed tritium via these reactions. Since the ^{7}Li reaction produces both a triton and another neutron which can also be used to breed, it is possible to breed more tritium than is consumed in a particular reactor design. The ratio of tritons produced to those consumed in a particular reactor design is called the Tritium Breeding Ratio (henceforth, TBR). The TBR for most reactor designs ranges between 1.0 and 1.3.

A schematic of a magnetic plasma confinement system is shown in Figure 1.1. The idea is to confine the plasma using either a magnetic field (e.g. tokamak), combination of magnetic fields and electrostatic potentials (e.g. tandem mirrors), or combination of magnetic fields and current stabilization (e.g. stellarators). Depending on the particular design, fusion reactors may be either pulsed or steady-state. The plasma will be heated by various

methods (ohmic heating, R-F current drive, or particle injection) to the "ignition point," where significant nuclear fusion occurs and alpha particles (i.e. ^4_2He) from the fusion reaction will be sufficient to "self-heat" the plasma. The plasma volume is surrounded by several components. The first wall is exposed to plasma radiation. The blanket region breeds tritium and absorbs and removes heat deposited by the neutrons and secondary γ-rays. The reflector/shield reduces neutron leakage from the blanket and protects the magnet system from the deleterious effects of neutrons which escape the blanket. The magnet system provides the primary confinement mechanism for the plasma. Our interest is primarily in the blanket region.

In order to breed tritium, lithium must be present in the blanket either as a solid or a liquid. Typical solid-breeder designs utilize lithium oxide (e.g. Li_2O) or ternary ceramic compounds of lithium (e.g. $LiAlO_2$) as breeding material with a helium coolant and tritium purge gas stream. Tritium breeding capability, tritium retention and tritium processing are critical design issues for solid breeder designs. Liquid metal designs currently use either natural lithium or a lithium-lead eutectic, 17 a/o Li and 83 a/o Pb, designated Li17-Pb83, alloy as a breeder and coolant. Li17-Pb83 is extremely corrosive [1.1-4], more so than pure lithium. Containment of tritium in the reactor system is more difficult in Li17-Pb83 than in lithium due to the low tritium solubility, and, thus, high permeation of hydrogen and its isotopes through structural materials. As such, Li17-Pb83 is currently thought to be less

desirable than natural lithium as both a breeder and coolant. Liquid lithium is an excellent tritium breeding material. Semi-stagnant lithium can be utilized as a breeding medium with a separate coolant, or liquid lithium can be used as both a coolant and breeder in so-called self-cooled designs. Lithium is an excellent high temperature coolant due to its high thermal conductivity and heat capacity as well as low viscosity and vapor pressure. Pumping power requirements and velocity profile effects on heat and mass transfer due to magnetohydrodynamic (MHD) effects, the extreme chemical reactivity of lithium with air and water, and corrosion and mass transport of structural materials are major uncertainties for liquid lithium designs [1.5].

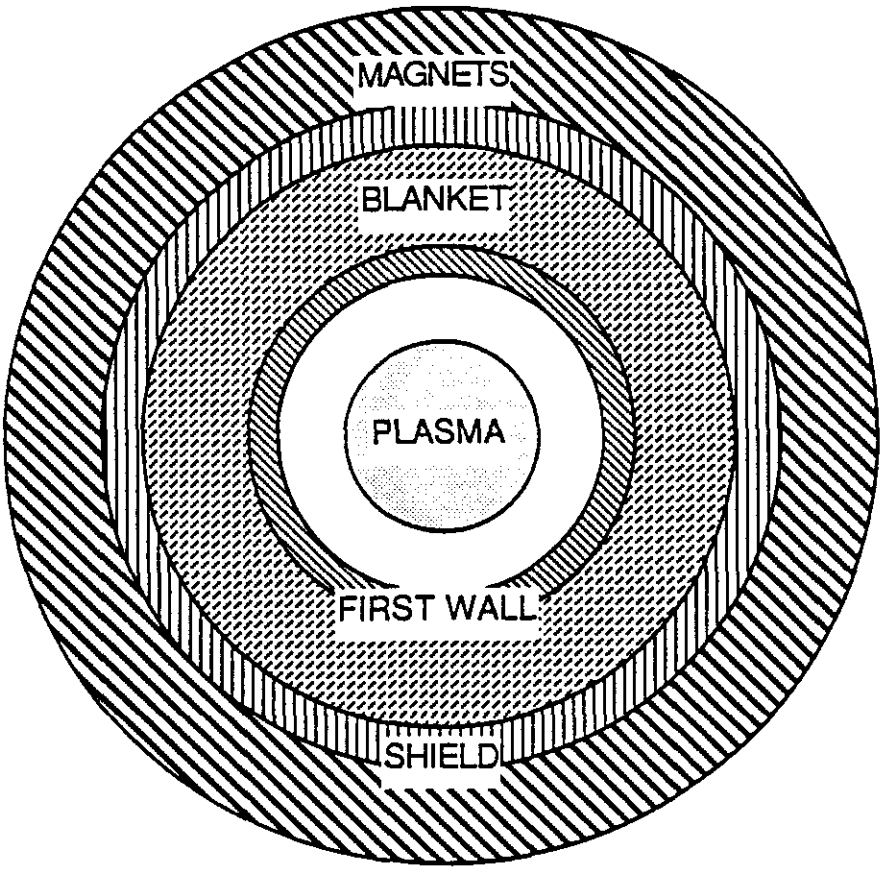

Figure 1.1 Schematic of Fusion Reactor

1.2 Structural Alloys of Interest to Fusion

Structural alloys currently considered for use in fusion liquid metal blankets are austenitic and ferritic/martensitic steels, and refractory alloys such as vanadium . A self-cooled liquid lithium blanket with ferritic steel structural alloy, (12% Cr-1% Mo- 0.25% V-0.5% W-0.5% Ni-0.2% C by weight = Fe-12Cr1MoVW), has been identified as a potentially attractive blanket system [1.5]. Without corrosion and mass transport considerations, the temperature range applicable to fusion technology for structural materials is from about 220 to 700 °C. Preliminary indications from limited data are that material strength and compatibility of structure with the lithium coolant will lower the temperature limit from 700 to 550 °C or less for ferritic and 480 °C or less for austenitic steels [1.5]. However, the temperature limit for ferritic steel is based on a very limited set of data points and the mechanisms of corrosion are not well understood. Vanadium alloys are not currently thought to be limited by general mass transfer considerations per se, but there is presently limited compatibility data. Other materials and economic considerations (fabricability, interstitial element transport, economics) may preclude the use of vanadium and refractory alloys in fusion reactors.

This research will focus on the mass transport (corrosion and deposition) of the ferritic alloy HT9, also known as Fe-12Cr1MoVW, in lithium as applied to fusion blanket concepts. The effects of corrosion can lead to weakening of thin-walled structural members in the reactor while mass transport and deposition can result in

increased personnel radiation exposure (due to activated corrosion products) and flow restriction caused by mass deposition in specific regions. Release, transport, and deposition of corrosion products and material outside the nuclear island may impose maximum temperature restrictions which would make a ferritic steel and lithium blanket economically unfeasible. Corrosion can also affect the mechanical properties of the structural alloy. Liquid metal embrittlement (henceforth, LME), however, can occur without mass transfer or corrosion and can reduce the toughness of the structural alloy. This research will not directly address LME.

1.3 Ferritic versus Austenitic Steels

Although this research will focus on a ferritic alloy Fe-12Cr1MoVW (HT9), much of the previous work in liquid lithium corrosion and mass transport applicable to fusion systems has been done for austenitic steels. Austenitic alloys are usually preferred as structural alloys in engineering applications because they are easier to fabricate into components and possess higher strength than comparable ferritic steels. However, when placed in contact with lithium, severe corrosion in the form of selective leaching (dissolution) of nickel and possibly interalloying of lithium with this element limits the maximum operating temperature for austenitic steels in liquid metal blankets. Chromium depletion by the formation of a ternary nitride corrosion product (Li_9CrN_5) also contributes to the relatively large weight losses in austenitic steels. Ferritic alloys appear not to be affected as much by contact with the

lithium environment primarily due to the absence of nickel from their composition.

Austenitic steels for application to fusion are similar to the type 316 stainless steel alloy (henceforth, abbreviated SS, as in 316 SS), and the titanium-modified 316 SS version for application in fusion is designated as the primary candidate alloy (henceforth, PCA). Low carbon austenitics are also favored and are normally designated with an "L", such as 316L SS. The nominal compositions of HT9, 316 SS, 316L SS and PCA are given in Table 1.1. Austenitic steels differ from ferritic steels primarily due to the presence of nickel, typically 8 to 11 weight % (note, weight % = w/o), which stabilizes the face centered cubic (FCC) austenite phase at temperatures below 910 °C, where the body centered cubic (BCC) ferrite is actually the equilibrium structure. Subsequent removal of the nickel, such as occurs when 316 or 304 SS are placed in contact with lithium or sodium, causes the FCC structure (γ-phase) to convert to the equilibrium BCC structure (α-phase). As a result of the addition of nickel, the iron content of austenitic steels is somewhat lower than ferritics. Chromium is present in both steels to increase ductility, allow for the formation of a chromium oxide layer which imparts corrosion resistance in oxidizing environments and promotes formation of stable metal carbides for increased strength. The chromium level in Fe-12Cr1MoVW (BCC) is just at the edge of a stainless classification, nominally set at 14 w/o chromium. Molybdenum is added to resist chloride attack and it further stabilizes the BCC and carbides phases. Carbon is added to increase

strength. Low carbon alloy steels typically have a total carbon content of less than 0.1 w/o carbon. Fe-12Cr1MoVW can have nearly twice that amount (0.2 w/o = 2000 wppm-C). Carbon is only slightly soluble in iron-chromium and iron-chromium-nickel alloys (typically less than 10 and 200 wppm for α and γ phases, respectively, at 700 °C). The remainder of the carbon in steels goes to forming metal carbides. Carbon strengthens the steel by forming dispersed metallic carbides with metal alloy constituents, specifically iron, chromium, molybdenum, and vanadium, generically denoted as M. These dispersed carbides act to inhibit dislocation movement, thereby resulting in a macroscopically stronger material. Depending on the heat treatment and alloy constituents, carbides may be found in many stoichiometries ranging from M_3C through such complex stoichiometries as $M_{23}C_6$.

Elemental w/o										
Alloy	Cr	Mo	V	W	Si	Ni	Mn	C	Ti	Fe
HT9[a]	11.5	1.0	0.3	0.5	0.4	0.5	0.6	0.2	---	85.0
PCA[b]	14	2.0	---	---	0.5	16	2.0	0.05	0.3	65
316SS[c]	17	2.0	---	---	1.0	12	2.0	0.08	---	65
316LSS[c]	17	2.0	---	---	1.0	12	2.0	0.03	---	65

[a] Ref. [1.7]
[b] Ref. [1.5]
[c] Ref. [1.15]

Table 1.1 Compositions of Steel Alloys for Magnetic Fusion

1.4 Characterization of Lithium

Lithium is the lightest of all metals. Lithium is a member of the alkali metal group which includes sodium, potassium, cesium and rubidium. At room temperature, lithium is a sticky solid. Lithium melts at 453.75 K and boils at 1615.15 K at atmospheric pressure. Some characteristic physical and chemical properties of lithium are given in Tables 1.2 and 1.3. Typical non-metallic impurities of lithium are nitrogen, oxygen and carbon. Metallic impurities in commercially available lithium include sodium, potassium, aluminum and iron. Transition metals, with the exception of nickel, are only slightly soluble in lithium. Non-metallic impurities, such as nitrogen, oxygen, and carbon are much more soluble by comparison. Figures 1.2 and 1.3 show solubilities of the pertinent metals and non-metals, in lithium.

Although lithium and sodium are adjacent elements in group IA of the Periodic Chart and possess some similar chemical properties due to their common single valence s-electron, lithium shows significant differences from sodium in its physical and solvent properties, chemical reactions which occur between dissolved species in the liquid metal (notably nitrides and carbides), and in its corrosion behavior towards transition metals and steels. There is a great deal of information regarding material compatibility and corrosion of structural alloys in sodium and other liquid metals available from the liquid metal fast breeder reactor (LMFBR) and other energy and nuclear power programs. The direct applicability of these data to lithium is not clear. The release of material from a

surface to an adjacent liquid is largely a chemical process. Changing the environment (liquid metal) or the alloy in the system can drastically alter the dissolution and other corrosion processes. Sodium corrosion of steel is quite sensitive to oxygen contamination probably due to a catalytic effect on the reaction of oxygen and iron to form $NaFeO_2$ and the formation of $NaCrO_2$ on the surface of the steel. Lithium is almost completely insensitive to this type of reaction due to the extreme thermodynamic stability of Li_2O. Conversely, lithium corrosion of steels is highly sensitive to dissolved nitrogen in the form of Li_3N which interacts with the chromium in the steel to form the ternary corrosion product Li_9CrN_5 [1.6]. A stable nitride of sodium has never been identified. Indiscriminate application of sodium concepts to lithium is highly speculative. Some aspects of mechanistic and physical models from sodium/steel interactions (e.g., preferential dissolution, impurity reactions and carburization/decarburization) are helpful in understanding the corrosion processes in lithium/steel systems.

Physical and Transport Properties and State Properties[1.8]

Density :	$\rho(kg/m^3) = 515 - 0.101 \{T(K) - 473\}$
Dynamic Viscosity:	$\log_{10} \mu(N\ sec/m^2) = -1.5064 - 0.7368 \log_{10} T(K) + \frac{109.95}{T(K)}$
Thermal Conductivity:	$\lambda\ (W/m\ K) = 42.26 - 1.23 \times 10^{-2} \{T(K) - 273\}$
Electrical Resistivity:	$\frac{1}{\sigma}(\mu ohm\text{-}cm) = 18.33 + 3.339 \times 10^{-2} \{T(K)-273\} - 6.795 \times 10^{-6} \{T(K)-273\}^2$
Vapor Pressure:	$\log_{10} p\ (N/m^2) = 12.40372 - \frac{8283.1}{T(K)} - 0.7081 \log_{10} T(K)$
Melting Point:	453.75 K
Boiling Point	1615.15 K
Heat of Fusion	30.002 kJ/gram-atom
Heat of Vaporization	157.8 kJ/gram-atom
Volume Change on Melting	1.5% of Solid Volume

Table 1.2 Physical Properties of Lithium

Solubilities of Selected Elements

Iron [1.9]:

$$\ln \{[Fe]_{Li}^{sat} \text{ (wppm) }\} = 10.41 - \frac{6988}{T(K)}$$

Chromium [1.9]:

$$\ln \{[Cr]_{Li}^{sat} \text{ (wppm) }\} = 10.98 - \frac{7508}{T(K)}$$

Nickel [1.9]:

$$\ln \{[Ni]_{Li}^{sat} \text{ (wppm) }\} = 15.33 - \frac{7814}{T(K)}$$

Nitrogen [1.10]:

$$\ln \{[N]_{Li}^{sat} \text{ (wppm) }\} = 17.22 - \frac{4688}{T(K)}$$

Oxygen [1.11]:

$$\ln \{[O]_{Li}^{sat} \text{ (wppm) }\} = 16.10 - \frac{6669}{T(K)}$$

Carbon [1.12]:

$$\ln \{[C]_{Li}^{sat} \text{ (wppm) }\} = 17.17 - \frac{8612}{T(K)}$$

Standard Free Energy of Formation of Simple Lithium Salts

Lithium Nitride [1.10]:

$$\Delta_f G^0_{Li_3N} \text{ (kJ/mole)} = -174.24 + 0.14343\ T(K)$$

Lithium Oxide [1.13}:

$$\Delta_f G^0_{Li_2O} \text{ (kJ/mole)} = -606.12 + 0.13982\ T(K)$$

Lithium Carbide [1.13]:

$$\Delta_f G^0_{Li_2C_2} \text{ (kJ/mole)} = -41.252 - 0.06188\ T(K)$$

Table 1.3 Chemical Properties of Lithium

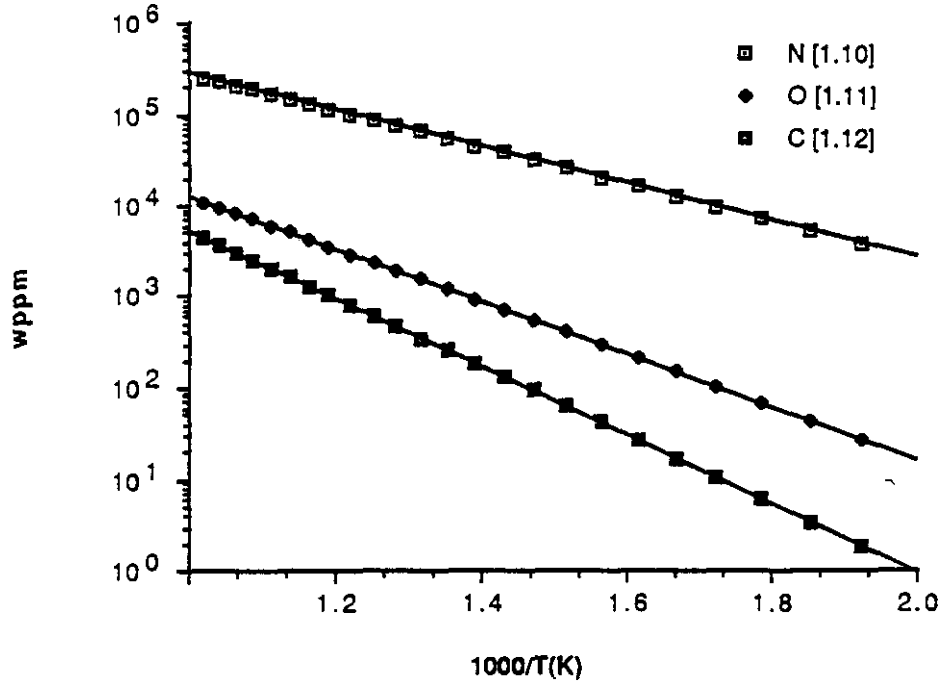

Figure 1.2 Solubility of Non-Metallic Elements in Lithium

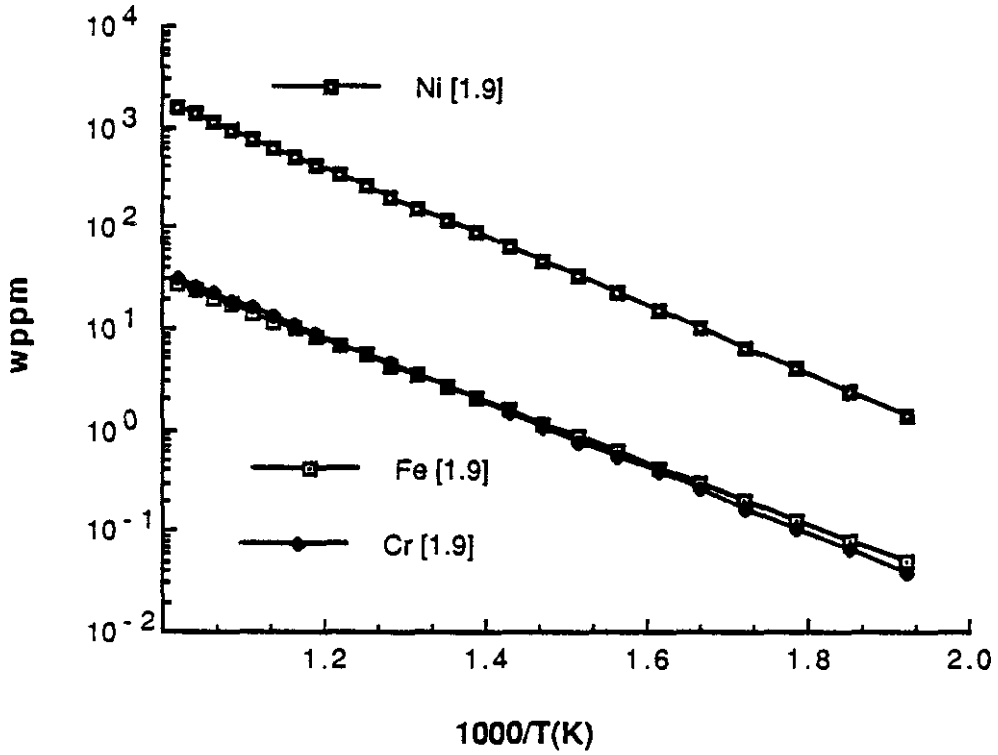

Figure 1.3 Solubility of Metallic Elements in Lithium

1.5 Overview of Liquid Metal Corrosion

Corrosion phenomena can be quite complex and liquid metal systems are no exception. The principal processes which contribute to the corrosion of structural alloys by liquid metals are simple solution (sometimes referred to as dissolution), thermal or concentration gradient mass transport, liquid metal/structural material alloying, intergranular penetration, impurity reactions, and interstitial transport [1.14]. These processes are described in Appendix A, section A.1. One or more of these typically dominate the corrosion behavior and the processes are not necessarily independent of each other. In a system which has either large changes in temperature or flow regime, the dominant mechanism may change as a function of the position in the system. Given the number and variety of processes occurring, the number of variables which affect the corrosion and deposition rates is correspondingly large. Corrosion of steels in liquid lithium is known to be a function of system temperature, system temperature differential, chemical composition (alloy, lithium and impurities), microstructure of the alloy, flow velocity, system geometry and configuration, and exposure time. Simple solution, impurity interaction, and thermal and concentration gradient transport seem to be of greatest importance in ferrous alloy systems. Interalloying of the liquid metal and structural materials may also be important, particularly for nickel-containing alloys. Interstitial transport and impurity reactions are important to vanadium alloys.

1.6 Summary

The breeding of tritium for fuel self-sufficiency in fusion reactors requires lithium in some form to be integrated into the reactor design. Liquid metal designs with liquid lithium in contact with ferritic steel alloys are thought to be attractive design concepts for fusion breeder blankets. Mass transport and corrosion processes are a major uncertainty in these design concepts. Current data and understanding are insufficient to set system parameter limits, explain observed behavior, and to help develop a suitable ferritic alloy for use in lithium systems. A better understanding of the physical processes of corrosion and mass transport must exist before technically feasible designs may progress and a ferritic alloy for lithium service for fusion reactors can be developed. This research investigates, experimentally, the interaction and develops a physical model of these processes to increase our understanding of the corrosion and mass transport processes in nonisothermal molten lithium.

This dissertation is divided into five chapters and three appendices. Chapter 2 gives a review of the most recent experimental data on corrosion in steel/lithium systems. Chapter 3 gives a description of the experiments and the results. Chapter 4 gives the analysis of the results and physical models of the corrosion processes. Chapter 5 gives a summary of the work and the conclusions. The appendices give supplemental information on previous research, elemental dissolution and deposition modeling and raw experimental data in appendices A, B and C, respectively.

1.7 References for Chapter 1

[1.1] P.F. Tortorelli and J.H. DeVan, "Corrosion of Ferrous Alloys Exposed to Thermally Convective Pb-17 At. Pct. Li," Journal of Nuclear Materials, 141-143 (1986) 592-598.

[1.2] M. Broc, T. Flament, P. Fauvet and J. Sannier, "Corrosion of Austenitic and Martensitic Stainless Steels in Flowing 17Li83Pb Alloy," Journal of Nuclear Materials, 141-143 (1986) 710-714.

[1.3] H. U. Borgstedt, G. Frees and G. Dreschler, "Corrosion of Stainless Steel in Flowing PbLi Eutectic," Journal of Nuclear Materials, 141-143(1986)561-65.

[1.4] O. K. Chopra and D. L. Smith, "Compatibility of Ferrous Alloys in a Forced Circulation Pb-17Li System," Journal of Nuclear Materials, 141-143 (1986) 566-570.

[1.5] D. L. Smith et al., Blanket Comparison and Selection Study-Final Report, Argonne National Laboratory, ANL/FPP-84-1, 1985.

[1.6] M. G. Barker, S. A. Frankham and N. J. Moon, "The Reactivity of Dissolved Carbon and Nitrogen in Liquid Lithium," in Liquid Metal Engineering and Technology, British Nuclear Energy Society, v. 2 (1985) 77-83.

[1.7] SANDVIK Steel Catalogue, S-1,720-ENG, Sandvik Steel Corporation, Scranton, PA.

[1.8] V. A. Maroni, E. J. Cairns and F. A. Cafasso, A Review of the Chemical, Physical and Thermal Properties of Lithium that are Related to Its Use in Fusion Reactors, Argonne National Laboratory, ANL-8001 (1973).

[1.9] H. W. Leavenworth and R. E. Cleary, "The Solubilities of Ni, Cr, Fe, Ti and Mo in Liquid Lithium," Acta Metallurgica, 9(1961)519-21.

[1.10] R. M. Yonco, E. Veleckis and V. A. Maroni, "Solubility of Nitrogen in Liquid Lithium and Thermal Decomposition of Solid Li_3N," Journal of Nuclear Materials, 57(1975)317-24.

[1.11] R. M. Yonco, V. A. Maroni, J. E. Strain and J. H. DeVan, "A Determination of the Solubility of Lithium Oxide in Liquid Lithium by Fast Neutron Activation," Journal of Nuclear Materials, 79(1979)354-62.

[1.12] R.M. Yonco and M.I. Homa, "The Solubility of Carbon in low Nitrogen Lithium," Journal of Nuclear Materials, 138 (1986) 117-122

[1.13] M. W. Chase, Jr. et al., "JANAF Thermochemical Tables, Third Edition," Journal of Physical and Chemical Reference Data, v. 14, no. 1, (1985).

[1.14] W. D. Manly, "Fundamentals of Liquid Metal Corrosion," Corrosion, 12(1956)336t-342t.

[1.15] D. Peckner and I. M. Berstein, Handbook of Stainless Steels, McGraw-Hill, San Francisco, (1977).

CHAPTER 2 REVIEW OF THE RECENT LITERATURE

2.1 Overview

Specific lithium compatibility research began in the early 1950's. The earliest information on lithium attack (corrosion) of materials came peripherally from the observations of chemists preparing lithium compounds. Their goal was to find a suitable container material for preparation of lithium compounds which would not contaminate the samples being prepared (DeVan et al. [2.1]). The information was qualitative and was first summarized by Miller [2.2].

Much of the early experimental work in lithium corrosion was done to screen alloys for the Aircraft Nuclear Program (ANP). The ANP materials program can be generally characterized as having high exposure temperatures, short exposure times, and variable and/or uncharacterized impurity levels in the lithium. Liquid metal compatibility research from about 1960 to 1980 was dominated by work with sodium and austenitic stainless steels with application to Liquid Metal Fast Breeder Reactors (LMFBR's). Recent interest in lithium compatibility testing comes from space nuclear and fusion power applications. The focus of this chapter is on recent experiments in lithium/ferrous alloy corrosion, specifically since approximately 1979. Prior work is summarized in Appendix A.

The emphasis of recent studies of corrosion and mass transport in lithium/ferrous alloy systems has generally been metallurgical in scope: generation of experimental data from thermal or forced convection apparatuses for a variety of alloys and microstructures.

Because of the long experimental time scales, the large number of variables affecting corrosion and mass transport, and the destructive nature of specimen examination, it is difficult to cover a significant portion of the parameter space with limited resources in a reasonable length of experimental time. Most of the corrosion data for lithium is for the behavior of austenitic steels in lithium. Some data for other ferritic alloys, including HT9, now exists.

2.2 Recent Experiments with Lithium and Steel Alloys

Plekhanov and Fedortsov-Lutikov [2.3] investigated the corrosion of 12 w/o chromium steels in a forced convection loop (FCL). The loop was constructed with both ferritic (12 w/o Cr) steel and an austenitic steel similar to type 316 SS. Only portions of the loop with lithium temperatures below 310 °C were made from the austenitic alloy. The experiment operated between ~225 °C in the "water-cooled-filter-trap" and 650 °C in the isothermal test section and specimen aging tank. Specific details of the experimental apparatus (geometry) and flow conditions (flow rate) were not given. Specimens of three different 12 w/o chromium steels with varying amounts of three strong carbide forming elements (molybdenum, vanadium and niobium) were tested for approximately 4000 hours. The results showed that mass transfer by dissolution and thermal gradient mass transfer (TGMT) of the main alloy components occurred, in descending order of severity, to chromium, iron and molybdenum. Transport of vanadium and niobium could not be detected presumably due to their low content in the alloy. Furthermore, alloying the 12 w/o chromium steel with increasing

amounts of molybdenum significantly reduced the weight losses of the specimens. Bulk decarburization (loss of carbon from the solid matrix below the surface) occurred for each of the alloys tested at 650 °C with the greatest decarburization occurring in the simple 12 w/o chromium alloy which contained no molybdenum, vanadium or niobium. Decarburization of the bulk alloy near the surface was attributed to the decomposition of $M_{23}C_6$ (M=Fe, Cr or Mo) mixed carbides in the steel due to the lithium. The steels which were alloyed with niobium, the strongest carbide former of the elements added, were the least decarburized. The decrease in decarburization was attributed to the presence of niobium carbides and molybdenum in the mixed carbide phase, which seemed to increased the stability of the $M_{23}C_6$ carbide phase. Weight losses were 31.6, 26.2 and 23.4 mg/m^2-h for the three alloys tested at 650 °C for the 12Cr, 12Cr-1MoNbV and 12Cr-2.35MoNbV, respectively. The largest weight loss was for the simple 12 w/o chromium steel (no carbide forming elements added) and the smallest weight loss was for the high molybdenum (2.35 w/o Mo) alloy. The decrease in weight loss with the addition of strong carbide formers such as molybdenum and niobium suggests that decarburization contributes to the weight loss behavior in these alloys at elevated temperatures.

Whitlow et al. [2.4] investigated the behavior of austenitic (316, 304 and 304L SS) and ferritic ($2\frac{1}{4}$Cr-1Mo and 9Cr-1Mo) steels with time in an FCL lithium loop system at 538 °C, with a system temperature differential (ΔT) of 152 °C and operating times up to 948 hours at a Reynold's number of $\sim 10^4$. The loop containment

material was 304 SS and specimens could be placed in both the hot and cold regions of the system. Nitrogen levels varied between 77 and 205 wppm during the experimental run. On-line hot trapping with titanium and zirconium foil and cold trapping and filtration were used to vary the purity of the lithium. Weight losses for all of the alloys were found to be linear with time even for the short duration (1000 hours) of the experiments. Austenitic steels were found to corrode at rates between 3 and 5 times those of the ferritic alloys due to the formation of a porous surface layer that accompanied the depletion of nickel and probably chromium [2.5]. The formation of the ferrite layer for austenitic materials was evident after only 210 hours. The 9Cr-1Mo steels had the lowest weight loss of the alloys tested. Heat treatment was found to lower weight losses by ~20 %. The most favorable heat treatment in terms of corrosion resistance to lithium was one which uniformly dispersed the carbide phase in the matrix with a minimum amount of the thermodynamically metastable Fe_3C carbide. The weight loss rates for the ferritic steels were 6.3 and 10.5 mg/m^2-h for the 9Cr-1Mo and $2\frac{1}{4}$Cr-1Mo alloys for ~1000 hours of exposure, respectively. Both types of alloys were found to exhibit a so-called "downstream effect," whereby the corrosion rate or mass flux (weight loss) decreased with downstream distance, presumably due to boundary layer saturation by the steel constituents or consumption of a reactant which forms a corrosion product. The dissimilar metal effects between the loop containment steel, however, are not assessed for the ferritic specimens and interpretation of the results is difficult due to the

competing effects of temperature and concentration gradient mass transfer, particularly for the ferritic alloys. No deposition data were reported.

Tortorelli, DeVan and Selle [2.6] conducted capsule tests with 316 SS containing 2000 wppm nitrogen at 500, 600 and 700 °C for periods up to 2000 hours. Attack of the specimens from the 500 °C test exhibited the characteristic uniform, ferritic layer which has been found to form on austenitic alloys exposed to both sodium and lithium (see Hoffman [2.5]) due to selective leaching of nickel from the surfaces in contact with the alkali metal. The tests at 600 and 700 °C exhibited severe attack along grain boundaries. The results from the higher temperature experiments were analyzed with a model for uptake of a solute (nitrogen) from a stirred solution. Temporal behavior in terms of grain boundary penetration was good for the 600 and 700 °C and poor for the 500 °C exposure. It should be noted that the nitrogen contents (activities) in these tests were extreme (2000 wppm) as compared with as-received, as-purified and system operational levels, 200-400, 10-50 and 50-100 wppm, respectively found in most experiments. These and other results from early experiments indicate that the phenomena which control corrosion at lower temperature (500 °C) were probably not the same phenomena which control at higher temperatures and that the effects of nitrogen and temperature on the processes are not singularly increasing.

Tortorelli and DeVan [2.7] and Tortorelli, DeVan and Selle [2.8] established thermal convection loop (TCL) corrosion rates for 316 SS

specimens in a 316 SS containment in lithium between 600 and 450 °C for a variety of conditions. Data from three TCL's [2.7] with T_{max}=600 °C and temperature differentials of 150 °C established, that *for austenitic systems, the shape of the mass transfer profile was such that the largest weight losses occurred at T_{max} and the largest weight gains occurred at T_{min}.* Such net transport of material from higher to lower temperature would be indicative of a corrosion process controlled by a simple solubility reaction (dissolution) of the alloy components. The transient weight loss (i.e. that period in which weight change is not linearly proportional to exposure time) period appeared to end at about 1000 hours. A maximum steady state corrosion rate of about 12 microns/year at the maximum loop temperature (T_{max}=600 °C) location was obtained for velocities on the order of 3 cm/s. Activation energy analysis of the corrosion specimens arrayed in a single hot leg yielded an activation energy for corrosion of about 25 kJ/mole. Based on this low activation energy and the linear mass loss behavior beyond 1000 hours, it was determined that boundary layer diffusion was controlling the corrosion process. The experiments and findings of Gill, et al. [2.9-10], in FCL's for much shorter exposure times give conflicting conclusions to those of Tortorelli and DeVan. Based on a different analysis of data from only the maximum temperature position in TCL's, Tortorelli and DeVan [2.11] would later conclude that mass removal was phase-boundary controlled, in agreement with Gill [2.9-10] and Hoffman [2.5], based on different, earlier data for lithium/austenitic stainless steel systems. *Deposition data for all the*

experiments were inconsistent with a single activation energy [2.7,9-10]. Stoichiometric deposition behavior was not observed. Analysis of the deposits [2.12] from one of the loops which plugged in only 1700 hours revealed that two basic types of compositions of deposits formed. X-ray diffraction of deposits salvaged from the loop showed diffraction lines characteristic of pure chromium. Semi-quantitative energy dispersive X-ray (EDX) analysis of the deposits showed compositions to be evenly distributed between iron, chromium and nickel (31Fe-47Cr-22Ni) while others were much more enriched in chromium (12Fe-83Cr-5Ni). However, elements such as oxygen, nitrogen and carbon could not be detected with EDX analysis. Further X-ray analysis on cross sections of the specimens of the underlying deposits showed that initial deposits tended to be enriched in nickel and chromium while longer term exposures gave rise to more iron-rich, indicating that the composition of the deposited material was dependent on time as well as temperature and loop position.

Additions of nitrogen and aluminum were made [2.8] to a TCL to determine the effect on corrosion behavior and profile. Aluminum was determined to inhibit corrosion by reacting with nickel on the surface to form a protective alloy layer. *Nitrogen was found to increase chromium depletion and the relative amounts of area in the loop undergoing weight loss as compared to that portion which was gaining weight.* However, additions of nitrogen did not increase the magnitude of the weight losses. Further, chromium depletion was found to be much more dependent on temperature than nickel. *Such*

behavior would indicate that a surface reaction, possibly involving nitrogen, contributes significantly to the transport of chromium.

The effect of nickel was investigated by Tortorelli and DeVan [2.13]. The results indicated that nickel depletion was so severe that use of high nickel alloys above 500 °C was doubtful. This is partially due to the high solubility of nickel in lithium. However, Barker et al. [2.14] found that the amount of nickel plate "dissolved" by 5 grams of lithium was far in excess of the solubility limit. It was suggested that interalloying of the nickel and lithium similar to that of lithium and copper might explain the large amounts of nickel consumed in their experiments. However, evidence of the nickel-lithium alloy has not been shown.

DeVan [2.15] noted that corrosion rates such as those observed by Whitlow, et al. [2.4], and Tortorelli and DeVan [2.7], could be aggravated in fusion devices due to boundary layer thinning induced by MHD interaction of the lithium with the magnetic confinement fields (see Branover [2.16]). Roy and Schad [2.17] and Schad [2.18] observed that sodium turbulent boundary layer thinning correlated well with velocity dependent corrosion behavior. Bauer [2.19] would later also find a significant velocity dependence of corrosion in lithium/316 SS systems, indicating a boundary layer rate-determining corrosion process for austenitic steels. These data indicate that convective transport may be significant for lithium/austenitic steel systems below 500 °C.

Increases in specimen weight loss with increasing velocity may be due to either an increase in the mass transfer coefficient arising

from a thinning of the velocity boundary layer or to erosion of the specimen material by the fluid. Down et al. [2.20], established that there were no significant erosive effects with lithium up to 24 m/s at 270 °C for type 304 SS. The velocity effect should then be due to increases in mass transfer coefficient with increasing velocity.

The most recent work in lithium/ferrous alloy systems has centered on characterizing the interactions of system chemistry and mass transport mechanisms. Work in both FCL's and TCL's has been performed. An increasing number of experiments are being performed on ferritic alloys with varying amounts of chromium and other alloying component (e.g., manganese and molybdenum). Austenitic steels are still being investigated, but selective leaching and transport of nickel are seen as limiting the usefulness of such alloys above 475 °C [2.21].

The importance of non-metallic impurities in lithium, particularly dissolved nitrogen, has been qualitatively known for more than 20 years, although no concrete evidence of the cause was known. Investigations at the University of Nottingham in the United Kingdom reported by Barker, et al. [2.22-23], Pulham, et al. [2.24-26] and Hubberstey et al. [2.27-28], have been primarily responsible for clarification and determination of the effects of nonmetallic impurities on lithium corrosion chemistry. It has been shown that the formation of a ternary compound of lithium, nitrogen and chromium (Li_9CrN_5) is favorable and extremely stable [2.22-23]. Barker observed that the corrosion product formed as a surface layer, which adhered to the surface after formation and was

insoluble in the lithium. However, the Li_9CrN_5 corrosion product residue is not normally observed in experiments because of the specimen cleaning procedures (i.e. washing with water and ethanol) followed in most investigations. Li_9CrN_5 is unstable in the presence of water or alcohol which are typically used to dissolve the residual lithium from specimens. Barker was only able to detect the Li_9CrN_5 by distilling off the residual lithium. Chopra and Smith [2.29] have also shown that this corrosion product may be at least semi-adherent to the surface of the alloy. In their tests, the residue from the specimen cleaning solvent (alcohol) was analyzed and evidence of the corrosion product was found. Carbon has also been shown to form dilithium cyanamide (Li_2NCN) in lithium in the presence of dissolved nitrogen in lithium. However, the extreme stability of this compound probably renders it inert in terms of corrosion processes [2.25] in a manner similar to Li_2O.

Bauer [2.19] investigated temperature and velocity effects on mass removal in a lithium/316 SS FCL system between 255 and 490 °C for exposures up to 4000 hours and lithium velocities from 0.45-1.36 m/s ($3500<Re_D<10500$) and 90 wppm nitrogen in the lithium. He used tubular specimens, which formed a continuous surface, to simultaneously measure mass removal in four isothermal test sections at different velocities. The long-term dissolution rate at 490 °C was less than that at 440 °C. Similar results have since been reported by Chopra and Smith [2.29] in both austenitic and ferritic alloys and Tortorelli and DeVan [2.30-32] in ferritic alloys. This reversal of behavior (i.e., decreasing corrosion with increasing

temperature) is thought to be a result of the competition between reactions with lithium, nitrogen, and possibly carbon with alloy elements [2.33]. Bauer found that the measured velocity dependence of mass removal was significant, but weaker than expected for boundary controlled mass transport theory or sodium mass transport behavior. However, mass deposition could not be monitored in Bauer's loop so the effect of velocity on the deposition processes could not be determined.

The work most applicable to the proposed research has been performed for the Alloy Development for Irradiation Performance (ADIP) program at Oak Ridge (ORNL) and Argonne (ANL) National Laboratories. Work at ANL is primarily in an FCL system and the work at ORNL is primarily in capsules and TCL's.

Chopra and Smith's ADIP work [2.34-37,40-41] has been devoted to both the characterization of mass transport behavior of type 316 SS and ferritic alloys, and the effect of the lithium environment on the mechanical properties of various alloys. The experimental loops at ANL are limited to a maximum temperature of about 532 °C and are constructed of 316 SS. The loop has been operated for in excess of 30000 hours, and it is assumed that the system containment is well equilibrated and does not significantly affect results for non-316 SS material specimens. Although this cannot be explicitly proven, results from this mixed metallic loop agree with those in other homogeneous loops. The specimens in the loop are located in isothermal test pots, through which the lithium flows at a total volumetric flow rate of 1 liter/minute. The results

from ANL indicate that the overall mass loss rate is linear in time after an initial transient period of 500 hours for ferritic steels and about 1500 hours for austenitic steels. The initial weight loss in ferritic alloys is due to the "etching" effect of the surface and the appearance of a dimpled or pebble-like surface structure. The source of the etching was not apparent. The size of the dimples increases with increasing temperature. In contrast, transient behavior of austenitic alloys is due to the selective leaching of nickel from the alloy surface and subsequent ferritic surface layer formation. Compositional analysis of the surface indicates that surface composition is still changing after 1700 hours for the ferritic layer even though total weight loss is linear with time. Chromium surface concentration eventually stabilizes somewhere between 6-8 w/o Cr for HT9 and austenitic alloy below 530 °C. It was concluded that surface chemistry and mass loss are not directly related. Corrosion rates in ferritic systems are typically 3-5 times lower than those in a similar austenitic system, in agreement with Whitlow, et al. [2.4].

The work of Tortorelli and DeVan at ORNL [2.30-33] is the most similar to the proposed work. Tortorelli and DeVan [2.30] were the first to investigate a structurally homogeneous lithium/HT9 TCL experiment. The temperature in the first lithium/HT9 TCL experiments was between 350-500 °C. The loop operated for about 10000 hours with small but measurable weight losses for all specimens, both in the hot and cold sections of the loop. The maximum weight loss did not occur at the maximum temperature,

but rather at the minimum loop temperature location. Additionally, more than half of the total weight loss for the 10000 hour period occurred in the first 522 hours. Although movement of steel components around the loop was not apparent from specimen weight loss data, EDX of the surface chemistry indicated depletion of chromium on the hot specimen and enrichment on cold zone surfaces. Furthermore, although the nickel content of HT9 is nominally low (0.5 w/o), nickel transport to the cold leg was observed similar to 316 SS systems. Results from a second set of experiments, with temperatures from 450-600 °C [2.33], indicate a return to "typical" net mass removal and deposition behavior from hot leg to cold leg. Surface analysis of specimens from the 600 °C location revealed a severely roughened surface, similar to the dimples reported by Chopra and Smith [2.40], and the surface was depleted of chromium. Chromium enriched nodules were found on the specimens located at 560 and 530 °C. A comprehensive explanation for this corrosion behavior is not apparent. It appears that raising the system temperature from 350-500 °C to 450-600 °C causes a shift in relative importance of at least two different and competing corrosion reactions.

Mass transport, removal and deposition in lithium/ferrous alloy systems has focused on austenitic steels. Lithium/HT9 has been investigated in 316 SS containment FCL's, where dissimilar metal effects cannot be quantified. The TCL experiments with lithium/HT9 at ORNL have investigated temperatures up to 600 °C. However, design limits have been extrapolated as high as 620 °C.

Furthermore, the observations of Tortorelli and Tortorelli and DeVan are so unexpected that independent confirmation and further investigation of the observations are needed. Additionally, there is a need to investigate temperatures at or above the extrapolated design values.

2.3 References for Chapter 2

[2.1] J. H. DeVan, J. E. Selle, and A. E. Morris, A Review of Lithium Iron-based Alloy Corrosion Studies," ORNL/TM-4927 (1976).

[2.2] E. C. Miller, "Corrosion of Materials by Liquid Metals, Liquid Metals Handbook, Second Edition, Lyon, R.N., Ed. (1952).

[2.3] G. A. Plekhanov and G. P. Fedortsov-Lutikov, "Corrosion of 12% Chromium Steel in a Nonisothermal Lithium Flow," Atomnaya Energiya, 45 (1978) 140-43.

[2.4] G. A. Whitlow, W. L. Wilson, W. E. Ray and M. G. Down, "Materials Behavior in Lithium Systems for Fusion Reactor Applications," Journal of Nuclear Materials , 85 & 86 (1979) 282-287.

[2.5] E. E. Hoffman, Corrosion of Materials by Lithium at Elevated Temperatures, ORNL-2674 (1959).

[2.6] P. F. Tortorelli, J. H. DeVan, and J. E. Selle, "Effect of Nitrogen and Nitrogen Getters in Lithium on the Corrosion of Type 316 Stainless Steel," NACE preprint no. 115, presented at Corrosion/79, March 1979, Atlanta, GA.

[2.7] P. F. Tortorelli and J. H. DeVan, "Thermal Gradient Mass Transfer in Lithium-Stainless Steel Systems," Journal of Nuclear Materials , 85 & 86 (1979) 289-293

[2.8] P. F. Tortorelli, J. H. DeVan, and J. E. Selle, "Corrosion in Lithium-Stainless Steel Thermal Convection Systems," Proc. of the Second Int. Conf. on Liquid Metal Tech. in Energy Production, J. M. Dalke, ed., Richland, WA, April 20-24, 1980 , CONF-800401-P2 (1980) 13-44 to 13-54.

[2.9] W. N. Gill, R. P. Vanek, R. V. Jalinek and C. S. Grove Jr., "Mass Transfer in Liquid Lithium Systems," A.I.Ch.E.J., 6 (1960) 139-144.

[2.10] W. N. Gill, R. P. Vanek and C. S. Grove Jr., "Mass Transfer with Liquid Lithium in Circular Conduits," A.I.Ch.E.J.,7 (1961) 216-220.

[2.11] P.F. Tortorelli and J.H. DeVan, "Mass Transfer Kinetics in Lithium-Stainless Steel Systems," Liquid Metal Engineering and Technology , BNES, London (1985).

[2.12] P. F. Tortorelli and J. H. DeVan, "Mass Transfer Deposits in Lithium-Type 316 Stainless Steel Systems," Proc. of the Second Int. Conf. on Liquid Metal Tech. in Energy Production, J. M. Dalke, ed., Richland, WA, April 20-24, 1980 , CONF-800401-P2 (1980).13-55 to 13-63.

[2.13] P. F. Tortorelli and J. H. DeVan, "Effect of Nickel Concentration on the Mass Transfer of Fe-Ni-Cr Alloys in Lithium," Journal of Nuclear Materials, 103 & 104 (1981) 633-638.

[2.14] M. G. Barker, S. A. Frankham and N. J. Moon, "The reactivity of Dissolved Carbon and Nitrogen in Liquid Lithium," *Liquid Metal Engineering and Technology*, BNES, Volume 2, (1985)77-83.

[2.15] J. H. DeVan, "Compatibility of Structural Materials with Fusion Reactor Coolant and Breeder Fluids," Journal of Nuclear Materials, 85 & 86 (1979) 249-256.

[2.16] H. Branover, Magnetohydrodynamics , John Wiley & Sons, New York (1978).

[2.17] P. Roy and M. Schad, "An Analysis of Corrosion of Steels by Liquid Sodium," Journal of Nuclear Materials, 47 (1973) 129-131.

[2.18] M. Schad, "Application of a Sodium Austenitic Corrosion Model to a Fuel Rod," Nuclear Technology, 50 (1980) 289-297.

[2.19] D. G. Bauer, Kinetics of the Degradation of 316 Stainless Steel by Lithium, Ph.D. Thesis, University of Wisconsin-Madison (1980).

[2.20] M. G. Down, A. R. Keeton, C. Bagnall and T. C. Tsu, "Erosive Effects in liquid Lithium," Journal of Materials for Energy Systems, 4 (1982) 69-77.

[2.21] D. L. Smith et al., Blanket Comparison and Selection Study-Final Report, Argonne National Laboratory, ANL/FPP-84-1, (1985).

[2.22] M. G. Barker and S. A. Frankham, "The Effects of Carbon and Nitrogen on the Corrosion Resistance of Type 316 Stainless Steel to Liquid Lithium," Journal of Nuclear Materials, 107 (1982). 218-221

[2.23] M. G. Barker, P. Hubberstey, A. T. Dadd, and S. A. Frankham, "The Interaction of Chromium with Dissolved Nitrogen in Liquid Lithium," Journal of Nuclear Materials, 114 (1983) 143-149.

[2.24] R. J. Pulham and P. Hubberstey, "Comparison of Chemical Reactions in Liquid Lithium With Those in Liquid Sodium," Journal of Nuclear Materials, 115 (1983) 239-250.

[2.25] R. J. Pulham , P. Hubberstey, M. G. Down and A. E. Thunder, "Chemical Reactions between Salts Dissolved in Liquid Lithium: Reaction of Lithium Nitride, Li_3N, with Dilithium Acetylide, Li_2C_2, to Form the Dilithium Salt of Cyanamide, Li_2NCN, in the Metal," Journal of Nuclear Materials, 85 & 86 (1979) 299-304.

[2.26] R. J. Pulham and W. R. Watson, " Corrosion of 316 Steel by Lithium-Lead Alloys under Nitrogen," Abstracts 14th Symposium on Fusion Nuclear Technology, 8-12 September 1986, Avignon, France.

[2.27] P. Hubberstey, "Dissolved Nitrogen in Liquid-Lithium a Problem in Fusion Reactor Chemistry," Liquid Metal Engineering and Technology, BNES, v. 2 (1985) 85-91.

[2.28] P. Hubberstey and P. G. Roberts, "Solutions of Lithium Salts in Liquid Lithium: The Interaction of Hydrides and Nitrides with Lead and Tin," Journal of Nuclear Materials, 120 (1984) 74-78, .

[2.29] O. K. Chopra and D. L. Smith, "Corrosion of Austenitic and Ferritic Steels in Flowing Lithium Environment," Alloy Development for Irradiation Performance: Semi-Annual Progress Report for the Period Ending March 31, 1983 , DOE/ER-0045/11.

[2.30] P. F. Tortorelli and J. H. DeVan, "Corrosion of an Fe-12Cr-1MoVW Steel in Thermally-Convective Lithium," Proc. of the Topical Conf. on Ferritic Alloys for Use in Nuclear Energy Technologies, AIME, (1984) 215-221 .

[2.31] P. F. Tortorelli and J. H. DeVan, "Corrosion of Low-Activation Austenitic Alloys and Standard Fe-12Cr-1MoVW Steel in Thermally Convective Lithium," Alloy Development for Irradiation Performance: Semi-Annual Progress Report for the Period Ending September 30, 1984, DOE/ER-0045/13.

[2.32] P. F. Tortorelli and J. H. DeVan, "Corrosion of Path A PCA, Type 316 Stainless Steel, and 12Cr-1MoVW Steel in Flowing Lithium," Alloy Development for Irradiation Performance: Semi-Annual Progress Report for the Period Ending March 31, 1983 , DOE/ER-0045/10.

[2.33] P. F. Tortorelli, "Corrosion of Ferritic Steels by Molten Lithium: Influence of Competing Thermal Gradient Mass Transfer and Surface Product Reactions," Journal of Nuclear Materials, 155-57 (1988) 722-727.

[2.34] O. K. Chopra and D. L. Smith, "Environmental Effects on Properties of Structural Alloys in Flowing Lithium," Alloy Development for Irradiation Performance: Semi-Annual Progress Report for the Period Ending September 30, 1984 , DOE/ER-0045/13.

[2.35] O. K. Chopra and D. L. Smith, "Corrosion of Austenitic and Ferritic Steels in Flowing Lithium," Alloy Development for Irradiation Performance: Semi-Annual Progress Report for the Period Ending March 31, 1985 , DOE/ER-0045/14.

[2.36] O. K. Chopra and D. L. Smith, "Corrosion of Austenitic and Ferritic Steels in Flowing Lithium Environment," Alloy

Development for Irradiation Performance: Semi-Annual Progress Report for the Period Ending September 30, 1985 , DOE/ER-0045/15.

[2.37] O. K. Chopra and D. L. Smith, "Corrosion of Austenitic and Ferritic Steels in Flowing Lithium Environment," Alloy Development for Irradiation Performance: Semi-Annual Progress Report for the Period Ending March 31, 1983 , DOE/ER-0045/11.

[2.38] O. K. Chopra, "Effects of Sodium and Lithium Environments on Mechanical Properties of Ferrous Alloys," Journal of Nuclear Materials , 115 (1983) 223-238.

[2.39] O. K. Chopra, D. L. Smith, P. F. Tortorelli, J. H. DeVan, and D. K. Sze, "Liquid Metal Corrosion," Fusion Technology , 8 (1985) 1956-1969 .

[2.40] O. K. Chopra and D. L Smith, "Influence of Temperature and Lithium Purity on Corrosion of Ferrous Alloys in a Flowing Lithium Environment," Journal of Nuclear Materials, 141-143 (1986) 584-591.

[2.41] O. K. Chopra and D. L Smith, "Compatibility of Ferritic Steels in Forced Circulation Lithium and Pb-17Li Systems," Journal of Nuclear Materials, 155-157 (1988) 715-721.

CHAPTER 3 EXPERIMENTAL RESEARCH

3.1 Introduction

In order to develop an understanding of the corrosion mechanisms of Fe-12Cr1MoVW in lithium, a cooperative effort between the Alloy Development for Irradiation Purposes (henceforth, ADIP) Program at Oak Ridge National Laboratory (ORNL) and the Fusion Nuclear Technology Program at the University of California, Los Angeles (UCLA) was initiated. The present dissertation research was performed in the context of this cooperation. Experiments for this dissertation were conducted at ORNL using a new thermal convection loop design. The experimental method and data collected for this dissertation are presented in this chapter. A discussion and analysis of the data and a description of the mechanism are given in Chapter 4.

The principal experiments involved thermal convection loops (TCL's). To facilitate understanding of the experimental results, material homogeneity and geometric simplicity were stressed during the design and fabrication of these TCL experiments. These modifications have necessitated changes in the design and fabrication of the TCL systems, relative to those of the ORNL design. The details of the design, methods, and results from the TCL experiment are presented below.

3.2 Experimental Design and Apparatus

3.2.1 Design of the Apparatus

A schematic of the UCLA TCL design used in this research is shown in Figure 3.2.1 and a photograph of one of the fabricated loops is shown in Figure 3.2.2. The two layers of 2.5 cm thick thermal insulation had been removed to show the details of the heater configuration. The body of the loop was formed by connecting 3.2 cm ID tubing to a 3.5 liter (3500 cm^3) surge tank, which served as the containment for the heated, cross-over and cooled legs. Standpipes on top of the surge tank, aligned with the centerlines of the heated and cooled legs, allowed periodic removal and insertion of the specimens and access to the surge tank for sampling of the molten lithium without interruption of the lithium flow. Full-port ball valves with teflon seals allowed limited access to the stand pipes and the loop.

A different style of mass transfer specimen was utilized for these experiments relative to other TCL experiments. The ORNL TCL design uses small (0.79 cm x 1.90 cm x 0.09 cm), flat, discrete specimens wired to flexible thin rods to insert their mass transport specimens into the heated and cooled leg tubes (1.57 cm ID) of the loop. The mass transfer specimens for these investigations were short tubular pieces (1.90 cm OD, 1.57 cm ID x approximately 3.81 cm long) and are shown in Figure 3.2.3. Each loop contained 42 specimens (20 and 22 in the heated and cooled legs, respectively). The specimens were stacked one on top of the other to form a continuous tube. The specimens were isothermally annealed (30

minutes @ 1050 °C , 2.5 hours @ 780 °C in argon atmosphere) and mechanically polished to 30 and 0.3 micron finishes on the outside and inside surfaces, respectively, to provide the starting microstructure and surface finish. The stack of specimens was axially supported by a specimen sheath (2.54 cm OD x 0.17 cm wall) tube which forms a close-fitting annular containment. Flow was directed through the inside diameter of the specimens by flow reducers at the bottom of both the heated and cooled legs on which the specimen sheath tube rested after insertion. Threaded retraction rods and matching threaded ends on the sheath tubes allowed insertion and removal of the specimens. The tapered end of the retraction rod also provided flow control at the top of the heated and cooled legs. The retraction rod, specimen stack and specimen sheath tube are shown in Figure 3.2.4. A comparison of the parameters of the UCLA and ORNL TCL designs is shown in Table 3.2.1. Details of the ORNL design can be found in DeVan and DiStefano [3.1].

The loops were filled through the surge tank and could be drained into a 14.0 liter (14000 cm^3) capacity, removable dump tank through a freeze-valve located at the bottom of the loop. The volume of the dump tank was sufficient to accommodate two charges of lithium from the loop. The freeze valve was formed by partially flattening a 1.27 cm OD x 0.1 cm wall 316 SS tube which was welded to the drain stub, the lowest point in the loop, and was connected to the dump tank inlet line via compression fittings. Since lithium is a solid at room temperature (T_{melt}^{Li}=181 °C), if an extended surface (the flattened portion of the tube) was cooled by blowing air over the

extended surface, the lithium froze in the near room temperature line and flow out of the loop was prevented during operation. Upon thawing the frozen section of the extended surface with an external tubular heater or by conduction from an over temperature loop, flow in the valve could be established in order to empty the loop, either by gravity or assisted by gas pressure applied in the surge tank. Thus, the freeze valve acted both as "non-mechanical" and over-temperature safety valves.

Although lithium is the least reactive of the alkali metals, lithium readily reacts with oxygen, nitrogen and moisture in the environment. However, if lithium is brought in contact with air at temperatures above 300 °C, it spontaneously ignites and burns exothermically. Molten lithium will also burn when contacted with thermal insulators and concrete. As mentioned in the introduction, lithium corrosion of structural materials is sensitive to atmospheric contaminants such as nitrogen. In the interest of safety and maintaining lithium purity, it was necessary to protect the lithium in the loops from contact with air and other impurities. A stagnant cover gas of commercial purity argon gas (99.999% Ar by volume) with a typical pressure of 100 to 150 kPa protected the lithium from contact with air. In addition, the surge tanks, access ports and vessels such as loop stand pipes, were evacuated to less than 1 Pa with a mechanical vacuum pump and purged with argon three times to reduce contamination. However, in spite of these precautions, some contamination by nitrogen and oxygen, probably from the

specimen insertion and removal procedures, of the loops was observed. See the section on lithium chemistry.

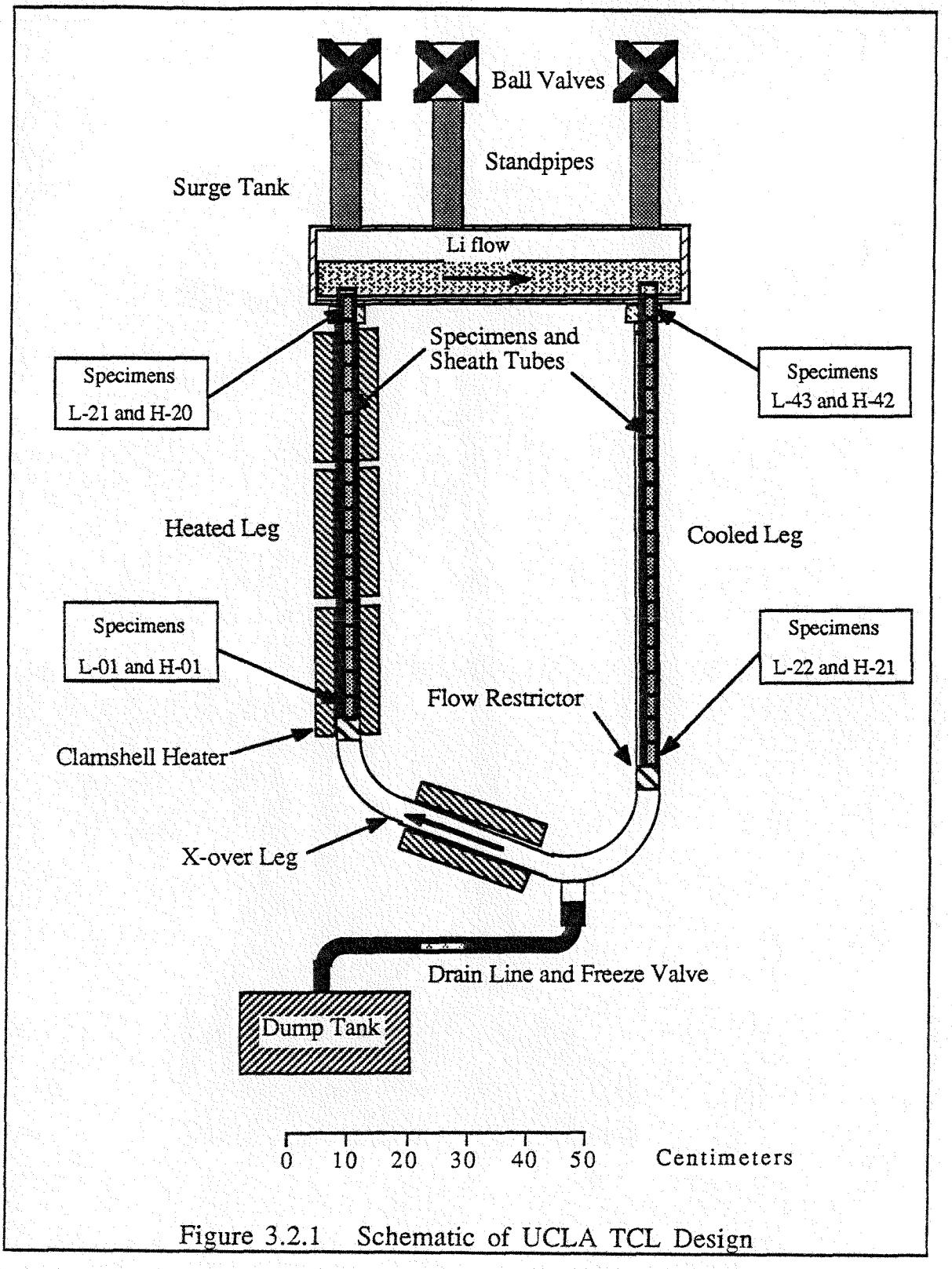

Figure 3.2.1 Schematic of UCLA TCL Design

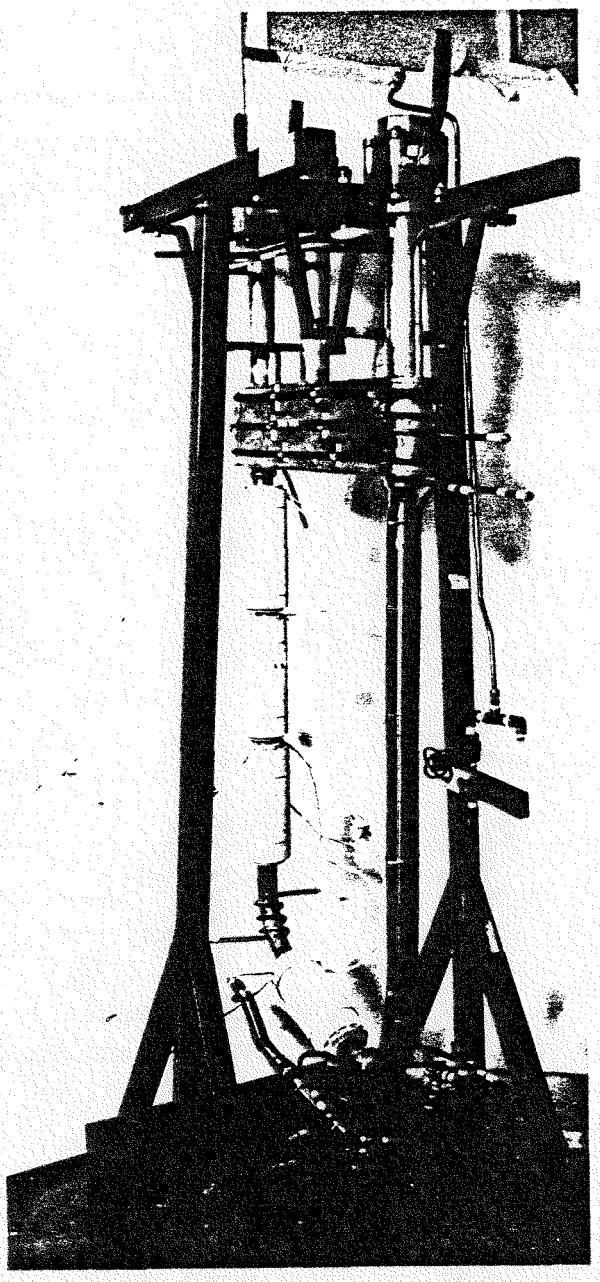

Figure 3.2.2 Photograph of Un-insulated TCL (YP-3437)

Design Characteristic	ORNL Design	UCLA Design
Specimen Geometry	Rectangular, flat	tubular
Surge Tanks	two	one
Main Body Tubing (cm)	1.6 ID	3.2 ID
Lithium Velocity (cm/s)	2-3	5-10
Flow Reynold's #	500-700	1200-2300
Volume of Lithium (liters)	2.5	5.3
Total Area to Lithium Volume Ratio (m^{-1})	77.2	144.7
Specimen Area to Lithium Volume Ratio (m^{-1})	1.7	34.9

Table 3.2.1 Comparison of UCLA and ORNL TCL Designs

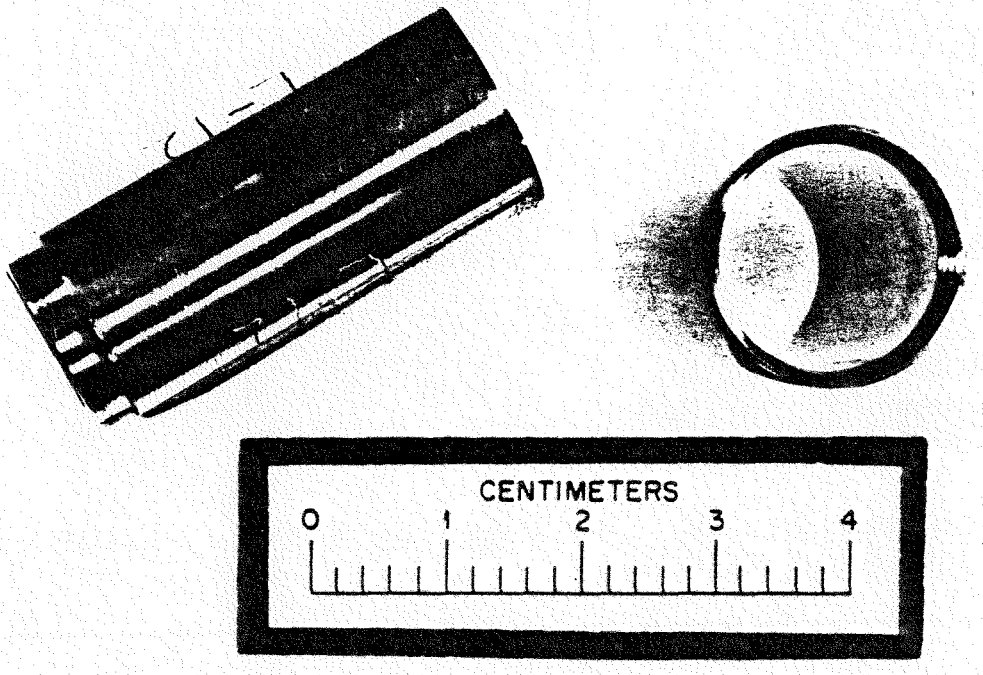

Figure 3.2.3 Mass Transfer Specimens (YP-3728)

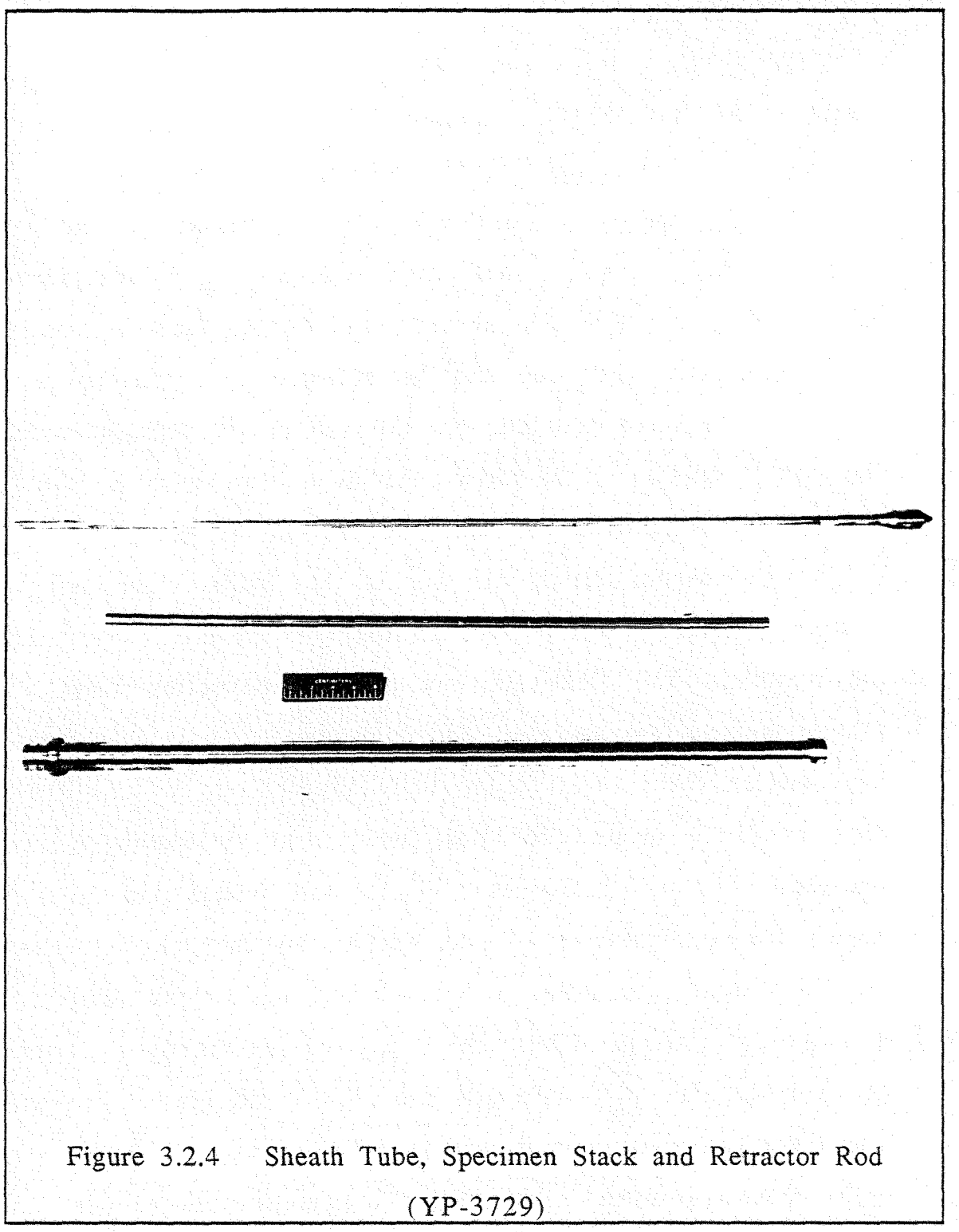

Figure 3.2.4 Sheath Tube, Specimen Stack and Retractor Rod (YP-3729)

3.2.2 Operation

Two TCL's were operated to cover the temperature range between 355 and 655 °C. Loops GEB-1 and GEB-2 operated from approximately 355 to 505 °C for 3040 hours and 520 to 655 °C for 2510 hours, respectively. Lithium velocities between 5 and 10 cm/s were measured using the "hot slug" [3.2] at temperature differentials of less than 150 °C. The absolute and differential temperatures and flow velocity in the loop can be adjusted by variation of heater inputs on the surge tank and the hot and cooled legs, adjustment of the flow restriction at the top of the heated leg specimen sheath tube and/or addition/removal of insulation around the loop.

Heat was provided to the loop via four pairs (eight total) of half clamshell heaters, which provide the temperature differential and the major driving force for the natural convection flow. Other tubular heaters are strapped and tack welded with Nichrome wire and stainless steel sheet to the body of the loop so that the entire loop could be heated for post weld heat treatment, filling and operation. Table 3.2.2 gives a list of the heaters and Figure 3.2.5 shows the configuration of the heaters on the loops. The total thermal input available to the loop was approximately 16.4 kilowatts. During operation, the average thermal input was approximately 6 and 7 kilowatts for GEB-1 and GEB-2, respectively. The higher thermal input power to GEB-2 was required due to the higher heat loss rates in the higher temperature range. In order to allow greater flexibility in temperature control, the clamshell heaters were electrically wired into two separate circuits of two pairs each.

Figure 3.2.6 shows the circuit diagram for the clamshell heaters. The top circuit of clamshell sets "C" and "D" was supplied by the 30 ampere 220 Volt controller power supply. The controller cycled the current to the "C" and "D" to maintain the set point temperature which was recorded on a strip chart recorder. The lower sets of heaters "A" and "B" were supplied by a constant current output separate, auxiliary 30 ampere 208 Volt power supply. By adjustment of the various heater inputs, temperature set point and control point, removal or addition of insulation and flow restriction with retractor rods, the temperature distribution around the loop could be tailored to suit the desired experimental conditions.

Heater Designation	Location	Type and Rating
A1	Cross-over	1/2 Clamshell, 640 W @ 115 V
A2	Heated Leg-1	1/2 Clamshell, 640 W @ 115 V
B1	Cross-over	1/2 Clamshell, 640 W @ 115 V
B2	Heated Leg-1	1/2 Clamshell, 640 W @ 115 V
C1	Heated Leg-2	1/2 Clamshell, 640 W @ 115 V
C2	Heated Leg-3	1/2 Clamshell, 640 W @ 115 V
D1	Heated Leg-2	1/2 Clamshell, 640 W @ 115 V
D2	Heated Leg-3	1/2 Clamshell, 640 W @ 115 V
T1, T2	Surge Tank	Tubular, 2600 W each @ 240 V
T3, T4	Cooled leg	Tubular, 1600 W each @ 240V
T5	Drain Stub	Tubular, 750 W @ 115 V
T6	Freeze Valve	Tubular, 1500 W @ 240 V
T7	Radius	Tubular, 600 W @ 240 V

Table 3.2.2 TCL Heater Specifications

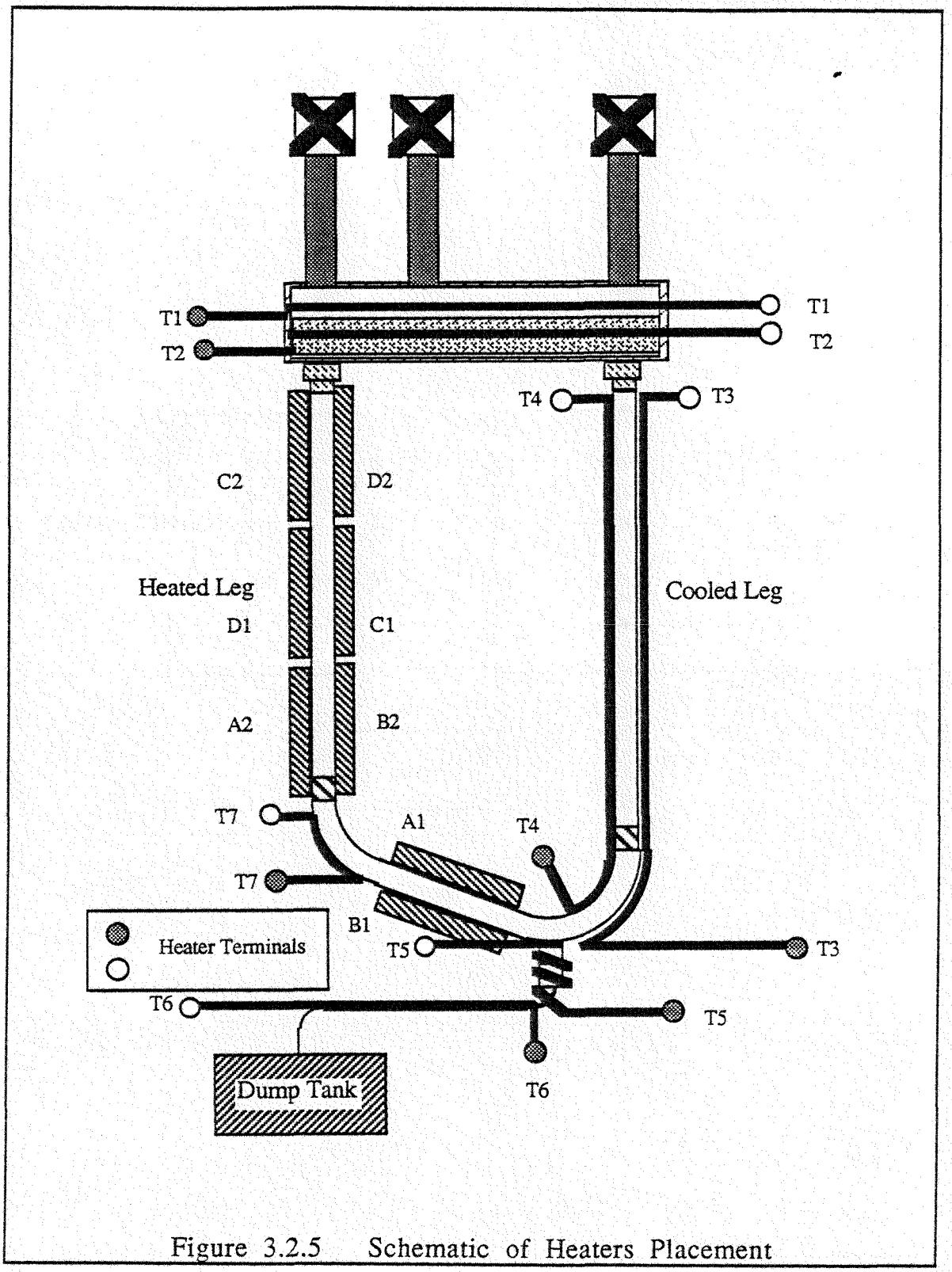

Figure 3.2.5 Schematic of Heaters Placement

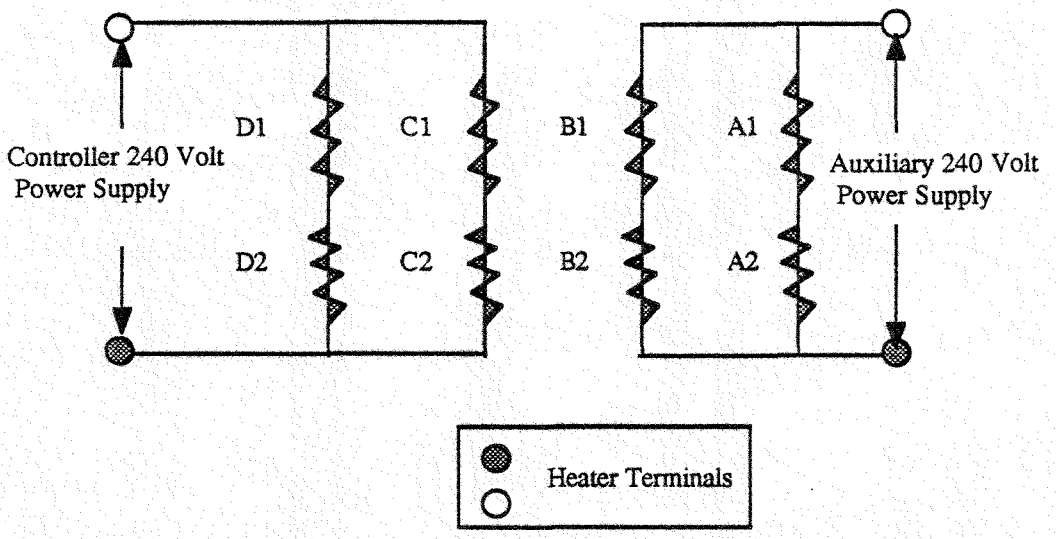

Figure 3.2.6 Circuit Diagram for Clamshell Heaters

3.2.3 Structural and Specimen Materials

All structural and specimen material in contact with liquid lithium was taken from the plate, bar and tube stock provided from GA Technologies from the fusion alloy stockpile which has been maintained for the ADIP program. The only exceptions were retraction rod ends for specimen insertion and withdrawal which were made from Fe-9Cr-1Mo material and the freeze valve which was 316L SS, due to a shortage of Fe-12Cr-1MoVW bar stock. The surface area of this Fe-9Cr-1Mo piece was less than 0.1% of the total loop and specimen surface area and the composition and microstructure were similar to that of the host material. The lithium frozen in the freeze valve could not enter the main stream flow. The presence of these slight chemical inhomogenieties does not significantly affect the overall mass transport process because of the small surface areas of the Fe-9Cr-1Mo material and austenitic steels. The composition of the Fe-12Cr-1MoVW plate, bar and tube stock was determined by spectroscopic methods. The results of the analysis are given in Table 3.2.3. The surge tank standpipes, in contact with the inert gas phase, were fabricated from 1 1/2" Schedule 40 pipe, type 304L stainless steel. Since these alloys were not in contact with the liquid phase, no chemical analyses were performed.

Sample	1.5" Tube	1.0" Tube	0.75" Tube	0.25" Plate	Average
Element	(w/o)	(w/o)	(w/o)	(w/o)	(w/o)
C	0.20	0.20	0.20	0.19	0.20
Mn	0.70	0.73	0.74	0.68	0.71
P	0.02	0.20	0.20	0.017	0.02
S	0.002	0.004	0.003	0.007	0.004
Si	0.14	0.16	0.14	0.20	0.16
Ni	0.42	0.42	0.41	0.41	0.42
Cr	11.91	12.00	11.93	11.95	11.96
Mo	1.04	1.04	1.05	1.04	1.04
V	0.24	0.24	0.23	0.24	0.24
Nb	0.005	0.009	0.008	0.004	0.006
Ti	0.002	0.002	0.002	0.002	0.002
Co	0.073	0.074	0.072	0.071	0.072
Cu	0.09	0.08	0.08	0.07	0.08
Al	0.010	0.008	0.009	0.001	0.006
B	<0.001	<0.001	<0.001	<0.001	<0.001
W	0.39	0.40	0.39	0.40	0.40
As	0.011	0.015	0.013	0.007	0.01
Sn	0.004	0.005	0.004	0.003	0.003
Zr	<0.001	<0.001	<0.001	<0.001	<0.001
N	0.040	0.043	0.045	0.045	0.043
Fe	balance	balance	balance	balance	84.65

Table 3.2.3 Chemical Composition of Materials Used

3.2.4 Fabrication and Preparation of the Loops

The specimens and specimen insertion/removal system used in this research were much larger and less flexible than the ORNL standard design which necessitated an increase in loop size (tubing diameter and tank volume) and the imposition of strict alignment tolerances for the fabrication of the loops. Alignment of the centerlines from the bottom of each of the heated and cooled legs to the top ball valve flange (~1.5 m) was required to be ± 1° during manufacturing in order to assure that tolerances for removal and insertion of specimens could be met at operating temperatures Relative to the ORNL design, the heated leg and cooled leg surge tanks have been joined to form a single surge tank volume. The heated leg cross over tube has been eliminated which provided greater mechanical stability, stiffness and alignment for the system and accommodated the less flexible specimen insertion and removal system.

The main body of the loops was constructed by the Central Shops at ORNL from the material provided by GA Technologies. All welds were made by the Tungsten Inert Gas (TIG) welding method. All similar metal (Fe-12Cr1MoVW to Fe-12Cr1MoVW) welds in contact with lithium were of the full-penetration-type with type ER505 filler rod material with a weld zone preheat to ~400 °C. Dissimilar metal weldments (304L to Fe-12Cr1MoVW at the standpipes) were fillet welded with Type 82T filler rod material. Each weldment was dye-penetrant checked for flaws after the initial root pass and after the final cover passes to check weldment

integrity. If flaws were discovered, the weld was ground out, re-prepped and welded and checked again for flaws. After manufacturing, the remainder of the loop equipment was assembled by ORNL personnel and the author. After assembly, the loops were flushed with acetone and alcohol to remove any grease or dirt which may have been left after manufacturing and each of the heater sub-systems were tested before filling the loops with lithium.

After assembly and prior to filling the loops with lithium, the loop assemblies were stress relieved and post-weld heat treated by heating the loop to 750 °C for 1 hour while evacuating the inside of the loops to less than 1 kPa (to prevent oxidation of the inside surfaces). After stress relief and before filling the loops with lithium, the loops were brought back to room temperature and pressure and vacuum tested to determine if any leaks had resulted. When leaks were detected in the loop after fabrication, assembly and heat treatment, the source of the leak(s) was determined by soap checking the weldments and the failed welds were repaired and stress relieved.

3.2.5 Lithium Purification and Preparation

Each loop had an operating volume of approximately 5.3 liters (5300 cm^3) with the surge tanks filled to 9 cm from the bottom. Due to its chemical reactivity, lithium is an excellent surface cleaner. A flush charge of lithium was used to remove any remaining surface contamination which may have persisted on the inside surfaces after other cleaning methods. The loops were filled with a flush charge of

purified lithium and operated nearly isothermally at 400 °C with temperature differential of less than 50 °C for 48 hours. After the loops operated for the 48 hours the flush charge was discarded into the dump tank and the loop immediately refilled with the operational charge of lithium from the same purification batch. Thus, each loop required approximately 11 liters for flush and operational fills or 22 liters of purified lithium for both experiments.

The lithium for these experiments was taken from the ORNL inventory designated as Drum-78. The material in Drum-78 was purchased in 1978 from Lithium Corporation of America as a 90 kg batch sealed in an inert environment of a specially designed 55-gallon drum. The chemical analysis of the as-received and as-purified batches 78-4 and 78-5 material are shown in Table 3.2.4.

Date	Batch Designation	Oxygen (wppm)	Nitrogen (wppm)
9/79	Drum 78	135	161
3/87	Drum 78	610	372
4/87	78-4[a]	200	25
6/87	78-5[b]	170	13

[a]Flush and Fill for GEB-1
[b]Flush and Fill for GEB-2

Table 3.2.4 Chemical Analysis of Drum 78, Batches 78-4 and 78-5

Purification of lithium for these types of experiments (i.e. material compatibility) centers on the removal of non-metallic impurities oxygen, carbon and nitrogen. As mentioned in the

introduction and literature reviews, dissolved nitrogen in lithium is known to affect the corrosion of steel. Oxygen is inert in lithium due to the thermodynamic stability of Li_2O. However, oxygen is easily removed and is done so routinely during the purification (cold trapping and filtration) processing. As-received lithium was first filtered and cold trapped and then hot trapped (gettered) to remove non-metallic elements. A description of this processing is given below.

Filtration and Cold Trapping

The lithium transferred out of Drum 78 was first passed through a 10 micron filter at approximately 250 °C before being delivered into the ORNL cold trapping system. The solubilities of nitrogen, oxygen and carbon in liquid lithium were shown in Figure 1.3. Cold trapping is a solubility-driven technique whereby impurity species are removed by precipitation of the impurities as salts (e.g. Li_2O and Li_2C_2). There are two types of cold trapping processes, physical and diffusion. Physical cold trapping relies on homogeneous precipitation and settling or filtration of salt species for removal. Diffusion cold trapping relies on diffusion of species to a frozen interface where heterogeneous nucleation and growth of salt deposits occurs. Both physical and diffusion cold trapping require that the elements be sparingly soluble near the melting point. Oxygen and carbon are most effectively removed by the cold trapping and filtering of Li_2O and Li_2C_2, respectively. Lithium nitride, Li_3N, cannot be removed by cold trapping, per se, due to its large solubility near

the melting point of lithium (> 1000 wppm @ 181 °C). Physical cold traps have been shown to be most effective for removing oxygen and carbon from lithium. Diffusion cold traps are ineffective in lithium as compared to sodium, where they are extremely effective in removing oxygen [3.3]. The ORNL cold trapping system used in this work was a physical cold trap, based on the General Electric design [3.4]. In the GE cold trap, natural convection flow is established by a small temperature gradient in the cold trap volume. The liquid lithium in batches 78-4 and 78-5 used for loops GEB-1 and GEB-2 was cold trapped by holding the system at 200 and 205 °C, respectively, with a temperature differential of less than 3 °C for more than 300 hours, which reduced the oxygen content of the lithium from more than 600 to approximately 200 wppm.

Hot Trapping (Hot Gettering)

The lithium transferred out of the cold trap was passed through a 5 micron filter at approximately 250 °C before being delivered into the ORNL hot trapping system. Removal of nitrogen was done by hot trapping, also known as hot gettering. When lithium is contacted with zirconium or titanium at elevated temperatures (700 to 800 °C), dissolved nitrogen can be favorably redistributed to the zirconium and titanium metal, forming a nitride film, and increasing the nitrogen content of the bulk refractory metal. The hot traps used were titanium-lined stainless steel vessels with corrugated zirconium (1.25 mm thick) foil inside the titanium liner as the getter material (surface area to volume ratio of

approximately 0.40 cm^{-1}). The lithium used to flush and refill the loops was purified by hot trapping 12.0 liter batches at 815 °C for more than 100 hours which reduced the nitrogen content of the lithium from 372 to less than 40 wppm.

3.2.6 Data Acquisition, Instrumentation and Control

The Thermal Convection Loop Facility (TCLF) at ORNL is capable of simultaneously operating up to nine TCL's at any one time. GEB-1 and GEB-2 occupied positions 4 and 6, respectively, in the TCLF. Each of the nine loop positions was instrumented with 13 type-K (Chromel-Alumel) thermocouples with an accuracy of ±1 °C and sensitivity ±0.1 °C. Ten of the thermocouples monitored the temperature distribution in the experiment and one thermocouple each were used for the temperature controller and high and low temperature alarm systems. The position of each thermocouple is shown in Figure 3.2.7. Spare thermocouples were installed at each position to minimize repair time due to the inevitable failure of thermocouples. The ten temperature distribution thermocouples send simultaneous inputs to a Leeds-Northrup 30-point cycling chart recorder and a Hewlett-Packard 3497A data logger. The chart recorder was intended as an analog output of the temperature distribution while the data logger periodically digitally records the temperature distribution. The data logger was driven by a Hewlett-Packard 9826 desk top computer. The computer was programmed to print and record the thermocouple outputs at intervals of 2 and 4 hours, respectively. The recorded temperatures were stored on floppy diskettes and provided the temperature history of the experiments. The high and low temperature alarms were Barber-Coleman model 72E meters, which sense when the input temperature was above or below pre-determined temperature set points (700 and 250 °C, respectively). These alarm systems provided both audible

and electronic signals. The electronic signals are transmitted via phone lines to the Shift Supervisor's office which was manned 24-hours a day. In the event of an alarm, Shift Patrol personnel are sent to investigate the situation and if necessary, personnel responsible for experiments in the TCLF were alerted.

The systems described above only monitor the temperatures in the loop. Temperature control was derived from a Leeds-Northrup proportional-band controller. The controller received input from a thermocouple located at the top of the heated leg. This was the control point temperature. The current to the top set of (C and D) clamshell heaters was cycled such that the control point thermocouple was maintained at the set point temperature on the chart recorder. The chart recorder gives an analog output of the control point variation. These variations were typically less than 5° C, primarily due to daily and seasonal changes in the laboratory heating, air-conditioning and ventilating system which removes heat from the cooled leg. Periodic adjustments were made in the control point and the controller parameters to re-adjust the temperature distribution to compensate for the seasonal changes. The total uncertainty in temperatures reported are ± 5 °C. Typical temperature profiles for the two experiments are shown in Figures 3.2.8 and 3.2.9.

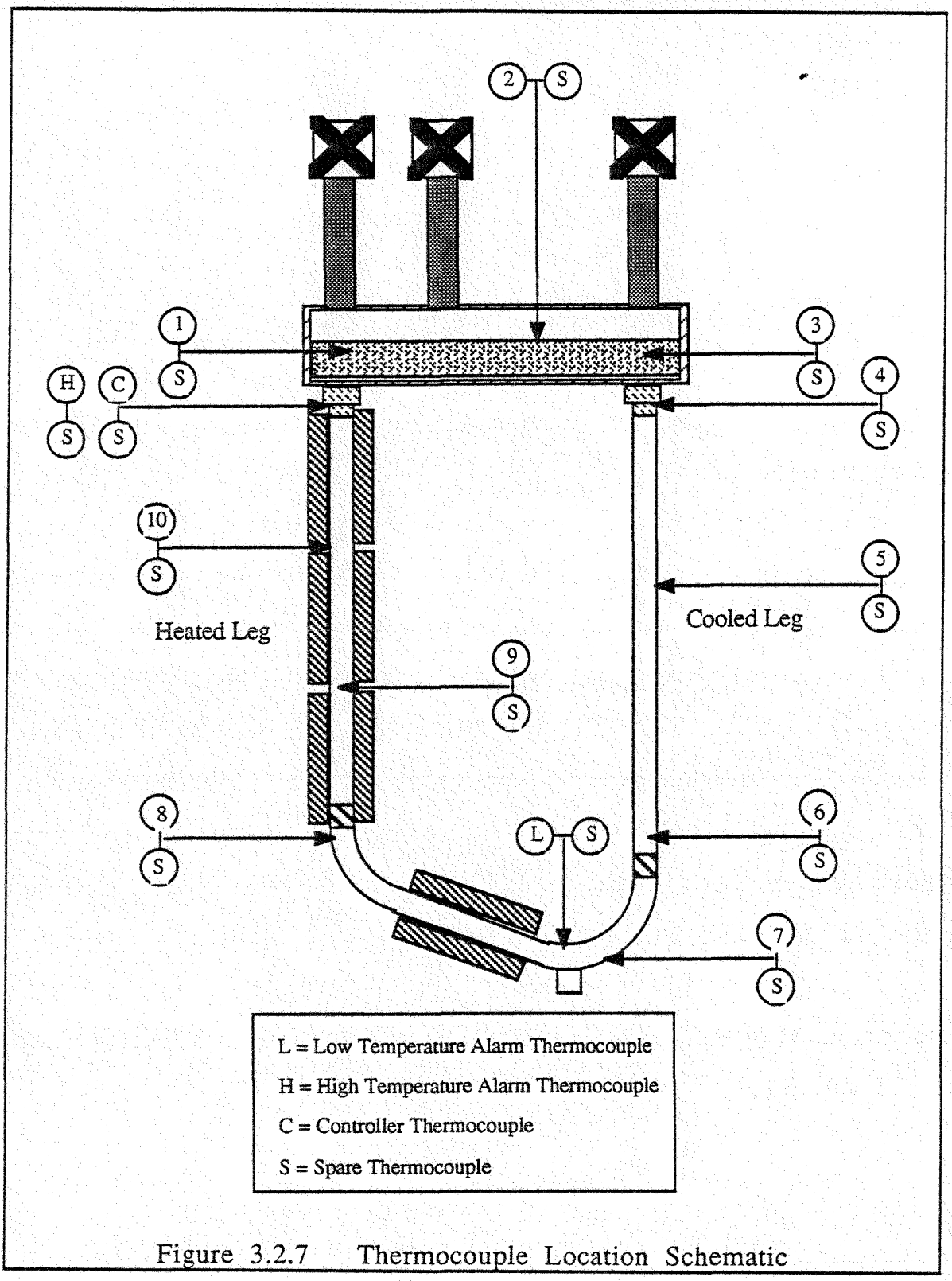

Figure 3.2.7 Thermocouple Location Schematic

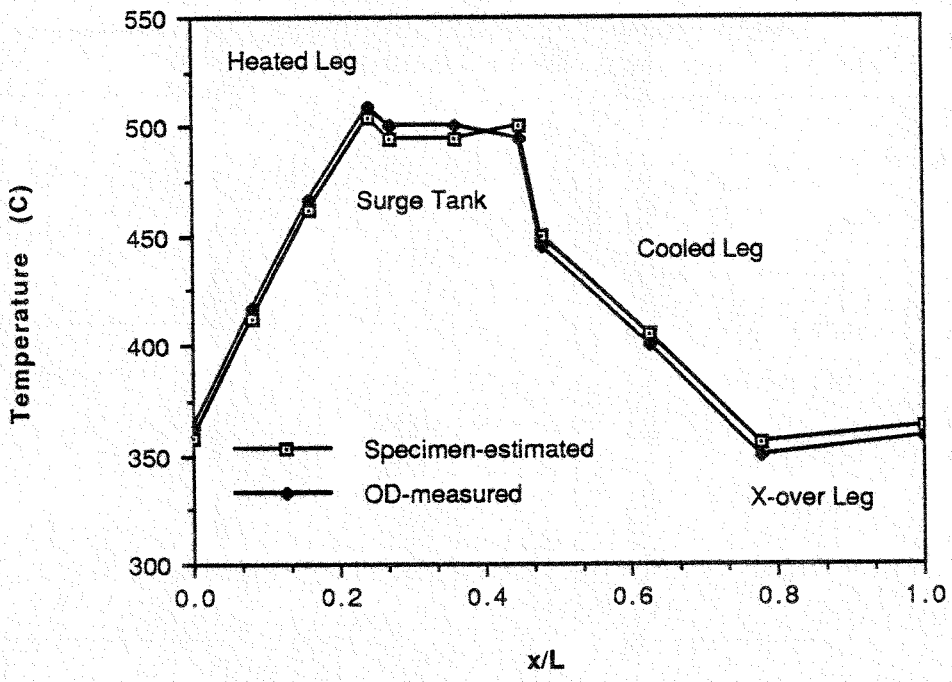

Figure 3.2.8 Typical Temperature Distribution GEB-1

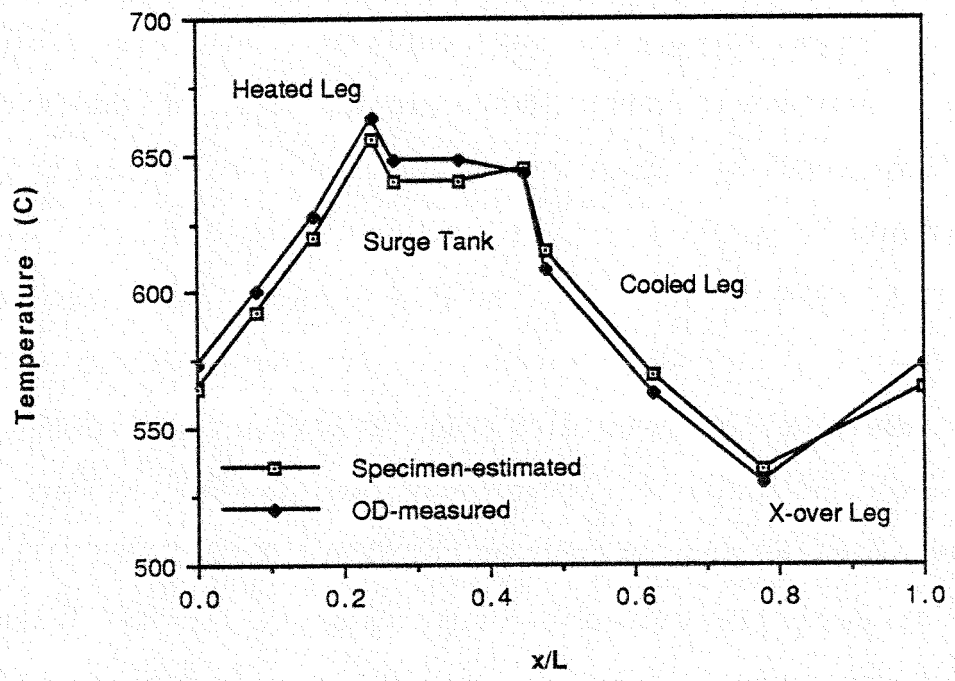

Figure 3.2.9 Typical Temperature Distribution GEB-2

3.2.7 Specimen Data

The specimens were withdrawn, or "pulled", 8 times during the course of operation for each loop. The times of the corresponding pull numbers are shown in Table 3.2.6. GEB-1 operated for 3040 hours of specimens exposure and is still in operation at ORNL at the time of this writing. GEB-2 has been drained and retired from service after 2510 hours due to failure of a teflon seal on the heated leg ball valve of GEB-2. Continued safe operation of loop GEB-2 could not be assumed and repair and/or replacement of the seal would have introduced an unknown amount of contamination into the experiment.

Both experiments experienced deviations in temperature for short periods of time due to controller problems. These errors were usually less than 10 °C for less than 48 hours. Additionally, GEB-2 had three unscheduled operational shutdowns. Two of the shutdowns were due to failure of the controller/power supply system and one was due to a faulty clamshell heater. In one case, the shutdown occurred while the specimens were already out of the loop for a scheduled pull. In the other two cases, the specimens were frozen in the loop. After repairs were made, the loop was slowly heated and the specimens were extracted at a relatively low temperature (~ 250 °C) and the specimens were cleaned and weighed as usual. The loop was then reheated to the operating temperature and allowed to equilibrate for at least 24 hours before re-inserting the specimens. The effect of these transients on the experimental

data cannot be easily assessed and does provide some unquantifiable, but small, amount of experimental error for GEB-2.

Exposure Time (hours)		
Pull #	GEB-1	GEB-2
1	97	95
2	292	292
3	460	459
4	984	1014
5	1496	1235
6	1996	1497
7	2505	1840
8	3040	2540

Table 3.2.5 Sample Pull Log

Specimens were inserted and withdrawn through the stand pipes. Special specimen transfer standpipes (STS) were fabricated by welding together pieces of 1-1/2" schedule 40, type 304L stainless steel and mild steel pipe. The mild steel end of the pipe was threaded with a standard pipe thread which matches the mild steel threaded coupling on the top of the ball valves on the surge tanks. Mild steel was used at the coupling joint to avoid galling problems encountered when both the male and female ends of the thread are stainless steel. A Conax™ fitting welded to a stainless steel reducing coupling on the stainless steel end of the STS allows the 3/8" diameter stainless steel rod on the retractor piece to pass through along the centerline of the STS. A teflon seal in the Conax fitting maintains a gas tight seal as the rod passes through it during insertion and removal of the specimens. Argon gas pressure (20 kPa gauge) inside the the STS prevents air from contaminating the STS

and, thus, the surge tank atmospheres. The STS's were evacuated to less than 1 Pa via a valve connected to a mechanical vacuum pump. After evacuation the STS's were back filled with commercial purity argon to the pressure of cover gas in th surge tank before opening the ball valves.

After removal from the loop, the specimens were rinsed with water and alcohol to remove residual lithium, dried in a drying oven at 170 °C for 30 minutes, and weighed on either a Mettler AK160 or AE240 analytical balance. The measured precision of the Mettler AE240 was $\pm$ 2 x 10^{-5} grams and that of the Mettler AK160 was $\pm$ 2 x 10^{-4} grams for determination of absolute weight. For specimens with a surface area of 4.3 x 10^{-3} m^2, the precision of weight change determinations was $\pm$ 1 x 10^{-1} and $\pm$ 1 x 10^{-2} g/m^2 for the Mettler AK160 and AE240, respectively. The Mettler AE240 was not purchased until after GEB-1 was put into operation and therefore, all weight change determinations were made with the less accurate Mettler AK160. The Mettler AE240 was, however, used for determination of the weight changes for GEB-2. After weighing, the specimen stacks were re-assembled and evacuated overnight prior to re-insertion into the experiments. The specimens were typically out of the loop for between 24 and 48 hours at each pull. The data from the weighings were processed and stored using a spreadsheet program (Excel™) on a personal computer (Apple Macintosh™). The final data sheets with the detailed raw data are shown in Appendix C

Samples of lithium were taken during the purification and transfer processes and periodically from the experiments during operation using flow-through and thief samplers. These samples were analyzed by the Analytical Chemistry Division of ORNL using micro-Kjedhal [3.5] and fast-neutron activation [3.6] techniques for nitrogen and oxygen, respectively, to provide a chemical history of the loops' lithium. Analyses for transition metals (iron, chromium, nickel and molybdenum) were made at the beginning (as-purified) and once at the end by Ion Coupled Photometry (ICP) [3.7]. The analytical evaluation of carbon in lithium was not available at ORNL, but Argonne National Laboratory graciously performed carbon analysis by acetylene evolution method [3.8] on one sample from GEB-1 at the end of the present set of experiments.

3.2.8 Safety Considerations

Safety was a major consideration in these operation of lithium compatibility experiments, particularly the higher temperature experiment. Standard ORNL safety procedures for handling liquid alkali metals were used. These procedures are outlined in reference [3.9]. No safety incidents occurred during the entire experimental period.

3.3 Experimental Results

Collected data included specimen weight changes, surface and cross-sectional morphologies obtained by scanning electron and optical microscopy, energy dispersive X-ray analysis, X-ray diffraction, electron microprobe analysis of exposed specimens and chemical analysis of the lithium from the loops.

3.3.1 Weight Change Data

Weight change data from these experiments are summarized and shown in Figures 3.3.1-8. The raw data are given in Appendix C.

Figures 3.3.1-4 show the time-dependent weight changes for each of the specimens which were in the respective loops for the entire duration of the experiment. Specimens which were removed during operation and destructively examined are not included in these figures.

GEB-1 (360 to 505°C):

All specimens in the cooled leg ($dT/dx < 0$) of GEB-1 (Figure 3.3.1) showed a net weight loss (net corrosion) which approached an asymptotic value between approximately -0.4 and -0.6 g/m^2 at the end of the 3040 hours of exposure. The transient weight change period was between 0 and 1000 hours. This initial transient accounted for most (50 to 80 %) of the total weight change for most specimens in the cooled leg of this experiment. Weight changes in the heated leg ($dT/dx > 0$) of GEB-1 (Figure 3.3.2) were less monotonic in behavior. Sixteen of the twenty specimens experienced weight losses similar in pattern and magnitude to those in the cooled leg (i.e. large initial drop followed by an asymptotic approach to a

negative weight change). *However, the four highest temperature specimens in the heated leg of GEB-1 (L-16, -18, -20 and -21) experienced relatively large, net weight gains (0 to 0.5 g/m^2), in spite of being at the highest temperature. The largest weight loss occurred at or near the lowest temperature in the loop while the largest weight gain occurred at the maximum loop temperature.* The scatter for the data in both the hot and cooled legs of GEB-1 was within the experimental error in determination of the weight change ($\pm 1 \times 10^{-1}$ g/m^2 on the Mettler AK160).

GEB-2 (525 to 655°C):

The magnitude of the weight changes in the cooled ($dT/dx < 0$) and heated ($dT/dx > 0$) legs of GEB-2 were ~10 to 15 times larger than those in GEB-1. The weight gains decrease with increasing temperature in both legs. The weight changes in the heated leg are ~20% higher in magnitude than in the cooled leg. The "balance point", the specimen/temperature which had near net zero weight change for the duration of the experiment, was 600 °C in the cooled leg and 555 °C in the heated leg. Approximately 30% (7 specimens) of the specimens in the cooled leg of GEB-2 were undergoing net corrosion and 55% (12 specimens) net deposition. In the heated leg of GEB-2, 80% were undergoing corrosion and 15% (3 specimens) net deposition. The transient period was less than approximately 500 hours. *The largest weight loss occurs at the maximum temperature in the heated leg and the largest weight gains were at the lowest temperature in the cooled leg.* The scatter was within the tolerance

of the weight change determinations ($\pm 1 \times 10^{-2}$ g/m^2 on the Mettler AE240) for GEB-2.

Figures 3.3.5-6 give the end of life weight change profiles for each of the loops. Figures 3.3.7 and 8 summarize the temperature variations of corrosion and deposition, respectively, for both experiments. As a clarification of nomenclature in this work, a specimen which had a weight change less than zero will be said to have undergone "net corrosion". Other investigators refer to specimen weight loss (our "net corrosion") as "dissolution". A specimen which had a weight change greater than zero will be said to have undergone a net weight gain or "net deposition".

Figures 3.3.5 and 3.3.6 show the weight change profiles at the end of life for GEB-1 and GEB-2, respectively. Note the difference in scale between the two figures and the change in behavior in the heated leg between the two experiments. In the cooled leg of GEB-1 (Figure 3.3.5), the weight losses are insensitive to temperature. In the heated leg of GEB-1, the weight loss initially increases with temperature and then, suddenly, the weight losses decrease and eventually become weight gains. Note also that corrosion (i.e. weight loss) was not a strong function of temperature in the cooled leg of GEB-1 as compared to all of GEB-2. It is clear from comparison of the results from these two experiments that weight loss and thus corrosion and deposition were not strictly increasing functions of temperature in these systems and that different processes were governing the corrosion, as determined from specimen weight change.

For those specimens which underwent net weight **losses** in both GEB-1 and GEB-2 (i.e. "net corrosion"), "corrosion rate" versus inverse of absolute temperature is plotted in Figure 3.3.7 assuming linear reaction kinetics. Similarly, for those specimens which underwent net weight **gains** in both GEB-1 and GEB-2 (i.e. "deposition"), "deposition rate" versus inverse of absolute temperature is plotted in Figure 3.3.8. Plots such as these (so-called Arrhenius plots) are used to derive an activation energy, E_a, for the "corrosion" or "deposition" reaction(s). If the corrosion or deposition data fall along a straight line on a semi-log plot, then the slope of the the semi-log line is equal to the activation energy divided by **R**, the gas constant (8.314 J/mole). Activation energy analysis of corrosion and deposition data **assumes** that a single chemical reaction or mass transfer process was controlling the weight changes over a range of temperature. It was not possible or prudent to derive a **single** activation energy relationship between temperature, for either corrosion or deposition, from these experiments which covers the **entire** temperature range investigated (360 to 655 °C) because all of the data do not lie along the same semi-log line. This behavior further suggested that different mass transfer processes may have been controlling the corrosion over different ranges of temperature. The corrosion rate plot (Figure 3.3.7) reflects the insensitivity of mass transport to temperature at low temperatures (360 to 450 °C). The data from the heated leg of GEB-2 exhibited linear behavior. A least squares fit of the data from the heated leg of GEB-2 gives an

activation energy for dissolution of 63.7 kJ/mole. The corrosion data from the cooled leg of GEB-2 are smaller in magnitude but exhibit a much steeper slope. This is due to the growth of $M_{23}C_6$ carbide nodules on the surfaces of some of these specimens which distort the weight change data as interpreted as dissolution. The deposition data do not exhibit linear behavior over any range of temperature for a semi-log Arrhenius plot and it is not possible to derive an activation energy for the deposition process. However, when plotted on a linear scale, the deposition data from the cooled leg of GEB-2 are linear with inverse temperature with a slope of approximately 42000 K^{-1} which correspond to a slope of 347 kJ/mole when plotted versus 1/RT.

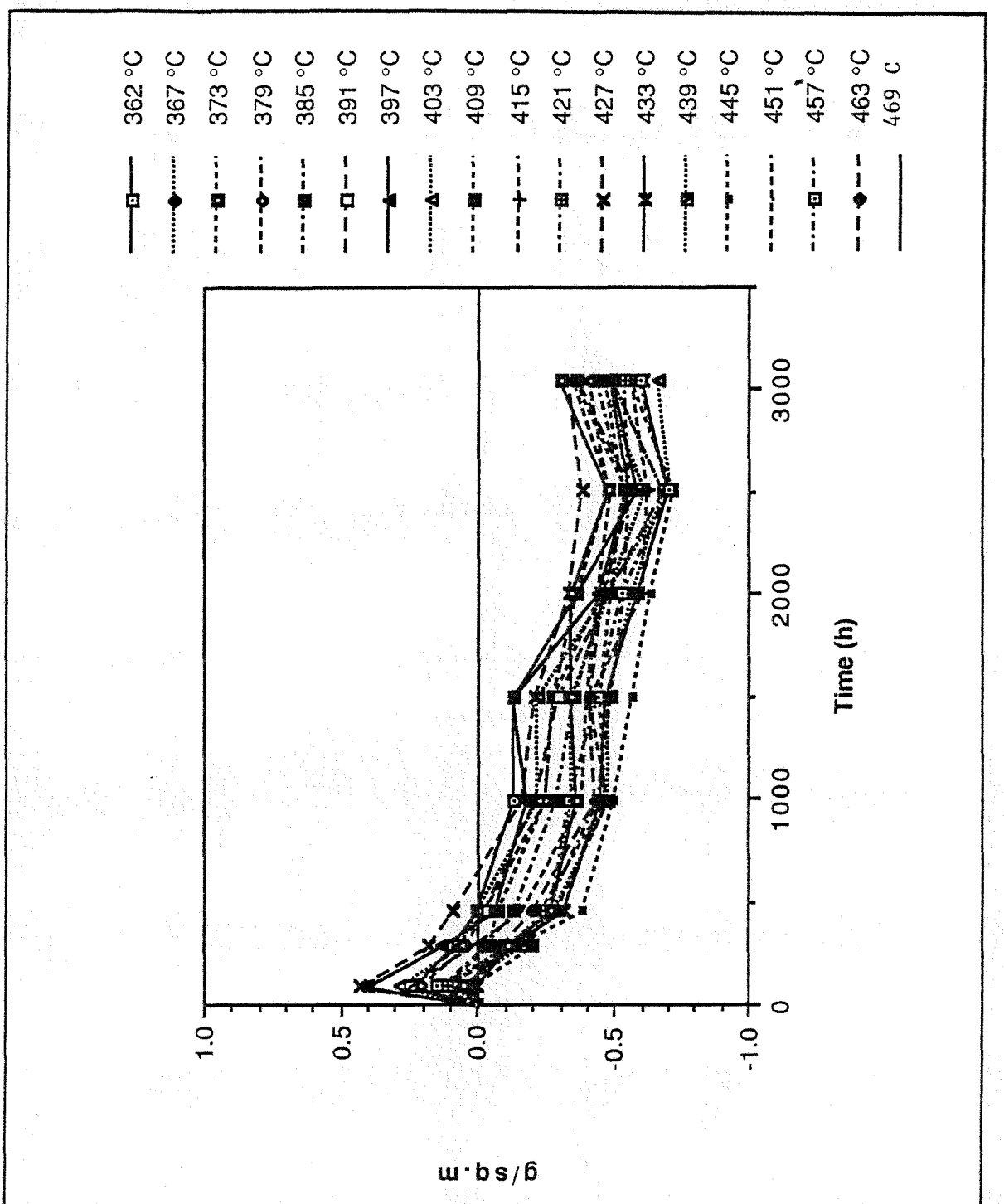

Figure 3.3.1 Time Dependent Weight Changes, Cooled leg (dT/dx < 0), GEB-1

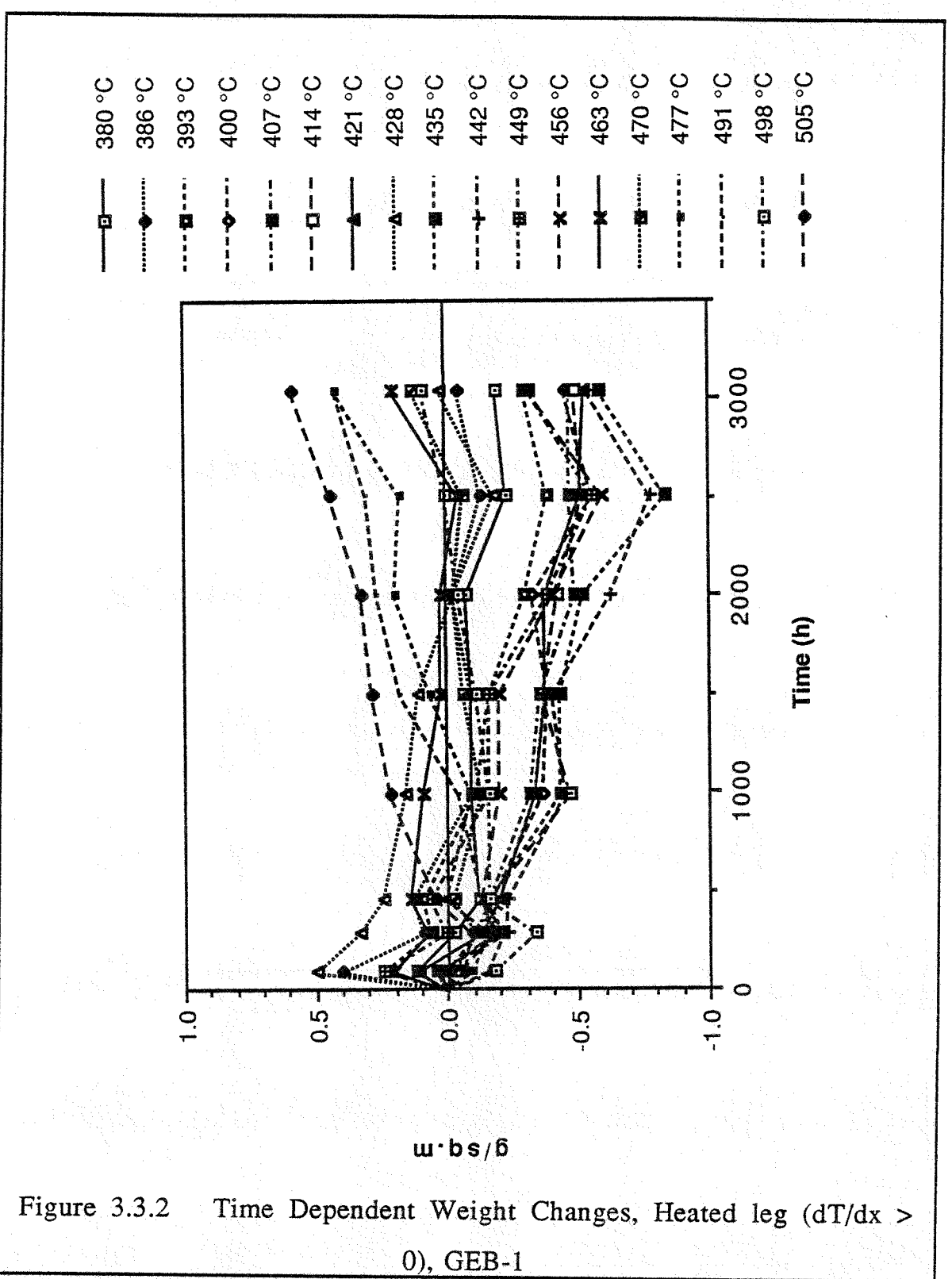

Figure 3.3.2 Time Dependent Weight Changes, Heated leg (dT/dx > 0), GEB-1

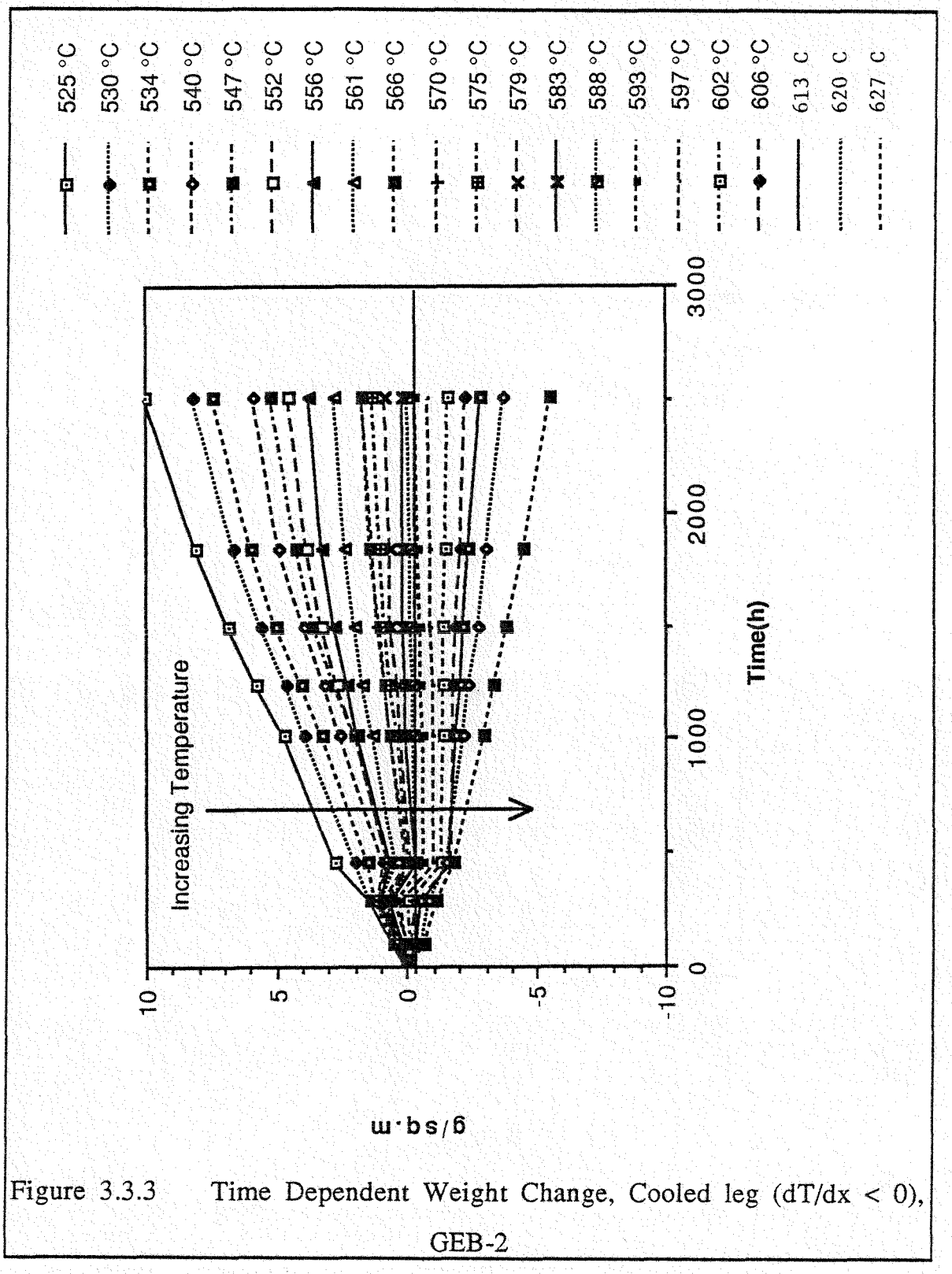

Figure 3.3.3 Time Dependent Weight Change, Cooled leg (dT/dx < 0), GEB-2

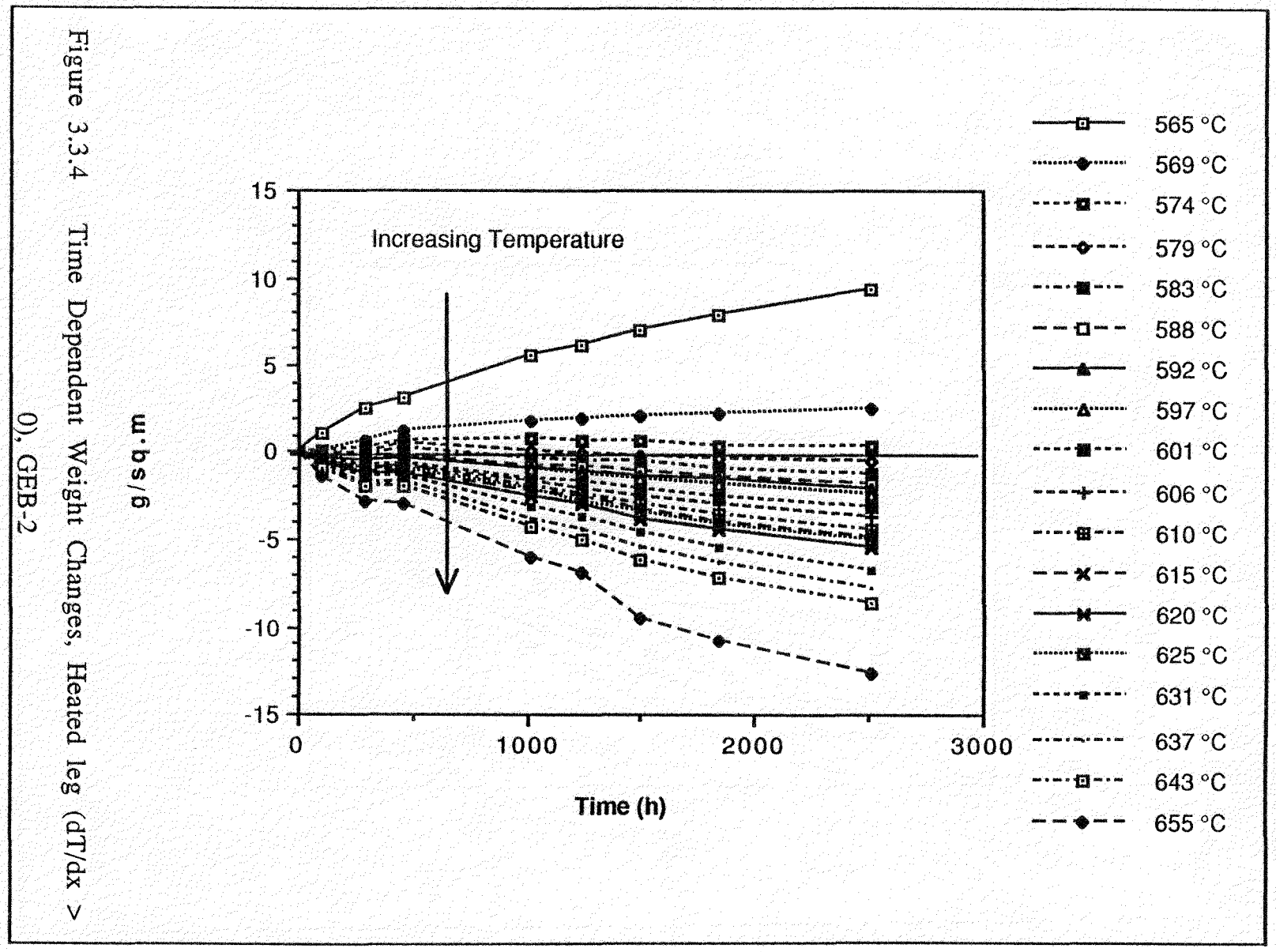

Figure 3.3.4 Time Dependent Weight Changes, Heated leg (dT/dx > 0), GEB-2

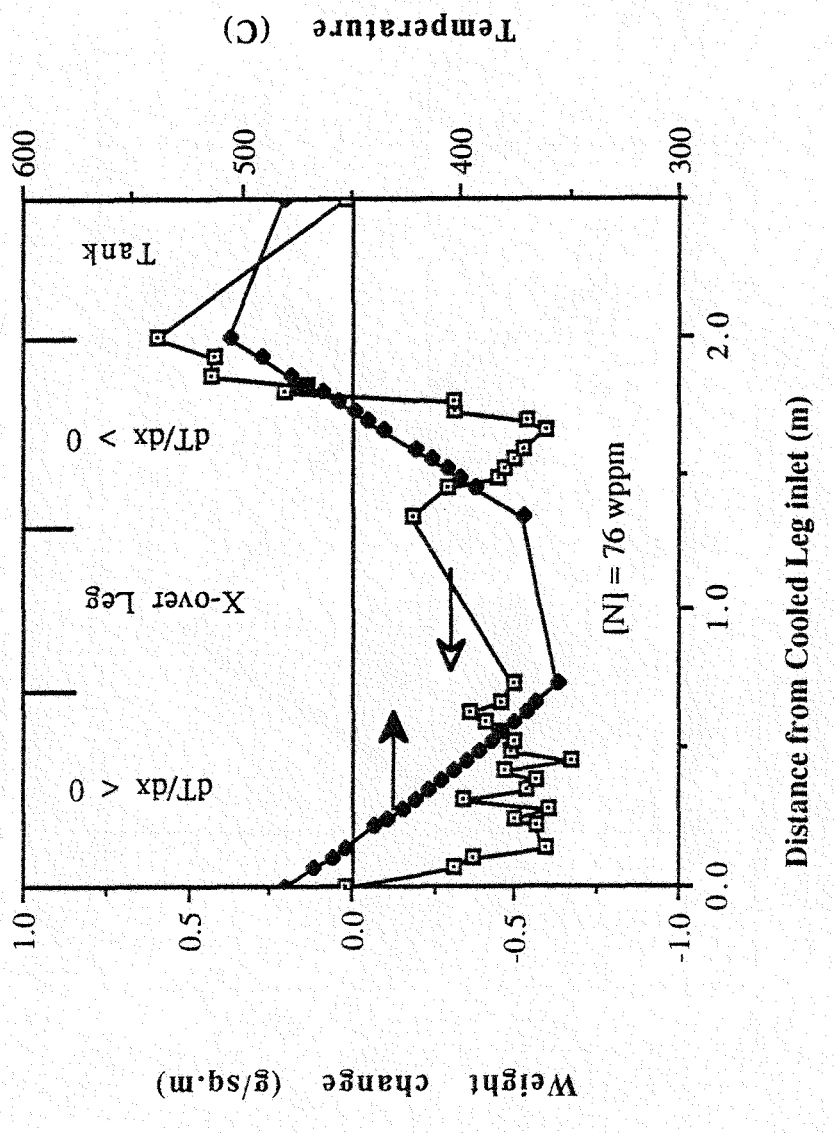

Figure 3.3.5 Weight Change Profile, GEB-1, 3040 hrs

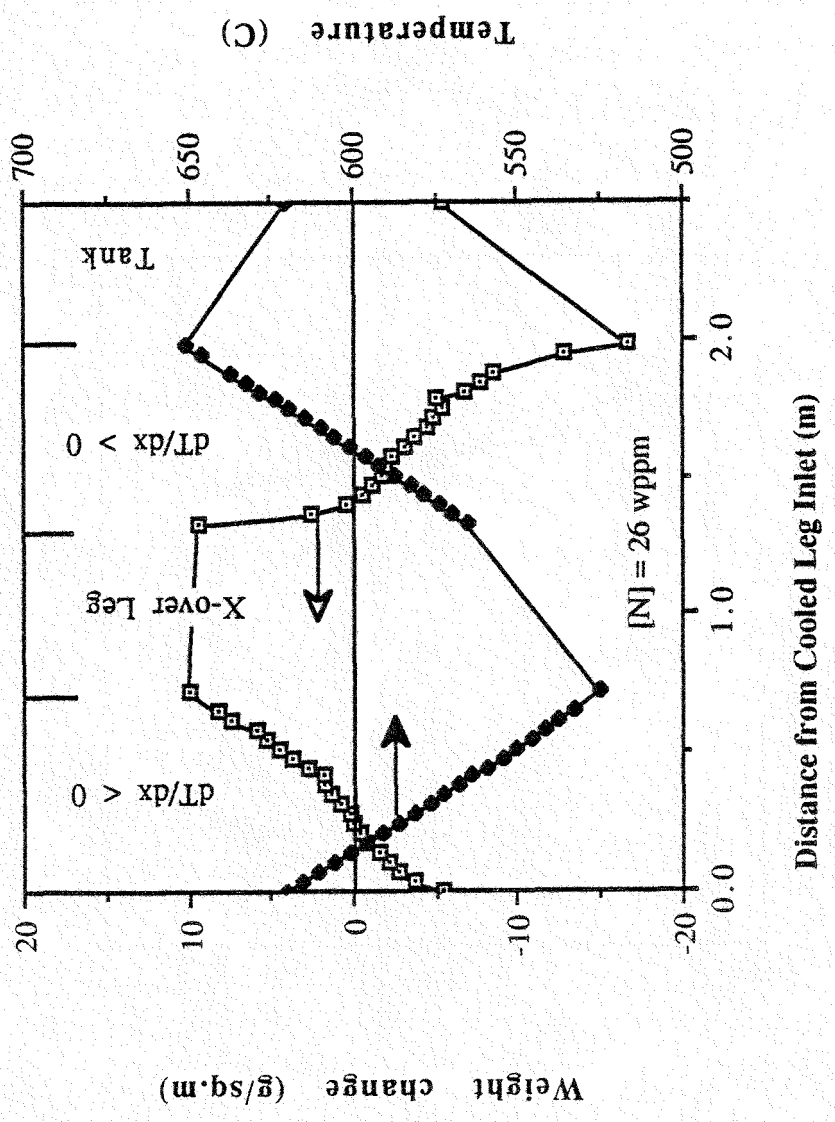

Figure 3.3.6 Weight Change Profile, GEB-2, 2510 hours

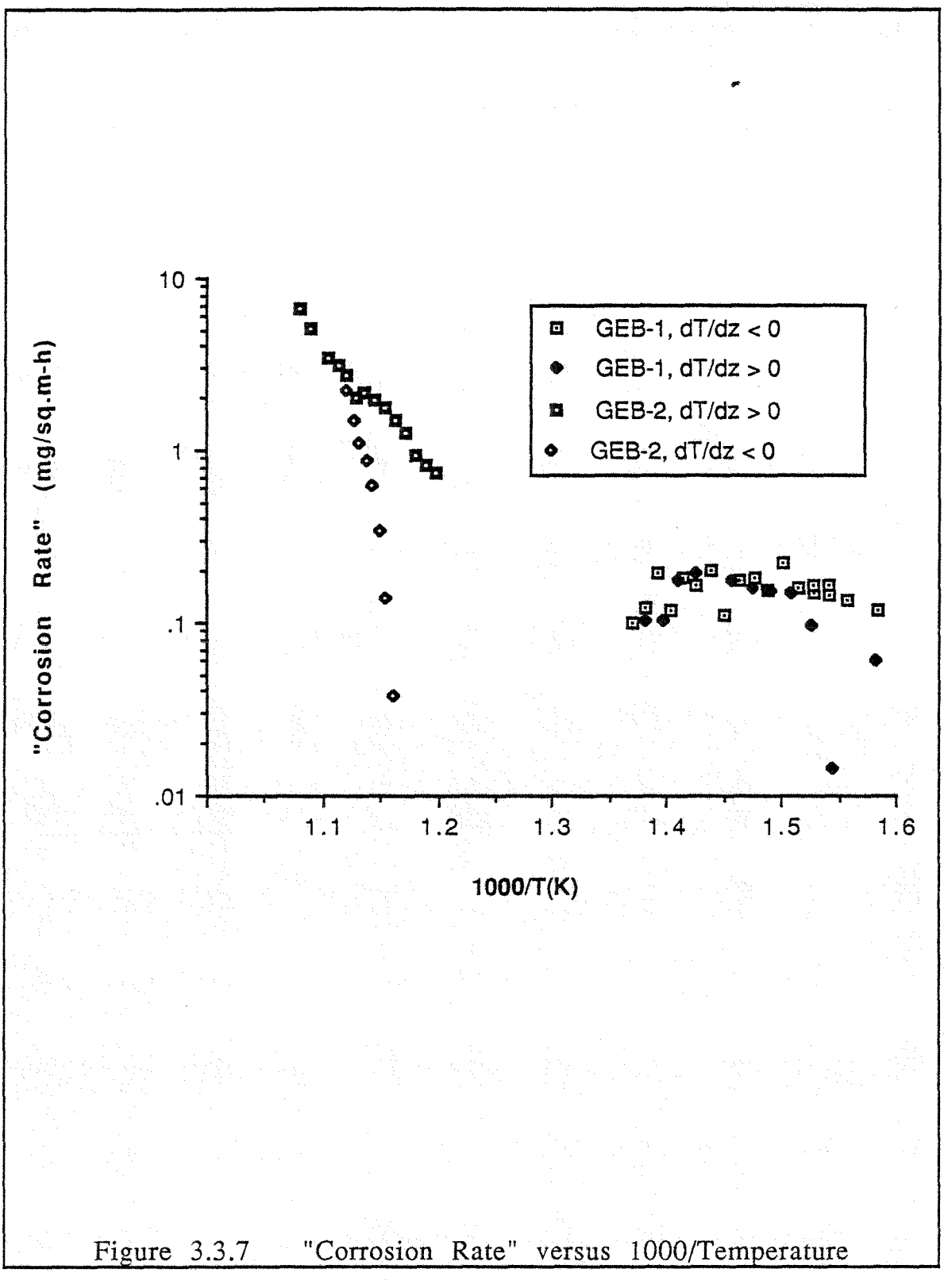

Figure 3.3.7 "Corrosion Rate" versus 1000/Temperature

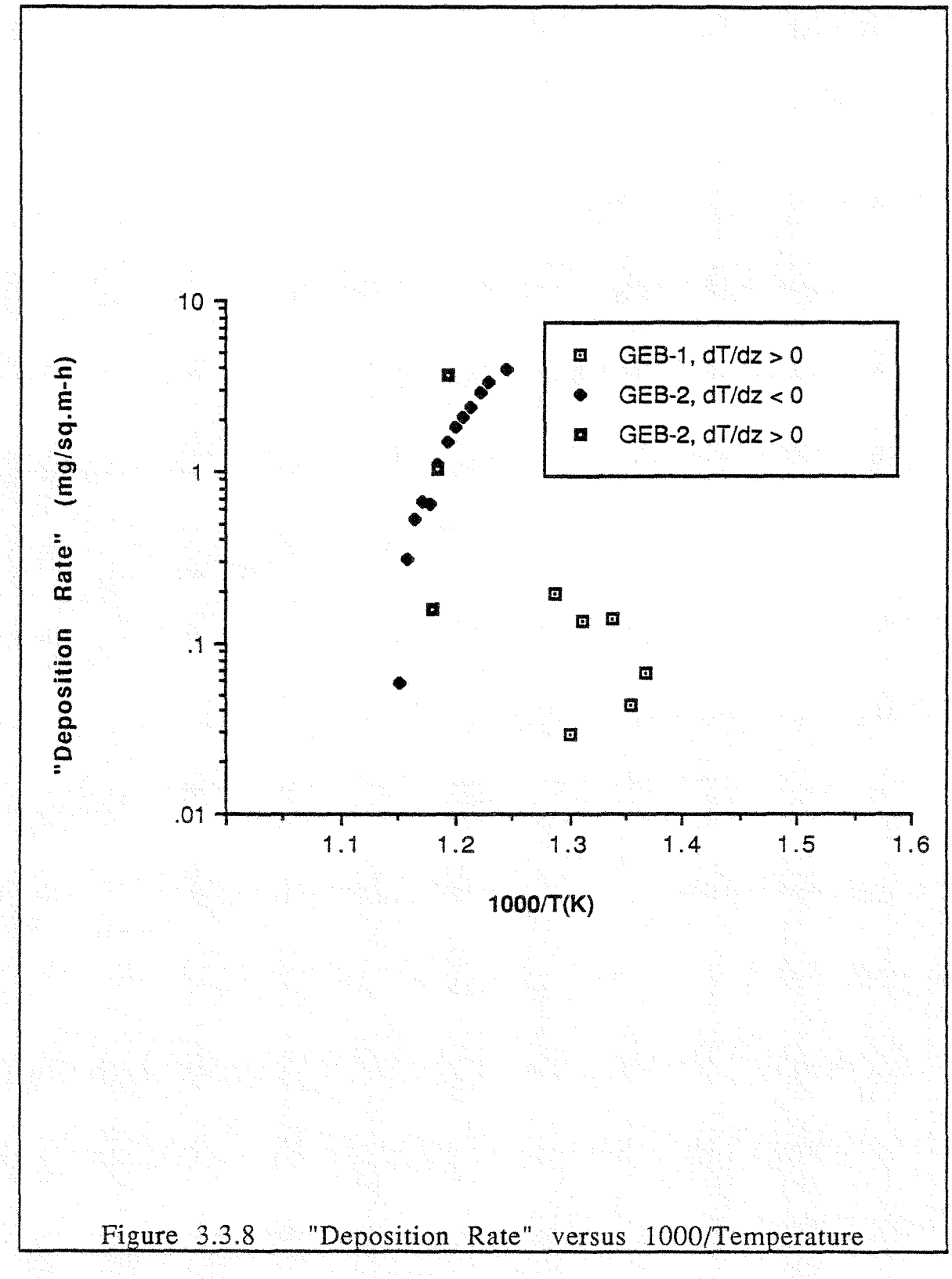

Figure 3.3.8 "Deposition Rate" versus 1000/Temperature

3.3.2 Surface Morphology and Cross-Sectional Views

The surface morphological and cross-sectional characteristics of some of the specimens exposed were investigated using optical (OM) and scanning electron microscopy (SEM). Fifty-five specimens were sectioned, mounted, polished and etched with a nitric and hydrofluoric acid for optical examination up to a 800X magnification of the cross-section. The purpose of the etchant was to accentuate the regions of carbon enrichment or depletion (carburization/decarburization) of the matrix material (α-Fe+Cr). One-hundred twenty optical micrographs (OM) were taken. Fifty-eight specimens were examined using the ORNL Metal and Ceramics Division's JEOL JSM-35CF scanning electron microscope. Two hundred and twelve SEM photomicrographs were taken. In the interest of brevity, only a representative sample of the micrographs is shown here.

GEB-1 (360 TO 505°C):

Figures 3.3.9 to 3.3.20 and 3.3.21 to 3.3.25 show a representative sample of the SEM and OM photos of specimens from GEB-1.

Two types of surfaces were found in GEB-1. For temperatures below 450 °C in both the cold and heated legs, the surfaces of the specimens were roughened to a pebble-like or "orange peel" appearance (e.g. Figures 3.3.9-13). The scale of the roughness increased with temperature as the surface chromium content of the base material decreased (see section on EDX analysis). Between 435

°C to 505 °C (11 specimens) in the heated leg and from 485 °C to 450 °C in the cooled leg (5 specimens), faceted nodules nucleated and grew on the specimen surfaces (e.g. Figure 3.3.14-20). The nodules first appeared at the grain boundaries and then eventually began to cover the grain surface (Figures 3.3.14-15). The number density and size of the nodules increased with temperature. The diameter of the nodules varied from about 0.1 to 5 microns. The number density of the nodules in the heated leg was higher than the corresponding position (temperature) in the cooled leg. These nodules were characterized by high chromium contents (~60 to 70 w/o by weight, see section on EDX analysis) as compared to the base material. The presence of these nodules on the four highest temperature and other specimens accounted for the weight gains at the highest temperatures in GEB-1. The nodules can be seen in cross-section (Figures 3.3.22A, 3.3.23B and 3.3.25B). By comparison of the control specimen cross sectional view (3.3.22A) with those from GEB-1, we can see that at the low temperatures in GEB-1, the bulk material was not affected by the presence of the lithium. See the section on electron microprobe for confirmation.

GEB-2 (525 TO 655°C):

Figures 3.3.26 to 3.3.39 and 3.3.40 to 3.3.46 show a representative sample of the SEM and OM photos of specimens from GEB-2.

The surface morphology of the specimens exposed in GEB-2 can be characterized by three distinct morphologies. Between 585 °C to

530 °C (10 specimens) in the cooled leg, Cr-rich faceted nodules similar to those found in GEB-1 grew on the specimen surfaces (Figures 3.3.26-31). No faceted chromium-rich nodules appear in the heated leg of GEB-2. However, Fe-rich deposits were found only on the first three specimens at the bottom of the heated leg (Figure 3.3.32). The GEB-2 heated leg deposits were very high in iron content (~90 w/o) as compared to those nodules found in the cooled leg. The size and shape were quite different from the nodules found in the cooled leg of GEB-2 and the heated and cooled legs of GEB-1. The number density and size of the Cr-rich nodules were larger in the cooled leg of GEB-2 as compared to GEB-1 (compare Figures 3.3.26 and 3.3.20). At temperatures higher than 585 °C, the nodules disappear and the surface takes on the appearance of cobblestones (Figures 3.3.33-39) with severe surface etching. Small white, fluorescent areas (speckles) rich in molybdenum and vanadium (Figure 3.3.33) appear on some specimens and the cobblestone pattern continues up to 655 °C, the maximum temperature of GEB-2. The nodules can again be seen in cross-section (Figure 3.3.40A&B). From the cross sectional views, it can be seen that the near surface region becomes slightly carburized (enriched in carbon as compared to the matrix, Figure 3.3.41B) as the Fe-rich nodules deposit. However, the bulk of the alloy was unaffected by the lithium up to approximately 580 °C. Only at the higher temperatures where the nodules no longer exist does the bulk of the material begins to be affected by the presence of the lithium (decarburize: absence of black etch residue, Figures 3.3.43B and 3.3.44A&B)

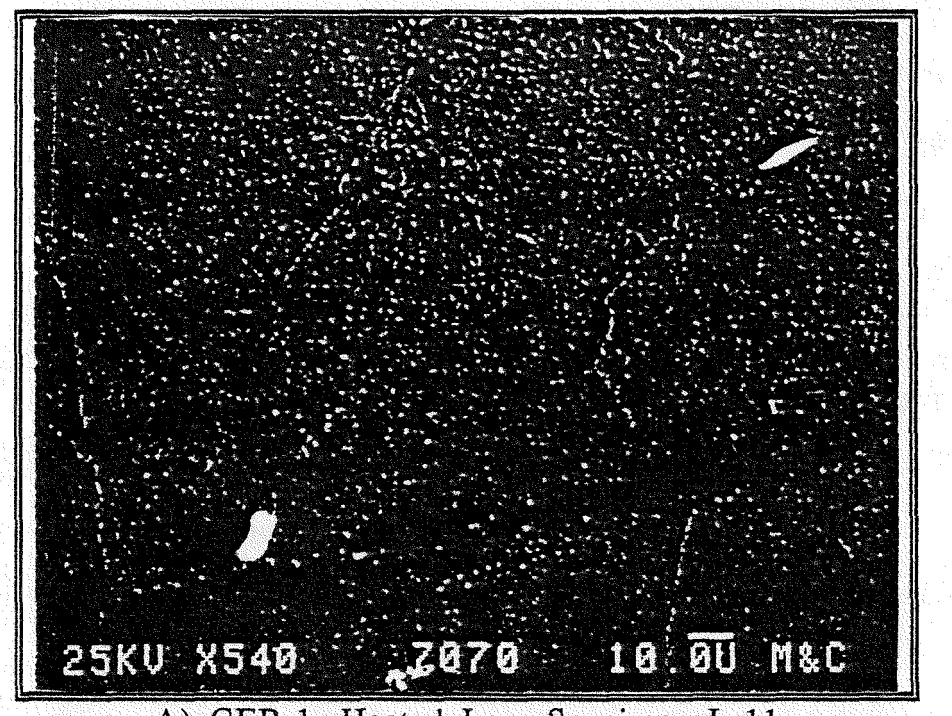

A) GEB-1, Heated Leg, Specimen L-11
436 °C, 3040 hours
Photo # 27070

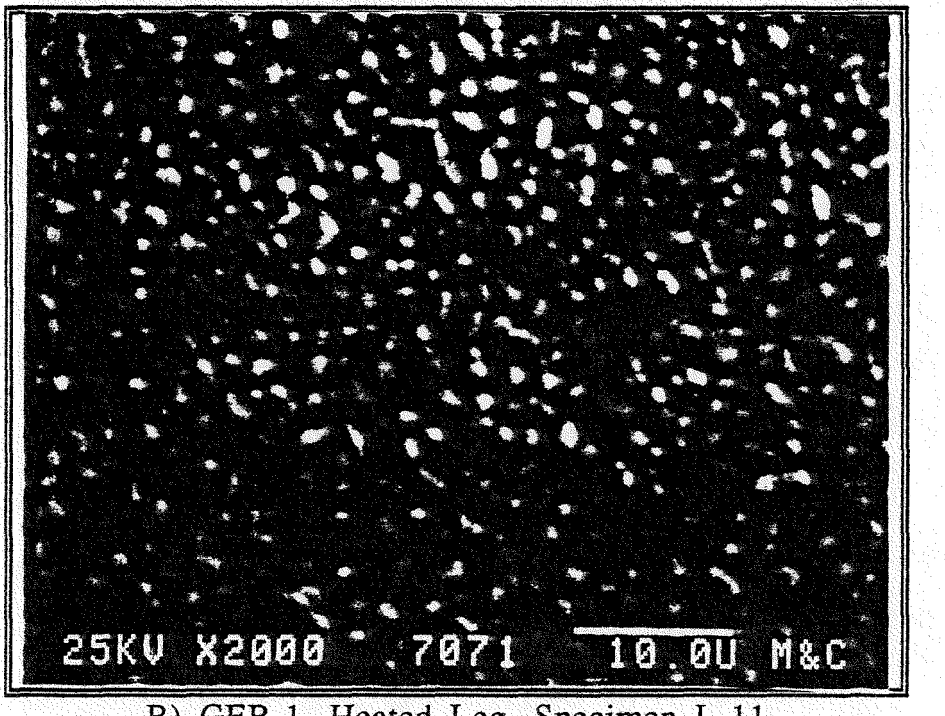

B) GEB-1, Heated Leg, Specimen L-11
436 °C, 3040 hours
Photo # 27071

Figure 3.3.9 Surface Morphology L-11

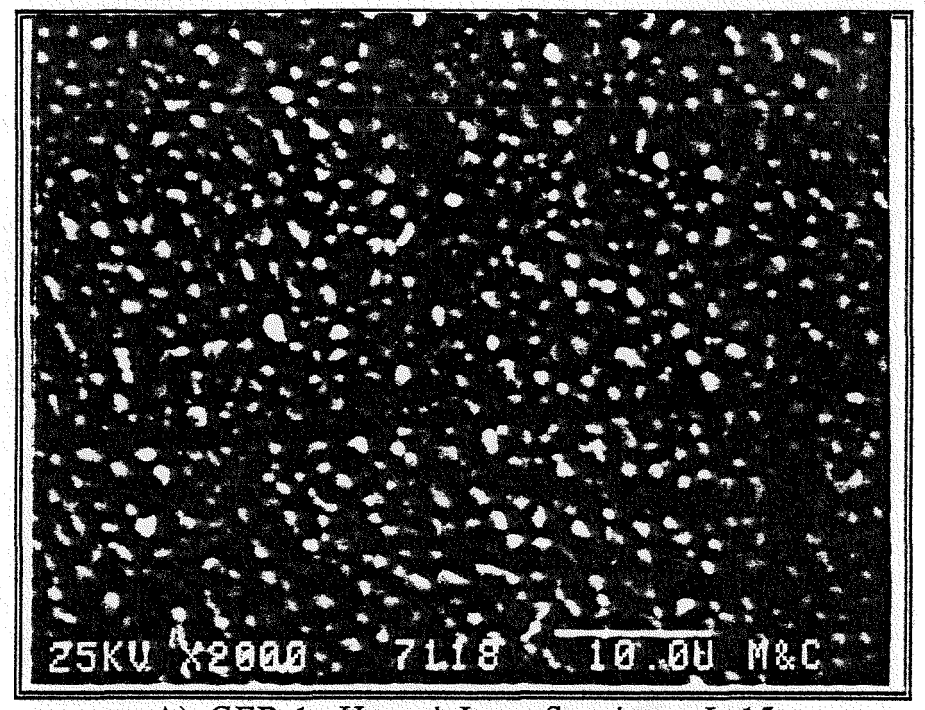

A) GEB-1, Heated Leg, Specimen L-15
420 °C, 3040 hours
Photo # 27118

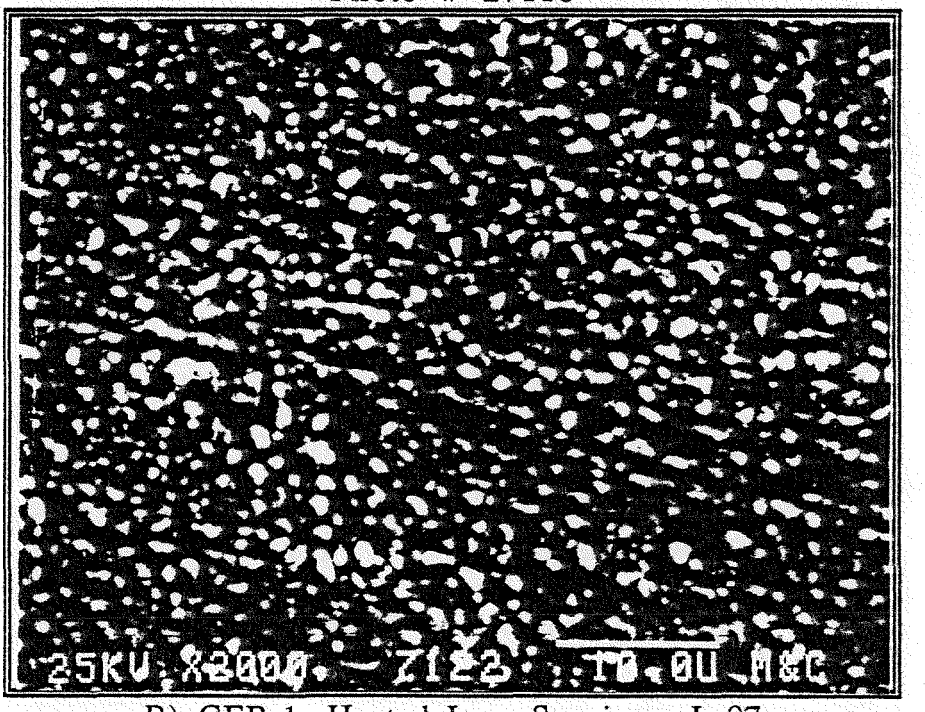

B) GEB-1, Heated Leg, Specimen L-07
405 °C, 3040 hours
Photo # 27122

Figure 3.3.10 Surface Morphologies for L-09 and L-07

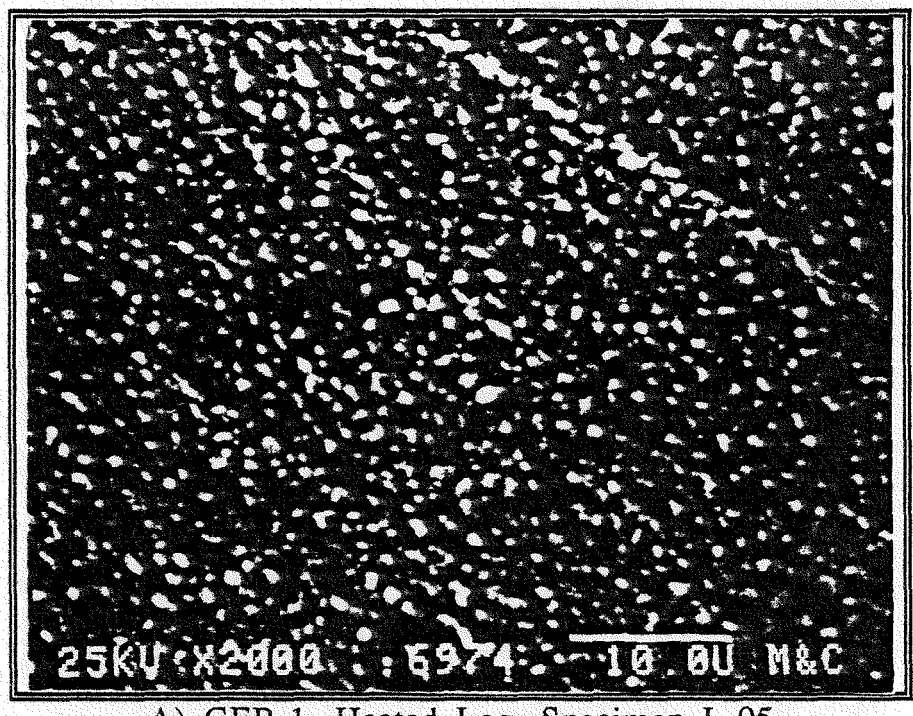

A) GEB-1, Heated Leg, Specimen L-05
390 °C, 3040 hours
Photo # 26974

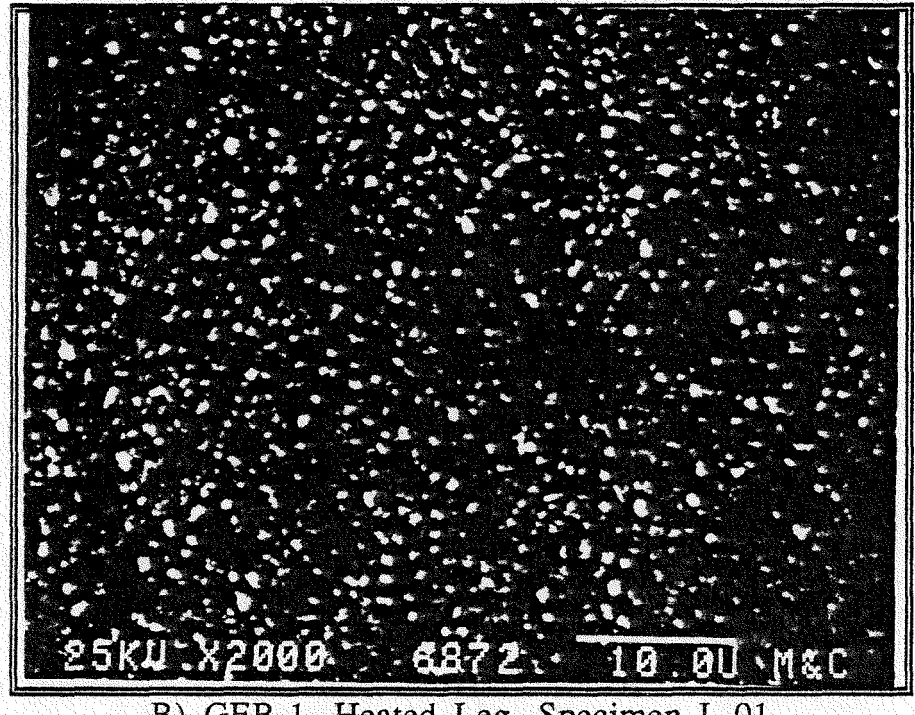

B) GEB-1, Heated Leg, Specimen L-01
359 °C, 3040 hours
Photo # 26872

Figure 3.3.11 Surface Morphologies for L-05 and L-01

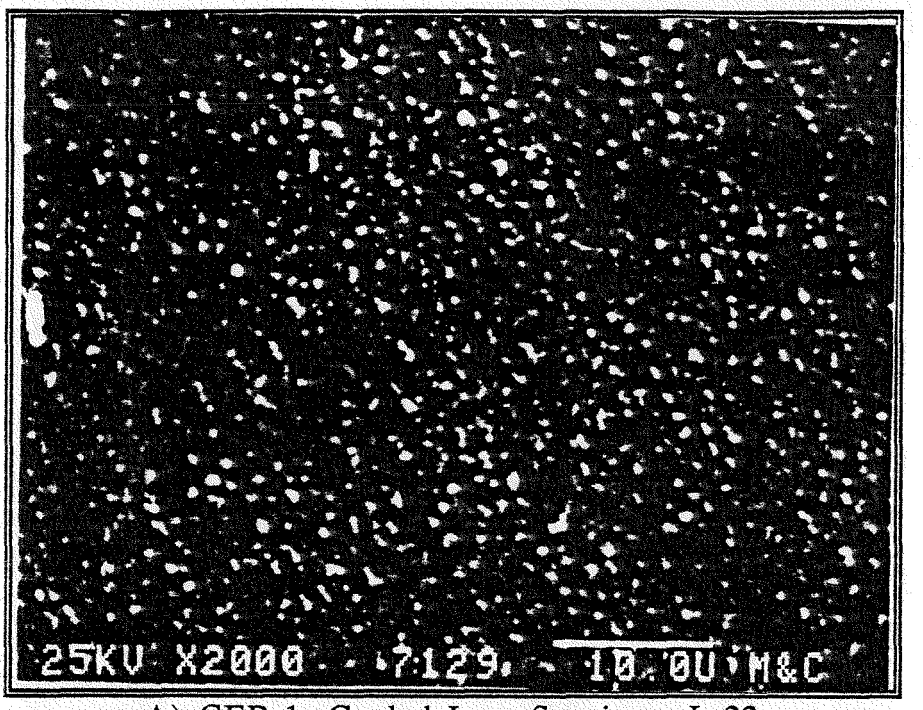

A) GEB-1, Cooled Leg, Specimen L-22
358 °C, 3040 hours
Photo # 27129

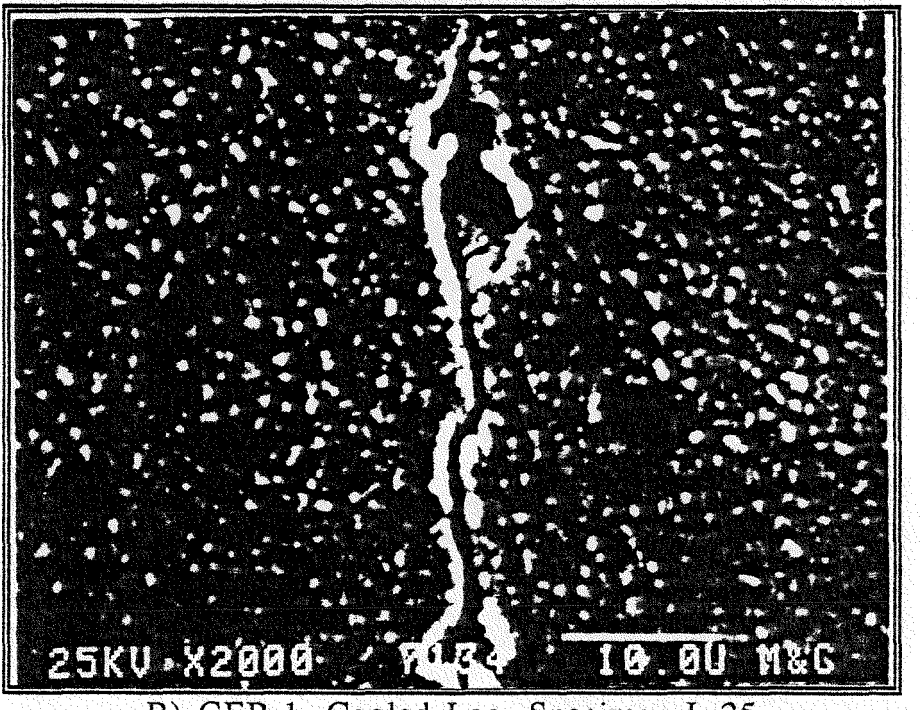

B) GEB-1, Cooled Leg, Specimen L-25
375 °C, 3040 hours
Photo # 27134

Figure 3.3.12 Surface Morphologies for L-22 and L-25

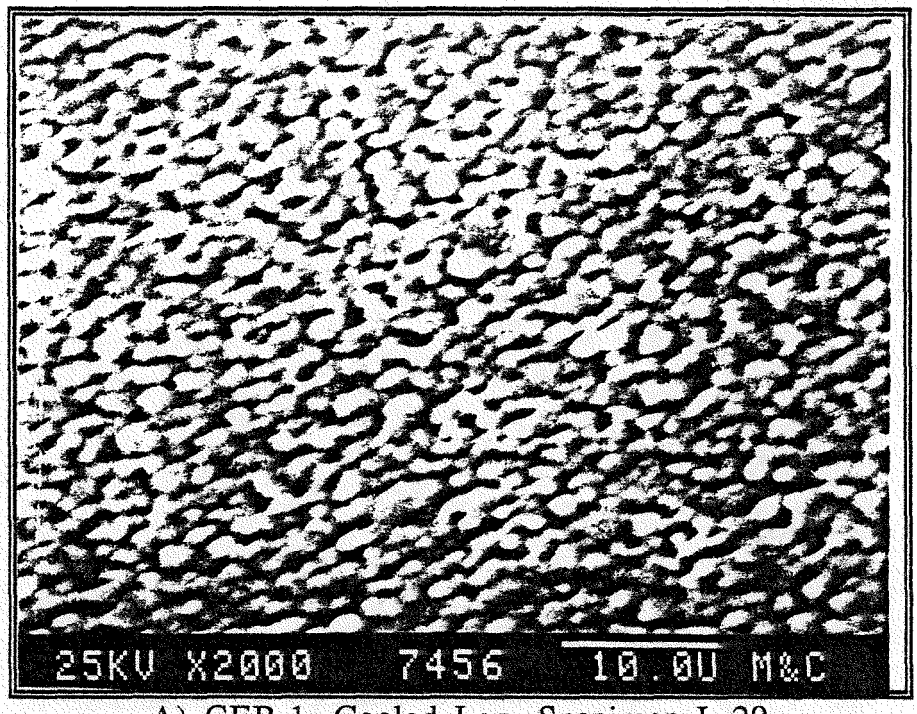

A) GEB-1, Cooled Leg, Specimen L-29
398 °C, 3040 hours
Photo # 27456

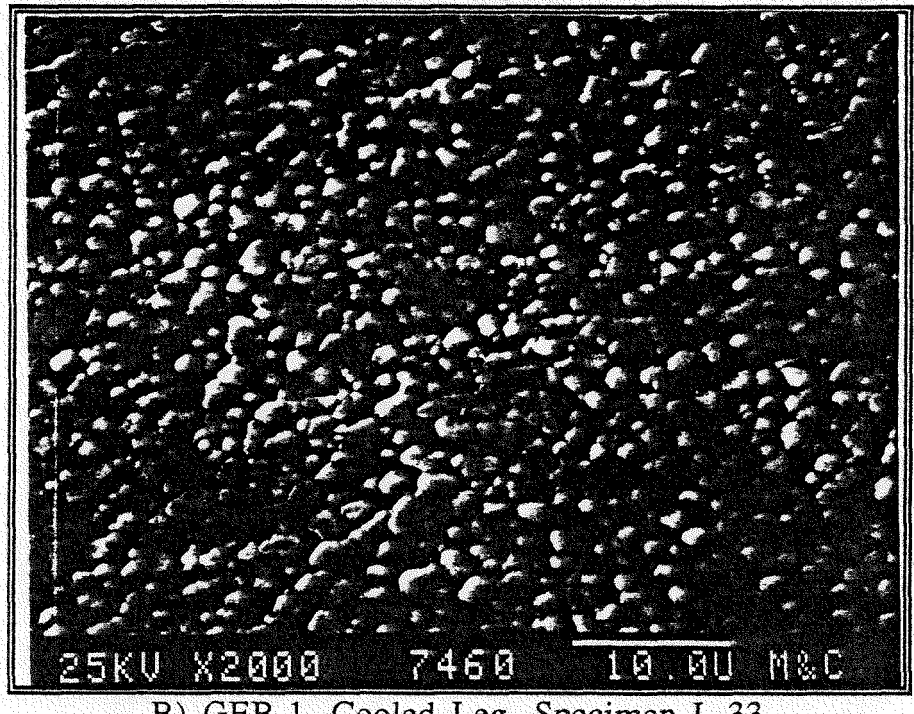

B) GEB-1, Cooled Leg, Specimen L-33
422 °C, 3040 hours
Photo # 27460

Figure 3.3.13 Surface Morphologies for L-29 and L-33

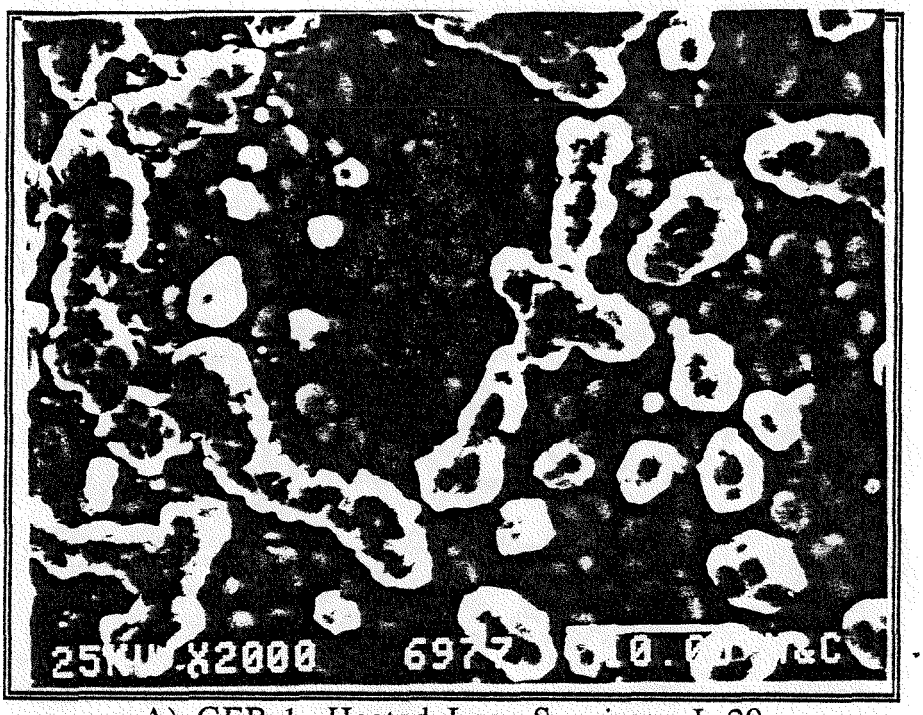

A) GEB-1, Heated Leg, Specimen L-20
496 °C, 3040 hours
Photo # 26977

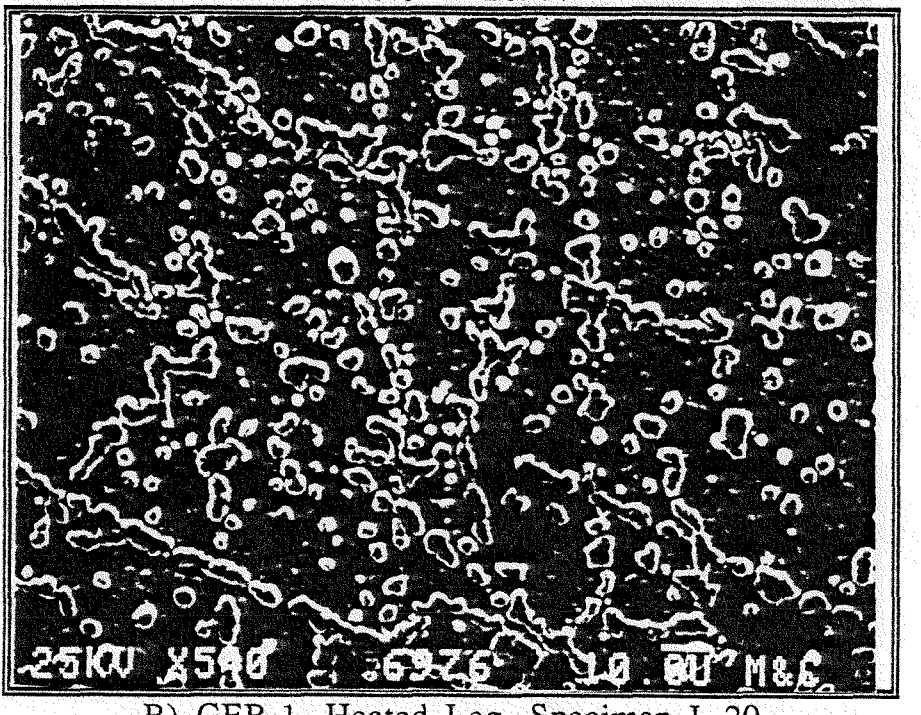

B) GEB-1, Heated Leg, Specimen L-20
496 °C, 3040 hours
Photo # 26976

Figure 3.3.14 Surface Morphology L-20

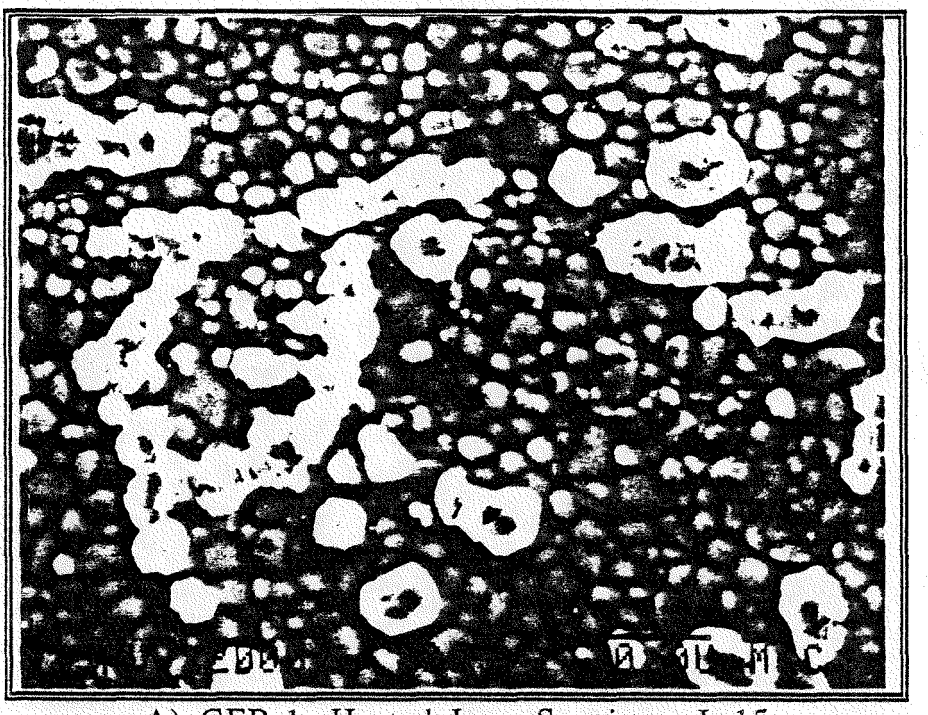

A) GEB-1, Heated Leg, Specimen L-15
466 °C, 3040 hours
Photo # 27063

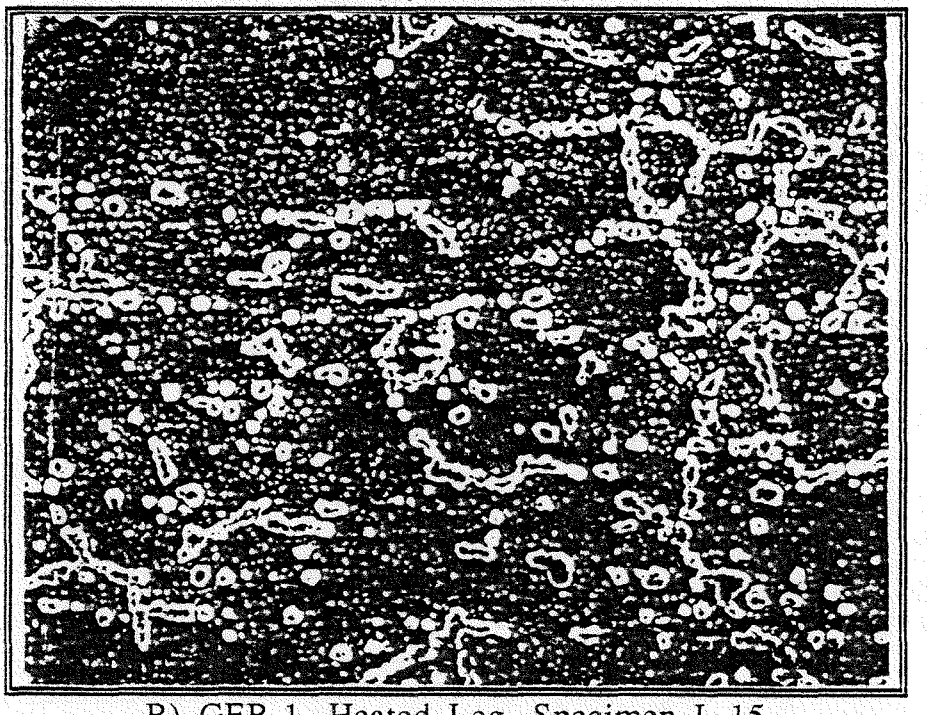

B) GEB-1, Heated Leg, Specimen L-15
466 °C, 3040 hours
Photo # 27062

Figure 3.3.15 Surface Morphology L-15

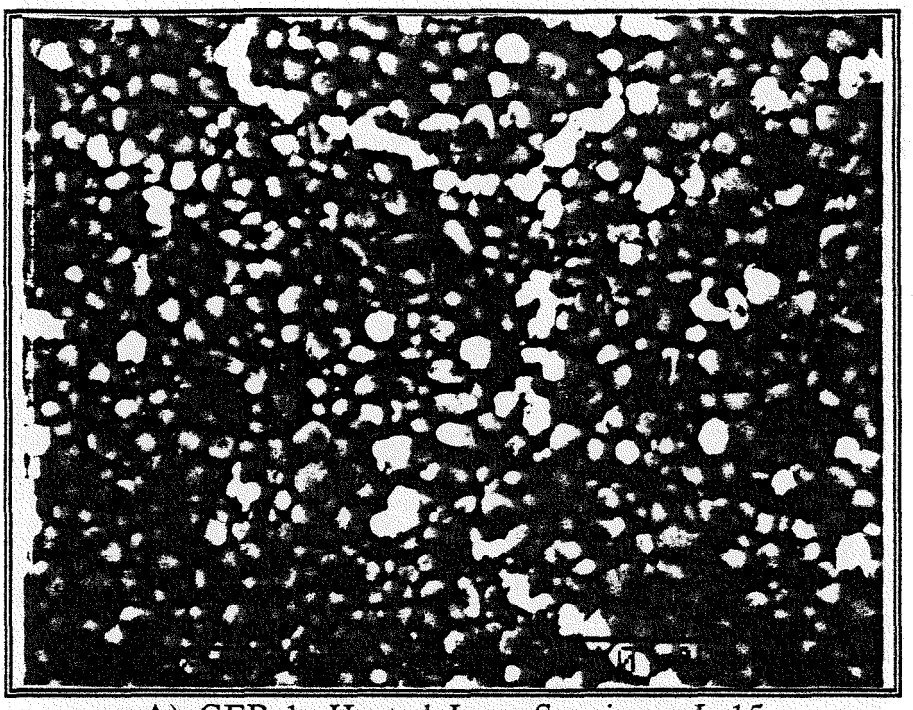

A) GEB-1, Heated Leg, Specimen L-15
443 °C, 3040 hours
Photo # 27069

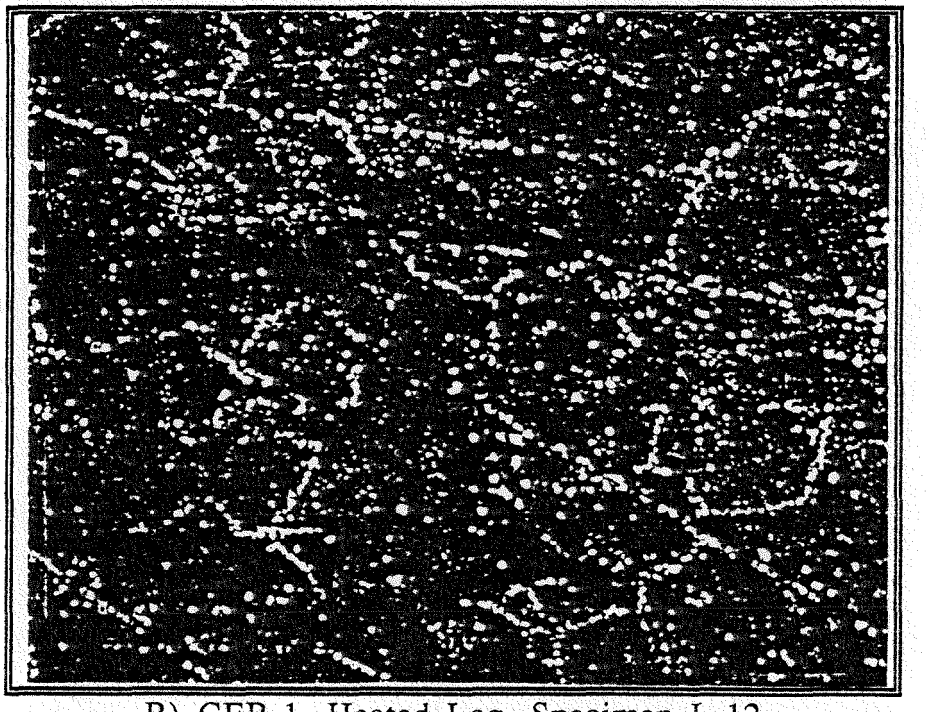

B) GEB-1, Heated Leg, Specimen L-12
443 °C, 3040 hours
Photo # 27068

Figure 3.3.16 Surface Morphology L-12

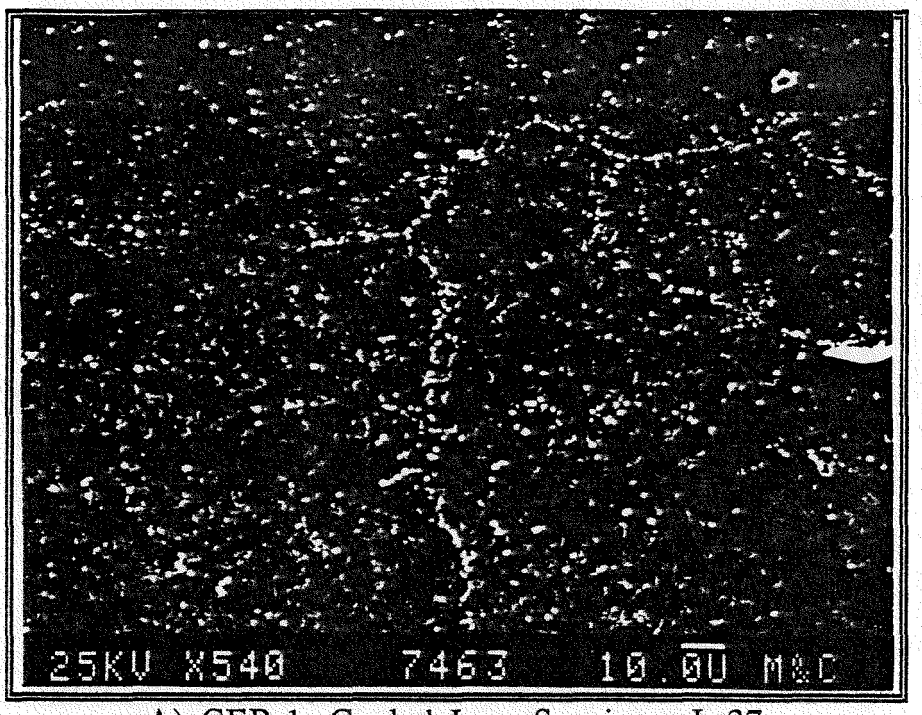

A) GEB-1, Cooled Leg, Specimen L-37
445 °C, 3040 hours
Photo # 27463

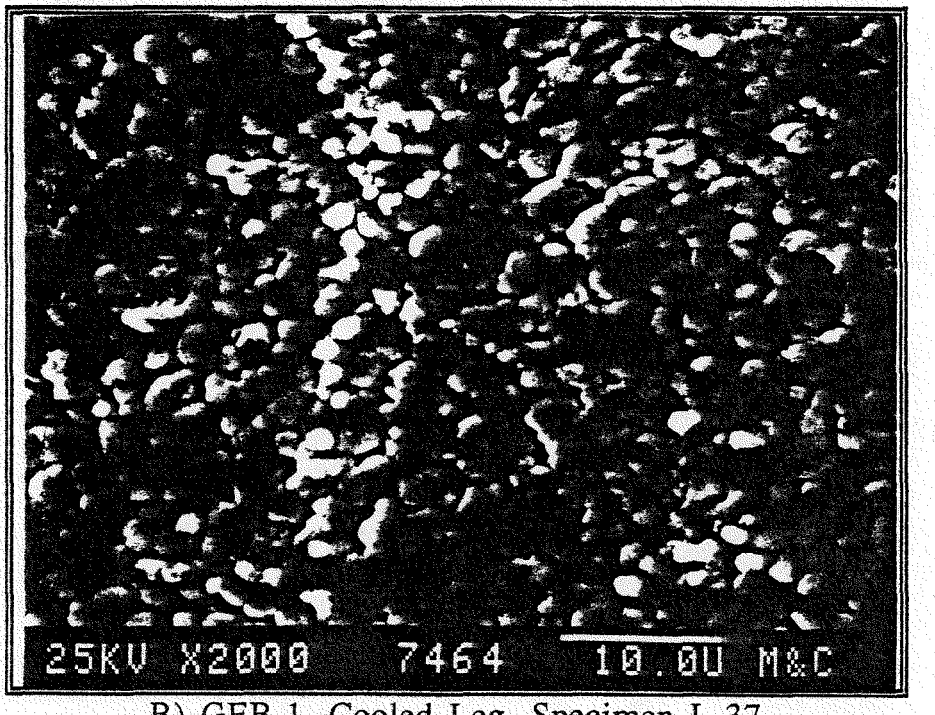

B) GEB-1, Cooled Leg, Specimen L-37
445 °C, 3040 hours
Photo # 27464

Figure 3.3.17 Surface Morphology L-37

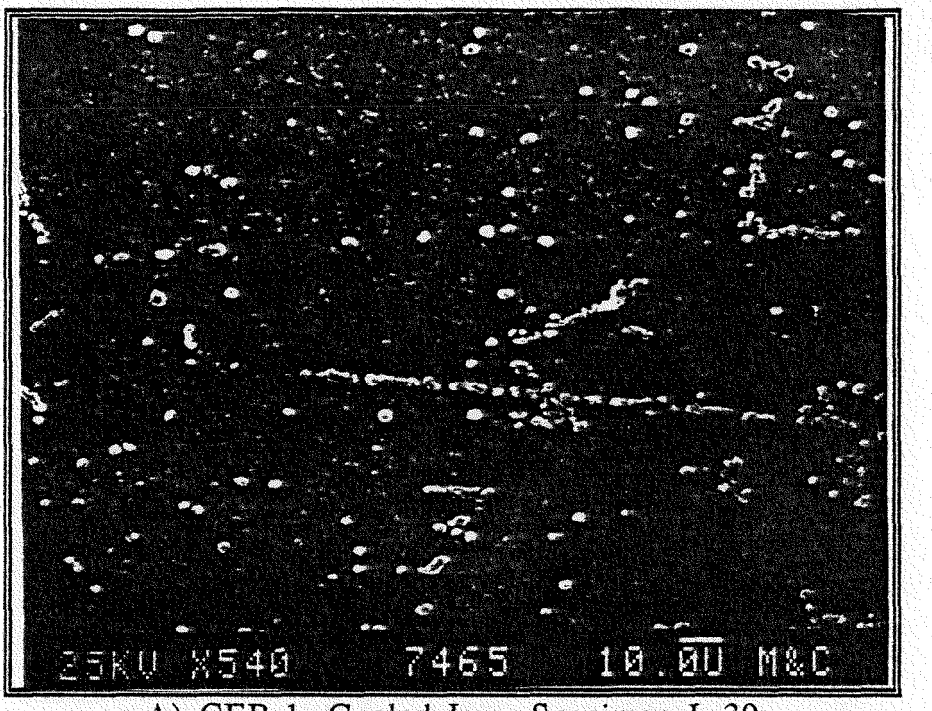

A) GEB-1, Cooled Leg, Specimen L-39
457 °C, 3040 hours
Photo # 27465

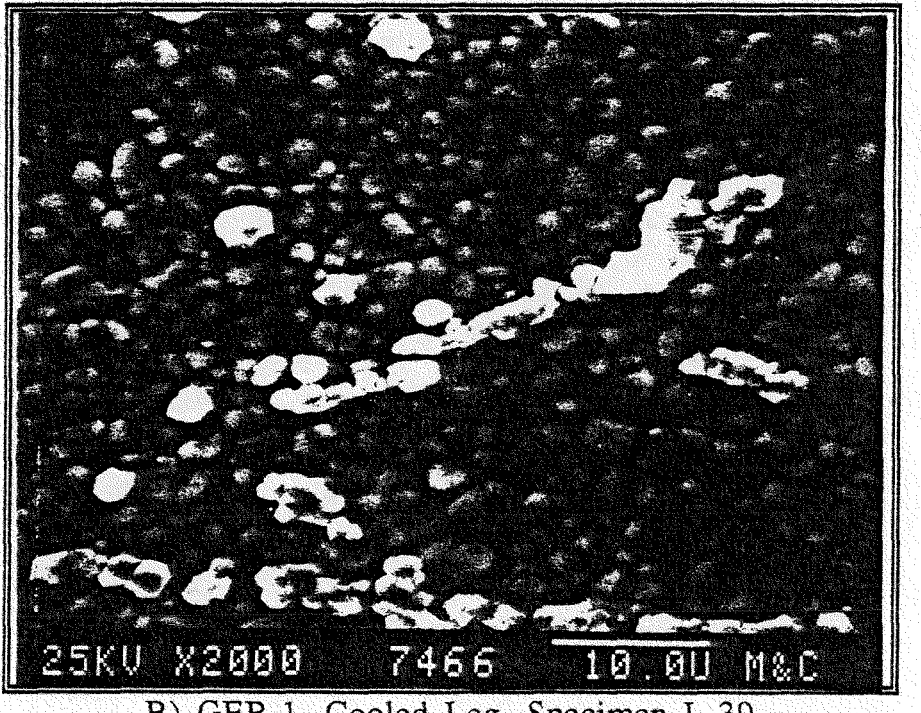

B) GEB-1, Cooled Leg, Specimen L-39
457 °C, 3040 hours
Photo # 27466

Figure 3.3.18 Surface Morphology L-39

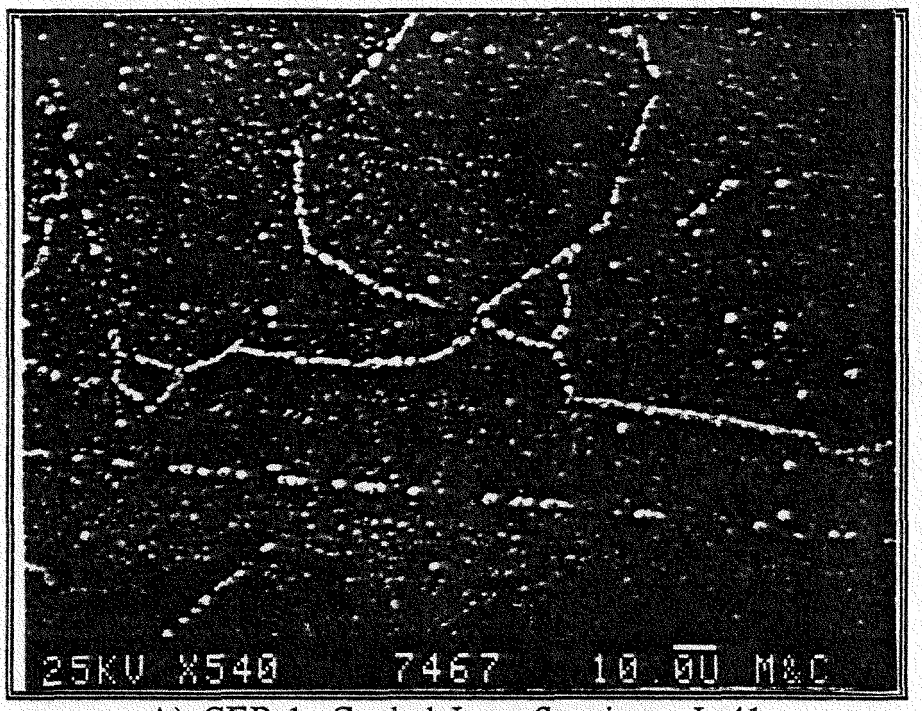

A) GEB-1, Cooled Leg, Specimen L-41
470 °C, 3040 hours
Photo # 27467

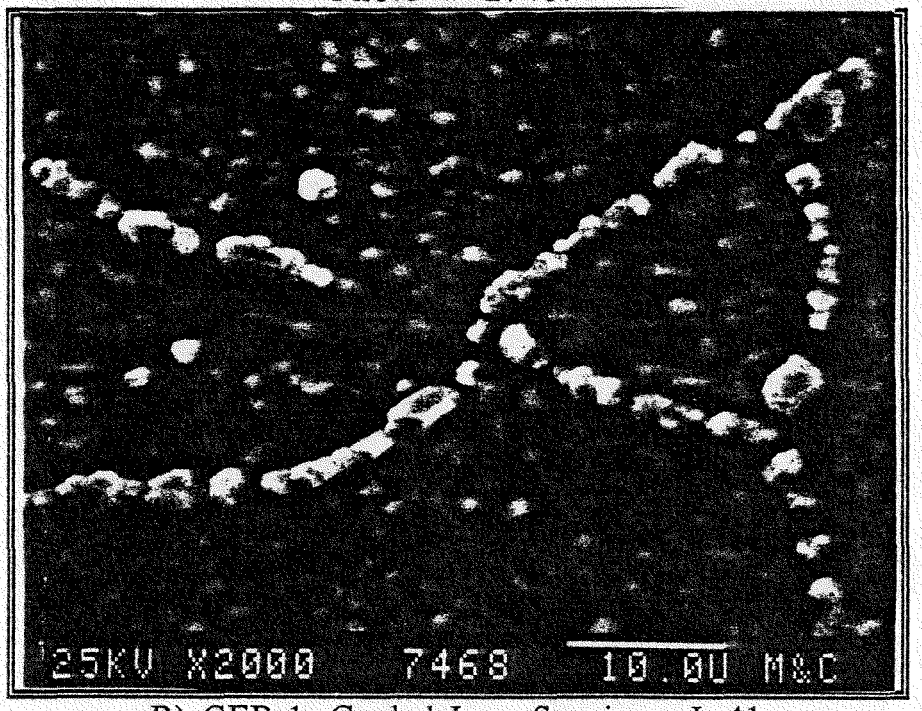

B) GEB-1, Cooled Leg, Specimen L-41
470 °C, 3040 hours
Photo # 27468

Figure 3.3.19 Surface Morphology L-41

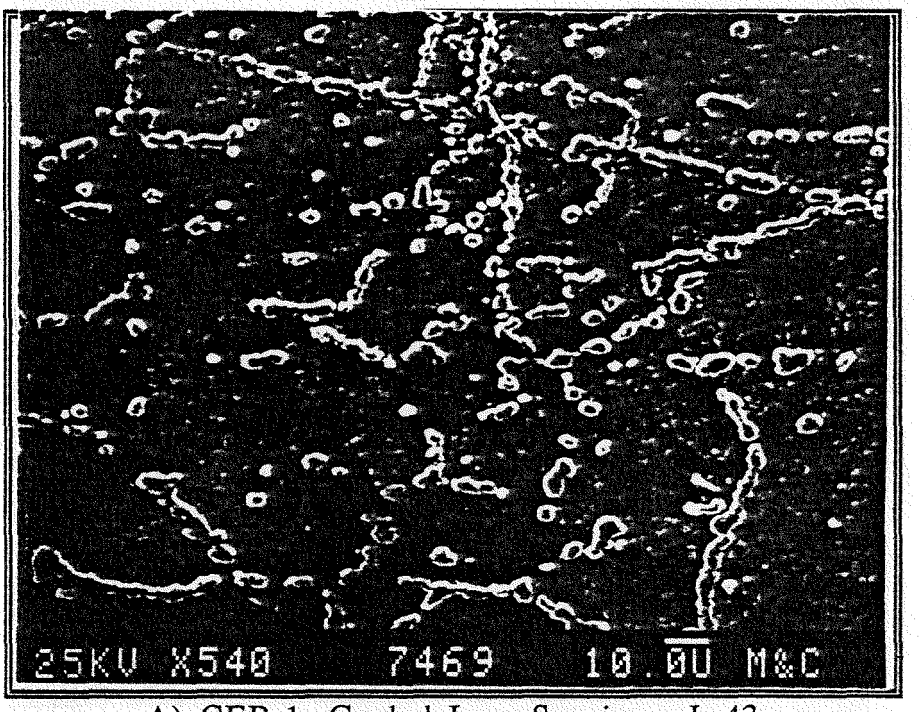

A) GEB-1, Cooled Leg, Specimen L-43
482 °C, 3040 hours
Photo # 27469

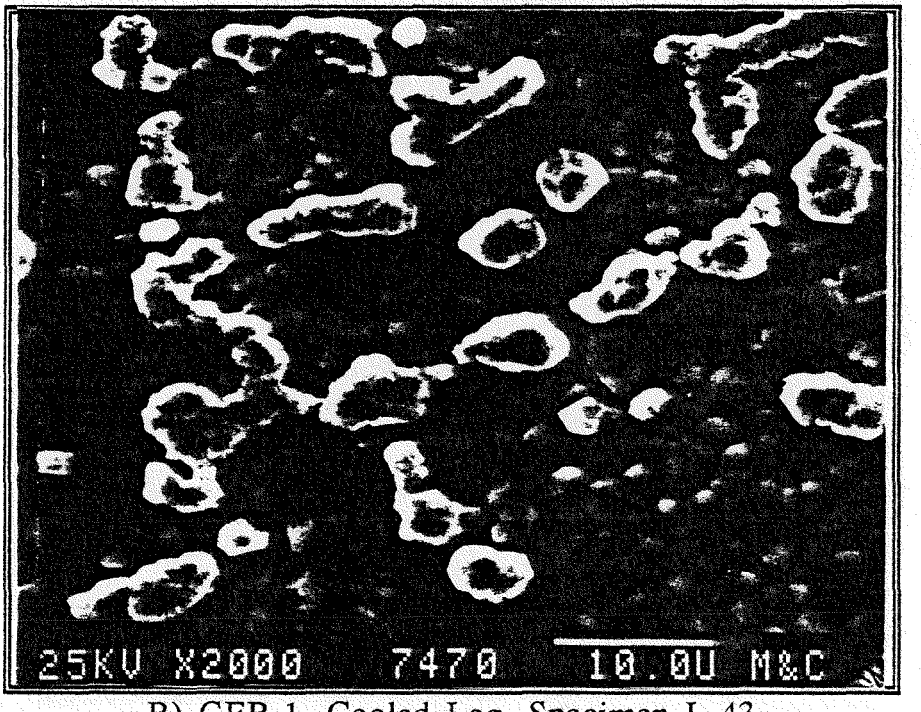

B) GEB-1, Cooled Leg, Specimen L-43
482 °C, 3040 hours
Photo # 27470

Figure 3.3.20 Surface Morphology L-43

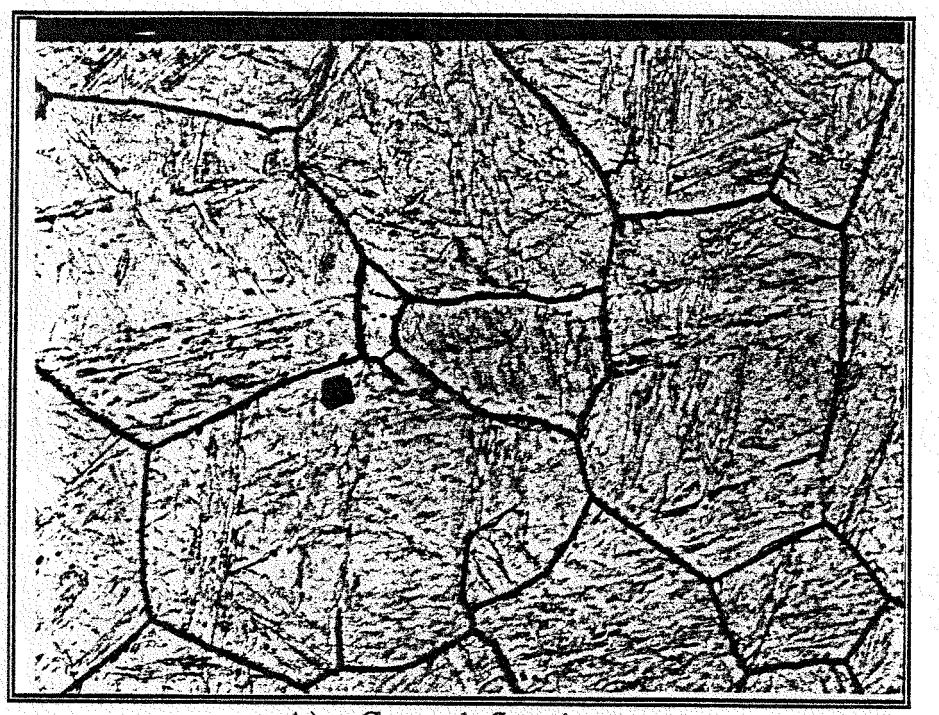

A) Control Specimen
400X
Photo # 87-1004

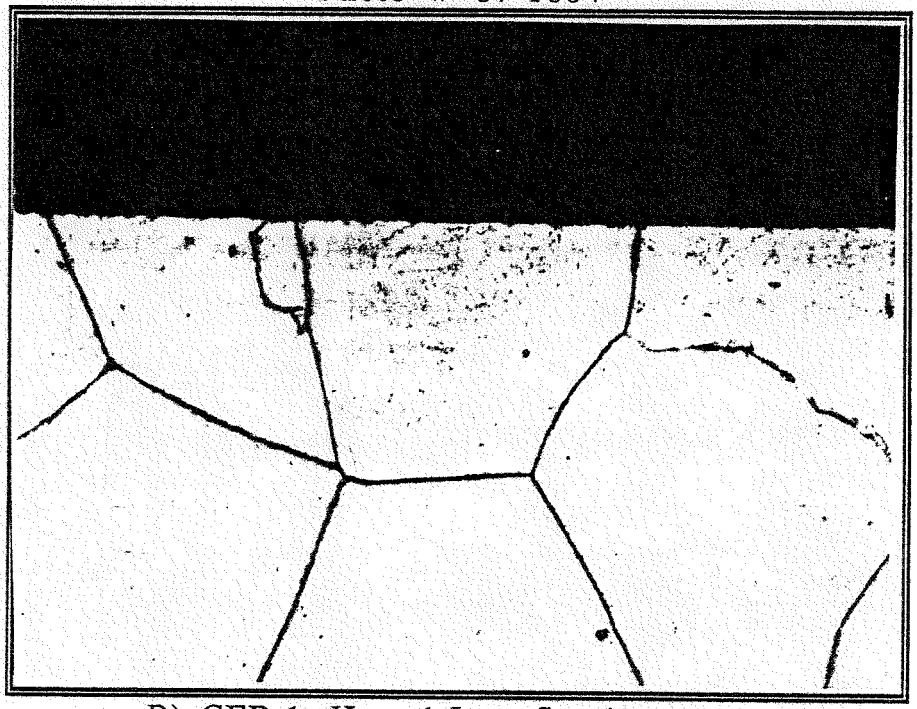

B) GEB-1, Heated Leg, Specimen L-01
360 °C, 3040 hours, 800X
Photo # Y210028

Figure 3.3.21 Cross Section View Control Specimen and L-01

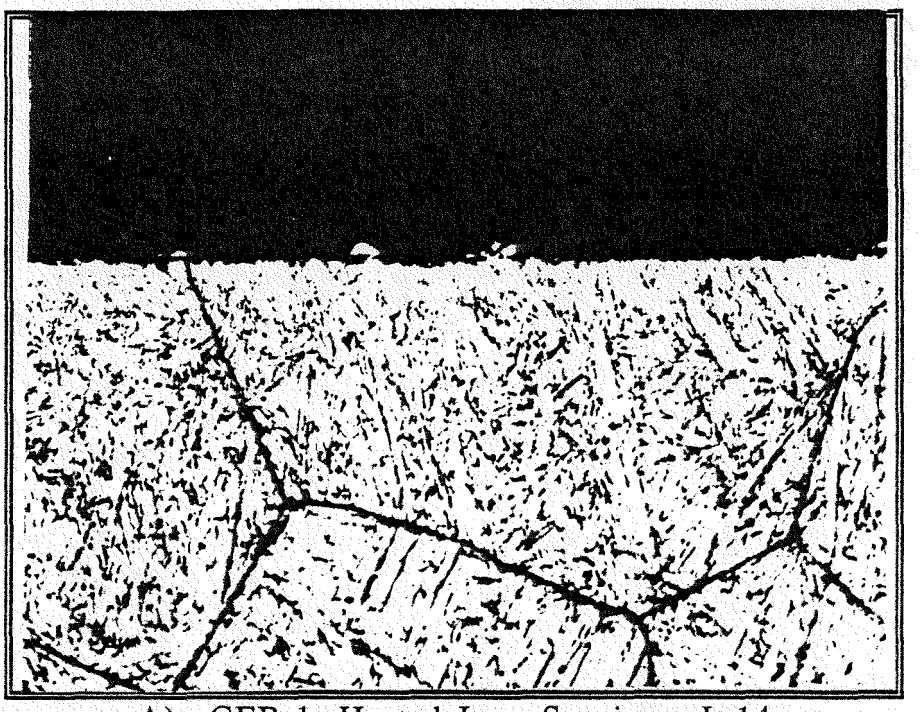

A) GEB-1, Heated Leg, Specimen L-14
458 °C, 3040 hours, 800X
Photo # Y210043

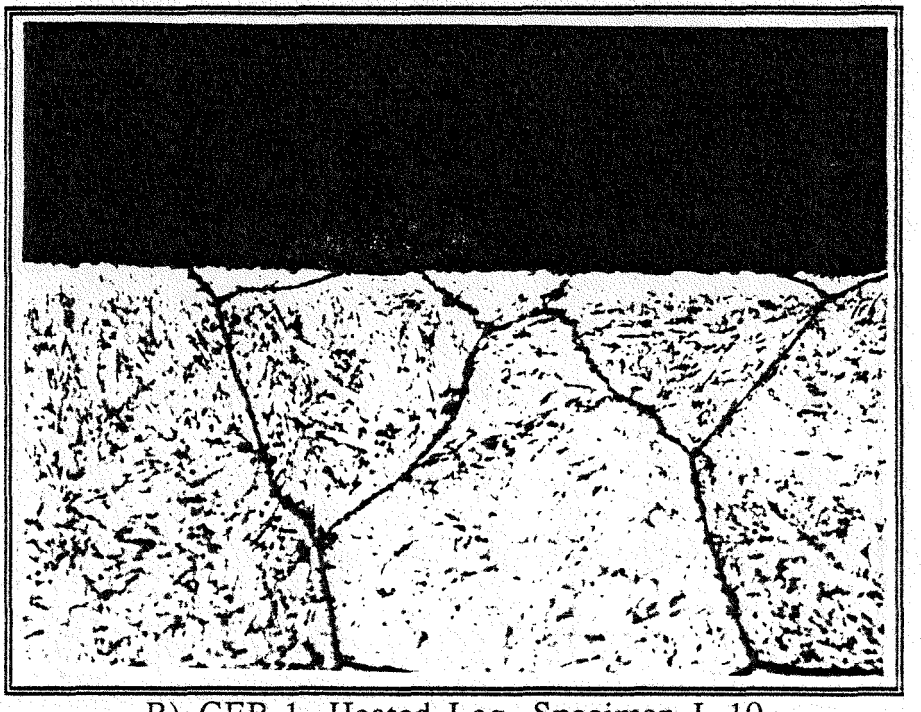

B) GEB-1, Heated Leg, Specimen L-10
428 °C, 3040 hours, 800X
Photo # Y210040

Figure 3.3.22 Cross Section View L-14 and L-10

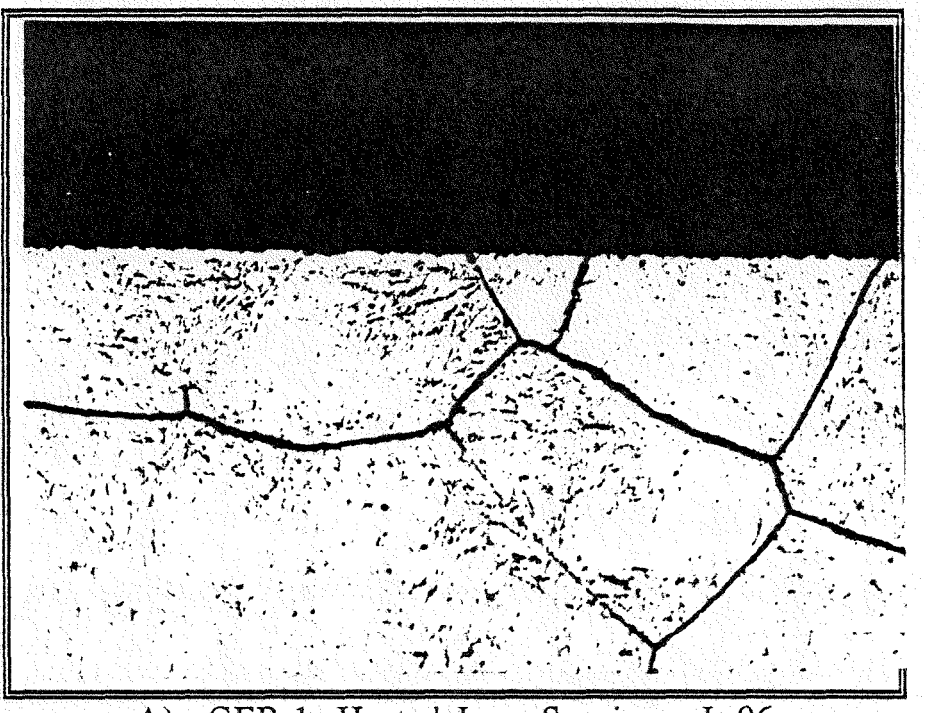

A) GEB-1, Heated Leg, Specimen L-06
398 °C, 3040 hours, 800X
Photo # Y210037

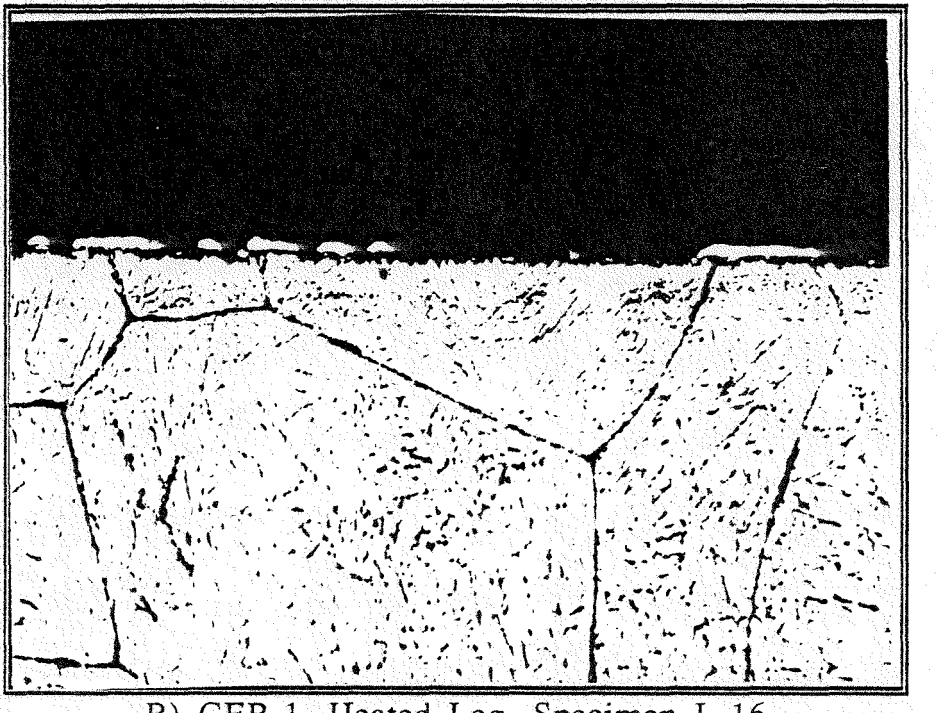

B) GEB-1, Heated Leg, Specimen L-16
473 °C, 3040 hours, 800X
Photo # Y210048

Figure 3.3.23 Cross Section View L-06 and L-16

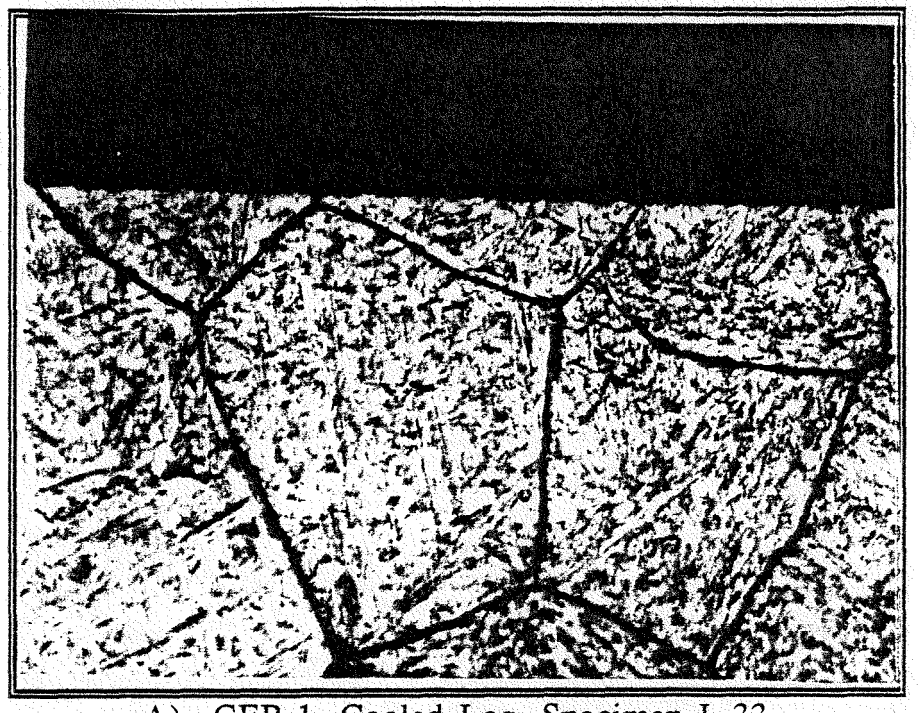

A) GEB-1, Cooled Leg, Specimen L-33
422 °C, 3040 hours, 800X
Photo # Y210072

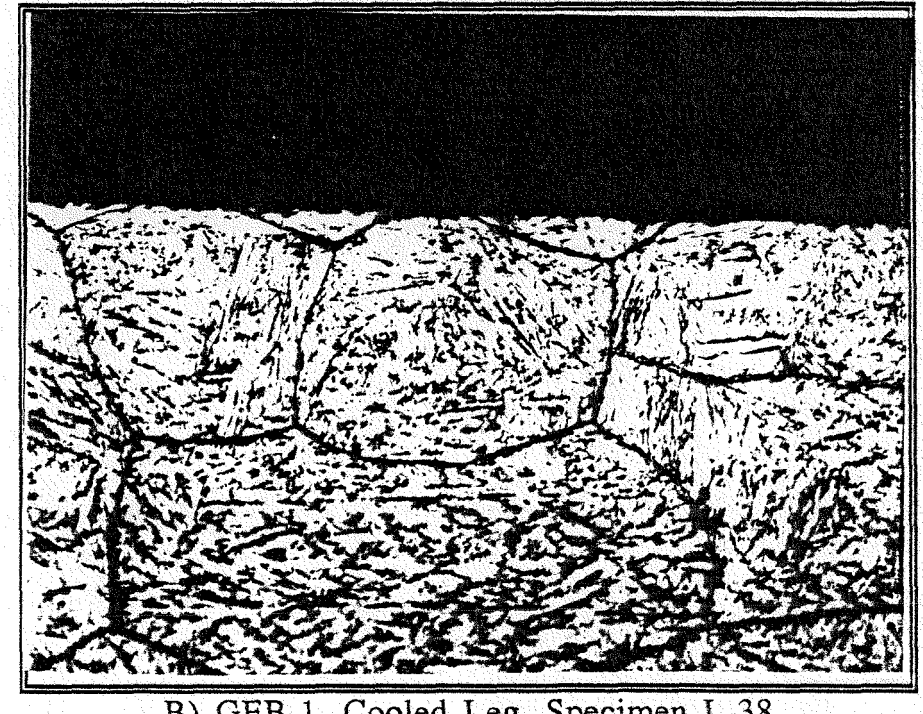

B) GEB-1, Cooled Leg, Specimen L-38
451 °C, 3040 hours, 800X
Photo # Y210075

Figure 3.3.24 Cross Section View L-33 and L-38

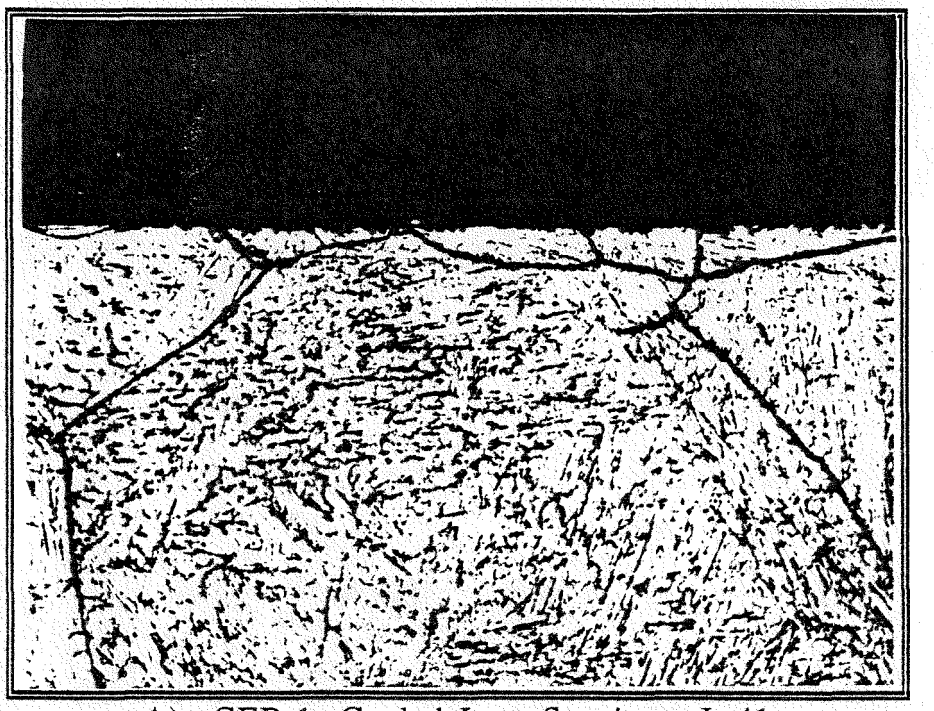

A) GEB-1, Cooled Leg, Specimen L-41
470 °C, 3040 hours, 800X
Photo # Y210078

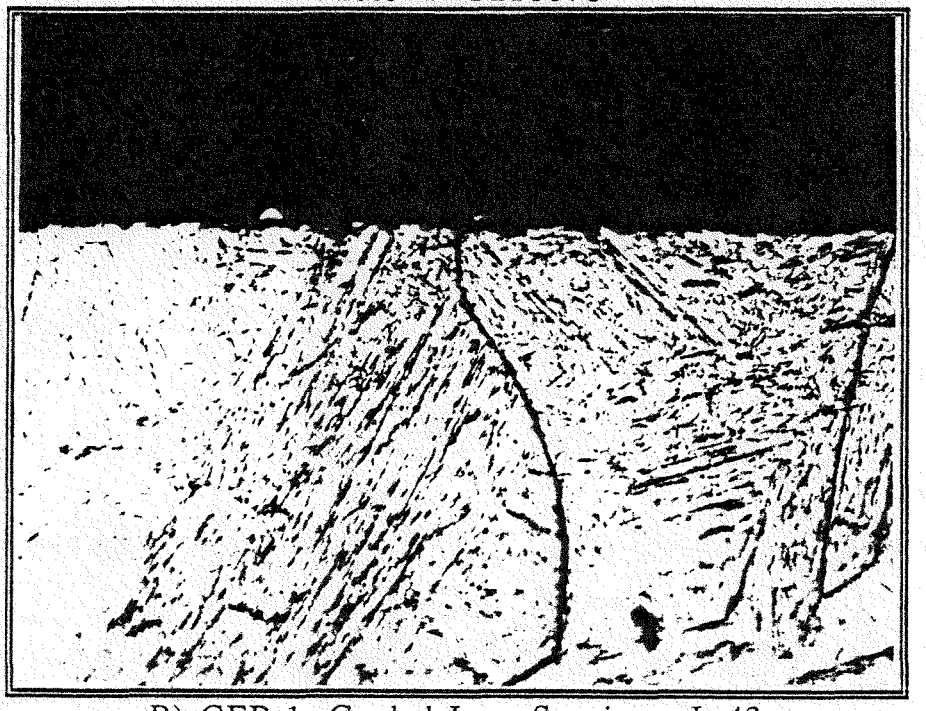

B) GEB-1, Cooled Leg, Specimen L-43
482 °C, 3040 hours, 800X
Photo # Y210088

Figure 3.3.25 Cross Section View L-41 and L-43

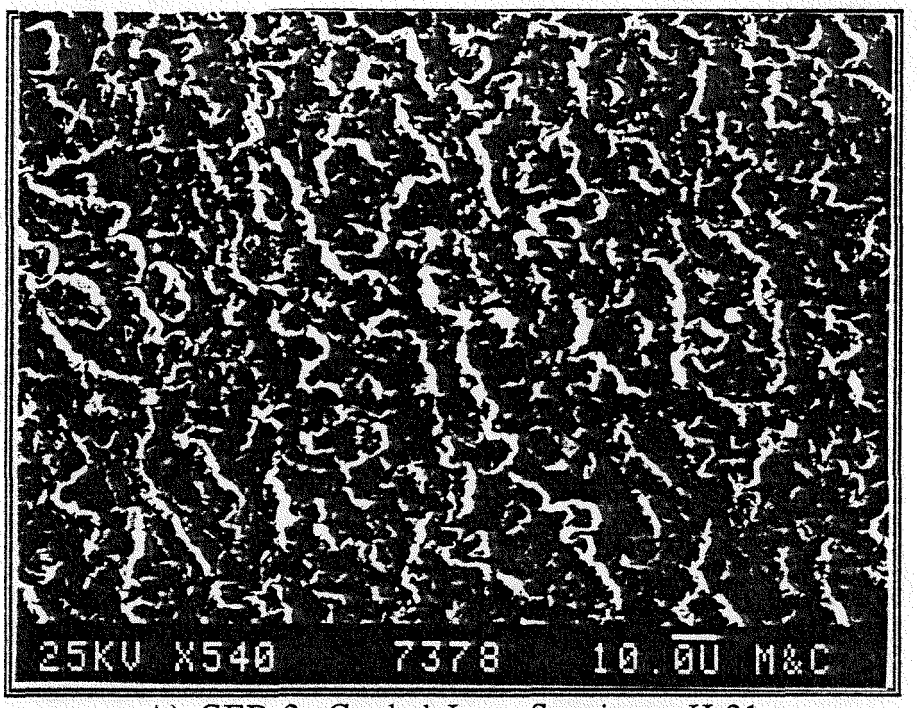

A) GEB-2, Cooled Leg, Specimen H-21
530 °C, 2510 hours
Photo # 27378

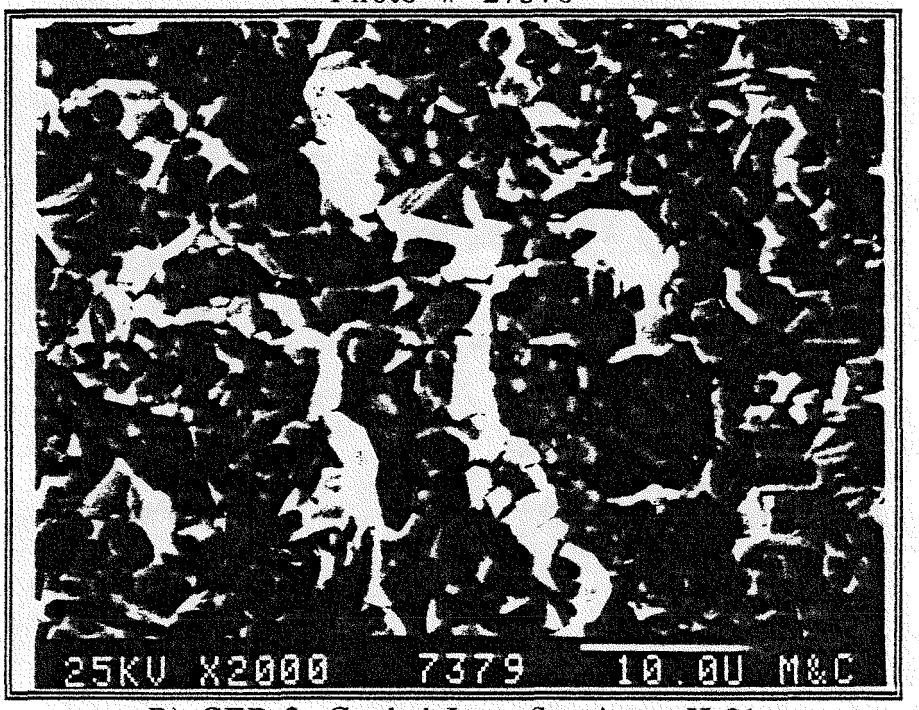

B) GEB-2, Cooled Leg, Specimen H-21
530 °C, 2510 hours
Photo # 27379

Figure 3.3.26 Surface Morphology H-21

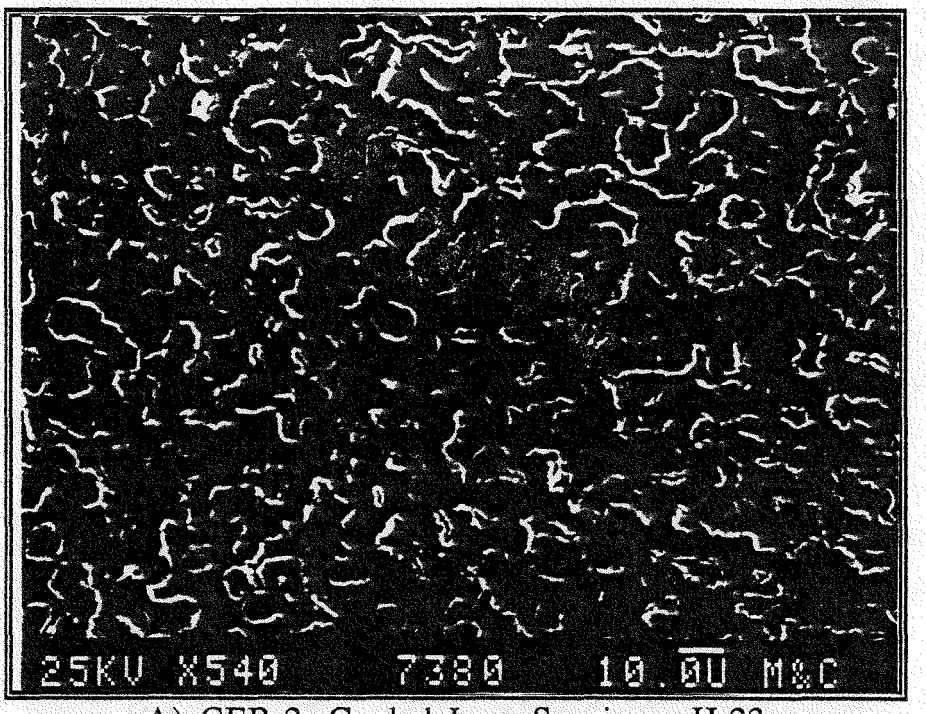

A) GEB-2, Cooled Leg, Specimen H-23
540 °C, 2510 hours
Photo # 27380

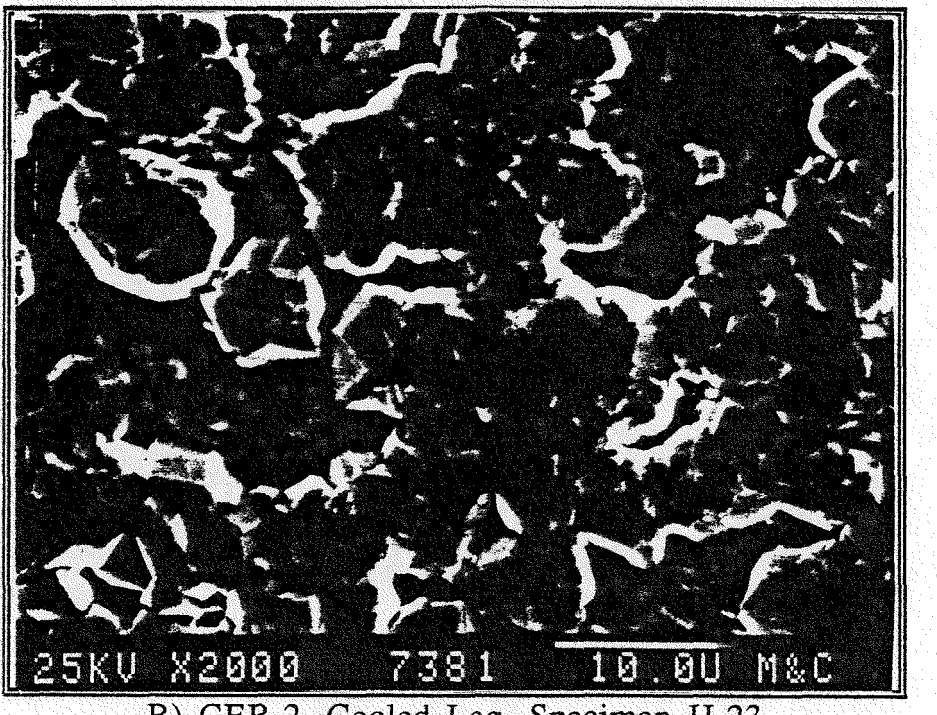

B) GEB-2, Cooled Leg, Specimen H-23
540 °C, 2510 hours
Photo # 27381

Figure 3.3.27 Surface Morphology H-23

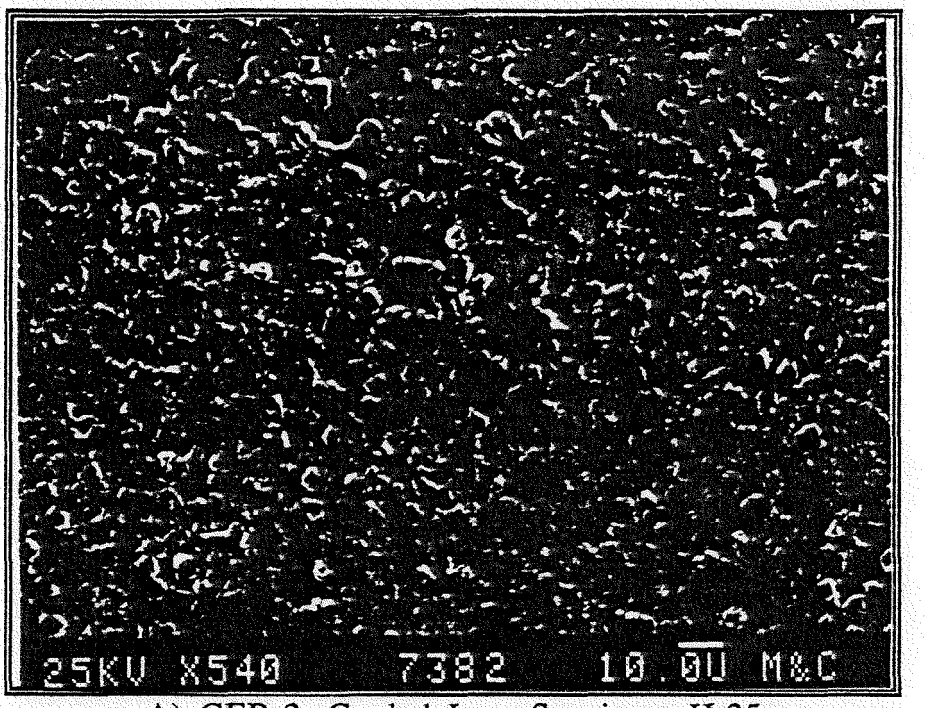

A) GEB-2, Cooled Leg, Specimen H-25
550 °C, 2510 hours
Photo # 27382

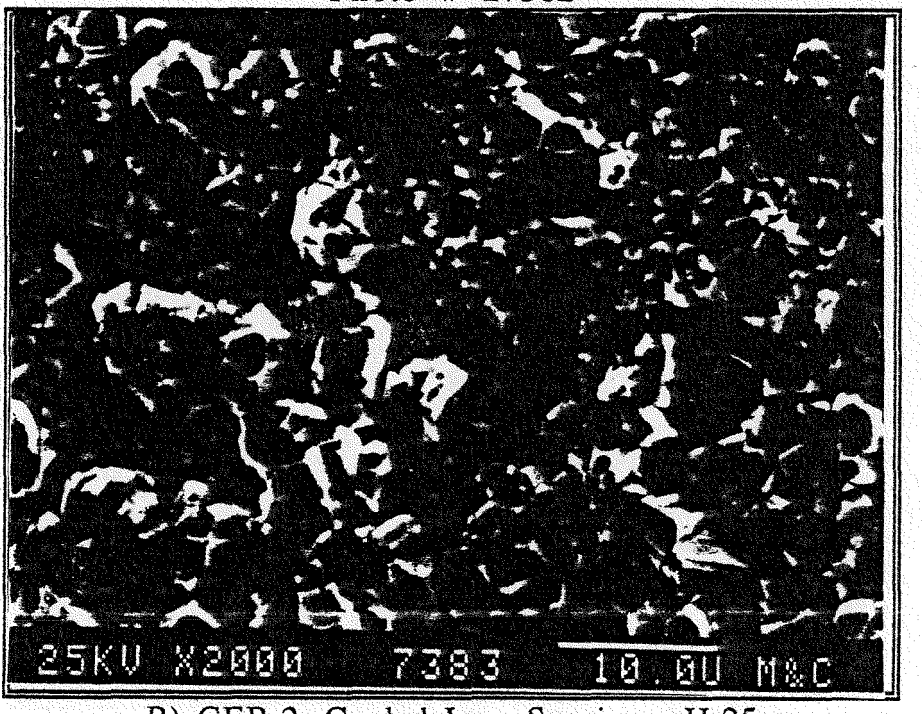

B) GEB-2, Cooled Leg, Specimen H-25
550 °C, 2510 hours
Photo # 27383

Figure 3.3.28 Surface Morphology H-25

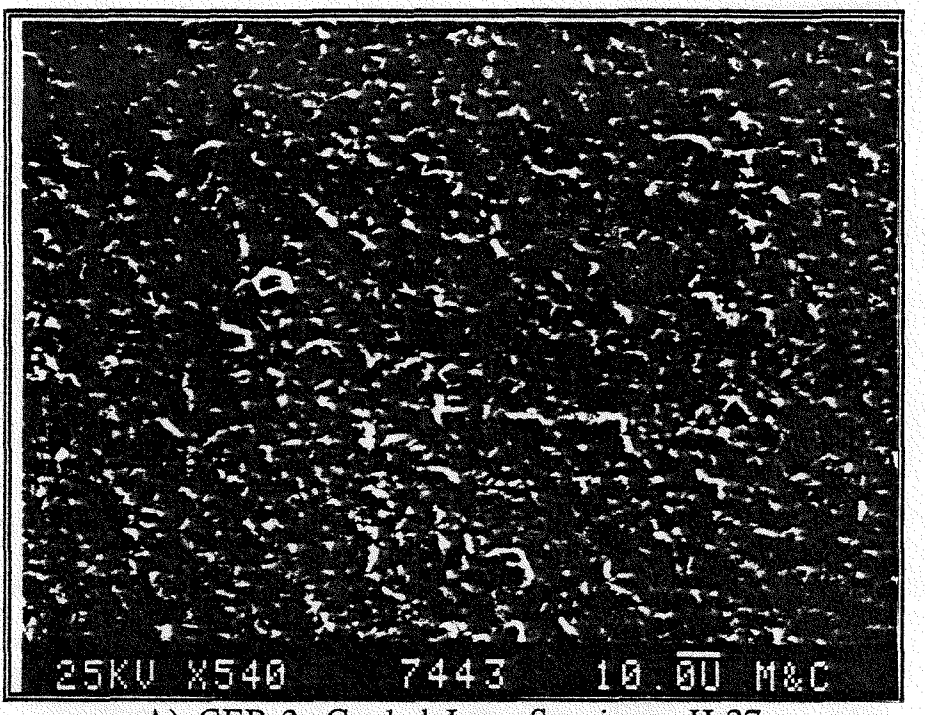

A) GEB-2, Cooled Leg, Specimen H-27
560 °C, 2510 hours
Photo # 27443

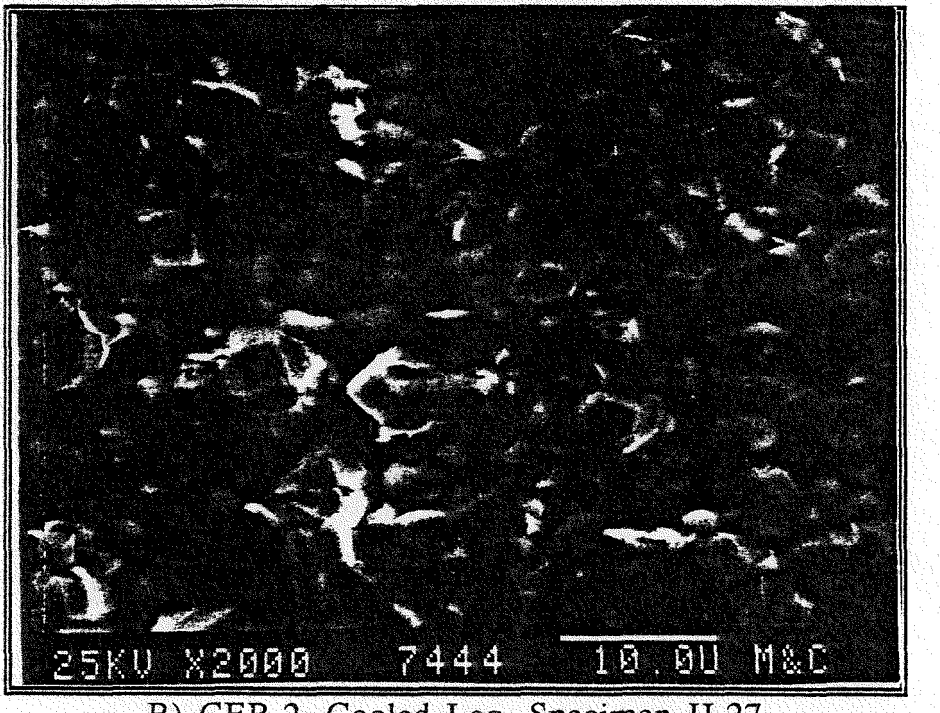

B) GEB-2, Cooled Leg, Specimen H-27
560 °C, 2510 hours
Photo # 27444

Figure 3.3.29 Surface Morphology H-27

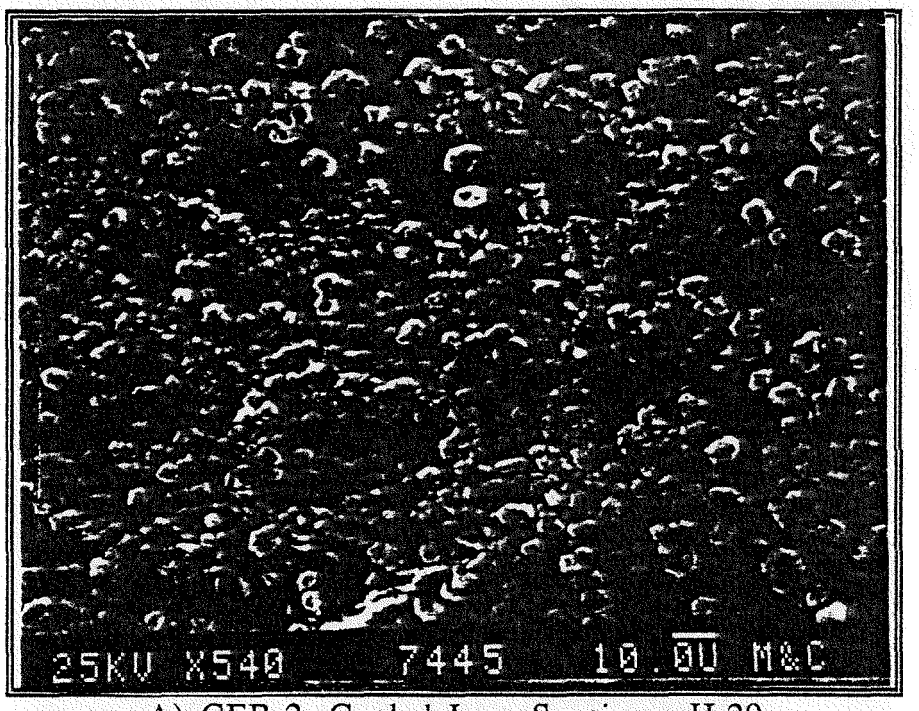

A) GEB-2, Cooled Leg, Specimen H-29
570 °C, 2510 hours
Photo # 27445

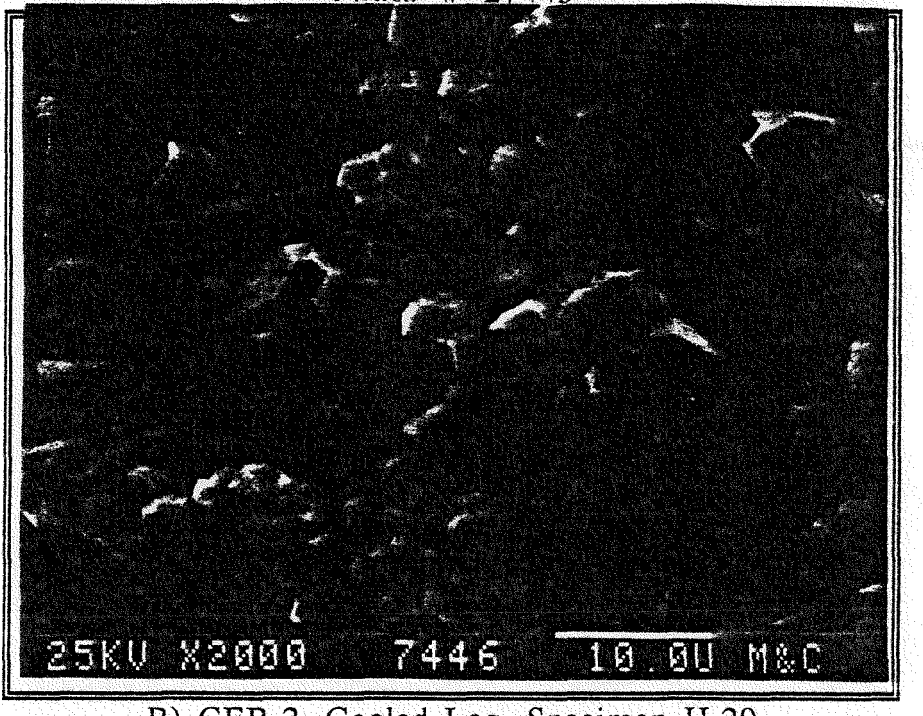

B) GEB-2, Cooled Leg, Specimen H-29
570 °C, 2510 hours
Photo # 27446

Figure 3.3.30 Surface Morphology H-29

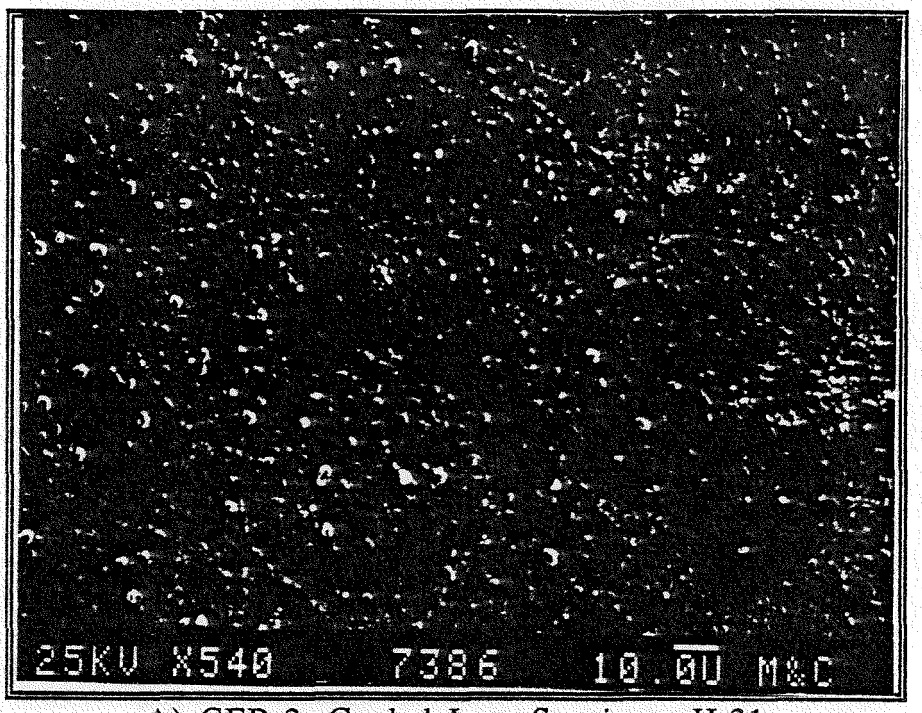

A) GEB-2, Cooled Leg, Specimen H-31
580 °C, 2510 hours
Photo # 27386

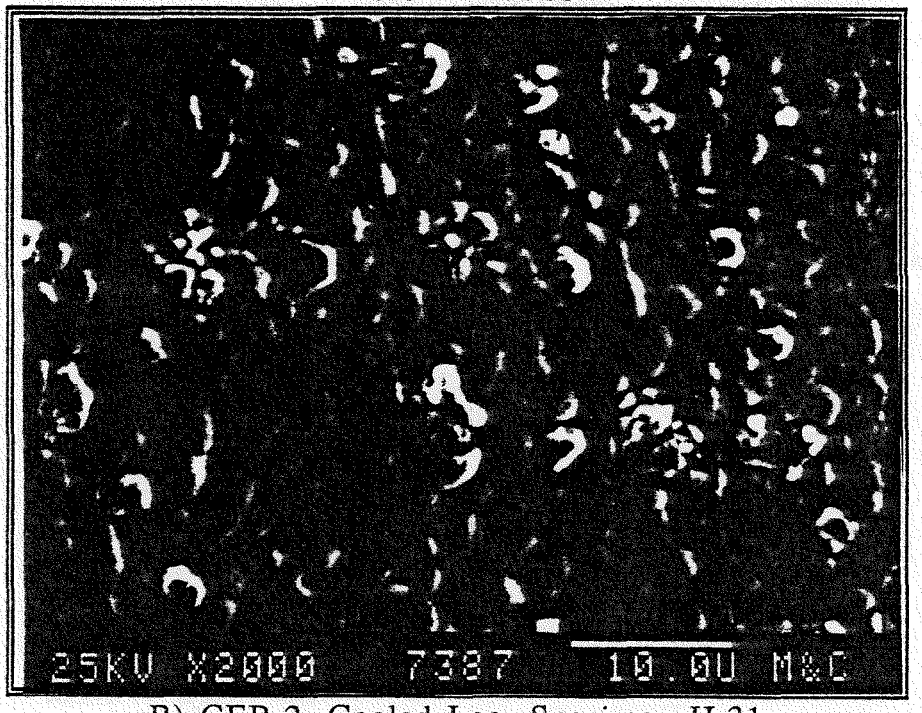

B) GEB-2, Cooled Leg, Specimen H-31
580 °C, 2510 hours
Photo # 27387

Figure 3.3.31 Surface Morphology H-31

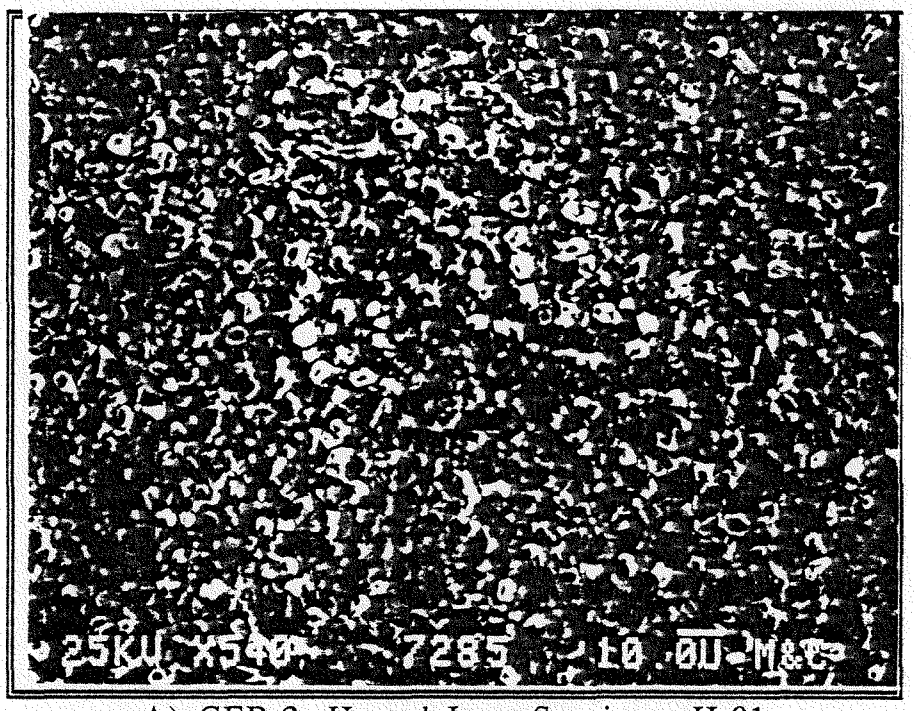

A) GEB-2, Heated Leg, Specimen H-01
529 °C, 2510 hours
Photo # 27285

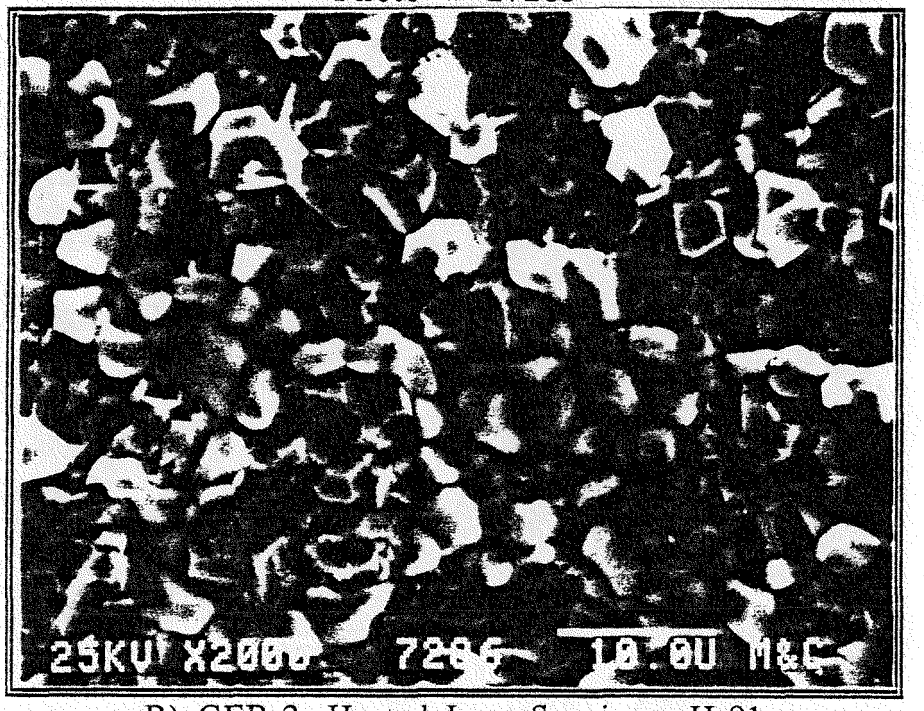

B) GEB-2, Heated Leg, Specimen H-01
529 °C, 2510 hours
Photo # 27286

Figure 3.3.32 Surface Morphology H-01

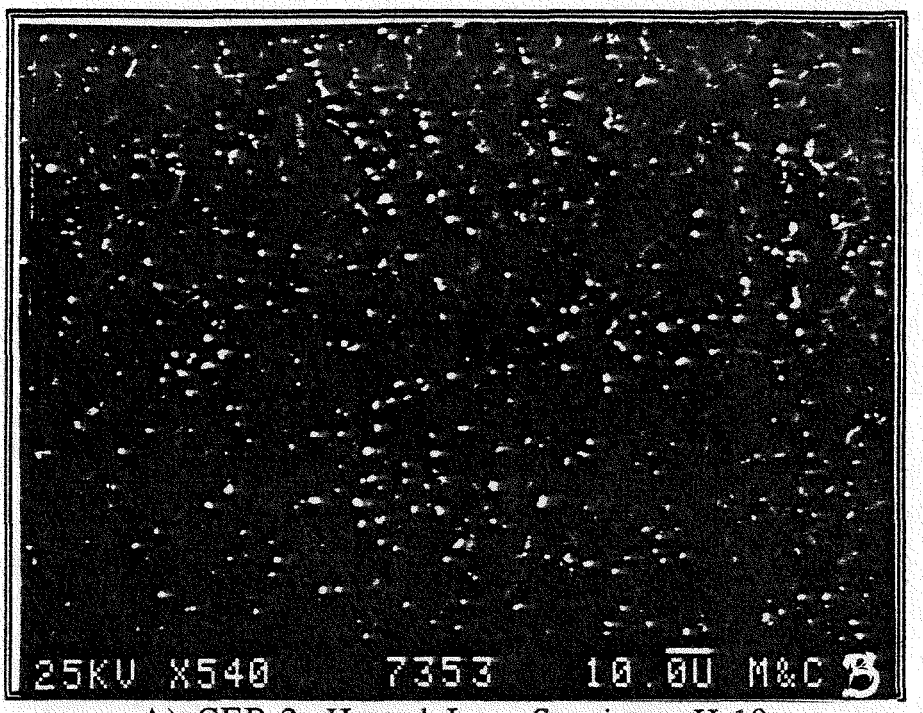

A) GEB-2, Heated Leg, Specimen H-19
645 °C, 2510 hours
Photo # 27353

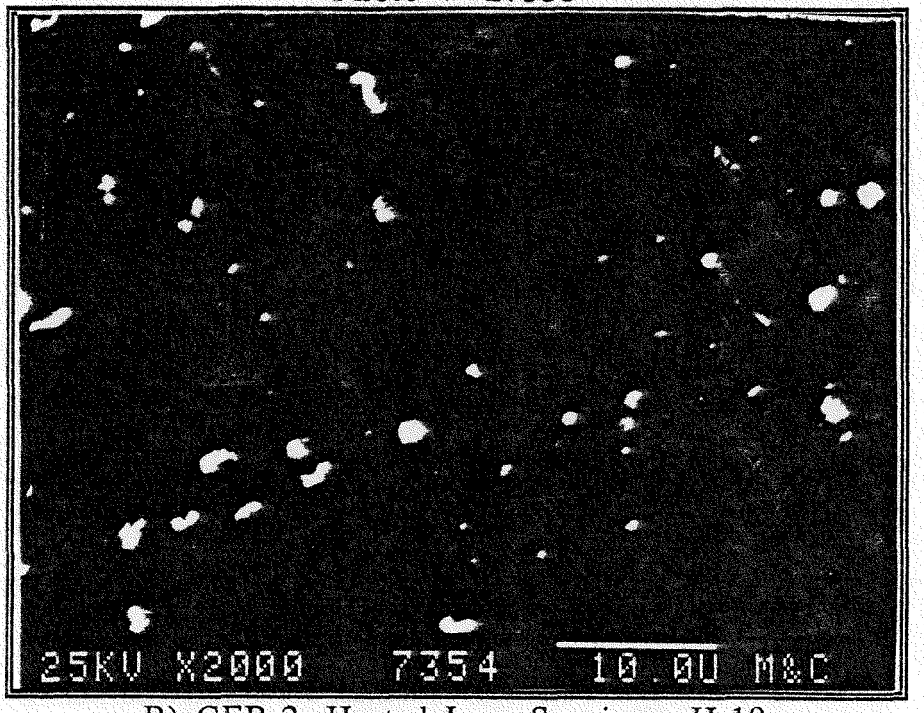

B) GEB-2, Heated Leg, Specimen H-19
645 °C, 2510 hours
Photo # 27354

Figure 3.3.33 Surface Morphology H-19

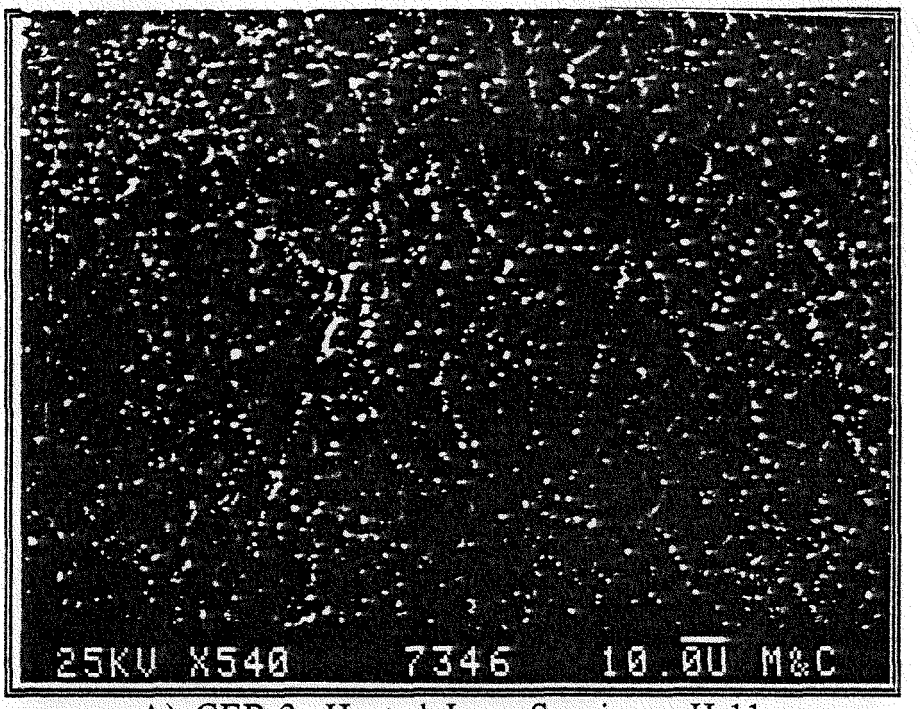

A) GEB-2, Heated Leg, Specimen H-11
595 °C, 2510 hours
Photo # 27346

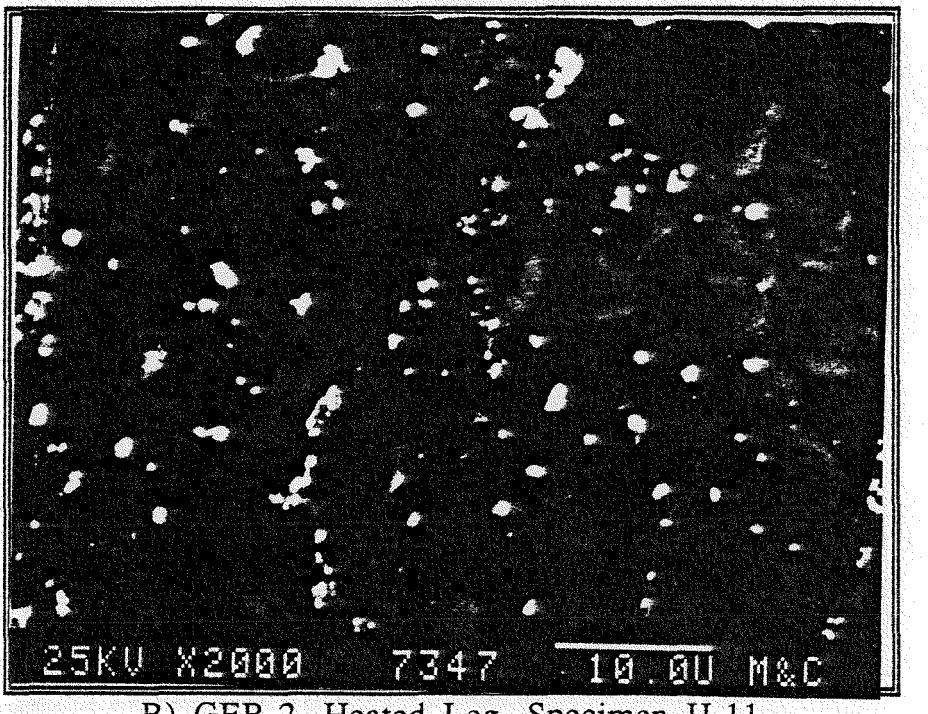

B) GEB-2, Heated Leg, Specimen H-11
595 °C, 2510 hours
Photo # 27347

Figure 3.3.34 Surface Morphology H-11

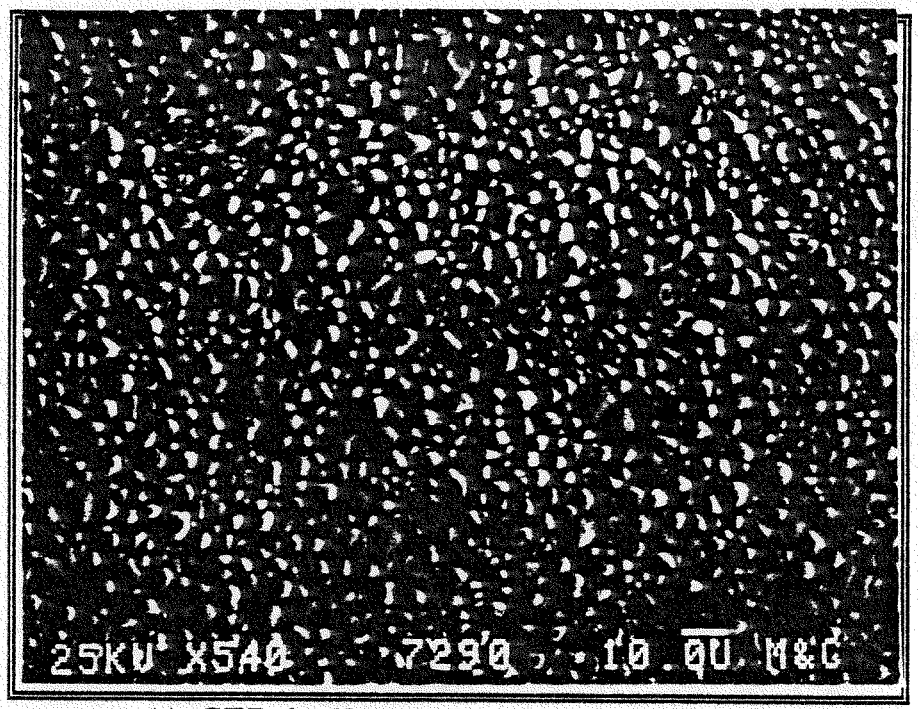

A) GEB-2, Heated Leg, Specimen H-05
555 °C, 2510 hours
Photo # 27290

B) GEB-2, Heated Leg, Specimen H-05
555 °C, 2510 hours
Photo # 27291

Figure 3.3.35 Surface Morphology H-05

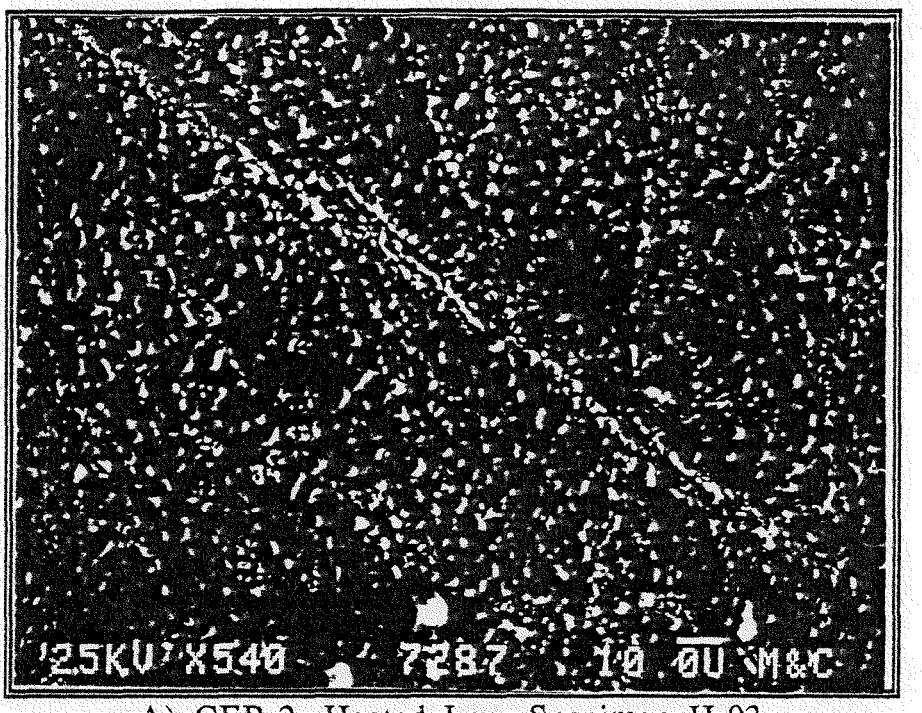

A) GEB-2, Heated Leg, Specimen H-03
542 °C, 2510 hours
Photo # 27287

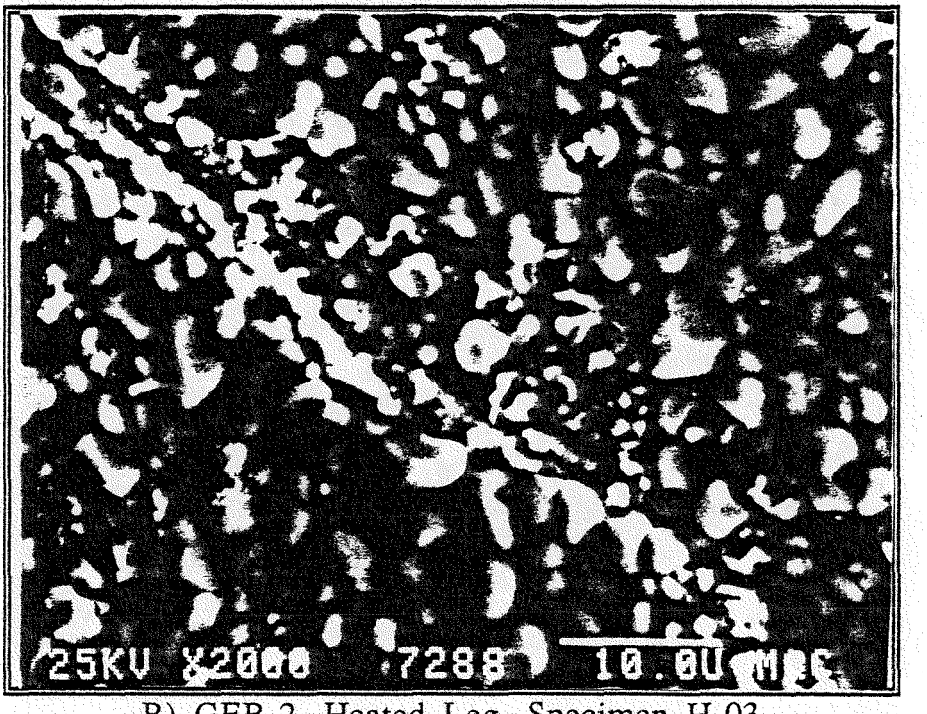

B) GEB-2, Heated Leg, Specimen H-03
542 °C, 2510 hours
Photo # 27288

Figure 3.3.36 Surface Morphology H-03

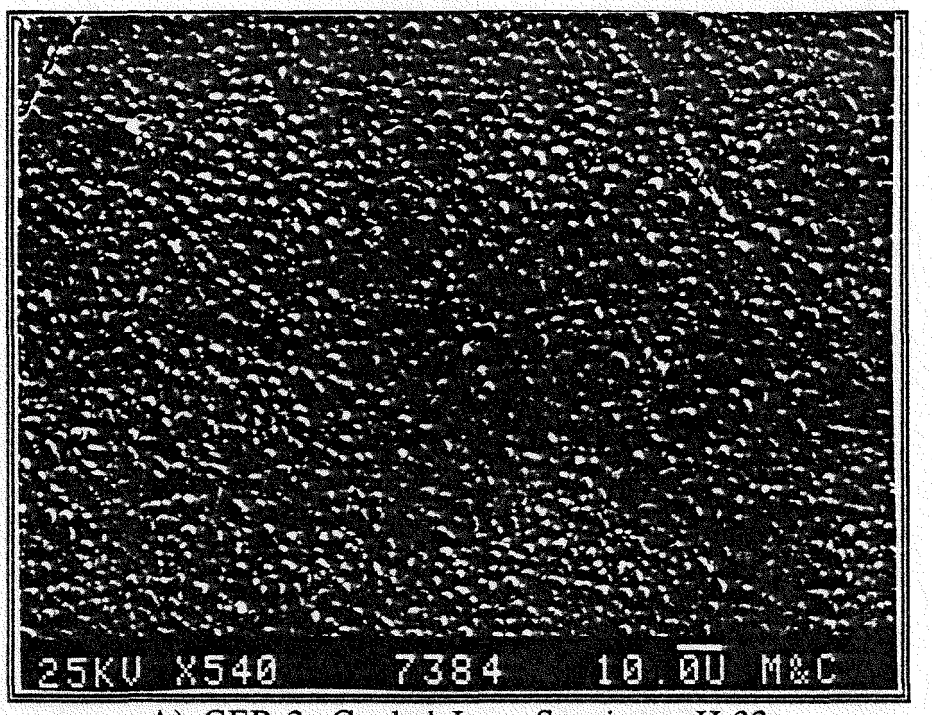

A) GEB-2, Cooled Leg, Specimen H-33
590 °C, 2510 hours
Photo # 27384

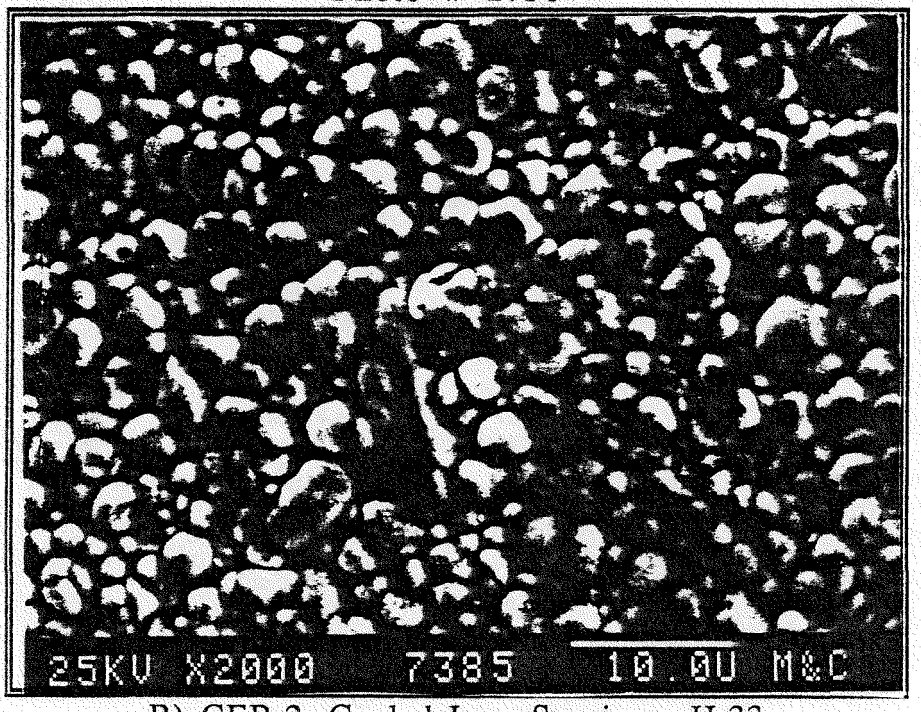

B) GEB-2, Cooled Leg, Specimen H-33
590 °C, 2510 hours
Photo # 27385

Figure 3.3.37 Surface Morphology H-33

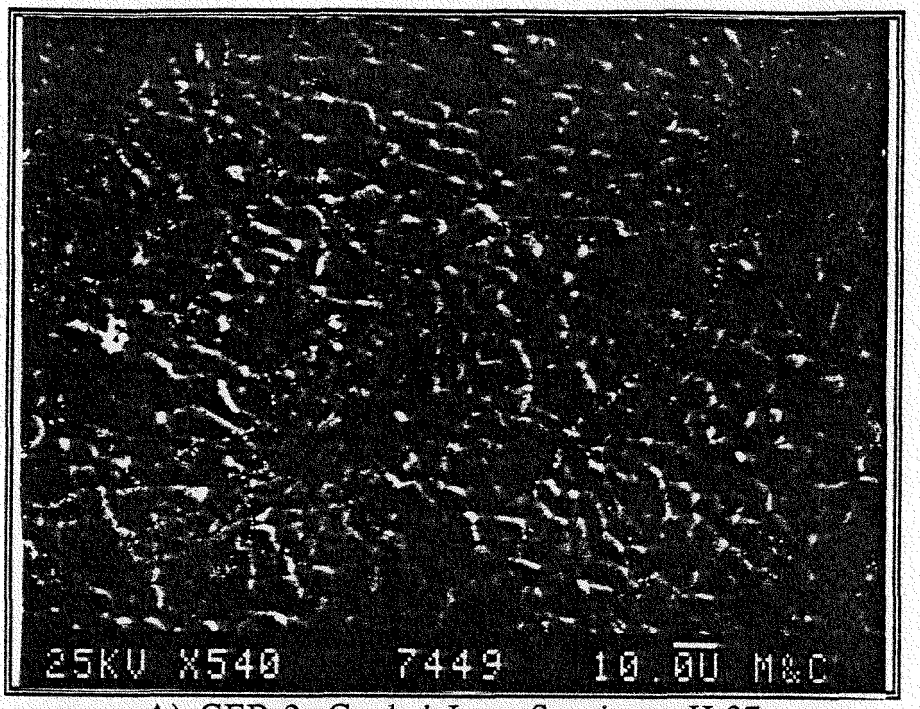

A) GEB-2, Cooled Leg, Specimen H-37
610 °C, 2510 hours
Photo # 27449

B) GEB-2, Cooled Leg, Specimen H-37
610 °C, 2510 hours
Photo # 27450

Figure 3.3.38 Surface Morphology H-37

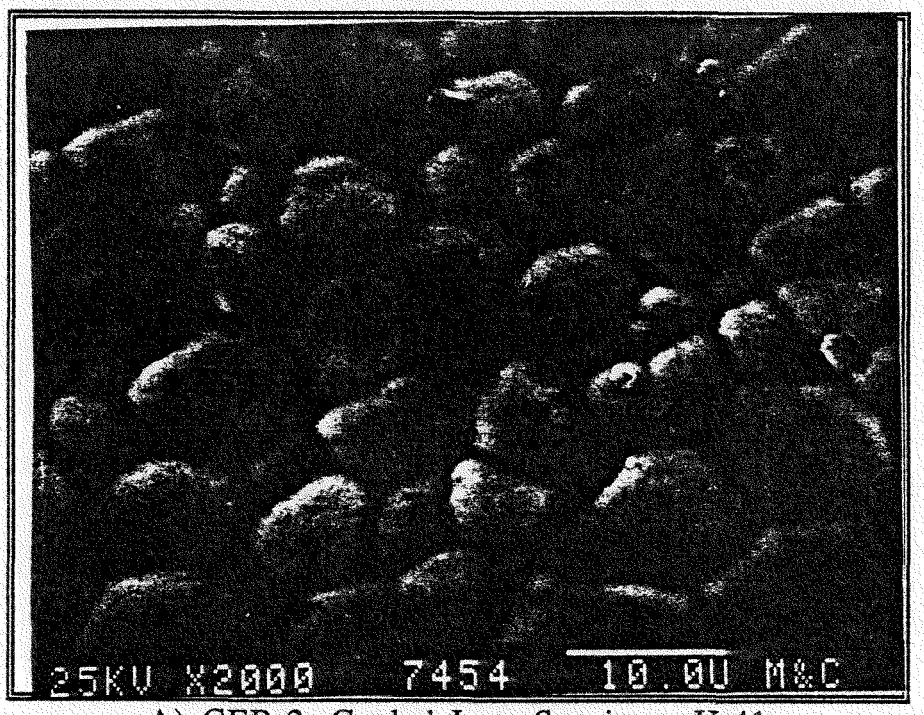

A) GEB-2, Cooled Leg, Specimen H-41
630 °C, 2510 hours
Photo # 27454

Figure 3.3.39 Surface Morphology H-41

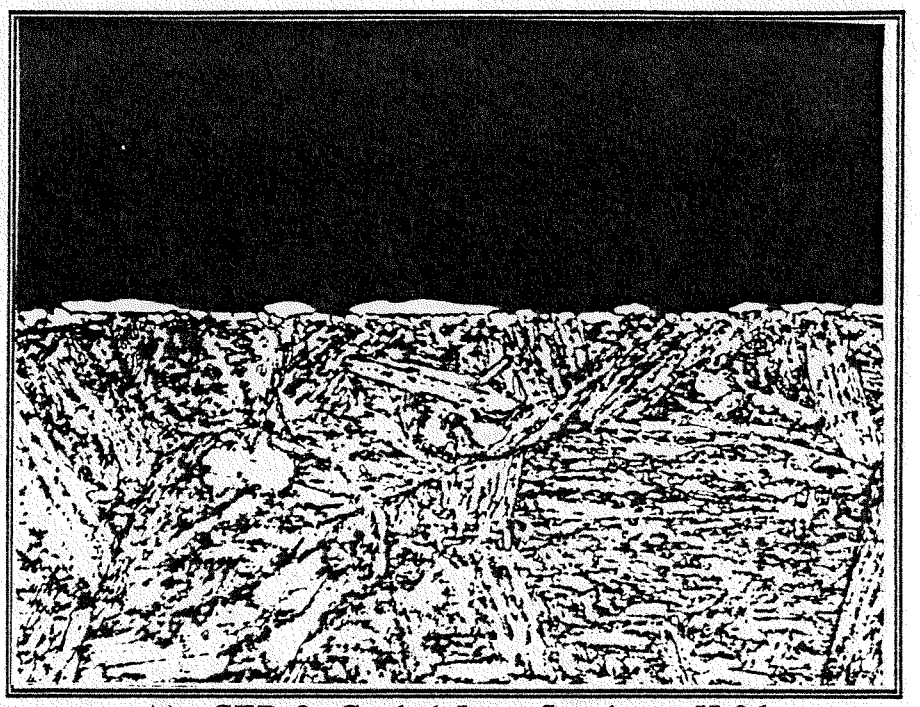

A) GEB-2, Cooled Leg, Specimen H-26
555 °C, 2510 hours, 800X
Photo # Y210343

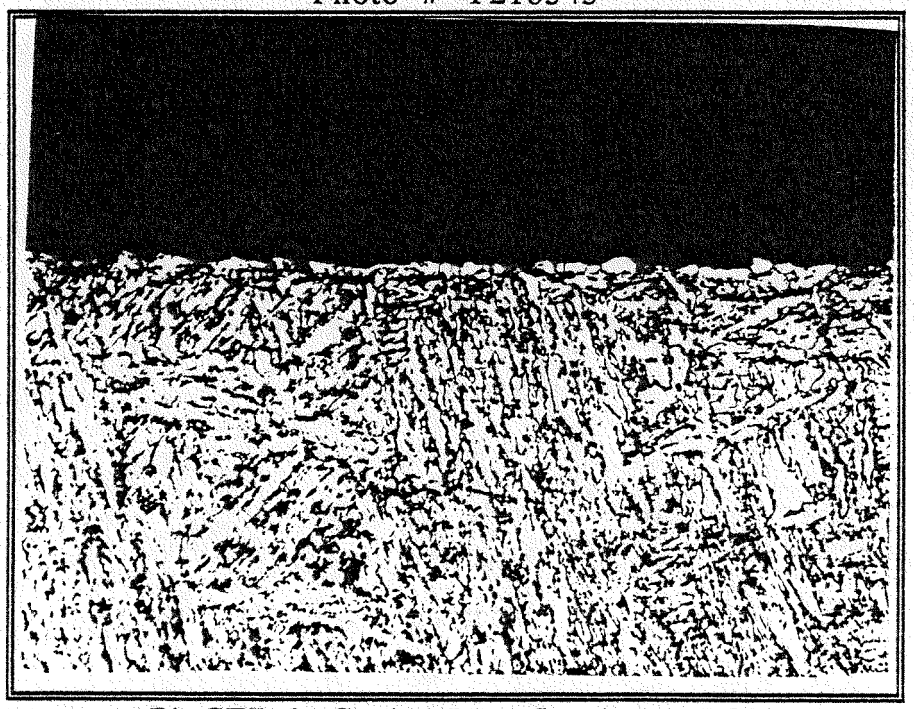

B) GEB-2, Cooled Leg, Specimen H-30
575 °C, 2510 hours, 800X
Photo # Y210348

Figure 3.3.40 Cross Section View H-26 and H-30

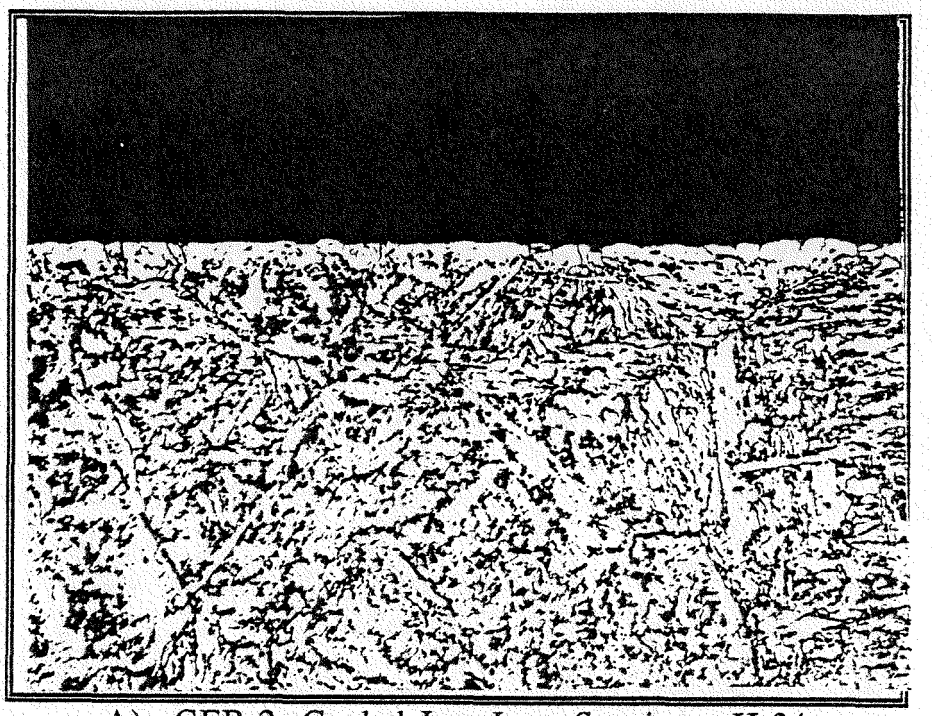

A) GEB-2, Cooled Leg Leg, Specimen H-34
595 °C, 2510 hours, 800X
Photo # Y210351

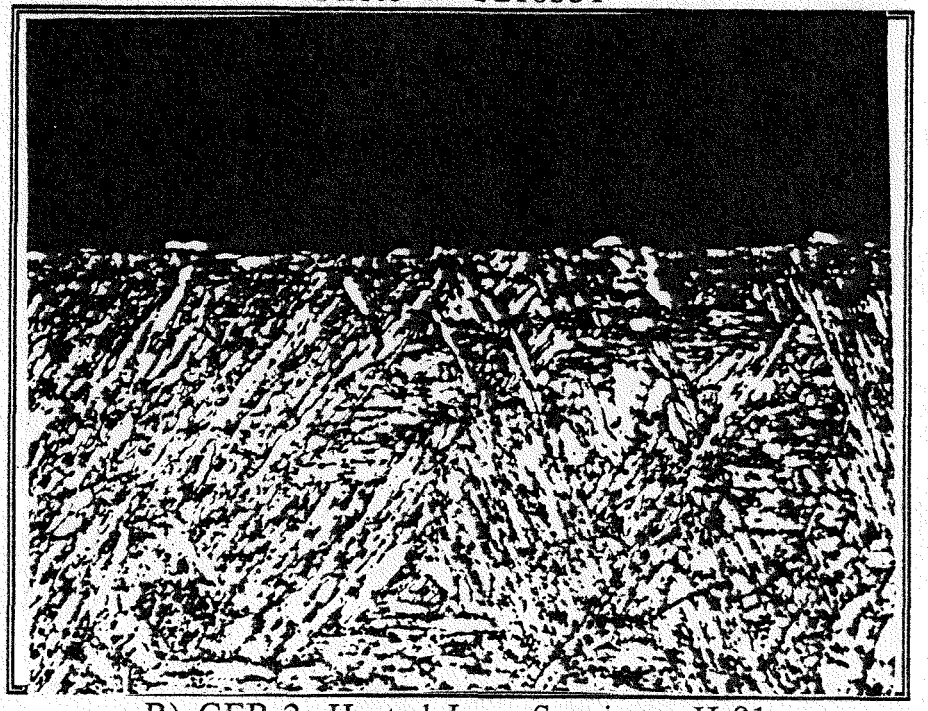

B) GEB-2, Heated Leg, Specimen H-01
529 °C, 2510 hours, 800X
Photo # Y210306

Figure 3.3.41 Cross Section View H-34 and H-01

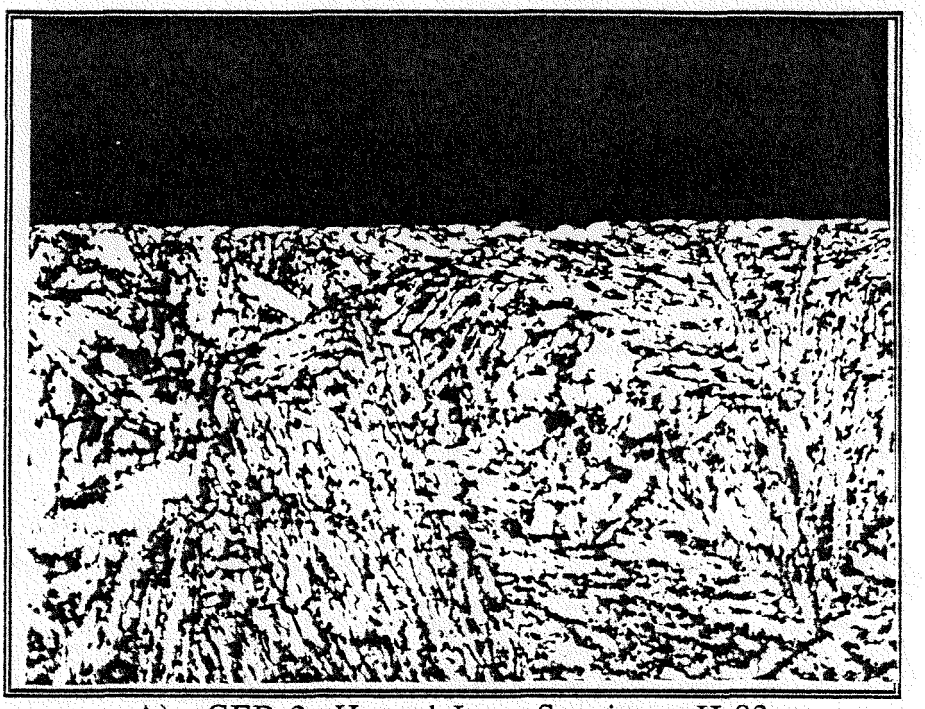

A) GEB-2, Heated Leg, Specimen H-03
541 °C, 2510 hours, 800X
Photo # Y210309

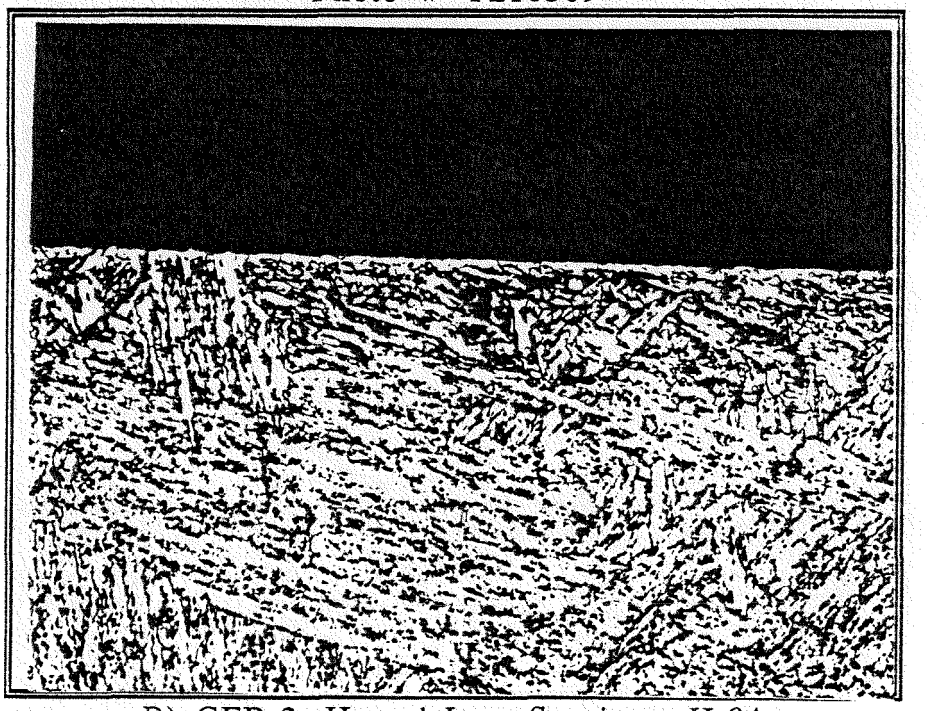

B) GEB-2, Heated Leg, Specimen H-04
548 °C, 2510 hours, 800X
Photo # Y210312

Figure 3.3.42 Cross Section View H-03 and H-04

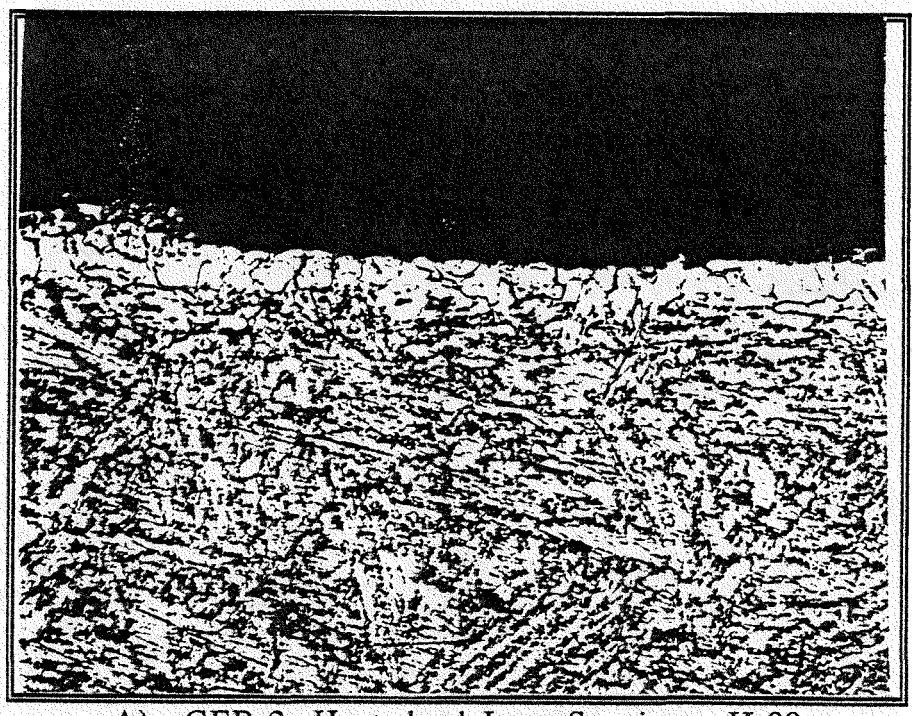

A) GEB-2, Heated ed Leg, Specimen H-09
580 °C, 2510 hours, 800X
Photo # Y210315

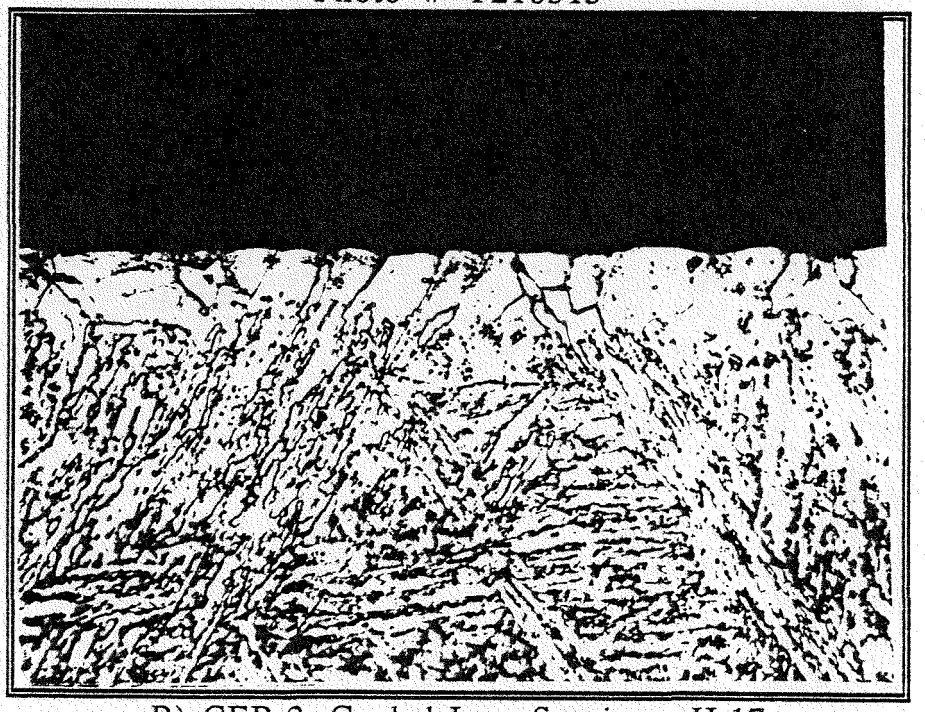

B) GEB-2, Cooled Leg, Specimen H-17
632 °C, 2510 hours, 800X
Photo # Y210321

Figure 3.3.43 Cross Section View H-09 and H-17

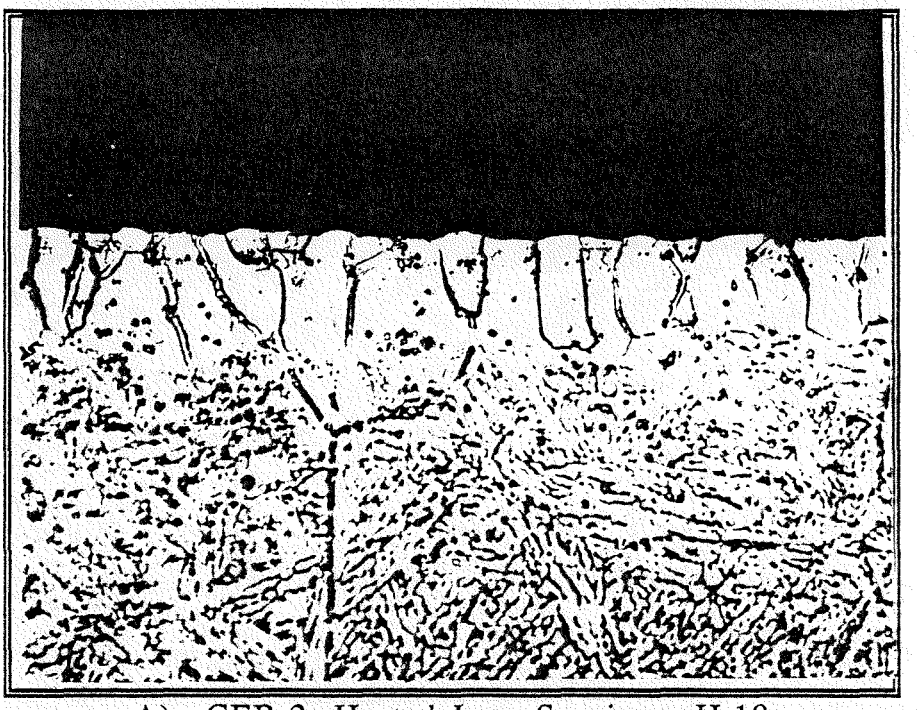

A) GEB-2, Heated Leg, Specimen H-19
645 °C, 2510 hours, 800X
Photo # Y210327

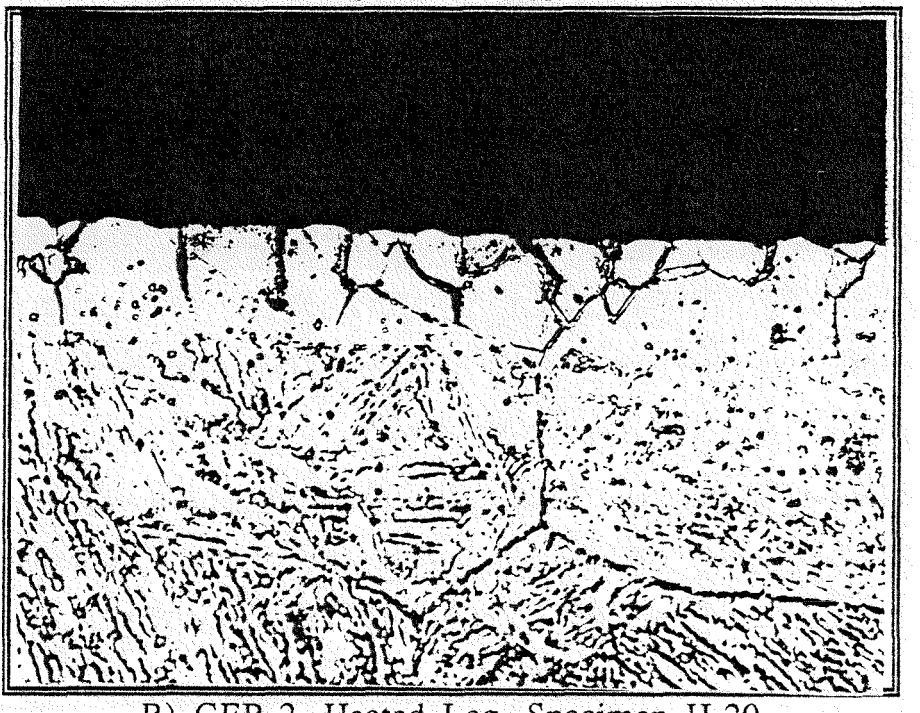

B) GEB-2, Heated Leg, Specimen H-20
652 °C, 2510 hours, 800X
Photo # Y210330

Figure 3.3.44 Cross Section View H-19 and H-20

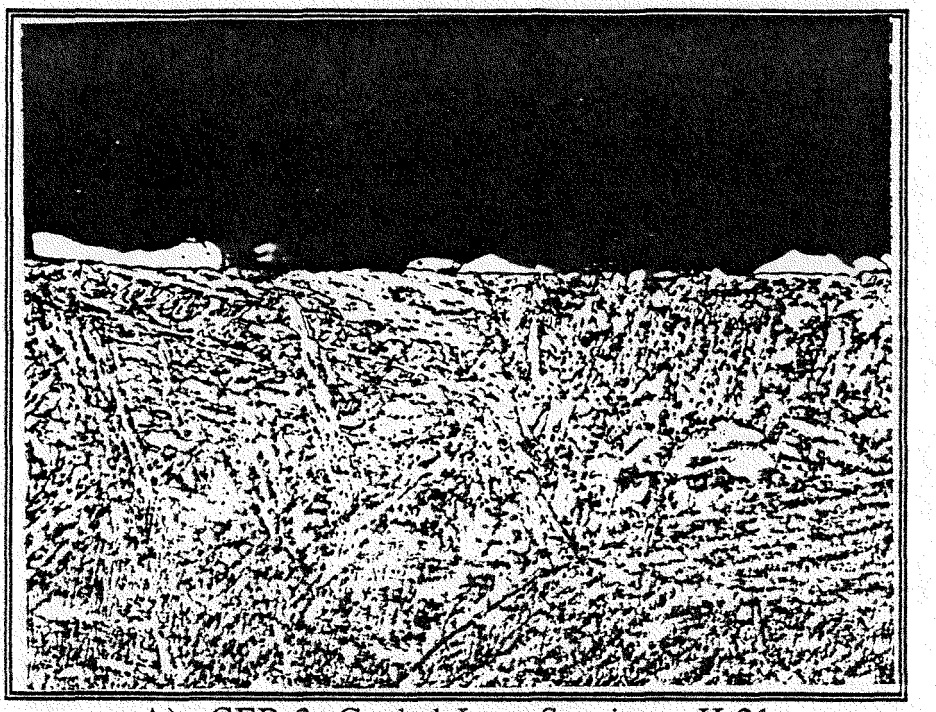

A) GEB-2, Cooled Leg, Specimen H-21
530 °C, 2510 hours, 800X
Photo # Y210333

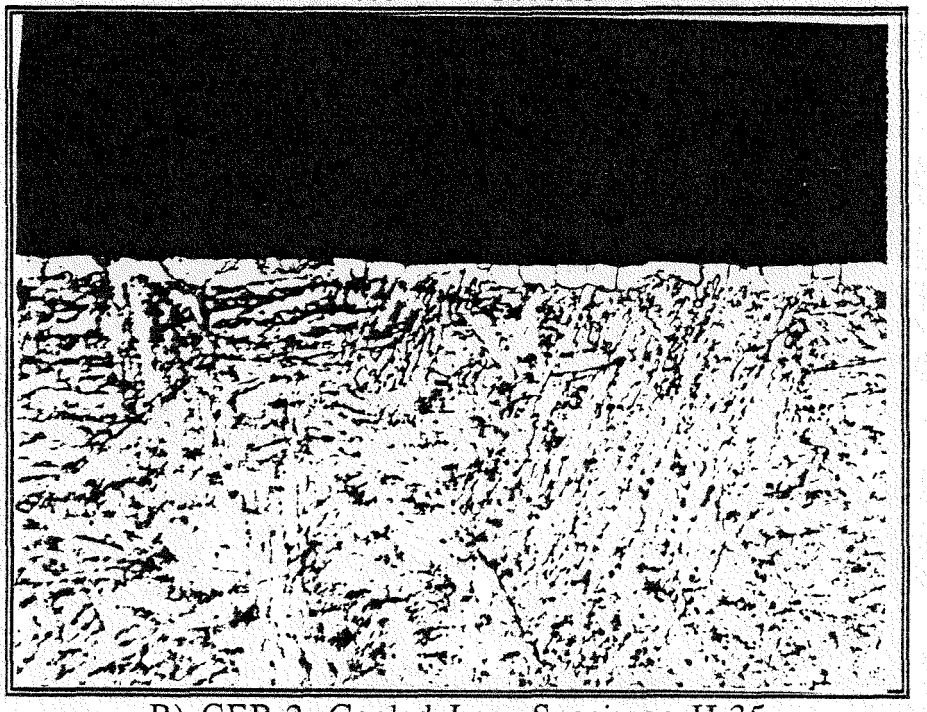

B) GEB-2, Cooled Leg, Specimen H-35
600 °C, 2510 hours, 800X
Photo # Y210354

Figure 3.3.45 Cross Section View H-21 and H-35

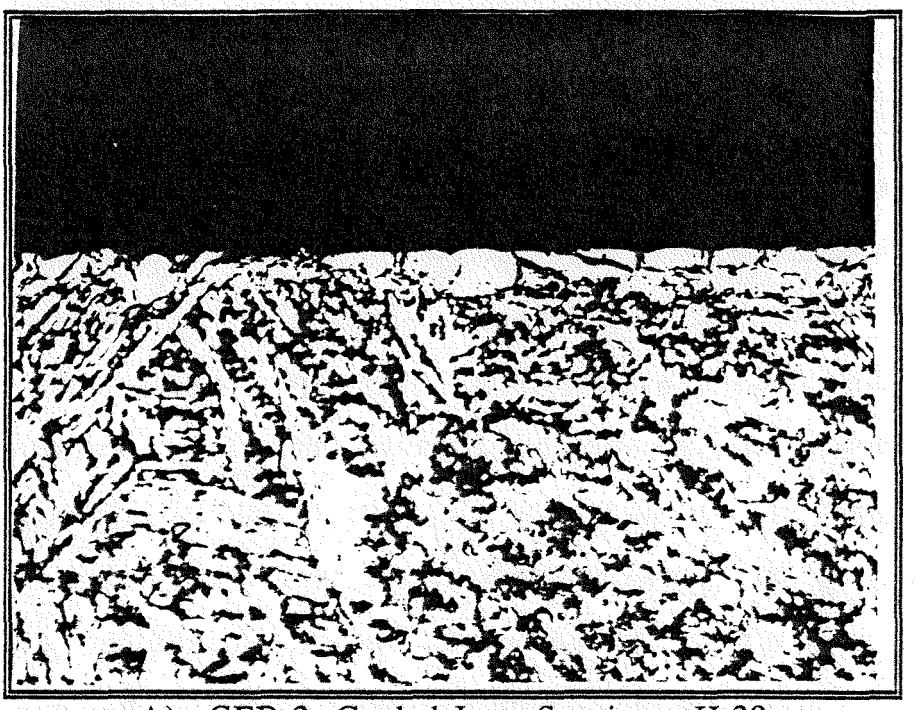

A) GEB-2, Cooled Leg, Specimen H-39
620 °C, 2510 hours, 800X
Photo # Y210357

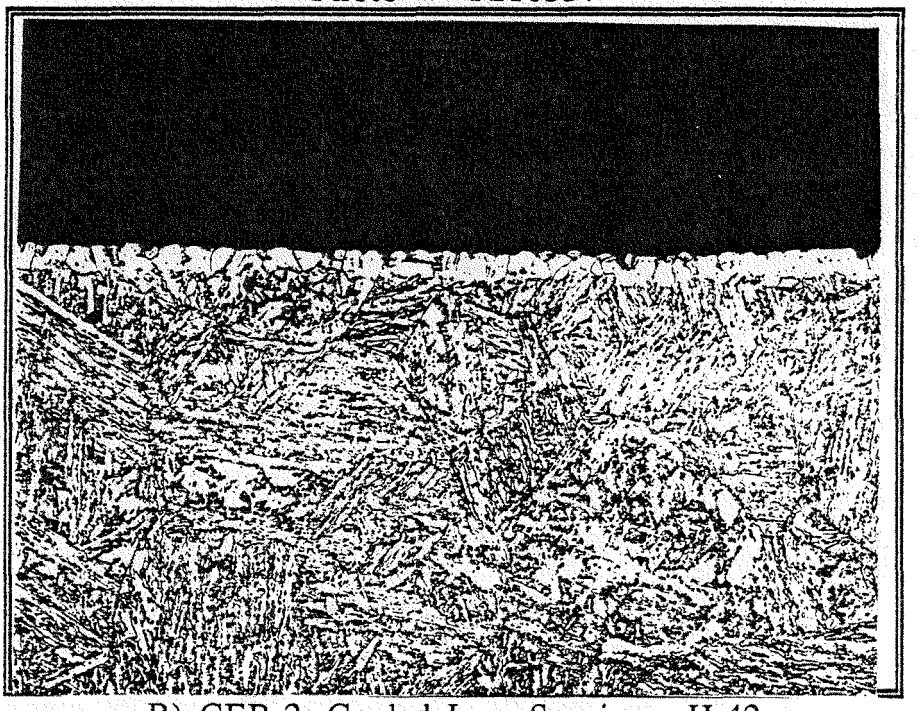

B) GEB-2, Cooled Leg, Specimen H-42
635 °C, 2510 hours, 400X
Photo # Y210359

Figure 3.3.46 Cross Section View H-39 and H-42

3.3.3 Specimen Surface Analysis

Energy Dispersive X-ray Analysis:

The SEM used for surface examination was equipped with a Tracor/Northern X-ray system with a Microtrace Series X-ray Detector (model #TX-3154-6600), a TN-5500 computer and Semi-Quantitative Analysis (SSQ) software which can perform compositional analysis of the X-rays emitted by a surface during bombardment of the surface by electrons. Details of the principle of operation can be found in references [3.10-3.11]. Briefly, the energy spectrum of the X-rays emitted from the incident electrons is statistically analyzed and compared with the known energy spectra of the elements of interest. From these data, quantitative determination of composition was possible to ± 5% of the measured value. However, determination of elements present in the alloy at levels below 1 w/o by weight was difficult and values of these data should be taken only as qualitative. The beryllium window, which protects the X-ray detector from contamination in the column, limits the detectable elements to those with atomic numbers higher than fluorine (mass number=9). As configured, EDX does not allow detection of oxygen, nitrogen, carbon and lithium. However, accurate determinations of most steel constituents (iron, chromium, molybdenum, nickel and silicon) were possible. EDX analysis of the base material and any "features" (e.g. nodules, speckles, etc) was made on each specimen.

Data from the EDX analysis are summarized in Figures 3.3.47 and 3.3.48. A summary of the EDX results for each specimen analyzed are given in tabular form in Appendix C.

The data in Figure 3.3.47 shows that the base surface chromium content decreases as temperature increases. The "scatter" in the data from the cooled leg of GEB-2 was probably due to the growth of chromium-rich nodules, which almost completely covered the specimen surface (see Figure 3.3.26). The scatter was not due to the inability of the analytical method but rather reflects the fact that the scale of examination (2000X) was roughly the same order as the scale of the surface nodules. X-rays emitted from the base material between nodules may have interacted with the chromium in the nodules and given an apparent higher than actual chromium content. Alternatively, surface carburization of the bulk alloy surface would precipitate chromium bearing carbides which would have caused surface chromium enrichment.

In both GEB-1 and GEB-2, the chromium content of the majority of nodules was significantly higher than the original matrix material and the Cr/Fe ratio increased rapidly with increasing temperature up to a maximum and then decreased slightly as the nodules began to disappear. The nodules were also found to have an increased amount of molybdenum as compared to the original matrix.

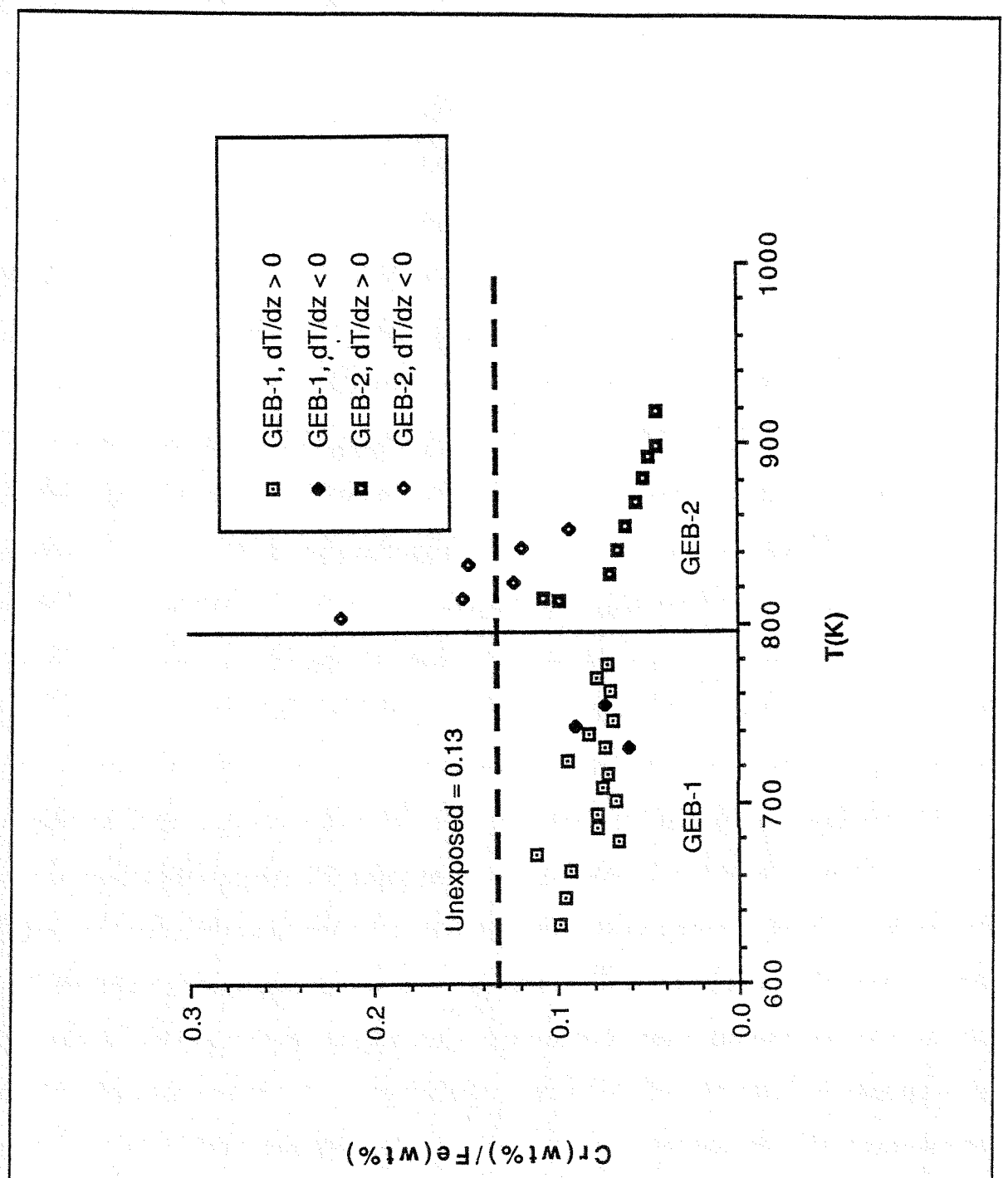

Figure 3.3.47 Summary of EDX Analysis Base Surface Metal

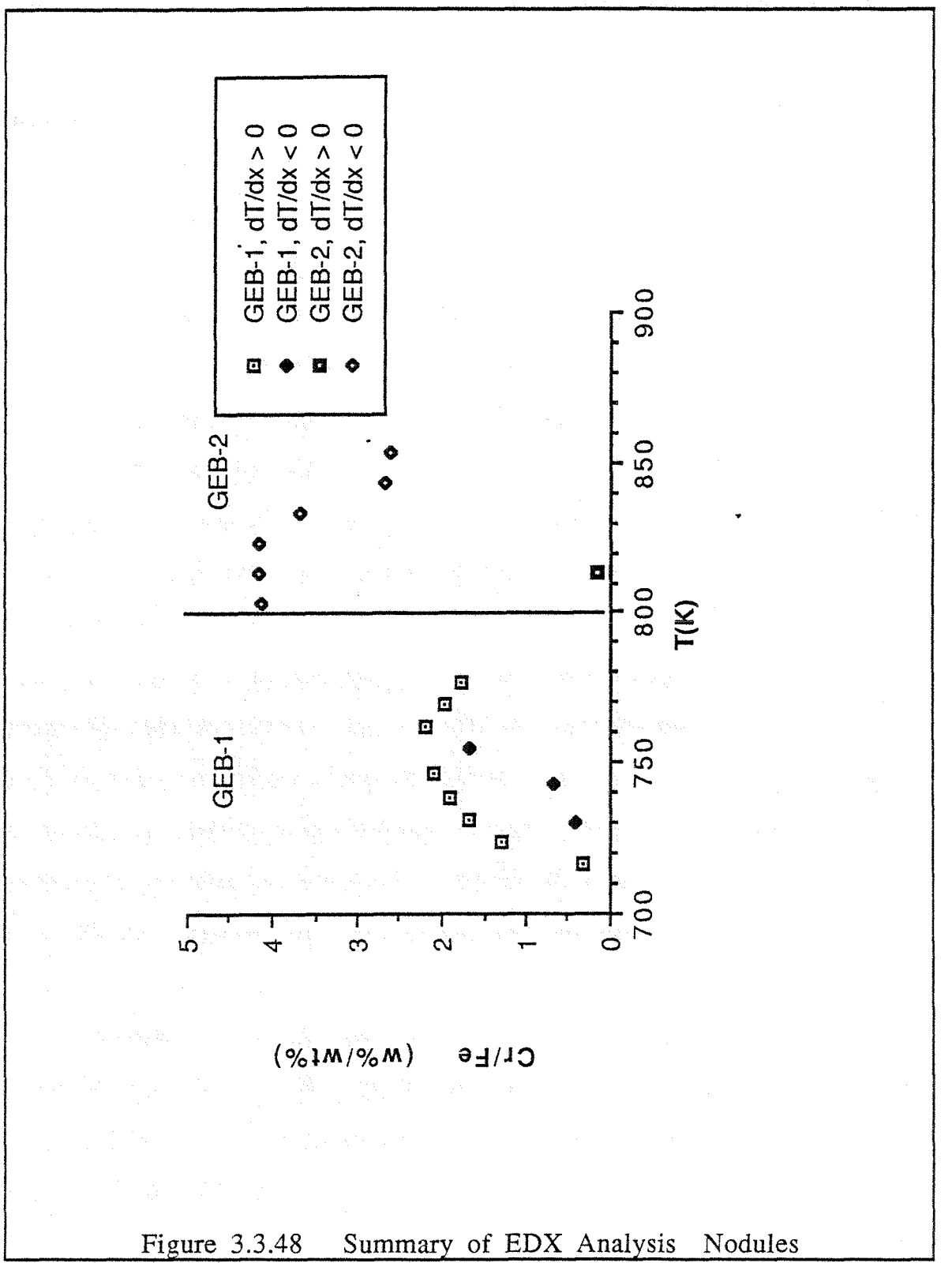

Figure 3.3.48 Summary of EDX Analysis Nodules

X-Ray Diffraction Analysis

Although EDX analysis can determine the composition of a surface within the limitations imposed by the beryllium window, identification of a particular compound, which may contain elements not detectable with EDX, and stoichiometry is best made using X-ray diffraction analysis. Diffraction analysis cannot determine composition, but instead determines lattice and crystal structure in terms of the angular distribution of a diffracted beam of X-rays impinging on the surface of interest. Each compound has a unique lattice parameter and crystal structure parameters. Combining EDX and diffraction analysis gives both compositional and crystallographic information necessary to determine the nature of a compound.

X-ray diffraction analysis was performed, using the X-ray diffractometry equipment in the High Temperature Materials Laboratory at Oak Ridge National Laboratory, on specimens H-21, H-23 and H-01 to determine the diffraction characteristics of both the chromium and iron-rich nodules. A typical diffraction pattern resulting from chromium rich noduled specimens (H-21 and H-23) is shown in Figure 3.3.49 along with the reference patterns for the metal carbide $Cr_{23}C_6$ and that typical of body centered cubic iron/chromium alloy similar to the HT9 base. The convolution of these two patterns shows fairly clearly the presence of both crystallographic structures on the surface. Figure 3.3.50 shows the diffraction pattern from the iron-rich noduled specimen (H-01) which is very similar to chromium-rich diffraction lines. These data

along with those from the EDX analysis indicate that "nodules" are a solid solution mixture of metal carbides of the form $M_{23}C_6$ (M= Fe, Cr or Mo). Iron and chromium-rich nodule-bearing surfaces produced similar diffraction patterns indicating that both iron- and chromium-rich nodules were metal carbides of the form $M_{23}C_6$, although they differ in metallic composition, morphology and surface topography. Slight perturbations of the diffraction pattern were probably due to the substitution of Fe and Mo for Cr in the carbide and/or the presence of some M_7C_6 carbides which would fractionate as the $M_{23}C_6$ carbides tempered. After determining that the nodules were of the form $M_{23}C_6$, the chromium stoichiometry of the nodules was calculated from the EDX compositional data. The resulting data are shown in Figure 3.3.51.

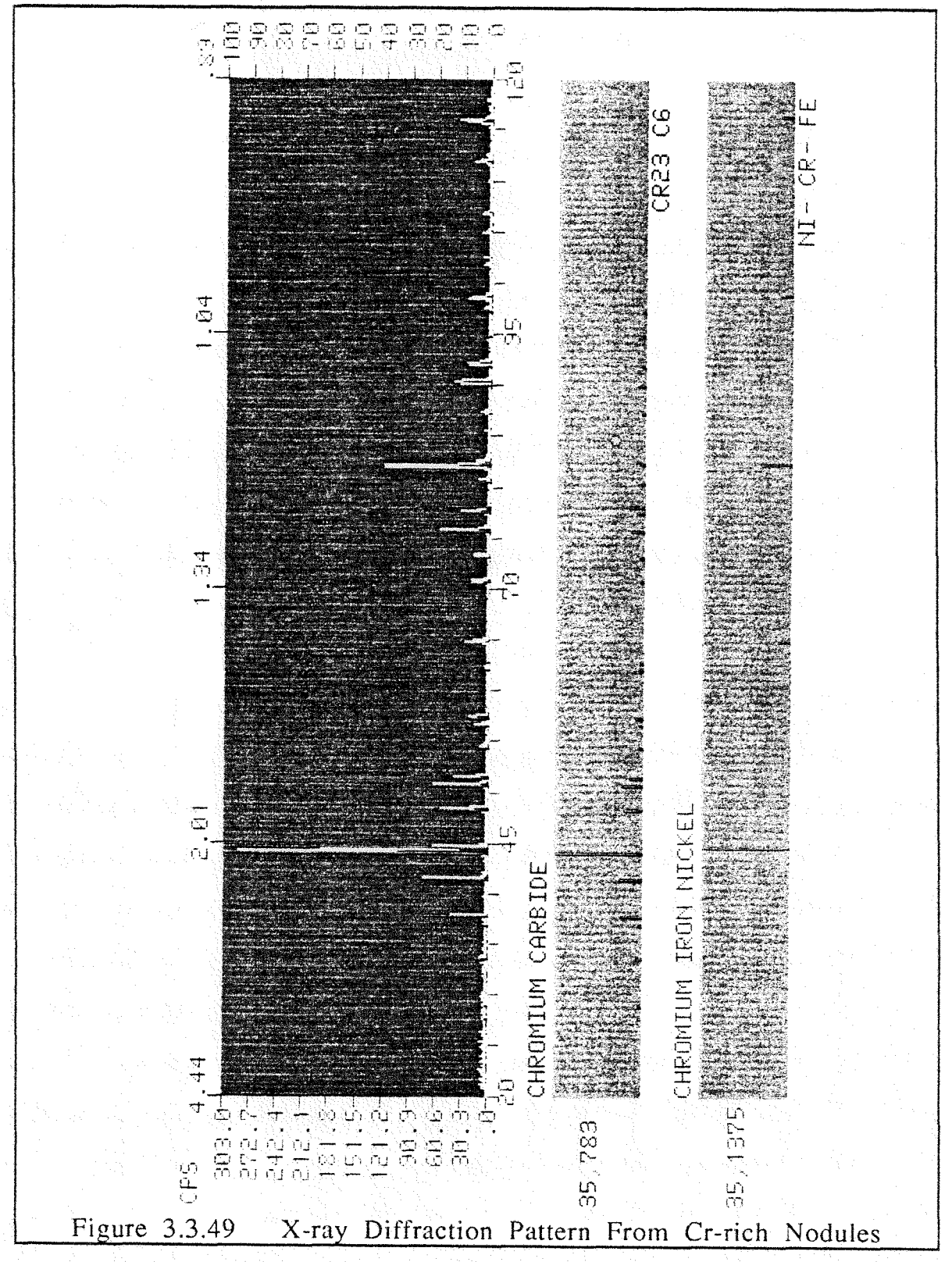

Figure 3.3.49 X-ray Diffraction Pattern From Cr-rich Nodules

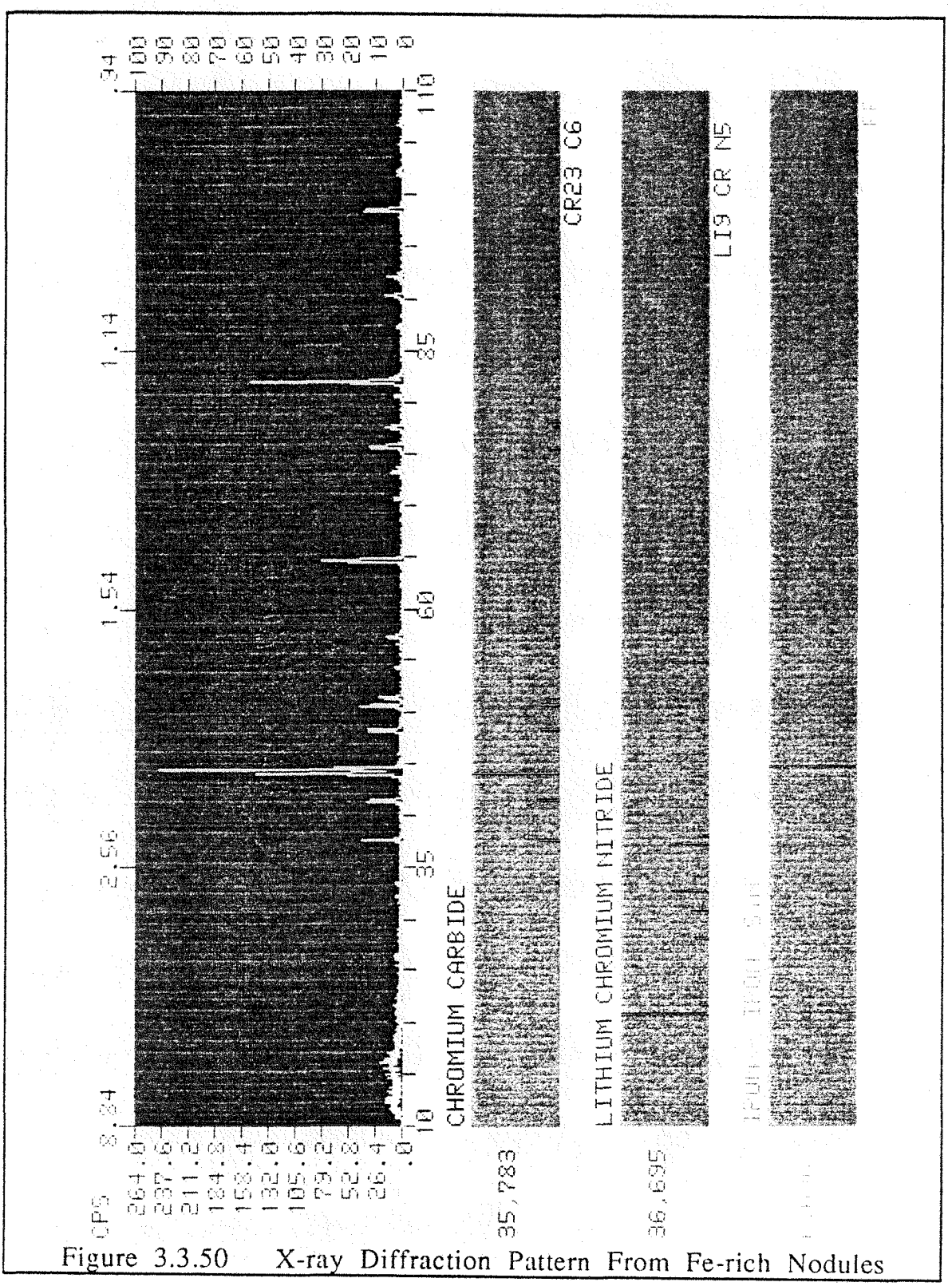

Figure 3.3.50 X-ray Diffraction Pattern From Fe-rich Nodules

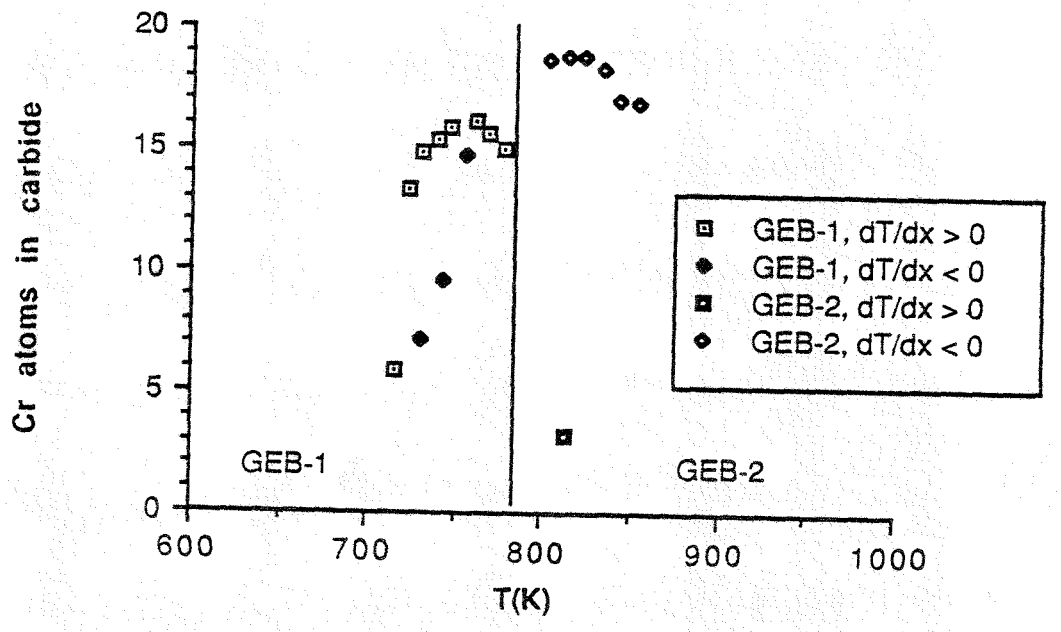

Figure 3.3.51 Stoichiometry of $M_{23}C_6$ Nodules

Electron Microprobe Analysis

Two specimens from each loop, L-01 and L-21 from GEB-1 and H-01 and H-42 from GEB-2, and the control specimen were examined using electron microprobe (EMP) analysis which uses wavelength dispersive X-ray scattering equipment in the High Temperature Material Laboratory (HTML) at ORNL. The value of the EMP instrument lies in its quantitative microanalytical capability. This is achieved by the excitation of characteristic elemental X-rays under the energy of a narrow electron beam (diameter less than 1 micron) with a beam energy generally less than 30 keV, similar to EDX. The resulting elemental X-rays, generally those characteristic of Kα radiation, are monitored with the detector set at the appropriate scattering angle for the element of interest. Unlike EDX, EMP is not as limited in the elements which it can detect. Two traces were taken on each sample and the data are summarized in Figures 3.3.52 to 3.3.56. Traces were taken so as to avoid any nodules on the surface.

GEB-1 (360 TO 505°C):

The microprobe traces for GEB-1 show no appreciable effect of the exposure within the limitation of microprobe analysis. The composition near the surface agrees quite well with that in the bulk material and as compared to the control specimen.

GEB-2 (525 TO 655°C):

Specimen H-42 (~630 °C) from GEB-2 shows a sharp drop in chromium content and rise in iron content at about 8 microns from

the surface. This drop coincided with the decarburized zone which could be seen in cross section optical micrograph (see Figure 3.3.46B). Specimen H-01 (~550 °C) shows a large near surface chromium content as compared to the original matrix which corresponds to the bulk carburized region near the surface which can also be seen in the cross sectional view in the optical micrograph (see Figure 3.3.41B). It should be noted that specimen H-01 had Fe-rich and not Cr-rich carbide nodules deposited on the surface.

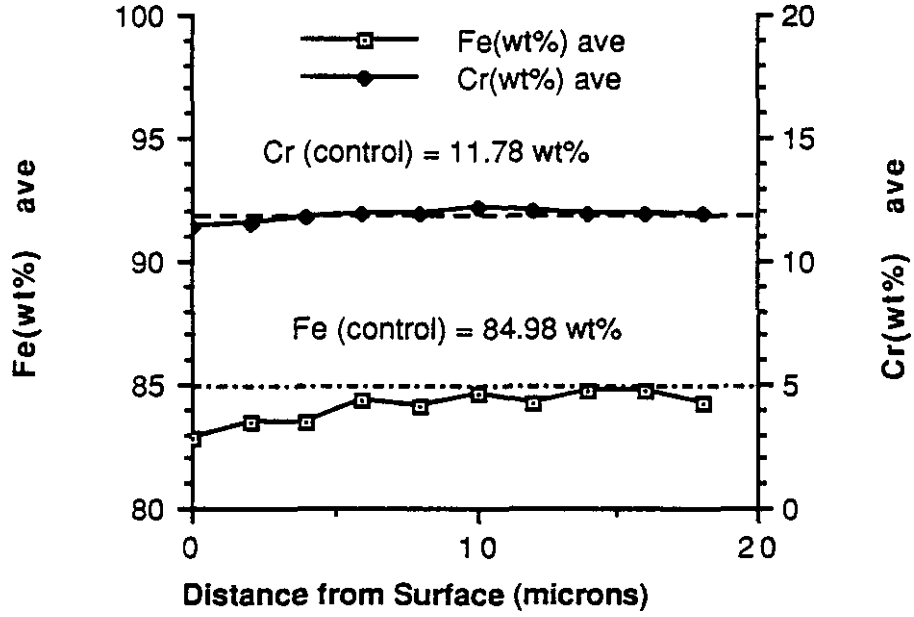

Figure 3.3.52 Microprobe Analysis Specimen L-01

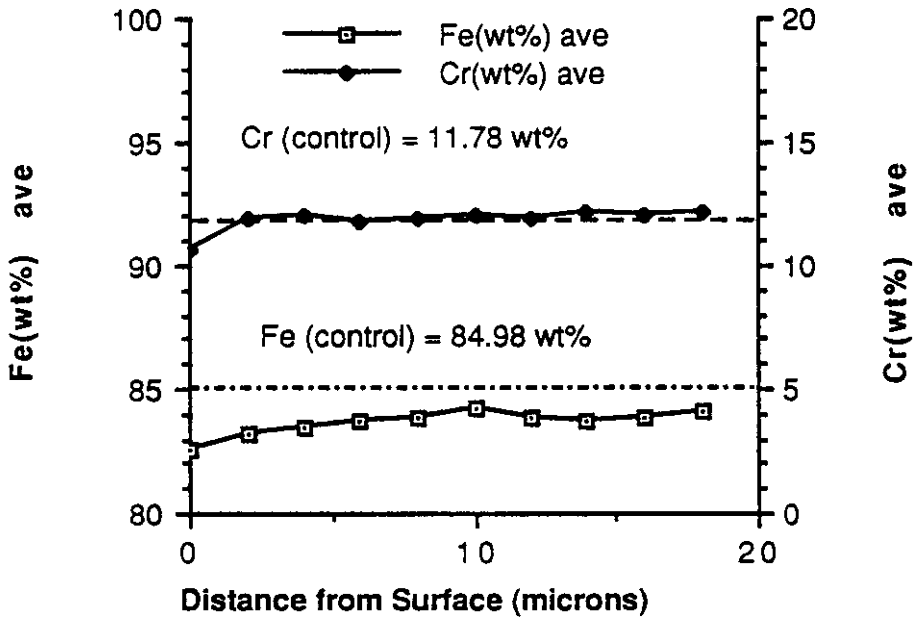

Figure 3.3.53 Microprobe Analysis Specimen L-21

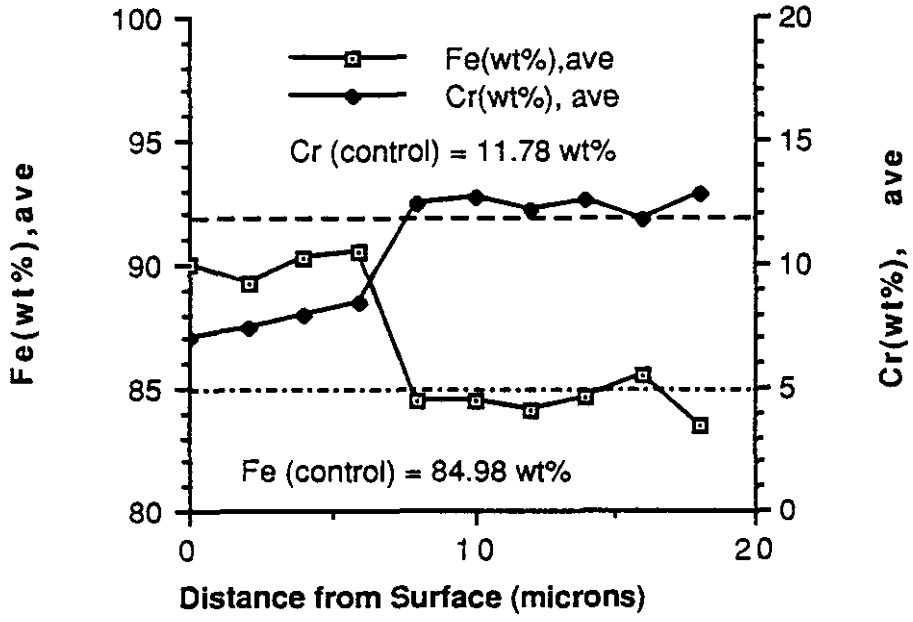

Figure 3.3.54 Microprobe Analysis Specimen H-42

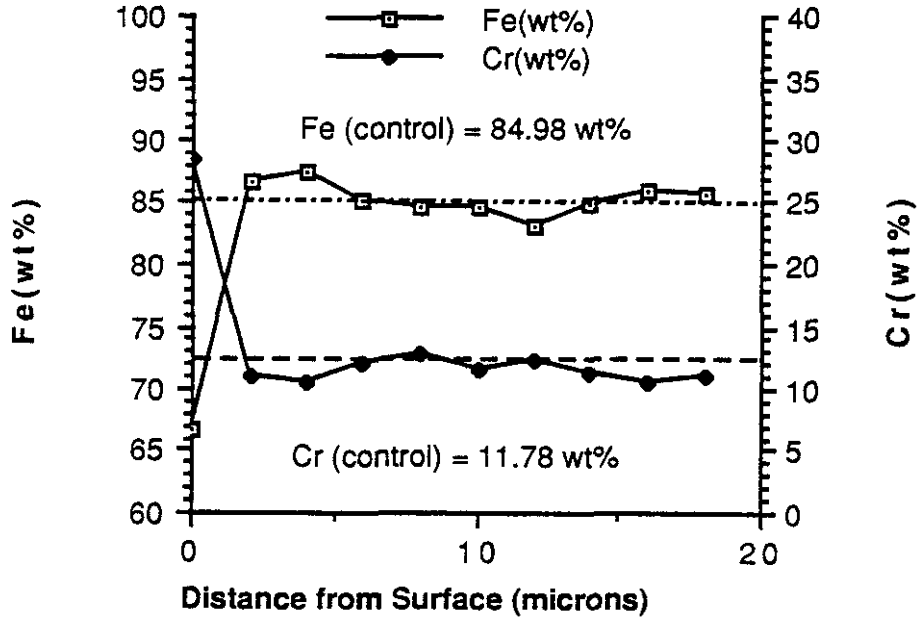

Figure 3.3.55 Microprobe Analysis Specimen H-01

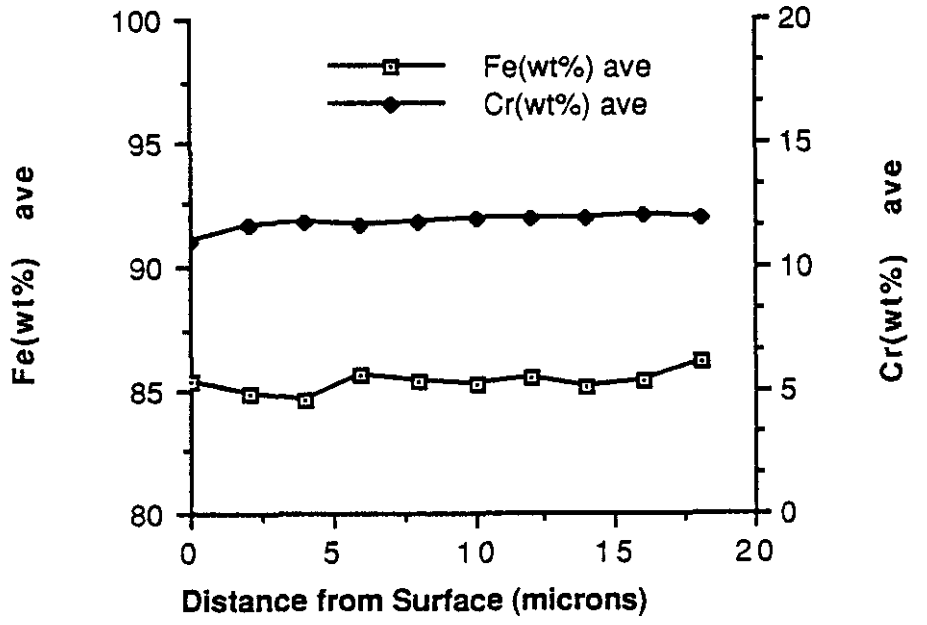

Figure 3.3.56 Microprobe Analysis Control Specimen

3.3.4 Lithium Chemical Analysis

Unfiltered samples of the lithium were taken using thief samplers [3.5] for chemical analysis of non-metallic and metallic elements. The results of the analyses for nitrogen and oxygen as a function of time are shown in Figure 3.3.57. ICP analysis of the lithium for transition metals for as-purified and end-of-life for GEB-1 and GEB-2 and results of the analysis for carbon in lithium from Argonne National Laboratory for end-of-life lithium in GEB-1 are shown in Table 3.3.2.

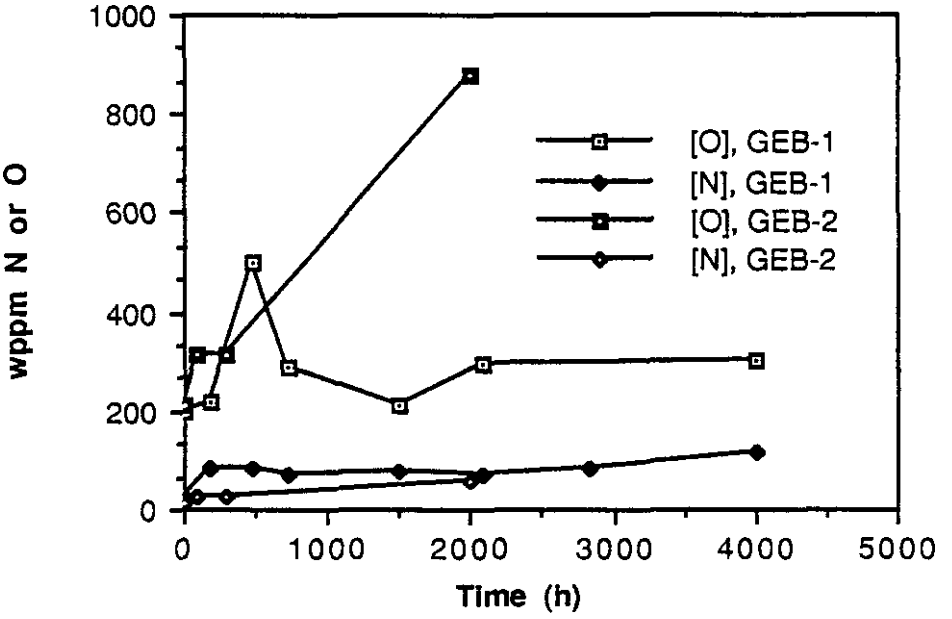

Figure 3.3.57 Oxygen and Nitrogen Profiles for GEB-1 and GEB-2

Sample	Fe (wppm)	Cr (wppm)	Mo (wppm)	Ni (wppm)	C[1] (wppm)
As-purified	96.	20.	NA[2]	24.	NA
GEB-1 End of Life	5000.[3]	1300.[3]	29.	590.	1.6
GEB-2 End of Life	5200.[3]	1500.[3]	25.	710.	NA

[1]Analysis performed by Argonne National Laboratory by acetylene evolution.
[2]Not Available
[3]Values in excess of solubility, probably due to segregated particles in solution.

Table 3.3.1 ICP and Carbon Analysis of Lithium

3.4 Summary of the Experiments and Experimental Results

Experimental data have been collected from two thermal convection loop experiments with lithium and Fe-12Cr-1MoVW between 360 and 655 °C. Results from the analysis of the specimens and data from these experiments indicate that the corrosion processes were not controlled by the simple dissolution of the metal constituents from the solid to the liquid phase. Surface morphology and weight loss behavior were closely linked and could be divided into three regimes.

1) Below 450 °C in GEB-1, surfaces in both the heated and cooled legs were roughened and had an "orange peel" appearance with surface chromium contents of between 6 and 8 % by weight. Specimen weight changes were small, in comparison to austenitic steels, and were weakly dependent on temperature. Microprobe traces and optical metallography showed that the solid phase was unaffected by the weight losses.

2) Between 450 and 505 °C in both heated and cooled legs of GEB-1 and between 530 and 580 °C in only the cooled leg of GEB-2, the deposition of Cr-rich $M_{23}C_6$ carbide (10 to 20 μm diameter) nodules influenced the weight changes. The deposition of the chromium-rich nodules cause net weight gains at the highest temperatures in the heated leg of GEB-1 and substantial weight gains in the cooled leg of GEB-2. No chromium-rich carbides

were found in the heated leg of GEB-2. Weight gains in the heated leg of GEB-2 were due to the deposition of iron-rich carbide nodules only on the first three specimens after the flow disturbance at the inlet in the heated leg. *In GEB-1, the number density, chromium atoms in the carbide, and size of the nodules increased with increasing temperature. In GEB-2, the number density, chromium atoms in the carbide and size of the nodules increased with decreasing temperature.* Deposition in GEB-1 was insensitive to temperature. In GEB-2, deposition was linearly related to the inverse of absolute temperature with a slope of 42000 K^{-1} (347 kJ/mole versus 1/RT). Weight gains in both GEB-1 and GEB-2 were due only to $M_{23}C_6$ carbide formation. Elemental or alloy deposition, in the form of elemental iron, chromium or iron chromium alloys, was not found on the surfaces. Carbide deposition was not uniform over the surface of the specimens with preferred precipitation at grain boundaries. The solid phase was unaffected by the deposition of the chromium-rich. Bulk carburization was only found on specimens in the heated leg of GEB-2 which had iron-rich carbide nodules deposited on the surface.

3) Between 580 and 655 °C in both the heated and cooled legs of GEB-2, the surface took on a cobblestone appearance and base metal surface chromium content decreased with increasing temperature. Weight losses were strongly dependent on temperature. Corrosion rates in the heated leg of GEB-2 had an

activation energy of 63.7 kJ/mole. Some of the cobblestoned specimens were decorated with fluorescent white vanadium and molybdenum rich speckles. Bulk decarburization of the alloy was evident both from optical micrographs and electron microprobe analysis to a depth of approximately 8 to 10 μm below the surface.

3.5 References for Chapter 3

[3.1] J. H. DeVan and J. R. DiStefano, "Thermal-Convection Loop Tests of Type 316 Stainless Steel in Lithium," ADIP Quarterly Progress Report, March 31 1978, DOE/ET-0058/1.

[3.2] E. E. Hoffman, Corrosion of Materials by Lithium at Elevated Temperatures, ORNL-2674 (1959).

[3.3] J. H. DeVan, Private Communication, 1987.

[3.4] H. Bradley, R. B. Hand, E. E. Hand, and T. P. Irwin, "Purification of Lithium by Cold Trapping," General Electric Company, GESP-693, November 1971.

[3.5] G .E. Meadows and R. F Keough, "Lithium Purity and Characterization", Journal of Materials for Energy Systems, 2 (1981) 44-49.

[3.6] R. M. Yonco, V. A. Maroni, J. E. Strain and J. H. DeVan, "A Determination of the Solubility of Lithium Oxide in Liquid Lithium by Fast Neutron Activation," Journal of Nuclear Materials, 79 (1979) 354-362.

[3.7] D. G. Bauer, Kinetics of the Degradation of 316 Stainless Steel by Lithium, Ph.D. Dissertation, University of Wisconsin-Madison (1980).

[3.8] R. M. Yonco and M. I. Homa, "The Solubility of Carbon in Low-Nitrogen Liquid Lithium," Journal of Nuclear Materials 138 (1986) 117-122.

[3.9] R. N. Lyon, Editor, Liquid Metals Handbook, Second Edition, Atomic Energy Commission, NAVEXOS P-733 (Rev.) (1952).

[3.10] J. I Goldstein and H. Yakowitz, Practical Scanning Electron Microscopy: Electron and Ion Microprobe Analysis, Plenum Press, New York (1976).

[3.11] J. C. Russ, Fundamentals of Energy Dispersive X-ray Analysis, Butterworth, Boston, Mass (1972).

CHAPTER 4 DISCUSSION, INTERPRETATION AND ANALYSIS OF THE EXPERIMENTAL RESULTS

4.1 Comparison of Results with Previous Investigations

The experiments of Tortorelli [4.1] and Tortorelli and DeVan [4.2] were the most similar to the ones in this investigation. Other experiments by Chopra and Smith [4.3-4] and Chopra and Hull [4.5] at Argonne National Laboratory with Fe-12Cr1MoVW and by G. A. Plekhanov and G. P. Fedortsov-Lutikov [4.6] in the Soviet Union with three different 12 w/o chromium steel alloys (Fe-12Cr, Fe-12Cr-1MoNbV and Fe-12Cr-2.35MoNbV) and lithium were performed in isothermal test sections of forced convection loops. The FCL's were constructed totally [4.3-5] or partially [4.6] of an austenitic alloy. The primary focus of these forced convection experiments was characterization of the mass release (dissolution) processes. In particular, deposition processes and behavior, the effects of material inhomogeniety and temperature gradient could not be assessed in the Argonne or Soviet experiments.

Figure 4.1.1 shows data as "steady-state corrosion rate" from reported weight losses versus exposure temperature from these experiments as compared with the results from references [4.1-4.6]. The "corrosion rates" from the present experiments were of the same order of magnitude as compared with the previous experiments up to 600 °C. Data for Fe-12Cr1MoVW in lithium above 600 °C with an imposed temperature gradient did not exist prior to this investigation.

For their low temperature experiments (350 to 500 °C), Tortorelli and DeVan [4.2] found that their specimens, both in the heated and cooled legs, lost weight, as also observed in the present experiments. *The largest weight loss occurred for the specimen at the lowest temperature.* No weight gains were reported in their lower temperature experiment. As also observed in this work, Tortorelli [4.1] reported a return to increasing weight losses with increasing temperatures and weight gains in the cooled leg when the temperature of the experiment was raised to 450-600 °C. Tortorelli [4.1] and Tortorelli and DeVan [4.2] reported finding chromium-rich nodules on their specimens of Fe-12Cr1MoVW. Tortorelli found chromium-rich deposits in both the heated and cooled legs of his experiments while in the present case, no chromium-rich nodules were found in the heated leg of GEB-2. The difference was probably due to the difference in maximum temperatures (T_{max}[4.1] =600 °C as compared to 655 °C) and carbon content of the lithium. The experiments of Tortorelli [4.1] and Tortorelli and DeVan [4.2] were of longer duration than in this investigation (7000 to 10000 hours as compared to 3000). The chromium-rich nodules were covered over by iron-rich deposits, similar in shape to those which deposited on the first three specimens in the heated leg of GEB-2, which formed/deposited at later times. Chopra and Smith [4.3] reported chromium-rich faceted deposits on a pure chromium sample exposed in their FCL. Chopra and Hull [4.5] reported iron rich deposits on the "downstream" side of their Fe-12Cr1MoVW specimens. Tortorelli [4.1], Tortorelli and DeVan [4.2] and Chopra and Smith [4.3-4] did not

determine the structure of the deposits and did not identify the compound(s). It was assumed that the deposits were the remnants of lithium corrosion products (i.e. Li_9CrN_5 or Li_3FeN_2) which had decomposed during specimen cleaning. Since the reporting of data from these experiments, independent confirmation of the $Cr_{23}C_6$ structure on surface of pure chromium and of $M_{23}C_6$ on ferritic steels have been obtained [4.5]. $M_{23}C_6$ was reported as a corrosion product by Barker and Frankham [4.7] when type 316 SS (austenitic stainless steel) was exposed to lithium with varying activities of carbon and nitrogen. However, the carbides formed in Barker and Frankham's experiments were distributed in the bulk of the 316 SS (i.e. *bulk carburization*) and not as surface deposits (*surface carburization*) as was found here.

The EDX analyses from the present experiments are similar to those reported by Tortorelli [4.1], Tortorelli and DeVan [4.2], Chopra and Smith [4.3-4] and Chopra and Hull [4.5]. Below 500 °C and nitrogen contents of approximately 100 wppm, surface chromium contents between 6 and 8 w/o have been observed for both austenitic and ferritic steel in lithium [4.4-5].

In short, the results from the present experiments were consistent with prior experiments with this type of ferritic steel. Some qualitative descriptions of the types of processes which might have been contributing to the weight change behavior have been made [4.1]. However, a thorough, physical, quantitative explanation of the observed overall weight change behavior and surface morphologies observed has not been put forth. The analysis given

below indicates that the corrosion behavior and surface morphologies can be understood in terms of the behavior of nitrogen and carbon in the lithium, in addition to the dissolution (solubilities) of iron and chromium in lithium. Further, the experimental results and analysis were utilized to make recommendations for the development of a fusion ferritic alloy which may be less susceptible to attack by lithium.

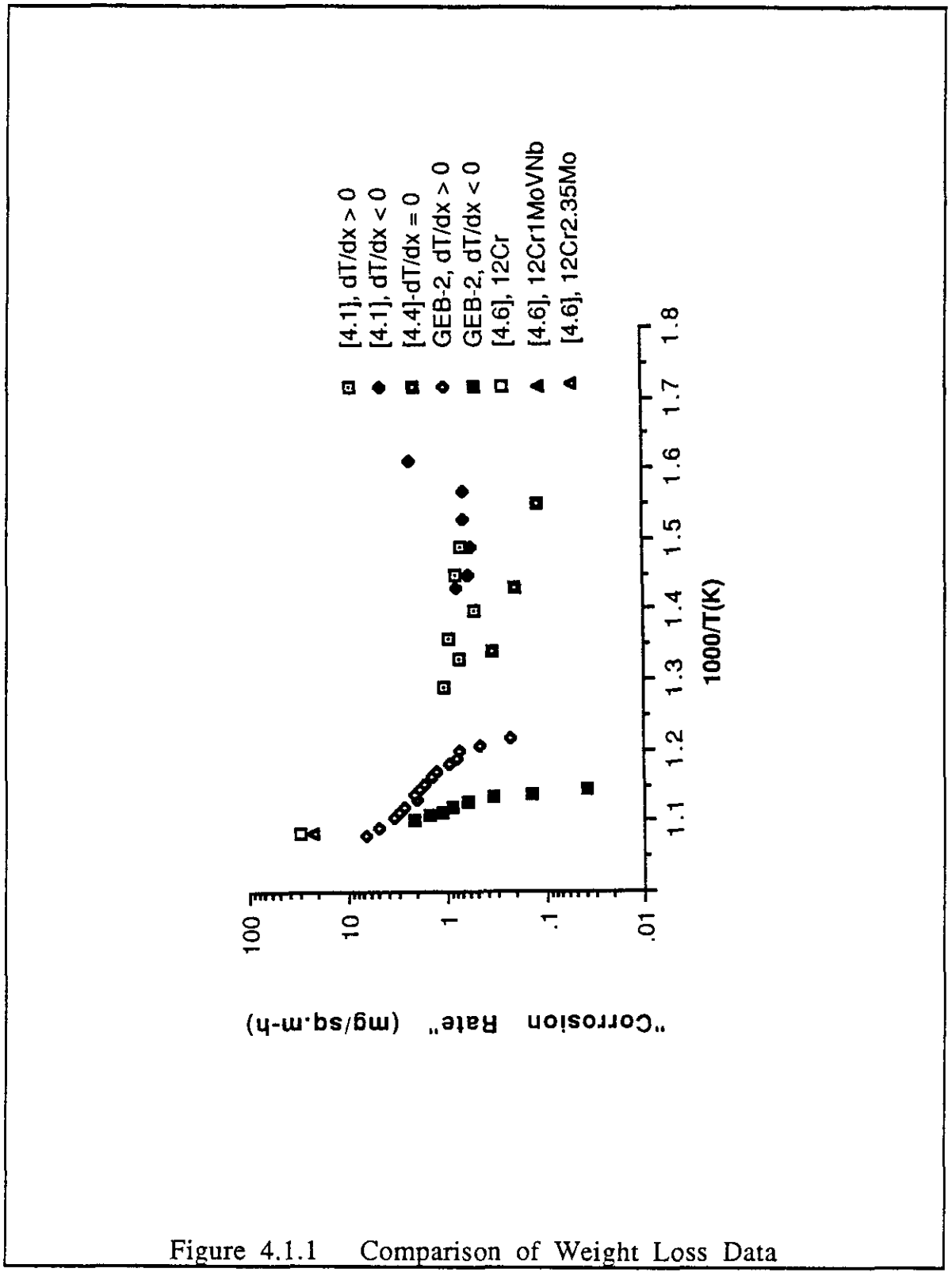

Figure 4.1.1 Comparison of Weight Loss Data

4.2 Effects of Temperature Gradients on Corrosion Processes

Thermal convection loops require large temperature differentials for operation. Since many of the processes of corrosion are chemical, the impact of temperature gradients should be understood in terms of their effect on the equilibria and kinetics of the chemical and corrosion processes.

Mass is transferred in a system due to a gradient in the chemical potential of a species and not simply due to concentration gradients. The chemical potential of a species in a phase is a function of composition and temperature.

$$\mu_i^{\alpha} = \mu_i^{\circ}(T, P) + \mathbf{R}\ T \ln a_i\ (x_i)$$

μ_i^{α}= Chemical potential of i in phase α

μ_i° (T, P)= Standard partial molar chemical potential of i

$a_i\ (x_i)$= Activity of i in phase $\alpha = \gamma_i\ x_i$

γ_i= activity coefficient of i

x_i= mole fraction of i

Mass is transported down the gradient in chemical potential. In an inhomogeneous or multiple material system, a difference in chemical potential for a species may exist between different materials at the same temperature. In a homogeneous system, thermal gradient mass transfer occurs in non-isothermal systems because of the temperature dependence of chemical potential (activity) of constituent elements. For an ideal dilute solution, the chemical potential of the solvent is proportional to the solute species activity

(concentration). *Concentration is not necessarily continuous across the interface between two separate phases; the chemical potential, however, is continuous across an interface.*

The flux of species i in dilute solution in a fluid near a solid surface of pure i (unit activity) can be written assuming equilibrium exists across the interface between the solid and liquid,

$$j_i = \rho_{liquid} K_i \{[i]^{Bulk} - [i]^{eq}\}$$

$$K_i = \frac{k_r^i k_B^i}{k_B^i + k_r^i}$$

where j_i [kg/m^2-s] is the species i mass flux, ρ_{liquid} is the density of the liquid [kg/m^3], K_i [m/s] is the overall mass transfer coefficient based on mass fraction, which combines the surface reaction velocity, k_r^i, and boundary layer and/or diffusion, k_B^i, mass transfer coefficients, and $[i]^{Bulk}$ and $[i]^{eq}$ are the bulk and equilibrium mass fractions of i in the liquid phase. k_r^i is a chemical kinetic quantity which is assumed dependent only on temperature. k_B^i is a transport quantity which may involve resistance in both solid and liquid phases.

For simple, elemental dissolution and deposition (solubility-driven mass transfer) of a pure solid, $[i]^{eq}$ is equal to the solubility of

i in the liquid, $[i]^{sat}$, because the reaction at the interface is assumed to be of the form

$$i_{pure\ solid} \Leftrightarrow i_{in\ liquid}$$

where i is an elemental species (e.g. Cr or Fe). A steady-state, simple dissolution and deposition over predicted corrosion and deposition rates for lithium and iron and chromium alloys by more than an order of magnitude. See Appendix B for details of the modeling.

Furthermore, the steady-state mass flux of an alloy constituent is equal to the mole fraction of the steel constituent in the bulk alloy times the total mass flux. Dissolution of constituents of an alloy may occur at different rates because of the difference in their solubilities in the liquid. The solubilities of iron and chromium in lithium are very similar in magnitude and enthalpy of solution (slope of the saturation curve versus inverse temperature). Typical values for saturation concentrations of iron and chromium in lithium at 350, 500 and 650 °C are 0.45, 3.93 and 17.1 wppm-Fe and 0.35, 3.55 and 17.2 wppm-Cr, respectively, using the data of Leavenworth and Cleary [4.8].

In the cold zone, elemental or alloy deposition theoretically occurs because the bulk concentration of the dissolved species becomes higher than the solubility of the dissolved elements as the local temperature decreases. Precipitation, in the form of elemental structures (e.g. dendrites for chromium) or an alloy, occurs on surfaces to relieve supersaturation of the bulk. If mass diffusion to

the surfaces (walls) is slow compared to the thermal energy transfer (Lewis #= Le = α/D = (Thermal Diffusivity/Mass Diffusivity) >> 1), which is the case for most liquid metals ($Le_{Li/Fe} \sim 10^4$) particulate precipitation in the bulk may occur to relieve the local supersaturation. These particles may either remain in the bulk flow or be physically transported to the walls of the containment. If the particles remain in the flow, they may either grow or dissolve, acting as a buffer for changes in saturation conditions. Precipitation of metallic compounds, such as oxides, nitride or carbides, may also occur both on surfaces and in the bulk liquid depending on the stability of the compounds.

In an isothermal system, in which corrosion is controlled by simple dissolution processes, the corrosion rate would continuously decrease with time as the concentration in the bulk approached the saturation limit at the system temperature. *In a system with a thermal gradient, where the corrosion process is solubility-driven dissolution, a steady-state corrosion and material transfer rate exists due to thermal Gradient Mass Transfer (TGMT). The corrosion rate in such a system would have the same activation energy as the enthalpy of solution for the major alloy components.* Because the solubilities of iron and chromium are similar in magnitude and temperature dependence (see Figure 1.3), the temperature behavior dissolution of an iron-chromium alloy should have an activation energy of approximately 60 kJ/mole [4.8]; the enthalpies of solution for iron and chromium (58.1 kJ/mole for Fe and 62.4 kJ/mole) [4.9] (see appendix A, section A.3). For metallic species in lithium, the

solubility increases with temperature and corrosion should increase with temperature and TGMT should be from the region of higher to lower temperature.

Large temperature differentials can also affect equilibrium of chemical corrosion reactions, which may be occurring in the system. The concentration (activity) at which a chemical compound (e.g. corrosion product) begins to form (precipitate) is determined by the chemical thermodynamics of the compound and the activities of the species from which it, the compound, forms. For example, consider the simple chemical reaction given by,

$$A + B \Leftrightarrow AB$$

where A and B are elements. Suppose AB precipitates as a solid or other pure, separate phase (corrosion product film or layer) and is being formed from a dilute solution of B in a liquid phase in contact with pure solid A. The law of mass action for this reaction at equilibrium yields,

$$\frac{a^{s}_{AB}}{\left(a^{s}_{A}\right) * \left(a^{\ell}_{B}\right)} = \exp\left(- \frac{\Delta G^{\circ}_{f\ AB}}{R\ T} \right)$$

where, a_i^{α} is the activity of the i^{th} component of phase α (s=solid or l=liquid) in the system, $\Delta G^{\circ}_{f\ AB}$ is the standard free energy of formation of AB and **R** is the gas constant (8.314 J/mole-K). If B is in dilute solution and AB is a separate, pure, solid phase then, from definition of activity and Henry's law we can show that,

$$a^{s}_{AB} = 1$$

$$a^{s}_{A} = 1$$

$$a^{l}_{B} = \frac{[B]^{l}}{[B]^{l}_{sat}(T)}$$

where $[B]^{l}$ is the concentration of B in the liquid and $[B]^{l}_{sat}(T)$ is the saturation concentration of B at temperature T. We can define $[B]^*$ and correspondingly a^{*}_{B} as the concentration and activity at which AB just begins to form.

$$a^{*}_{B} = \frac{[B]^*}{[B]_{sat}(T)} = \exp\left(\frac{\Delta^{\circ}_{f}G_{AB}}{R\ T}\right)$$

$$[B]^* = [B]_{sat}(T)\ \exp\left(\frac{\Delta^\circ_f G_{AB}}{R\ T}\right)$$

For $[B]^\ell < [B]^*$, solid AB cannot thermodynamically exist in equilibrium with the the liquid phase; AB will decompose into elemental A and B in solution. For $[B]^\ell > [B]^*$, formation of solid AB is thermodynamically, but not necessarily kinetically, possible. If $[B]^\ell$ is nearly constant in the bulk, which is true for relatively small mass transfer rates typical of corrosion processes, then the activity of B in the liquid phase will decrease as the temperature and solubility increase. Thus, in some portions of an experiment, the formation of a corrosion product may be thermodynamically favored while in others, formation of the corrosion product is thermodynamically prohibited.

Large changes in temperature can also affect the kinetics of a chemical reaction. The overall reaction rate for any given reaction is dependent on temperature. Reaction rates normally increase exponentially with increasing temperature and are usually represented by an Arrhenius equation

$$K_r(T) = K_r^\circ\ \exp\left(\frac{-E_a}{R\ T}\right)$$

where $K_r(T)$ is the reaction rate at a specified temperature T, K_r° is the pre-exponential factor, E_a is the activation energy for the reaction

and **R** is the gas constant. Depending on the activation energy, the effect of the changing temperature may or may not be important.

4.3 Discussion, Analysis and Interpretation of the Data

4.3.1 Weight Change and Surface Morphology Data

The weight change data from these two experiments were confusing when viewed in ignorance of the morphology, surface composition and lithium chemistry. Specimen weight change data are a macroscopic indication of the net result of, in some cases, several simultaneous corrosion and deposition processes. In both GEB-1 and GEB-2, weight changes were closely related to surface morphology. Surface morphological data gave information and insight into the microscopic processes of corrosion and deposition. Surfaces which were roughened by exposure to lithium at temperatures below 450 °C in GEB-1 had weight losses which were insensitive to temperature and the surface chromium content decreased with increasing temperature. Specimens which gained weight in both GEB-1 and GEB-2 characteristically had either chromium or iron-rich $M_{23}C_6$ carbides on their surfaces. There was little or no evidence of an effect on the bulk of the alloy for any of the specimens below 580 °C. Surfaces which were cobblestoned by exposure to lithium with no nodules had weight losses which were extremely sensitive to temperature and showed evidence of decarburization and severe attack of the bulk of the base material. The results from these TCL experiments indicate that weight changes were not simply a function of absolute temperature and that the chemistry of the lithium and steel were important in determining the weight changes. It is our opinion that each of the resulting surface morphologies were indicative of a different corrosion process.

Further, it is important to distinguish between the phenomena occurring in the two experiments and within the same experiment in order to understand the mechanisms and processes of corrosion. In particular, mass removal (corrosion) and deposition are not controlled by the same mechanisms or chemical reactions. Corrosion, specimen weight loss, was related to the formation of the protective insoluble compound Li_9CrN_5 from chromium both in the α-ferrite matrix and in surface carbides in GEB-1 and the solubility of iron and chromium in lithium in GEB-2. Deposition, in both experiments, was dominated by the precipitation of metal carbides and not elemental or alloy (solubility) deposition of the steel constituents.

4.3.2 GEB-1 (360 TO 505°C) Reactions of Nitrogen in Lithium with Chromium in Steels

Nitrogen in Lithium

Nitrogen is present in lithium as lithium nitride, Li_3N. The thermodynamics of the lithium-nitrogen system can be described by the free-energy of formation of lithium nitride and the solubility of nitrogen in lithium. The formation of lithium nitride from its elements can be expressed as,

$$3\ Li_{(solid)} + \frac{1}{2}\ N_{2\ (gas)} \Leftrightarrow Li_3N_{(solid)}$$

The free energy of formation is given by [4.10]:

$$\Delta \overset{\circ}{G}_{f\ Li_3N}\ [kJ/mole] = \overset{\circ}{A}_{Li_3N} + \overset{\circ}{B}_{Li_3N}\ T[K]$$

$$\overset{\circ}{A}_{Li_3N} = -\ 174.24\ [kJ/mole],\ \overset{\circ}{B}_{Li_3N} = 1.4343 \times 10^{-1}\ [kJ/mole\text{-}K]$$

The solubility of nitrogen in lithium has been investigated by R.M. Yonco et al. [4.11] and Hoffman [4.12]. We adopted the more recent data from Yonco,

$$\ln [N]^{Li}_{sat}\ [wppm\ of\ N] = A^N_{sat} + \frac{B^N_{sat}}{T[K]}$$

$$A^N_{sat} = 17.17,\ B^N_{sat} = -8612$$

Nitrogen in lithium follows Henry's Law for dilute solutions which states that the activity of the solute in the solvent is proportional to its concentration. Since nitrogen is present as Li_3N, the activity is linearly proportional to the solubility

$$a_N^{Li} = \frac{[N]^{Li}}{[N]^{Li}_{sat}(T)}$$

Chromium Activity in Steels

The activity of chromium in Fe-9Cr-Mo ferritic steels with chromium contents near 9 w/o was characterized by Saltelli et al.[4.13]. Data specifically for Fe-12Cr1MoVW steel are not available. However, Fe-9Cr is similar in properties to Fe-12Cr and we adopted the data of Saltelli et al. [4.13] for the activity coefficient of chromium in α-ferrite as a reasonable approximation.

$$a_{Cr}^{\alpha} = \gamma_{Cr}^{\alpha} X_{Cr}^{\alpha}$$

$$\ln \gamma_{Cr}^{\alpha} = 1.23 + \frac{1204.8}{T(K)} - 9.56 \times 10^{-4}\ T(K)$$

where γ_{Cr}^{α} and X_{Cr}^{α} are the activity coefficient and mole fraction of chromium in the α-Fe phase, respectively. The γ_{Cr}^{α} is plotted in Figure 4.3.1. Note, extrapolation of the activity coefficient to chromium contents significantly different from 9 w/o is highly

speculative because the activity coefficient is a function of composition. However, lacking data at lower chromium contents, we make the extrapolation bearing in mind that such results may not be valid. Data for an austenitic steel (18Cr-8Ni [4.14]) are also plotted for comparison. As compared with a typical austenitic steel, chromium activity coefficient for ferritic steels increases faster as temperature decreases than does the activity coefficient for austenitic steels. For an iron-chromium alloy such as Fe-12Cr1MoVW, the mole fraction of chromium is approximately equal to the ratio of the molecular weights of iron to chromium times the weight fraction (~0.13 for 12 w/o Cr).

Formation of the Lithium/Chromium/Nitrogen Compound

Barker and Frankham [4.7] showed that the ternary compound Li_9CrN_5 formed on a chromium bearing steel (316 SS) exposed to high nitrogen activity lithium. Pulham and Watson [4.15] determined the standard free-energy of formation of Li_9CrN_5 as,

$$\Delta G^{\circ}_{f\ Li_9CrN_5}\ [kJ/mole] = A^{\circ}_{Li_9CrN_5} + B^{\circ}_{Li_9CrN_5}\ T[K]$$

$$A^{\circ}_{Li_9CrN_5} = -\ 1059\ [kJ/mole],\ B^{\circ}_{Li_9CrN_5} = 6.85 \times 10^{-1}\ [kJ/mole\text{-}K]$$

$$850 < T < 950\ K$$

The reaction to form Li_9CrN_5 from dissolved nitrogen in lithium and chromium in a BCC ferrite matrix can be expressed by

$$5\ Li_3N_{(in\ Li)} + Cr_{(in\ \alpha\text{-}Fe)} \ <===>$$

$$Li_9CrN_{5\ (on\ steel)} + 6\ Li$$

From the definition of activity and Raoult's law, lithium and Li_9CrN_5 are near or at unit activity. Nitrogen in the lithium and chromium in the steel are not. The equilibrium for this reaction is given by the law of mass action.

$$K_{Li_9CrN_5} = \frac{1}{a_{Cr}^{\alpha}\left(a_N^{Li}\right)^5} = \exp\left(\frac{-\Delta G^{\circ}_{Li_9CrN_5}}{RT}\right)$$

$$[N]^{*}_{Li} = [N]^{sat}_{Li}\left(\frac{1}{K_{Li_9CrN_5}\ a_{Cr}^{\alpha}}\right)^{1/5}$$

where $K_{Li_9CrN_5}$ is the equilibrium constant, a_{Cr}^{α} and a_N^{Li} are the activities of chromium in the α-Fe and nitrogen in lithium, respectively, $\Delta G^{\circ}_{Li_9CrN_5}$ is the free-energy for the reaction and $[N]^{*}_{Li}$ is the concentration of nitrogen in lithium at which Li_9CrN_5 begins to precipitate on a chromium-bearing surface. The free energy for the reaction can be obtained by combining the free energies of formation of Li_9CrN_5 and Li_3N and is plotted in Figure 4.3.2 along with the free

energies of both Li_9CrN_5 and Li_3N. The free energies of the equation is large and negative, indicating that formation of Li_9CrN_5 is favored.

From the equilibrium constant, solubility, and chromium and nitrogen activity information, the concentration of nitrogen, $[N]^*_{Li}$, at which Li_9CrN_5 should begin to form, at equilibrium, on a surface with a specified chromium content (activity) can be calculated and is plotted in Figure 4.3.3 along with the average nitrogen content of the lithium in both GEB-1 and GEB-2 (~80 wppm-N). The region above the curve represents the region in which Li_9CrN_5 can form. In regions below the curve, Li_9CrN_5 cannot form. *Figure 4.3.3 indicates that the Li_9CrN_5 corrosion product was thermodynamically favored to form over most of the surfaces in GEB-1. However, nitrogen activities were insufficient to allow formation of Li_9CrN_5 in GEB-2.* We conclude that Li_9CrN_5 probably formed in GEB-1. Below, we address the effect this formation on the specimen weight changes.

The physical condition of the Li_9CrN_5 corrosion product has been observed by Barker et al. [4.16] to be a face centered cubic structure with lattice parameter 14.2 angstroms which formed as an adherent surface layer to the steel surface that was insoluble in lithium. The density of the Li_9CrN_5 can be estimated to be approximately 1500 kg/m^3 which makes Li_9CrN_5 more than three times more dense than lithium. The formation of a dense, adherent, insoluble corrosion product would help to explain the difference in the magnitude (factor of 10 to 15) of weight changes in GEB-1 and GEB-2 and the surface roughening and insensitivity of weight

changes to temperature in GEB-1 at temperatures below 450 °C. If the Li_9CrN_5 corrosion product did form in GEB-1, as was theoretically predicted above, and was insoluble and adherent, as observed elsewhere [4.7,4.15-16], then it would act as a protective barrier for both further formation of the corrosion product and elemental dissolution of the alloy. In order to continue to react with chromium on the steel surface, lithium nitride would have to move by solid-state diffusion across this Li_9CrN_5 surface layer to the interface where the nitrogen content is fixed by the surface equilibrium at [N]* for the formation of Li_9CrN_5. Solid-state diffusion is a very slow process, particularly at the temperatures where Li_9CrN_5 formed, and if diffusion through the ternary nitride layer were controlling the mass transport, the mass fluxes would be much smaller than predicted by boundary layer limited transfer. Transport of other steel constituents would also be inhibited by the presence of the surface product layer. For solubility transport of the steel constituents, the constituents would also have to diffuse across the layer into the lithium. We have estimated the thickness of the Li_9CrN_5 layer which formed on chromium-plated surfaces, to be of the order of 10 μm. In the next section, we estimated the boundary layer mass transfer coefficient to be 2×10^{-6} m/s at 450 °C. If we assume the thickness of the Li_9CrN_5 which formed on the lower chromium activity steel surface was an order of magnitude thinner than that which formed on the chromium-plated surfaces (1 μm), we can estimate an upper bound on the diffusion coefficient of a species

i for diffusion through the surface layer to be of the same magnitude as the boundary layer diffusion.

$$k_B^i = \left(\frac{1}{k_{bl}^i} + \frac{\delta}{D_i} \right)^{-1}$$

$$D_i \sim k_{bl}^i \, \delta \sim 2 \times 10^{-12} \text{ m}^2/\text{s at } 450 \text{ °C}$$

If the actual diffusion coefficients are lower than 2×10^{-12} m^2/s at 450 °C then diffusion through the surface product layer would be the rate limiting step for corrosion. Data for diffusion coefficients in Li_9CrN_5 do not exist. By comparison with other solid state diffusion coefficients (e.g. carbon in 316 SS steel at 600 °C, $D_C \sim 10^{-15}$ m^2/s [4.7]), the upper bound (2×10^{-12} m^2/s at 450 °C) is large. We would expect the actual values to be lower and, therefore, diffusion through the Li_9CrN_5 probably controlled the transport on surfaces where Li_9CrN_5 formed.

Further, we believe the "roughening" of the surface corresponds to the formation of Li_9CrN_5. The roughened surfaces of the Fe-12Cr1MoVW are similar to that of the chromium-plated surface exposed to high nitrogen activity lithium in capsule tests (see Figure 4.3.4).

The formation of the Li_9CrN_5 would also explain the transient period of weight loss in GEB-1. Initially, the activity of chromium in the ferrite phase is unity due to the large activity coefficient and amount of chromium in the alloy. The solubility of chromium in α-ferrite is less than 6 w/o [4.17] and approximately 2.5 w/o

chromium is bound up as $Cr_{18}Fe_5C_6$ [4.13] carbides. There initially exists an "excess" of chromium (~ 3 -4 w/o) in the initial composition of the alloy. The initially large chromium activity makes formation of Li_9CrN_5 thermodynamically easier. When Li_9CrN_5 forms on the steel surface, it consumes the "excess" surface chromium. At low temperatures, chromium is essentially immobile in the steel (see section on electron microprobe in chapter 3) and diffusion from the bulk of the alloy cannot replenish the chromium consumed at the surface of the steel. Chopra [4.18] has suggested that the 6 to 8 w/o chromium content which develops on both austenitic and ferritic steels exposed to lithium at temperatures below 500 °C with approximately 100 wppm nitrogen may represent some sort of equilibrium chromium content of the steel in the Li_9CrN_5/Fe+Cr system. Since the cleaning method (alcohol and water) used for the specimens removed the Li_9CrN_5 layer, the layer would have to form again when the specimen was reinserted. Weight changes measured in the transient period were probably much higher than would be experienced in a non-experimental setting, such as a reactor where the Li_9CrN_5 layer would remain, at least partially, intact. Further, removal of this product during the cleaning of lithium from the specimens leads to the continued weight losses as the specimens are removed during the operation of the experiments. However, steep velocity gradients [4.19] or unsteady velocity profiles [4.20], such as might be encountered in liquid metal flowing in a large magnetic field (MHD), may shear and spall the protective corrosion product

layer from the surface and corrosion rates could be higher than those measured here.

The occurrence of the largest weight losses at the lowest temperatures both in these and other experiments [4.2] can also be explained by the formation of Li_9CrN_5. The driving force for the formation of Li_9CrN_5 is the difference between $[N]_{Li}$ and [N]*. For low mass transfer rates, $[N]_{Li}$ should have been nearly constant around the entire experiment. However, [N]* decreases with temperature and, thus, the driving force for formation of Li_9CrN_5 would have been the greatest at the lowest temperature.

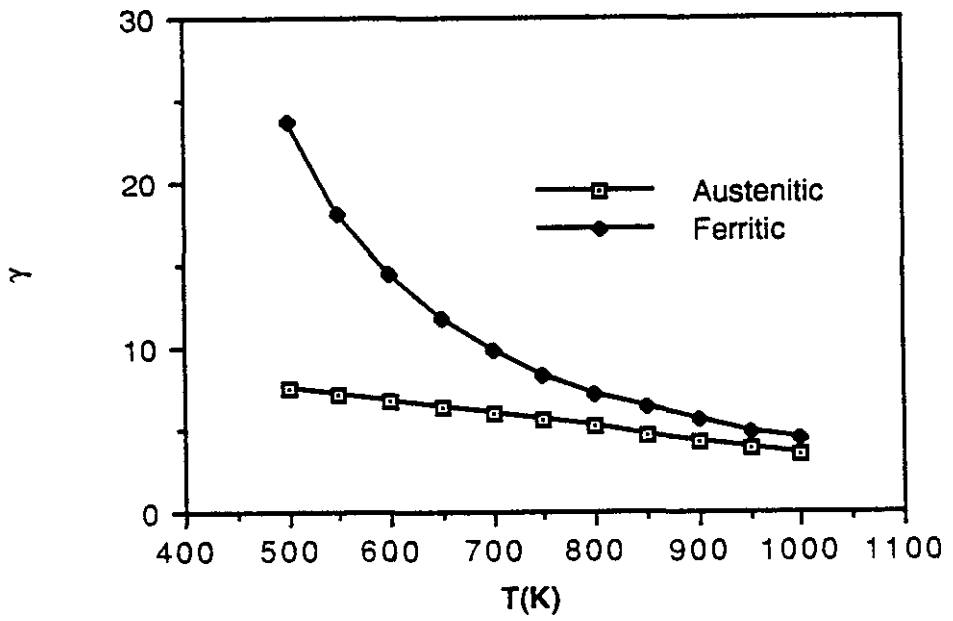

Figure 4.3.1 Activity Coefficients of Chromium in Steels

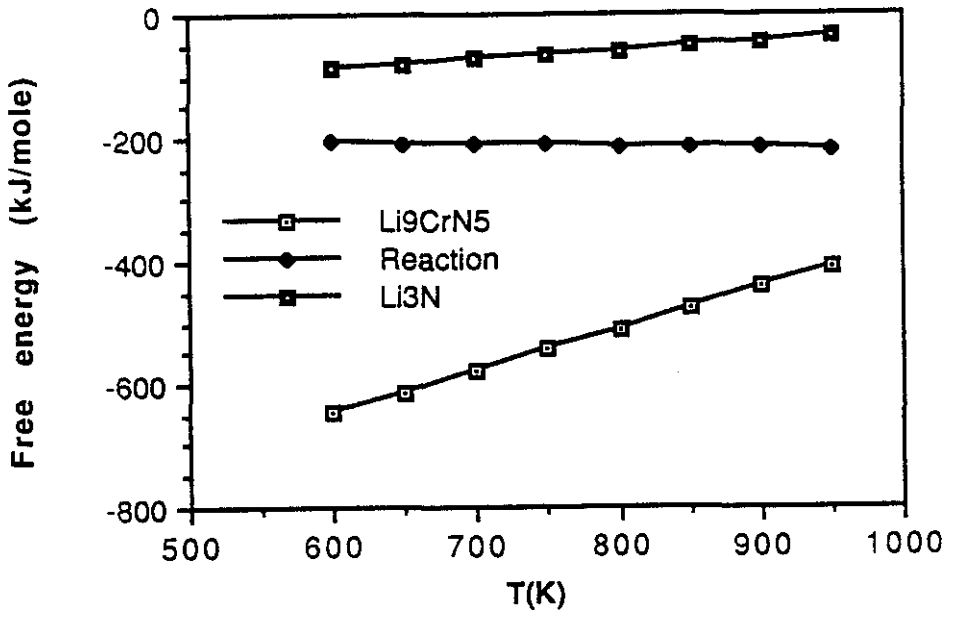

Figure 4.3.2 Free-energy of Formation for Li_9CrN_5

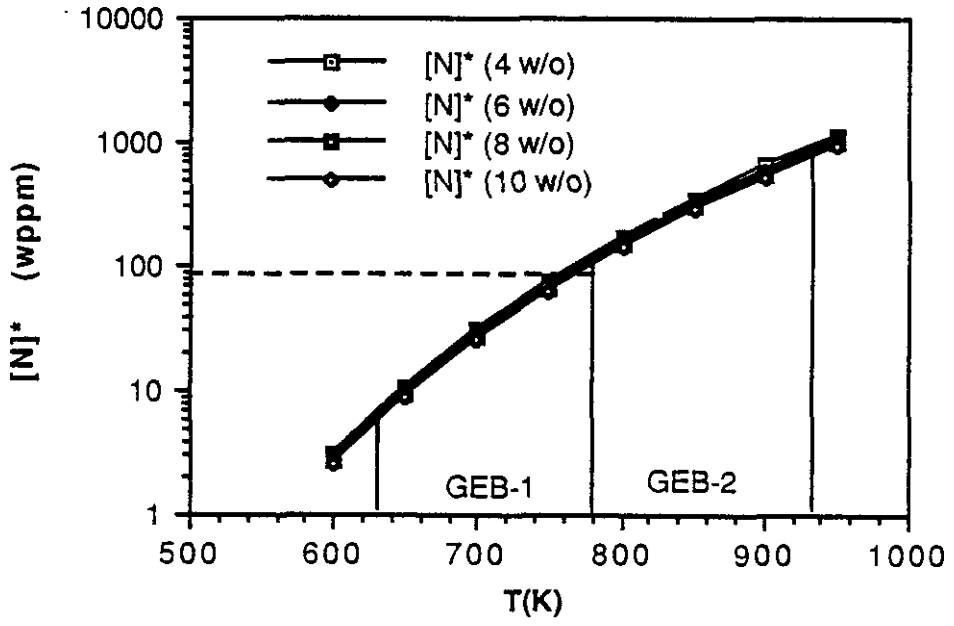

Figure 4.3.3 Equilibrium Nitrogen in Lithium with Chromium

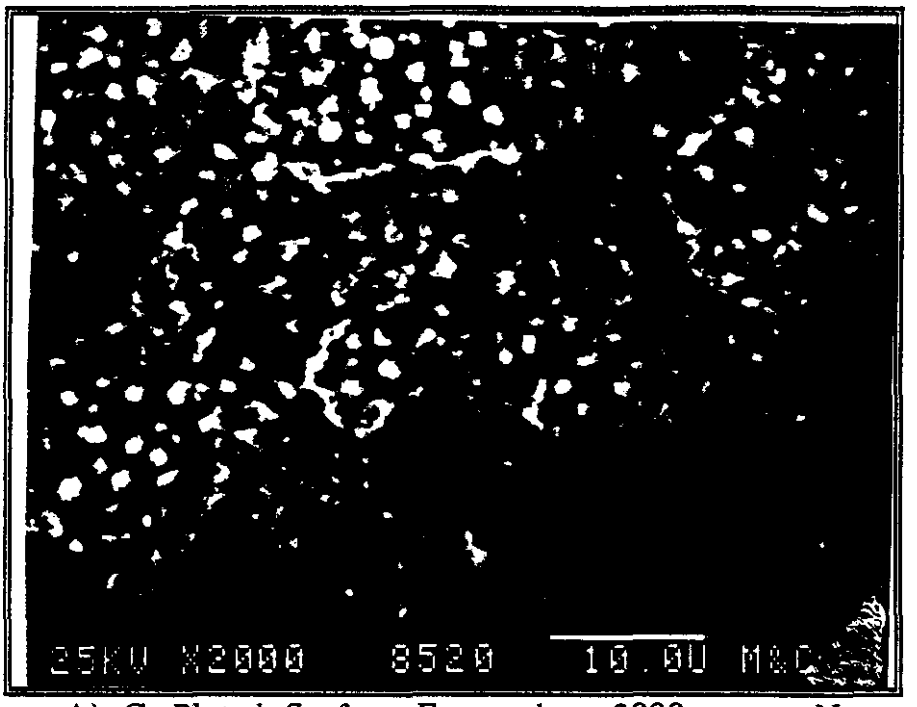

A) Cr-Plated Surface Exposed to 2000 wppm N
450 °C, 500 hours
Photo # 28520

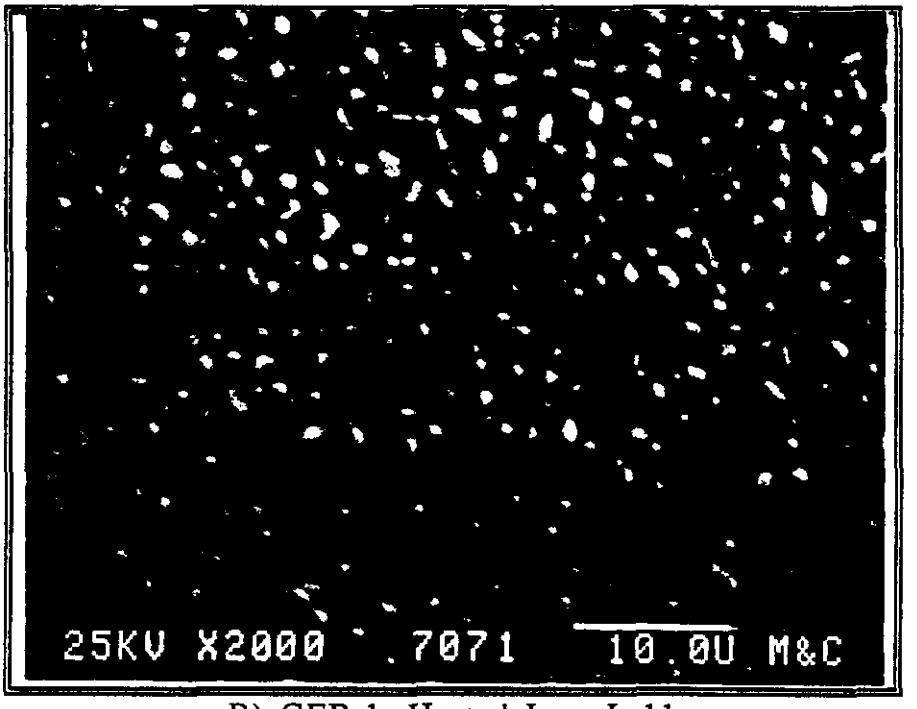

B) GEB-1, Heated Leg, L-11
436 °C, 3040 hours
Photo # 27071

Figure 4.3.4 Comparison of Cr-plated Surface to Fe-12Cr-1MoVW

Surface and Boundary Layer Mass Transfer Coefficients

If the Li_9CrN_5 surface reaction layer were soluble in the lithium or not adherent to the surface of the steel, then the rate of formation of a corrosion may have been kinetically limited either by the surface reaction rate or the transport of nitrogen to the steel surface from the liquid phase. In order to determine if this is possible, we must characterize both the surface reaction velocity, k_r^i, and the boundary layer mass transfer coefficients, k_B^i.

The activation energies for formation of the corrosion product in lithium/austenitic stainless steel and lithium/Cr systems has been estimated from weight loss data from capsule tests to be between 16 and 37 kJ/mole (Figure 4.3.5) which is a function of the activity of chromium on the surface. The 16 kJ/mole value was obtained for 304L SS with a chromium activity of approximately $a_{Cr}^{304}=0.3$ and the 37 kJ/mole value was determined on chromium plated surfaces with chromium activity of approximately $a_{Cr}^{Cr\text{-}plated}\sim 1$. The pre-exponential factor was estimated from the kinetic data of Barker et al [4.16] to be 2.5×10^{-2} m/s. If we assume that 20 kJ/mole as an average value of the activation energy applicable to Fe-12Cr alloys which have higher chromium activities as compared to the austenitic alloys tested, the reaction rate is given by

$$K_r^{Li_9CrN_5}(T) = 2.5 \times 10^{-2} \exp\left(\frac{-20000}{R\ T}\right) m\ s^{-1}$$

In systems going from 350 to 500 °C, $K_r^{Li_9CrN_5}$ changes by a factor of 2 from lowest to highest temperature. The difference in reaction rate between 350 and 650 °C is about a factor of 3.5.

By comparing the magnitude of the boundary mass transfer coefficient to that of the surface reaction rate coefficient, $\frac{k_B^i}{k_r^i}$, the relative importance of these two processes can be estimated. The dimensionless equations which describe heat and mass transfer are given by:

$$\frac{D\,T^*}{D\,t^{**}} = \frac{1}{Pr}(\nabla^* \cdot \nabla^*)\,T^* \qquad \text{(heat transfer)}$$

$$\frac{D\,X^*}{D\,t^{**}} = \frac{1}{Sc}(\nabla^* \cdot \nabla^*)\,X^* \qquad \text{(mass transfer)}$$

where,

$$\frac{D}{D\,t^{**}} = \left(\frac{\partial}{\partial\,t^{**}} + \mathbf{V}^{**} \cdot \nabla^*\right)$$

∇^* = dimensionless gradient operator $= \frac{\nabla}{L}$

$\mathbf{V}^{**}$ = dimensionless velocity vector $= \frac{\mathbf{V}\,L}{\nu}$

t^{**} = dimensionless time $= \frac{t}{\nu\,L^2}$

T^* = normalized temperature = \F(T - T_{Ref}, T_{Bulk} - T_{Ref})

Pr = Prandtl number = $\frac{\nu}{\alpha}$

X^* = normalized mass fraction = $\frac{X - X_{Ref}}{X_{Bulk} - X_{Ref}}$

Sc = Schmidt number = $\frac{\nu}{D_i}$

ΔT = temperature differential

α = thermal diffusivity

ν = kinematic viscosity

D_i = Diffusion coefficient for species i

= $\frac{kT}{6\pi\mu R_a^i}$ (Stokes-Einstein model)

k = Boltzmann's constant

μ = Dynamic viscosity

R_a^i = Atomic radius of species i (~ 1-2 x 10^{-10} m)

T = Absolute temperature

The three parameters which determine the momentum, heat and mass transfer in natural convection flows are the Grashof, Prandtl and Schmidt numbers. The similarity between the equations for heat and mass transfer suggests that mass transfer coefficients can be obtained from corresponding heat transfer correlations by replacing Pr with Sc:

$\frac{hD_h}{k}$ = $Nu_H(Gr_D, Pr)$

Gr = Grashof number = $\left(\frac{g\beta\Delta TL^3}{\nu^2}\right)$

L = length scale $= D_h$ = 3 x 10^{-2} m

$$\beta = -\frac{1}{\rho}\frac{\partial \rho}{\partial T} \sim 2.2 \times 10^{-4}\ K^{-1}$$

$$\frac{k_B D_h}{D_i} = Nu_M(Gr_D,Sc) = Nu_H(Gr_D,Sc)$$

The Grashof numbers for these experiments were approximately 2-4 x 10^7 which would be indicative of laminar natural convection [4.21]. Sparrow and Gregg [4.22] concluded that flat vertical surface solutions gave acceptable predictions for air when,

$$(Gr_D Pr)^{0.25}\frac{D_h}{L} > 38$$

$$(3 \times 10^7\ (4 \times 10^{-2}))^{0.25}\ (3 \times 10^{-2}) \sim 1 \quad \text{in experiments}$$

Raithby and Hollands [4.23] recommend correcting <u>flat-surface</u> Nusselt numbers for curvature effects or low Gr_D when the boundary layer is thick compared to the diameter of the cylinder by using

$$Nu_{ave} = \frac{2}{ln\left(1+\frac{2}{Nu_L}\right)}$$

Ede [4.24] gives the correlation for local laminar Nusselt number and the average Nusselt number is 4/3 times the local value ([4.21])

$$Nu_{H,ave}(Gr,Pr) = \frac{hL}{\lambda} = \left(\frac{2Pr}{5(1+2\sqrt{Pr}+2Pr)}\right)^{0.25}(Gr_L\ Pr)^{0.25}$$

Replacing Pr with Sc in Ede's correlation, we arrive at the following relationship for the boundary layer mass transfer coefficient

$$k_B = \frac{D_i}{L} Nu_M(Gr,Sc) = \frac{D_i}{L}\left(\frac{2Sc}{5(1+2\sqrt{Sc}+2Sc)}\right)^{0.25} (Gr_L\ Sc)^{0.25}$$

The ratio of boundary layer mass transfer coefficient to surface reaction is plotted in Figure 4.3.6 for $10^8 < Gr < 10^{10}$. The ratio is much less than unity indicating that boundary layer transport would be controlling for the laminar natural convection in these systems, if the Li_9CrN_5 layer were not adherent. A similar results are obtained if the flow is assumed turbulent natural convection or forced convection with Reynolds number based on average velocity. It is unlikely, however, that the shear stress produced by the natural convection flow in these experiments would be sufficient to remove a surface layer. As stated previously, magnetohydrodynamic forces in liquid lithium fusion blankets will produce steep, possibly unstable, velocity profiles which might remove (spall off) the layer and continuously expose the underlying surface to dissolved lithium nitride in the lithium. This effect (physical removal of an adherent surface layer) of MHD velocity profiles may be more significant than the increased mass transfer coefficient due to the steepened velocity profiles. As shown in the last section, it is more likely that the layer does form and that solid-state diffusion through the surface layer would be controlling.

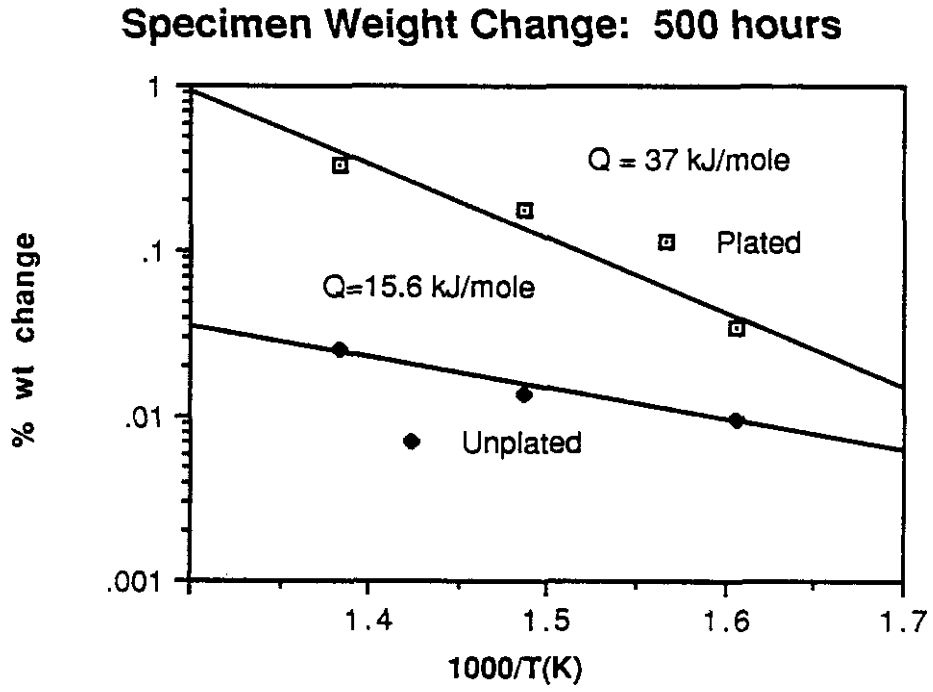

Figure 4.3.5 Capsule Test Specimen Weight Change Data

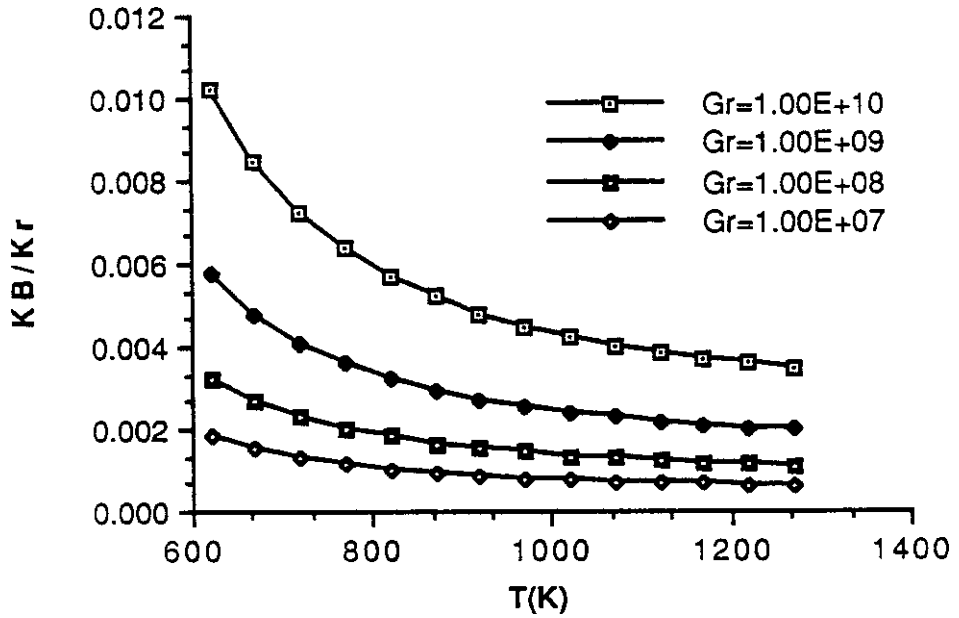

Figure 4.3.6 Comparison of Boundary Layer to Surface Reaction Mass Transfer Coefficient

Effect of Lithium/Chromium/Nitrogen Compound on Surface Carbon Activity

The removal of chromium from the steel surface, by the formation of Li_9CrN_5, affects the activity of carbon on the steel surface. Chromium and carbon in Fe-12Cr-1MoVW reside both in solid solution in the α-ferrite matrix and as dispersed, segregated metal carbides in the matrix or at grain boundaries. The heat treatment of the alloy determines the composition and stoichiometry of carbide which forms. Isothermally annealed Fe-12Cr-1MoVW contains primarily $M_{23}C$ carbides [4.25]. The free energy of formation of mixed metal carbides based on an ideal mixing theory for measured carbon activities in an austenitic stainless steel (18Cr-8Ni) has been reported by Pillai and Mathews [4.14]. The minimum free energy of $M_{23}C$, the most stable carbide, should be for chromium-rich precipitates with a stoichiometry near $Cr_{19}Fe_4C_6$. Data for Fe-9Cr-Mo were found to have such stoichiometry with molybdenum replacing some of the chromium. Carbon is nearly insoluble in the α-ferrite matrix. Data from Fe-9Cr-Mo ferritic alloys [4.13] at 700 °C show that saturation carbon concentrations in the ferrite matrix are less than 10 wppm as given by

$$\ln[C]^{\alpha}_{sat}\ (\text{wppm}) = 5.3 - 0.438\ [Cr]^{\alpha}(\text{w/o}) \quad \text{at } 700\ ^\circ\text{C}$$

The solubility of carbon in α-ferrite is dependent on the chromium content and temperature. However, data for the solubility of carbon

in α-ferrite as a function of both chromium content and temperature are not available. Carbon was present in the initial alloy at approximately 0.2 w/o (2000 wppm). Most of the carbon was in carbides dispersed in the matrix and collected at the grain boundaries. However, some carbon was dissolved in the α-ferrite.

The conditions for equilibrium on the steel surface can be expressed in terms of the activities of carbon in the two phases of the steel as

$$a_C^{M_{23}C_6} = a_C^{\alpha}$$

where a_C^{α} and $a_C^{M_{23}C_6}$ are the activities of carbon in the α-ferrite matrix and $M_{23}C_6$-carbide, respectively. The equilibrium of $M_{23}C_6$ carbides in the steel is represented by

$$X\ Cr_{(\alpha-Fe)} + (23 - X)\ Fe_{(\alpha-Fe)} + 6\ C_{(\alpha-Fe)} <==> Cr_XFe_{(23-X)}C_6$$

$$K_{Cr_XFe_{(23-X)}C_6} = \frac{1}{\left(a_{Cr}^{\alpha}\right)^{x}\left(a_{Fe}^{\alpha}\right)^{23-X}\left(a_C^{\alpha}\right)^{6}} = \exp\left(\frac{-\Delta G_f^{\circ}\ Cr_XFe_{(23-X)}C_6}{RT}\right)$$

$$a_C^{\alpha} = \left(\frac{1}{K_{Cr_X Fe_{(23-X)} C_6} \left(a_{Fe}^{\alpha}\right)^{23-X} \left(a_{Cr}^{\alpha}\right)^{X}} \right)^{1/6}$$

Data specifically for carbon activity and solubility as a function of chromium concentration and temperature in Fe-12Cr-1MoVW alloys are not available. However, the relationship for the equilibrium shows that as the chromium activity decreases, the carbon activity of the ferrite phase must increase to maintain equilibrium.

We can estimate the initial chromium activity of the α-ferrite below approximately 450 °C to have been unity. Nitrogen levels in the lithium below 450 °C in GEB-1 were sufficient to allow the formation of Li_9CrN_5 which forms as a separate phase. *The formation of Li_9CrN_5 on the α-ferrite phase of the surface decreases the chromium activity of the surface of the steel and increases the surface carbon activity of the α-ferrite phase.* Carbon would be released from the surface of the α-ferrite phase into the lithium to maintain equilibrium.

Carbon in Lithium

Carbon is present in lithium as a dimeric species [4.26] which can be either dilithium acetylide, Li_2C_2 or the dicarbide ion C_2^{-2}. The formation of lithium acetylide from its elements can be expressed as

$$2\ Li_{(liquid)} + 2\ C_{(solid)} \Leftrightarrow Li_2C_{2(solid)}$$

where $C_{(solid)}$ represents graphite and Li_2C_2 is pure. The free energy of formation is given by [4.26]:

$$\Delta G^{\circ}_{f,Li_2C_2}\ [kJ/mole] = A^{\circ}_{Li_2C_2} + B^{\circ}_{Li_2C_2}\ T[K]$$

$$A^{\circ}_{Li_2C_2} = -41.252\ [kJ/mole],\ B^{\circ}_{Li_2C_2} = -6.1879 \times 10^{-2}\ [kJ/mole\text{-}K]$$

The solubility of carbon in lithium has been investigated by Yonco and Homa [4.27] and Fedorov and Su [4.28]. The earlier findings by Fedorov and Su on carbon solubility from 463 to 1173 K were determined using X-ray analysis. Yonco and Homa reported carbon solubility in lithium from 463 to 1023 K using acetylene evolution technique. The data of Fedorov and Su, been suspect for more than 20 years, were found to be in error by at least 2 orders of magnitude. The data of Yonco and Homa were adopted for use in this work:

$$\ln [C]^{Li}_{sat} \text{ [wppm - C]} = A^{c}_{sat} + \frac{B^{c}_{sat}}{T[K]}$$

$$A^{c}_{sat} = 17.17 \text{ , } B^{c}_{sat} = -8612$$

where $[C]^{Li}_{sat}$ is the saturation concentration of carbon in lithium at temperature T in degrees Kelvin. Yonco and Homa also showed that although dilithium cyanamide (Li_2NCN) is thermodynamically stable, the solubility of carbon in lithium is not significantly affected unless the nitrogen activity of the lithium is near unity. The activity of nitrogen in our experiments was of the order of 10^{-3} and we therefore do not expect the solubility of carbon to have been effected by the formation of Li_2NCN.

The solubility of carbon in lithium means the weight of carbon in the form Li_2C_2 when lithium is contacted with pure graphite. The free-energy of formation of Li_2C_2 is negative indicating that the formation of Li_2C_2 is thermodynamically favored. Solutions of Li_2C_2 exist in lithium provided the activity of Li_2C_2 and carbon are less that unity. When the carbon contained in the lithium is less than unit activity, the law of mass action for the formation of Li_2C_2 is

$$K_{Li_2C_2} = \exp\left(\frac{-\Delta G^{\circ}_{f\,Li_2C_2}}{RT}\right) = \frac{a_{Li_2C_2}}{a_C^{\,2}}$$

$$a_{Li_2C_2} = a_C^{\,2}\, K_{Li_2C_2}$$

Note, the lithium activity is assumed to be unity since it is essentially in a pure state. When lithium is contacted with pure graphite, $a_C = 1$, the solution becomes saturated with lithium carbide, and we can write,

$$K_{Li_2C_2} = (a_{Li_2C_2})_{sat} = \exp\left(\frac{-\Delta G^{\circ}_{f\,Li_2C_2}}{RT}\right)$$

where $(a_{Li_2C_2})_{sat}$ is the activity of Li_2C_2 in lithium that is saturated with carbon. Since solutions of carbon are dilute, Henry's Law is applicable to the dissolved dilithium acetylide. Therefore, $a_{Li_2C_2}$ is proportional to $[C]_{Li}$; the concentration of carbon in the lithium.

$$a_{Li_2C_2} \sim [C]^{Li}$$

We can combine these relations to give,

$$\left(a_C^{Li}\right)^2 = \frac{a^{Li}_{Li_2C_2}}{(a^{Li}_{Li_2C_2})_{sat}} = \frac{[C]_{Li}}{(K_{Li_2C_2})\,[C]^{sat}_{Li}}$$

Chromium-rich Nodule Precipitation

The epitaxy of the chromium-rich surface $M_{23}C_6$ carbide nodules and their preferential nucleation and growth along grain boundaries

indicate that the carbides were being precipitated from the adjacent liquid phase. The carbon activity in lithium at which $M_{23}C_6$ carbides will begin to precipitate from a lithium solution is governed by the same reaction as in the steel, with the activity of carbon in the ferrite replaced by the activity of carbon in the lithium. The condition for equilibrium between the carbide and lithium phases is given by

$$a_C^{M_{23}C_6} = a_C^{Li}$$

If the activities are unequal, then the species is transported in the direction of decreasing activity (chemical potential). Since the solubility of carbon in lithium decreases with temperature, for a fixed carbon content, the activity of carbon in lithium should increase as temperature decreases. Thus, the driving force for carbon transport should also increase and we would expect that the number density and size of nodules would increase as the temperature decreased. This was the case in GEB-2 where the most noduled specimens were found at the lowest temperature. This was not the case in GEB-1. The nodules in GEB-1 gradually formed and the number density and size increased with increasing temperature. There are several possible explanations for this behavior. When the Li_9CrN_5 layer can no longer form over the entire surface, particularly at the grain boundaries, the nodules can begin to precipitate, first at areas where the protective layer has been unable to form. The bulk of the alloy was relatively unaffected because solid state diffusion is slow at the lower temperatures in GEB-1. The microprobe data

showed no significant effect of the lithium environment within the resolution of the microprobe. This implies that solid state diffusion was not important at these temperatures for these exposure times. Saltelli et al. [4.13] noted that, for carburization of Fe-9Cr-Mo steels in sodium, the phase boundary reaction between the carbides and the steel α-Fe matrix may have been limiting the process even at 700 °C. However, austenitics steel were more easily carburized because the γ-Fe/carbide reaction is not limiting. This may be a result of the more stable BCC (α-Fe) as compared to FCC (γ-Fe) phase.

Competition Between Nitrogen and Carbon

Since both nitrogen and carbon form compounds with chromium, Li_9CrN_5 and $M_{23}C_6$ (M=Cr and Fe), it is possible that there was a competition for chromium on the surface. The equations which describe this competition are as follows:

$$3\ Li_{(solid)} + \frac{1}{2}\ N_{2\ (gas)} \Leftrightarrow Li_3N_{(solid)}$$

$$2\ Li_{(solid)} + 2\ C_{(solid)} \Leftrightarrow Li_2C_{2(solid)}$$

$$\frac{5}{2}\ N_{2\ (gas)} + Cr + 9\ Li_{(solid)} \Longleftrightarrow Li_9CrN_5$$

$$X\ Cr + (23 - X)\ Fe + 6\ C \Longleftrightarrow Cr_XFe_{(23-X)}C_6$$

which can be combined into the overall equation

$$5\ X\ Li_3N_{(in\ Li)} + Cr_X\ Fe_{(23-X)}\ C_{6\,(on\ \alpha\text{-}Fe)} \Longleftrightarrow$$

$$X\ Li_9CrN_{5\ (on\ steel)} + 3\ Li_2C_{2\ (in\ Li)} + (23-X)\ Fe + 6X\ Li$$

The equilibrium for this equation is given by,

$$K = \frac{\left(a_{Fe}\right)^{23-X}\left(a_C\right)^6}{\left(a_N^{Li}\right)^{5X}} = \exp\left(\frac{-\Delta G°(X)}{RT}\right)$$

If we assume that the lithium is at or near saturation, $a_{Fe} = 1$, then we can relate a_C^* to a_N^{Li} as,

$$a_C^* = \left(a_N^{Li}\right)^{\frac{5X}{6}} \exp\left(\frac{-\Delta G°(X)}{6RT}\right)$$

The left hand side of the equation is favored at low nitrogen activities ($Cr_XFe_{(23-X)}C_6$ forms) and the right hand side at high nitrogen activities (Li_9CrN_5 forms). The free energy of the equation can be obtained by combining the free energies of formations of the elemental equations. Pillai and Mathews [4.14] determined that the free energy of mixed carbides and showed that the minimum in free energy of formation, the most stable carbide, has a stoichiometry between $18 < X < 19$. The data for X= 17, 19 and 21 and for pure $Cr_{23}C_6$ are represented by:

$$\Delta G°_{f,M_{23}C_6}\ [kJ/mole] = A°_{M_{23}C_6}(X) + B°_{M_{23}C_6}(X)\ T[K]$$

$$A^{\circ}_{X=17} = -209.0 \text{ [kJ/mole]}, \quad B^{\circ}_{X=17} = -1.6 \times 10^{-1} \text{ [kJ/mole-K]}$$

$$A^{\circ}_{X=19} = -224.0 \text{ [kJ/mole]}, \quad B^{\circ}_{X=19} = -1.5 \times 10^{-1} \text{ [kJ/mole-K]}$$

$$A^{\circ}_{X=21} = -242.0 \text{ [kJ/mole]}, \quad B^{\circ}_{X=21} = -1.2 \times 10^{-1} \text{ [kJ/mole-K]}$$

$$A^{\circ}_{X=23} = -314.5 \text{ [kJ/mole]}, \quad B^{\circ}_{X=23} = -6.1 \times 10^{-2} \text{ [kJ/mole-K]}$$

At 500 °C, we can obtain a expression for the free energy of formation as a function of X

$$\Delta G^{\circ}_{f, M_{23}C_6}(X;\ 500\ ^{\circ}C)\ \text{[kJ/mole]} = 321.44 - 69.2\ X + 1.81\ X^2$$

The free energy for the overall equation is plotted in Figure 4.3.7.

The activity of nitrogen in lithium in the surge tank of GEB-1 (500 °C), $a_N^{GEB\text{-}1\ Li}$, was approximately 10^{-3}. The corresponding activity of carbon, a_C^*, for precipitation of $Cr_{16}Fe_7C_6$ carbides at 500 °C from the above equation is approximately 10^{-2}. The measured activity (acetylene evolution by Argonne National Laboratory) was 6 x 10^{-2} which is consistent with the formation of the observed carbides. Further, the result of the reaction should be to put more iron into solution relative to chromium. The ratio of iron to chromium in GEB-1, 6.7, was in fact larger than that in GEB-2, 4.1, which is consistent with the reaction. The absolute magnitudes of iron and chromium in solution in GEB-2 were higher as compared with GEB-1. The ratio of the activities at equilibrium is controlled

by the equilibrium constant. This equilibrium may be the most consistent explanation of the appearance of the nodules over a specific temperature range. At the lower temperatures in GEB-1, the nitrogen activity is sufficiently high to allow formation of Li_9CrN_5 *from both chromium in the α-ferrite and from chromium in metal carbides* on the steel surface. The decomposition of the metal carbides puts carbon and iron into solution leaving behind Li_9CrN_5 on the surface. The activity of carbon in the lithium increases, while the formation of Li_9CrN_5 removes nitrogen from solution, decreasing the nitrogen activity. The changing temperature around the loop causes solubilities and activities of nitrogen and carbon to decrease. However, carbon activity is parabolically related to the solubility change while nitrogen is linearly proportional. The equilibrium is shifted from the right hand side to the left hand side of the reaction. Since the Li_9CrN_5 no longer forms, surface roughening, characteristic of surfaces below 450 °C where the nodules do not form, disappears. The substrate on which the nodules form begins to take on the cobblestoned pattern which was similar, but smaller in scale, to the cobblestoning of the surfaces of GEB-2 at high temperature. We believe the cobblestone pattern is indicative of surface exposed to lithium on which Li_9CrN_5 does not form and from which solubility effects take place. Nodules form in GEB-1 when the equilibrium of the nitrogen-assisted decarburization shifts such that Li_9CrN_5 can no longer form. Carbon and iron and chromium combine in the liquid phase and precipitate on the <u>surface</u> at grain boundaries where carbides pre-exist from the heat treatment. <u>Bulk carburization</u> may

not be possible due to a phase-boundary reaction limited kinetics in the bulk at the carbide/α-ferrite interface in the bulk of the alloy [4.14 and 4.29]. The composition of the nodules varies as the temperatures and activities of the components of the carbide and nitrogen vary around the experiment.

A physical model of the corrosion processes for GEB-1 is shown in Figure 4.3.8.

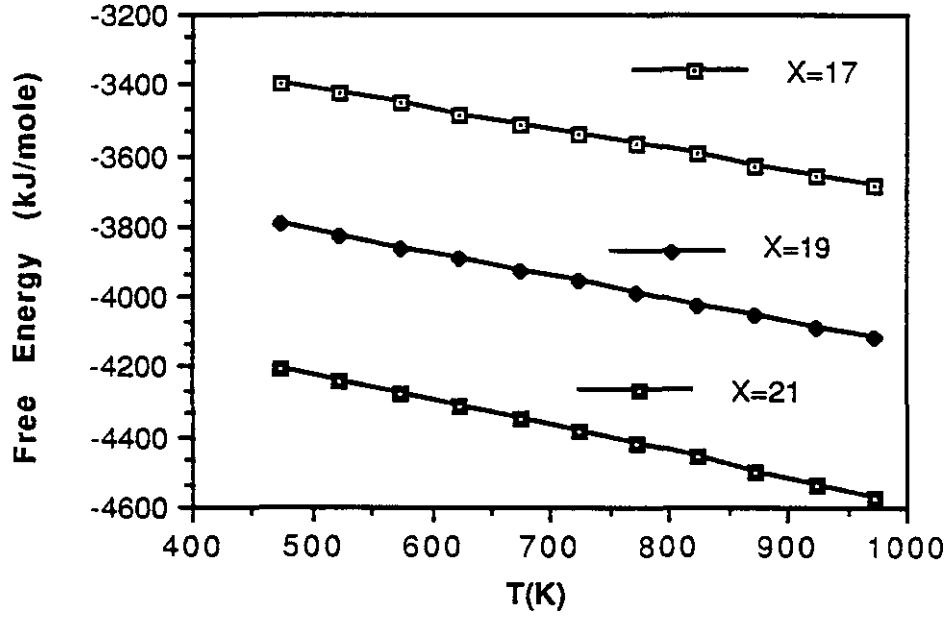

Figure 4.3.7 Free-energy of Competition Reaction for Chromium

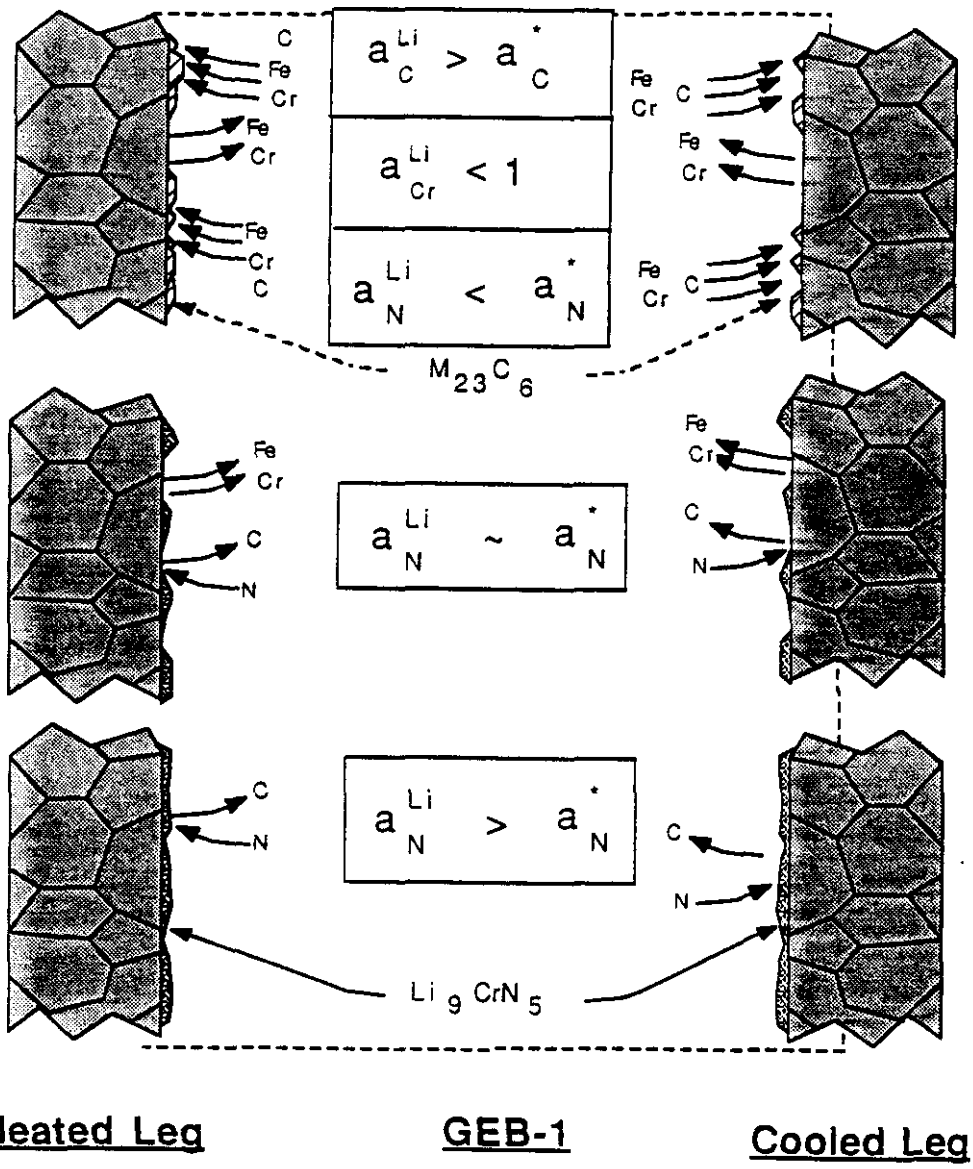

Figure 4.3.8 Physical Model of Compatibility Processes in GEB-1

4.3.3 GEB-2 A Return to the Dominance of Solubility

The mass transport in GEB-1 was dominated by the interactions of dissolved nitrogen with chromium and metal carbides via the formation of Li_9CrN_5 and the subsequent release of carbon from the steel. The behavior in GEB-2 cannot be related to Li_9CrN_5. There was insufficient nitrogen to allow its formation (see Figure 4.3.3). However, the behavior of GEB-2 can be understood in terms of simple dissolution mass release of iron and chromium and carbon in the heated leg and surface carburization via the formation of $M_{23}C_6$ in the cooled leg.

Carbon Transport in GEB-2

We did not observe deposits which were purely metallic in nature, such as occurs in austenitic steel systems [4.30]. Weight gains (deposition) in both the heated and cooled legs of this system were due entirely to the precipitation of surface carbide nodules, either iron or chromium-rich.

The activity of carbon in the steel increases with temperature due to the decreasing activity of chromium (γ^{α}_{Cr}) with temperature. Carbon transport is via the lithium from the highest temperature, where decarburization was evident, to the low temperature where surface (chromium rich nodules) carburization was evident.

Above 580 °C in the cooled leg of GEB-1, carbon activities in the liquid phase were insufficient to support surface nodule/carbide growth and the chromium-rich nodules could no longer form. We

can estimate the activity of carbon in the lithium from the formation of the first (X=19 @ 530 °C) and last (X=17 @ 580 °C) carbides which formed and in the cooled leg of GEB-2 at about 580 °C assuming the activities of iron and chromium are near unity,

$$\Delta G^{\circ}_{f,Cr_{17}Fe_6C_6} = -345.5 \text{ kJ/mole} \qquad \text{at } 580\ ^{\circ}\text{C},$$

$$a_C^{\text{Li-GEB-2}} \sim 3.0 \times 10^{-4}$$

$$[C]^{Li} \sim 62 \text{ wppm-C}$$

$$\Delta G^{\circ}_{f,Cr_{19}Fe_7C_6} = -344.0 \text{ kJ/mole} \qquad \text{at } 530\ ^{\circ}\text{C},$$

$$a_C^{\text{Li-GEB-2}} \sim 1.8 \times 10^{-4}$$

$$[C]^{Li} \sim 17 \text{ wppm-C}$$

The activity of carbon in the lithium must have been at or above this value in order to allow the formation of these nodules. The number density, the number of chromium atoms per carbide and the size of the chromium-rich nodules increased as the temperature decreased (as compared to GEB-1 where the number density, number of chromium atoms per carbide and the size increased with temperature) and the activity of the components of the carbide increased in the liquid phase. Pre-existing carbides at grain boundaries on the surface serve as nucleation sites for the grow of nodules with similar stoichiometries. The iron-rich carbide nodules which appeared in the heated leg of GEB-2 did not exhibit any preferred orientation relative to the grains and/or grain boundaries.

This is because there were no iron-rich surface carbides to serve as nucleation sites for the deposition.

Further, the iron-rich nodules appeared only in the vicinity of the large flow disturbance (i.e. flow restriction) at the inlet of the flow to the heated leg in GEB-2. If carbide particles were suspended in the flow then the disruption of the boundary layers at this flow disturbance would increase the deposition rate of particles in the flow. Chemical analysis of unfiltered samples of lithium from both GEB-1 and GEB-2 showed iron and chromium levels in excess of the elemental solubilities. Chopra [4.18] also observed iron and chromium concentrations in excess of solubility levels in unfiltered samples of lithium from his forced convection loop experiments. However, Chopra's filtered samples showed a decrease in iron and chromium and carbon analyses. Chopra's and our results indicate that these metallic elements (Fe and Cr) may be in the form of particles as compounds, possibly with carbon (metal carbide particles). However, if this were the case, then we would expect to find chromium-rich nodules also deposited at this point. *However, iron is a less stable carbide former than chromium. For this reason, iron-rich carbides are less thermodynamically stable than chromium-rich carbides and precipitate at correspondingly higher carbon activities. Further, bulk carburization was evident from both electron microprobe traces and cross sectional views of the specimens which had iron-rich nodules deposited on them. The carburization of the bulk of the steel and high iron content of the deposited particles may indicate that the activity of chromium in the*

lithium was insufficient for precipitation of chromium-rich nodules ($a_{Cr}^{Li} < 1$). The carbon activity of the lithium would have been sufficient to allow formation of more chromium rich nodules but there was insufficient chromium available. Data for free energy of formation of iron-rich $M_{23}C_6$ carbides are not available. Extrapolation of the data of Pillai and Mathews for chromium-rich carbide formation to X=3 (iron-rich carbides) gives a positive free energy of formation, indicating that on the basis of their model iron-rich carbides are thermodynamically unstable and should not exist. Obviously, the model cannot be extrapolated to low values of X and iron rich carbides are thermodynamically stable at some carbon activity. Tortorelli [4.1] reported that chromium-rich nodules formed first and eventually iron-rich nodules formed at longer times. This observation is consistent with limited chromium for precipitation. Initially, chromium is removed rapidly from the high temperature surface due to its high activity and so there is sufficient chromium available for formation of chromium-rich nodules at short exposure times. Eventually, chromium transport is limited by diffusion in the solid phase and the surfaces at the higher temperature become enriched in iron. On the other hand, carbon is much more mobile in the solid phase and so the activity of carbon and iron in the lithium increases relative to chromium as time increases. Eventually, the activity of carbon builds to a point where iron-rich carbide precipitation is thermodynamically possible.

The data points for deposition of chromium-rich nodules in the cooled leg of GEB-1 were <u>linear</u>, not exponential, with respect to

inverse temperature with a slope of 42000 K^{-1}, or of 349 kJ/mole if they were plotted versus 1/RT. An explanation of this behavior is not obvious. However, the free energy of formation for $Cr_{19}Fe_4C_6$ (the stoichiometry of nodules which were precipitating in the cooled leg of GEB-2) at and near 550 °C is 347 kJ/mole [4.14]. This coincidence should not be ignored.

Iron and Chromium Transport

The cobblestone pattern, which begins to form in GEB-1 as the corrosion layer no longer forms and which is most evident in GEB-2 above 580 °C, seems to be indicative of dissolution behavior. Experiments with Fe-2$\frac{1}{4}$Cr-1Mo steel (Whitlow et al. [4.31]) in lithium produced the same cobblestone pattern at a lower temperature (538 °C) in an austenitic FCL where the substantially lower chromium contents of the alloy probably would not allow formation of the protective Li_9CrN_5 layer. Further, the slope of the log of the corrosion rate versus inverse temperature produces an activation energy very close to that of the enthalpies of solution for iron and chromium in lithium. As also suggested by Tortorelli [4.1], the corrosion behavior (surface morphologies and weight losses) at higher temperatures (above 580 °C) was controlled by elemental solubility of the steel (Fe, Cr and C) constituents in the lithium.

The appearance of the vanadium- and molybdenum-rich speckles at higher temperature was consistent with previous observations in austenitic steels. Tortorelli and DeVan [4.32] observed fluorescent molybdenum enriched "speckles" on the ferrite surface layer of 316 stainless steel exposed to lithium in thermal convection loops at temperatures near 600 °C similar to the speckles which formed on the grooved surface above 580 °C in these experiments. The speckles observed in these investigation and by Tortorelli and DeVan were probably molybdenum/vanadium-containing MC or M_4C_3 carbide precipitates that grew at elevated temperatures and were exposed as the surface of the alloy receded.

Molybdenum and vanadium are less soluble in lithium as compared to iron and chromium and stronger carbide formers. Further, M_4C_3 carbides are very stable [4.34] carbides and thus can remain even in contact with high temperature lithium. Local increases in the molybdenum and vanadium with the dissolution of chromium would allow these carbides to form. At higher temperatures and after sufficiently long periods of time, the mobility of the elements is sufficient to allow these carbide particles to grow in size where they are observed.

The microprobe analysis showed significant attack (decarburization) into the depth of the bulk alloy to about 8 to 10 microns. However, the weight change data as a function of time showed a linear profile from the beginning of exposure indicating that the solid phase transport was not controlling the corrosion mechanism. The microprobe analysis also showed a sharp, discernable drop in chromium content followed by a near linear profile of chromium versus distance from the lithium contacted surface at the edge of the decarburized zone of the steel. Decarburization is also evident from the cross-sectional views of the specimens. Chromium, in the form of $M_{23}C_6$ carbides dispersed throughout the bulk matrix, is released along with carbon as the surface of the steel is decarburized and the dispersed carbides decompose. Solubility of chromium is higher and lower chromium activity in the lithium provides the driving force for chromium. However, if the reaction at the phase boundary (α-Fe/carbide) is slow in comparison to the diffusion of chromium and iron in the

ferrite matrix then a sharp drop in chromium activity will be present at the transition. In accordance with this, Saltelli et al. [4.14] observed that ferritic steels (Fe-9Cr-Mo) carburized or decarburized by a sodium environment were not indicative of a chromium diffusion profile but rather a phase boundary limited behavior.

Deposition Limitations on Carbon in Lithium

The primary compatibility concern for fusion reactor designers is the deposition rate. In particular, the deposition of high specific induced activity metallic elements such as molybdenum and niobium will be limiting long before the limit set by thinning of the base material. Deposition in these systems was controlled by carbon. Carbides can precipitate with metallic elements present below unit activity (elemental deposition). The only way to prevent metallic element deposition is by controlling carbon activities levels below that at which the most stable carbide ($Cr_{19}Fe_4C_6$) would precipitate, if metallic elements were present at unit activity (a_{Fe} and $a_{Cr} = 1$).

$$a_C^{Li} \leq \left(\frac{1}{K_{Cr_{19}Fe_4C_6}} \right)^{1/6}$$

We can use this expression and the relationship between carbon activity and concentration to evaluate the carbon concentration in lithium at which $Cr_{19}Fe_4C_6$ begins to precipitate (Figure 4.3.9). In order to have a minimum temperature of 350°C, a carbon concentration below 1 wppm-C would need to be maintained to avoid metal carbide precipitation.

A physical model of the corrosion processes in GEB-2 is shown in Figure 4.3.10.

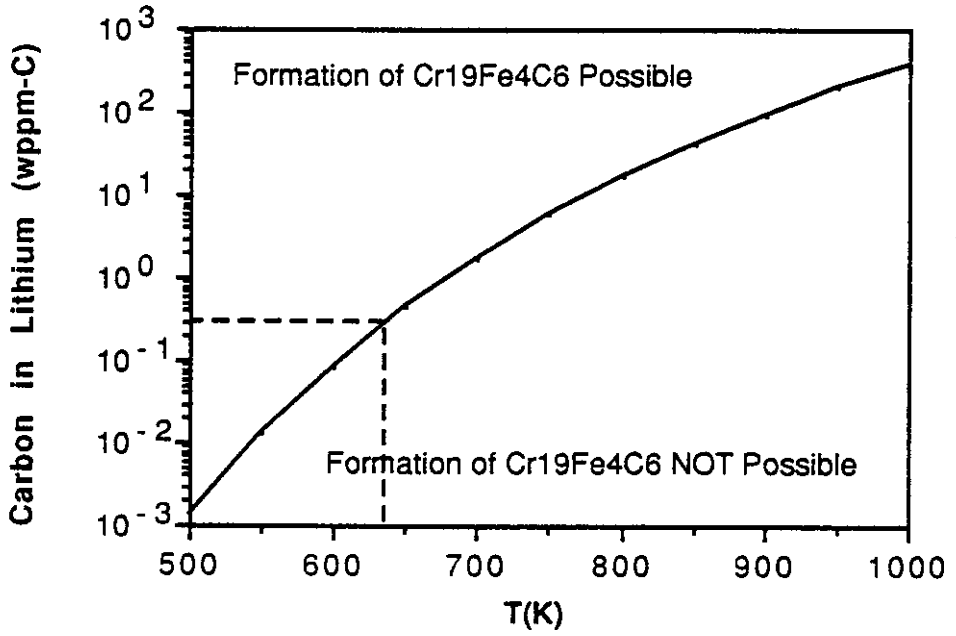

Figure 4.3.9 Carbon in Lithium for Precipitation of Carbides

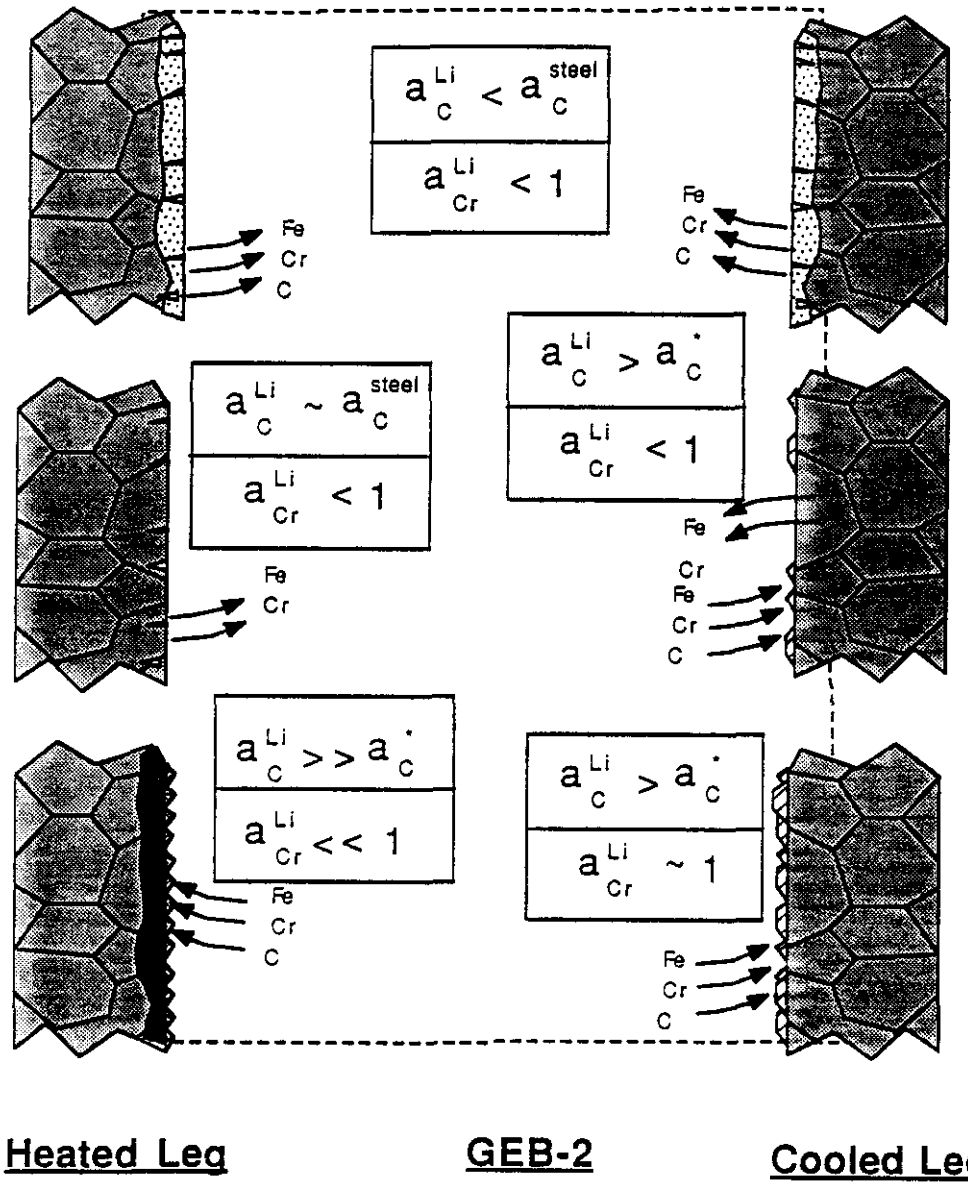

Figure 4.3.10 Physical Model of Compatibility Processes in GEB-2

4.4 Ferritic Alloys for Use with Lithium in Fusion Reactors

Fe-12Cr1MoVW (HT9), Fe-9Cr1MoVNb and Fe-2.25Cr1Mo (HT9) are commercially available ferritic alloys which are considered the baseline ferritic steel options for the fusion program. For reasons beyond their compatibility with lithium, these alloys are not the "optimal" choices for a structural material in a fusion reactor blanket. In particular, the presence of molybdenum and traces of niobium in their compositions make near surface disposal of these baseline alloys impossible (Klueh, Maziasz and Corwin [4.33]). Additionally, creep-rupture temperature limitations may be more restrictive than compatibility temperature limitations (Ghoniem et al. [4.34-35]).

Several investigations to develop a suitable ferritic alloy for use in fusion reactors have been undertaken [4.33-35]. Ghoniem, Shabaik and Yousseff [4.35] developed and mechanically tested a low-activation ferritic alloy, UCVS-1 (vanadium stabilized Fe-$2\frac{1}{4}$Cr). Ghoniem, Blink and Hoffman [4.34] compared UCVS-1 to three other ferritic alloys, HT9 (Fe-12Cr1MoVW), Fe-$2\frac{1}{4}$Cr-1Mo and Nb-stabilized Fe-$2\frac{1}{4}$Cr-1Mo on the basis of mechanical and irradiation performance, lithium compatibility and waste disposal index. Lithium compatibility evaluation was limited to a comparison of the stability of metal carbides in the steel. The formation and benefit of a Li_9CrN_5 protective layer in terms of compatibility was not addressed for the compatibility considerations. All four steels were found to be approximately equal on all levels of comparison except waste disposal index. The steel without molybdenum and niobium, UCVS-1,

was deemed preferable to the other steels on the basis of the waste disposal index. Klueh, Maziasz and Corwin [4.33] have investigated the development of ferritic Fast Induced Radioactive Decay (FIRD) steels based on commercial Fe-$2\frac{1}{4}$Cr-1Mo, Fe-9Cr-1Mo and Fe-12Cr1MoVW steels. Tungsten behaves like molybdenum in simple steels and does not have the long-term radioactivity problem associated with molybdenum. For these reasons, tungsten was used as a replacement for molybdenum on an atom-for-atom basis (1 w/o Mo = 2 w/o W). Tantalum was used to replace niobium. The resulting steels would be expected to have lower waste disposal indexes as compared to the baseline steels due to these replacements. Chromium contents of the 8 steel compositions investigated ranged from 2.25 w/o to 12 w/o. The structural properties of these FIRD steel alloys were similar (hardness and tensile strength) and in some cases superior (impact properties) to the baseline commercial alloys. Compatibility of the alloys with lithium was not addressed by Klueh et al. [4.33], but it was concluded that it would be possible to develop ferritic FIRD steel with chromium contents between 2.25 and 12 w/o chromium which would possess better mechanical and waste disposal properties than the commercially available Fe-Cr-Mo alloys currently considered for the fusion program.

The formation of a Li_9CrN_5 layer on the surface of a steel can be both a blessing and a curse. The layer can act to prevent transport by dissolution of the alloy constituents and further

formation of corrosion product. However, the release of carbon from the surface due to changes in chromium activity and/or nitrogen-assisted decarburization of the surface causes preferential deposition of carbides when the Li_9CrN_5 can no longer form. The problem with a relatively high chromium content steel, such as Fe-12Cr1MoVW, is that the carbides in the steel are chromium-rich ($Cr_{18}Fe_5C_6$). This is due to the strong carbide forming properties of chromium and its large weight fraction as compared to other carbide formers, such as molybdenum or vanadium, which may be present in the steel. The nitrogen competes for the chromium in the carbides. Figure 4.4.1 shows the carbon potential for many common alloying elements in steels. Niobium and titanium are the strongest carbide formers. By using stronger carbide-forming elements in the steel, the activity of carbon in the carbide phase could be reduced by forming more stable carbides. However, some portion of the total carbon in the alloy (although small by comparison to the carbide inventory) is dissolved in the ferrite matrix. At equilibrium, the activity of the matrix and the carbide would be equal. This would not be the case for a system undergoing net transport of mass. Darken and Ryba [4.36] and Small [4.37] showed that it was possible to lower carbon activities in the matrix of iron-based alloys by the addition of small amounts of other metal such as vanadium and niobium. The reduction of activity is attributable to preferential clustering of carbon atoms in solution with the solute molecules and is related to the relative (to iron) interaction energy $\Delta\mathcal{E}$, where

$$a_C^{\alpha\text{-Fe}} \sim \exp\left(\frac{\Delta\mathcal{E}}{RT}\right)$$

The interaction energy for several elements is plotted versus electronegativity in Figure 4.4.2 [4.37]. Small [4.37] found that vanadium was the strongest carbon clustering element.

By allowing the Li_9CrN_5 corrosion product to form and suppressing the carbon activity in both the carbide phase and in α-Fe matrix by appropriate alloy additions, an alloy with adequate mechanical, superior lithium compatibility and excellent waste disposal properties could be developed for fusion. The following suggestions for an alloy are made:

1) Chromium should be present at a sufficient level to allow formation of the protective Li_9CrN_5 corrosion product layer. Data from ferritic and austenitic steels indicate that for use below 550 °C and with 100 wppm nitrogen, 6 to 8 w/o chromium would be sufficient.

2) Stronger carbide forming elements should replace the chromium and molybdenum in the alloy; titanium (~3 w/o), vanadium (~1 w/o) and tungsten (~2 w/o) are the elements of choice. These levels, or higher, would be necessary to give sufficient activity for carbide formation from these elements instead of chromium. Selection of heat treatment for such an alloy will be crucial.

3) Niobium should be removed and, if deemed necessary, replaced with tantalum.

4) The total carbon content of the alloy should be no more than 0.15 w/o.

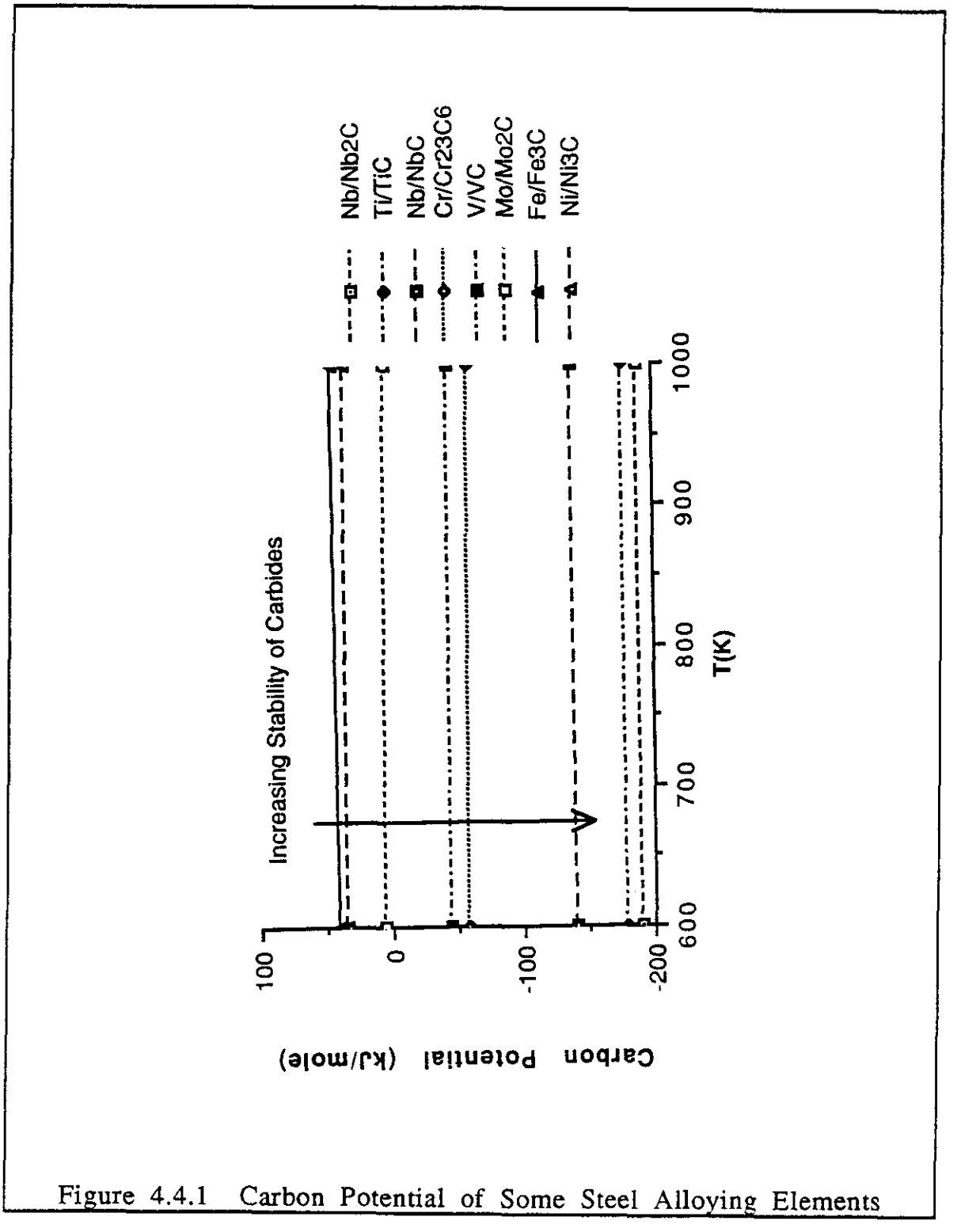

Figure 4.4.1 Carbon Potential of Some Steel Alloying Elements

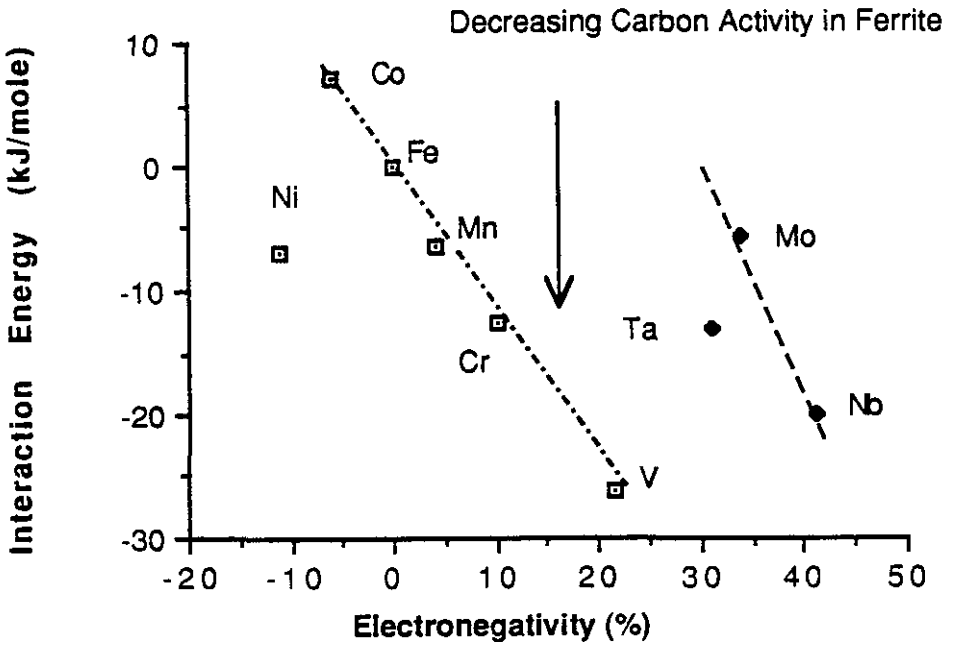

Figure 4.4.2 Interaction Energy versus Electronegativity

4.5 References for Chapter 4

[4.1] P.F. Tortorelli, "Corrosion of Ferritic Steels by Molten Lithium: Influence of Competing Thermal Gradient Mass Transfer and Surface Product Reactions," Journal of Nuclear Materials, (1988).

[4.2] P.F. Tortorelli and J.H. DeVan, "Corrosion of an Fe-12Cr-1MoVW Steel in Thermally-Convective Lithium," Proc. of the Topical Conf. on Ferritic Alloys for Use in Nuclear Energy Technologies, Snowbird, Utah, June 19-23, 1983, 215-221 (1983).

[4.3] O. K. Chopra and D. L Smith, "Influence of Temperature and Lithium Purity on Corrosion of Ferrous Alloys in a Flowing Lithium Environment," International Conference on Fusion Reactor Materials-2, April 13-17, 1986, Chicago, IL.

[4.4] O. K. Chopra and D. L Smith, "Compatibility of Ferritic Steels in Forced Circulation Lithium and Pb-17Li Systems," Journal of Nuclear Materials, (1988).

[4.5] O. K. Chopra and A. B. Hull, "Influence of Carbon and Nitrogen on Corrosion of Structural Materials in Flowing Lithium," ANS 8th Topical Meeting on the Technology of Fusion Energy, October 9-13, 1988, Salt Lake City, UT.

[4.6] G. A. Plekhanov and G. P. Fedortsov-Lutikov, "Corrosion of 12% Chromium Steel in a Nonisothermal Lithium Flow," Atomnaya Energiya, 45 (1978) 140-43.

[4.7] M.G. Barker and S.A Frankham, "The Effect of Carbon and Nitrogen in the Corrosion Resistance of Type 316 Stainless Steel to Liquid Lithium," Journal of Nuclear Materials, 107 (1982) 218-221.

[4.8] H.W. Leavenworth and R.E. Cleary, "The Solubility of Ni, Cr, Fe, Ti and Mo in Liquid Lithium," Acta Metallurgica , v.9, 519-520(1961).

[4.9] L.F. Epstein, "Static and Dynamic Corrosion and Mass Transfer in Liquid Metal Systems," Liquid Metal Technology -- Chemical Engineering Progress Symposium Series , No. 20, v.53 (1957)

[4.10] D. W. Osborne and H. E. Flotow, "Lithium Nitride (Li_3N): Heat Capacity from 5 to 350 K and Thermochemical Properties to 1086 K," Journal of Chemical Thermodynamics, 10 (1978) 675-682.

[4.11] R. M. Yonco, E. Veleckis and V. A. Maroni, "Solubility of Nitrogen in Liquid Lithium and Thermal Decomposition of Solid Li_3N," Journal of Nuclear Materials, 57 (1975) 317-24.

[4.12] E. E. Hoffman, "Solubility of Nitrogen and Oxygen in Lithium and Methods of Lithium Purification," Symposium on Newer Metals, Special Technical Publication No. 272, American Society for Testing Materials (1959).

[4.13] A. Saltelli, O. K. Chopra and K Natesan, "An Assessment of Carburization-Decarburization of Fe-9Cr-Mo Steels in a Sodium Environment," Journal of Nuclear Materials, 110 (1982) 1-10.

[4.14] S. Rajendran Pillai and C. K. Mathews, "Carbon Potential and Carbide Equilibrium in 18/8 Austenitic Steels," Journal of Nuclear Materials, 150 (1987) 31-41.

[4.15] R. J. Pulham and W. R. Watson, " Corrosion of 316 Steel by Lithium-Lead Alloys Under Nitrogen," Abstracts 14th Symposium on Fusion Nuclear Technology,8-12 September 1986, Avignon, France, (1986).

[4.16] M. G. Barker, P Hubberstey, A. T. Dadd and S. A. Frankham, "The Interaction of Chromium and Nitrogen Dissolved in Liquid Lithium," Journal of Nuclear Material, 114 (1982) 143-149.

[4.17] R. P. Elliot, Constitution of Binary Alloys, First Supplement, McGraw-Hill Book Company, New York (1975).

[4.18] O. K. Chopra, Private Communication, April 1988.

[4.19] M.A. Abdou et al., "A Study of the Issues and Experiments for Fusion Nuclear Technology," Fusion Technology , v.8, #3, 2595-2645 (1985).

[4.20] K. Fujimura, unpublished work (1988).

[4.21] W. M. Kays and M. E. Crawford, Convective Heat and Mass Transfer, Second Edition, McGraw-Hill Book Company. New York. (1980).

[4.22] E. M. Sparrow and J. L. Gregg, Transactions of the ASME, 78 (1956) 1823-1828.

[4.23] G. D. Raithby and K. G. T. Hollands, Journal of Heat Transfer, 98 (1976) 72-80.

[4.24] A. J. Ede, Advances in Heat Transfer, vol. 4, Academic Press, New York, (1967).

[4.25] R. L. Klueh, Private Communication, 1987.

[4.26] E. W. Hobart and R. G. Bjork, "Validity of Determining Carbon in Lithium by Measurement of Acetylene Evolved on Hydrolysis," Analytical Chemistry, 39 (1967) 202-205.

[4.27] M. W. Chase, Jr. et al., "JANAF Thermochemical Tables, Third Edition," Journal of Physical and Chemical Reference Data, v. 14, no. 1, (1985).

[4.28] R.M. Yonco and M.I. Homa, "The Solubility of Carbon in low Nitrogen Lithium," Journal of Nuclear Materials, 138 (1986) 117-122

[4.29] P.I. Fedorov and M.T. Su, "The Lithium Carbon System," Acta Chimica Sinica, 23 (1957) 30-39. (in Chinese)

[4.30] P. F. Tortorelli and J. H. DeVan, "Mass Transfer Deposits in Lithium-Type 316 Stainless Steel Systems," Proc. of the Second Int. Conf. on Liquid Metal Tech. in Energy Production, J. M. Dalke, ed., Richland, WA, April 20-24, 1980 , CONF-800401-P2 (1980).

[4.31] G.A. Whitlow, W.L. Wilson, W.E. Ray and M.G. Down, "Materials Behavior in Lithium Systems for Fusion Reactor Applications," Journal of Nuclear Materials , v.85 & 86 (1979) 282-287.

[4.32] P. F. Tortorelli and J. H. DeVan, "Effects of a Flowing Lithium Environment on the Surface Morphology and Composition of Austenitic Stainless Steel," Microstructural Science, 12 (1982) 213-226.

[4.33] R. L. Klueh, P. J. Masiasz and W. R Corwin, "Development of Ferritic Steels for Reactor Applications," Oak Ridge National Laboratory, ORNL-6472 (1988).

[4.34] N. M. Ghoniem, J. Blink and N. Hoffman, "Selection of Alloy Steel Type for Fusion Power Applications in the 350° - 500 °C Temperature Range," Proc. of the Topical Conf. on Ferritic Alloys for Use in Nuclear Energy Technologies, Snowbird, Utah, June 19-23, 1983 , (1983).

[4.35] N. M. Ghoniem, A. Shabiak and M. Z. Youseff, "Development of Low Activation Vanadium Steel For Fusion Application," Proc. of the Topical Conf. on Ferritic Alloys for Use in Nuclear Energy Technologies, Snowbird, Utah, June 19-23, 1983, (1983).

[4.36] L. S. Darken and E. R. Ryba, Report EPRI-AF-1176, The Pennsylvania State University (1979)

[4.37] M. Small, "Theoretical Analysis of Carbon Cluster Formation in Solid Iron-based Alloys: A Review of the Alex-Mclellan Mathematical Model," Pennsylvania State University, Interim report EPRI AP-1478 (1980).

CHAPTER 5 SUMMARY, CONCLUSIONS AND RECOMMENDATIONS

Summary

Experimental data on mass transport in lithium/12Cr-1MoVW steel were obtained from two thermal convection loops; one, GEB-1, operated from 360 to 505 °C for 3040 hours and the other, GEB-2, from 525 to 655 °C for 2510 hours. The experimental effort was supported by analysis of the mechanisms of mass transport. It was found that mass transfer and deposition, as measured by specimen weight change, were not simple functions of increasing temperature over the entire temperature range. Specimen surface morphologies and weight changes were closely related and indicative of several different mechanisms of corrosion. The weight changes and surface morphologies in GEB-1 were dominated by lithium impurity reactions of nitrogen and carbon. At higher temperature in GEB-2, surface morphologies and weight losses were controlled by elemental solubility of the steel (Fe, Cr and C) constituents in the lithium while, deposition was controlled by carbide precipitation.

Below 450 °C in GEB-1, the surfaces were roughened in appearance with surface depletion from 12 w/o to between 6 and 8 w/o chromium. The morphology, the reduction in chromium content, and weight losses were attributed to the removal of segregated chromium and/or metal carbides from the steel by the formation of the adherent, and insoluble in lithium, corrosion product, Li_9CrN_5. The resulting weight changes below 450 °C were small, within the

sensitivity limits of the experimental method, and were not strongly dependent on temperature due to the protective nature of the Li_9CrN_5 corrosion product layer, which inhibited diffusion transport.

Between 450-505 °C in GEB-1, carbon, which was only present at 0.2 w/o by weight in the steel and at less than 10 weight part per million in the lithium, was important in determining the weight change profiles. Carbon transfer via surface carburization by the formation of massive carbide (1 to 10 μm diameter) nodules dominated the mass transfer weight changes in the intermediate range of temperature causing significant weight gains even for the highest temperature specimens in the 360 to 505 °C experiment. Carbon, chromium and iron from the liquid phase combined to grow the nodules beginning at the grain boundaries, where the epitaxy of pre-existing carbides provide preferential sites for deposition. The number density and size of the carbide nodule increased with increasing temperature. However, carburization of the bulk of the alloy did not occur. The formation of these carbides was inhibited at lower temperatures due either to the presence of the protective Li_9CrN_5 corrosion product or competition between carbon and nitrogen for chromium.

In GEB-2, the activity of nitrogen in the lithium was insufficient to allow formation of the Li_9CrN_5 layer anywhere in the loop. As such, weight changes were a factor of 10 to 15 higher than in GEB-1. Chromium-rich carbide nodules similar to those found in GEB-1 were also found in the cooled leg (only) of the higher temperature experiment from 525 to 580 °C. However, the number density and

size increased with decreasing temperature. Iron-rich carbides were found only in the heated leg of GEB-2 on the first three specimens after the flow disturbance at the inlet to the heated leg. Some carburization of the near-surface bulk was observed on these iron-rich noduled surface specimens. Above 580 °C, the carbon activity in the liquid phase was insufficient to support surface carbide growth in both the heat and cooled legs of GEB-2. Weight changes were strongly dependent on temperature with an activation energy of 63.7 kJ/mole for corrosion. This activation energy was very close to the enthalpies of solution for both iron and chromium in lithium suggesting that, at these high temperatures, solubility-driven dissolution of the steel constituents was the dominant mechanism for weight losses. Deposition of the steel constituents was dominated by the carbides and was linear with respect to inverse temperature with a slope of 42000 K^{-1}. Elemental and/or alloy deposition was not found in either GEB-2 or GEB-1. Only deposits in the form of metal carbides ($M_{23}C_6$) were found, suggesting that carbon and chromium control the deposition mechanism.

Weight changes in this work were consistent with other data and were significantly lower than the "corrosion rates" adopted in recent blanket design studies. The results from the experiments have been used to develop physical models of the mechanisms of corrosion in these systems and to make recommendations for the development of a ferritic alloy for application in fusion reactors which is more resistant to attack by lithium.

5.2 Conclusions

1) Compatibility considerations do not simply place an upper limit on operating temperature. It is the activity of impurities, in particular nitrogen and carbon, in the lithium along with temperature which should be considered restrictive. Since deposition of activated alloy components is considered a limiting process for use of an alloy in fusion systems, it will be necessary to prevent the precipitation of carbides in systems operating at above 500 °C by maintaining carbon below 1 wppm.

2) Release of carbon at low temperature from the steel can be induced by the competition of carbon and nitrogen for chromium in the steel via the reaction:

$$5\ X\ Li_3N_{(in\ Li)} + Cr_X\ Fe_{(23-X)}\ C_{6\,(on\ \alpha\text{-}Fe)} \Longleftrightarrow$$

$$X\ Li_9CrN_{5\ (on\ steel)} + 3\ Li_2C_{2\ (in\ Li)} + (23-X)\ Fe + 6X\ Li$$

The formation of surface carbides is preferred at low nitrogen activities, while the formation of Li_9CrN_5 is preferred at high nitrogen activities.

3) Deposition in both experiments was dominated by surface carburization in the form of $M_{23}C_6$ carbides. The effect of

carbon was most prominent in these experiments in the fusion-relevant temperature range between 450-505 °C in GEB-1 and 525-580 °C, in GEB-1 where metal carbides precipitate from the lithium. However, if nitrogen activities were increased the equilibrium of the above equation could be forced such that metal carbides could not precipitate in GEB-1. However, chromium was probably the limiting constituent for deposition in GEB-2.

4) The formation of the adherent, insoluble Li_9CrN_5 surface layer in GEB-1 limited mass transfer by forming a protective layer. By comparison, the boundary layer and surface reaction mass transfer coefficients were estimated to be much larger and therefore not controlling, as compared to solid state diffusion through the Li_9CrN_5 surface layer. Formation of the layer may actually be advantageous in controlling mass transfer. The specimen cleaning methodology employed in most corrosion experiments (washing of specimens in alcohol and/or water) removes the protective layer from the steel surfaces and leads to larger corrosion rates than would be observed in a reactor where the corrosion product were left undisturbed. Distillation of residual lithium or single exposure of specimens would give more accurate determinations of the corrosion rates indicative of surfaces with an undisturbed corrosion layer. However, steep velocity gradients or unsteady velocity profiles such as might be encountered in liquid metal flowing in large magnetic

field (MHD) may shear and spall the protective corrosion product layer from the surface and corrosion rates could actually be higher than those measured in non-magnetic corrosion experiments.

5.3 Recommendations

1) Currently, lithium sampling and subsequent wet chemical analysis is the only technique for determining nitrogen and carbon in lithium. The development of on-line (in-situ) monitoring systems for the activities carbon and nitrogen (carbon and nitrogen meters) in lithium will be needed for safe, reliable long-term operation of lithium cooled fusion blankets and should be considered along with the development of alloys for service in lithium.

2) Further work is needed to characterize the thermodynamics of the ferritic steels which may be developed. In particular, data for carbon activity as a function of alloy composition and temperature are needed in order to have any predictive capability for transport of carbon in both the steel and the lithium.

3) Indepth physical characterization of the Li_9CrN_5 corrosion product is needed to determine if it can be used as a protective coating for reducing mass transport.

4) In order to develop an alloy for successful application in lithium for fusion reactors it will be necessary to alter the composition of alloys to meet the specific needs of fusion. In particular, induced radioactivity can be significantly reduced by removing niobium and molybdenum from the steels. Further, by reducing chromium to a level (6 to 8 w/o) where the protective

Li_9CrN_5 layer can still form and subsequently substituting stronger carbide forming and carbon clustering elements (titanium 2 - 3 w/o and vanadium 1 - 2 w/o) for chromium to reduce the effects of formation of Li_9CrN_5 on carbon activity of the steel may lead to an alloy with suitable mechanical, radiological, irradiation and lithium compatibility properties for use in lithium above 500 °C.

APPENDIX A REVIEW OF THE LITERATURE PRIOR TO 1979

A.1 Work Prior to 1960

Pure iron was reported as preferable to ferrous alloys below 600 °C by Burton, et al. [A.3] (as cited by DeVan [A.1] and Miller [A.2]). This would be true for short duration exposure experiments with very low carbon steels when contamination of the lithium melt is of paramount concern. The relatively high solubilities of other alloying elements (e.g., nickel for austenitic stainless steels) compared to iron causes preferential leaching (i.e., removal of the alloying components at a faster rate than the bulk iron material) and contaminates the lithium. However, iron with fractional amounts of carbon is prone to intergranular penetration by lithium due to unstable carbides (Fe_3C) which exist at the grain boundaries after heat treatment. Pure iron is soft and would not be suitable structural material. For longer duration applications (> 100 hours), pure iron could not maintain structural integrity [A.4]. For example, early testing of ferrous alloy (AISI 1010) carbon steel in a thermal convection loop failed due to intergranular penetration in less than 50 hours at 593 °C [A.4].

Anderson and Stephen [A.5] used variably air-contaminated lithium in agitated and static capsule tests to study the attack of iron, and types 304, 309, 310, 316, 321, 347 and 446 stainless steels in lithium between 482 and 1204 °C for periods up to 100 hours. Intergranular penetration was observed in these alloys up to 732 °C, but not at 816 °C and higher where the carbide phase would dissolve.

Coarse grained material was more resistant to attack than fine grained material. Wilkinson and Yagee [A.6] reported low-carbon iron and steel were more resistant to attack at 600 °C for up to 140 hours than low-carbon, high-chromium steels. Ordinary 304 SS and high-carbon, high-chromium steels were somewhat less resistant than these others to similar attack by lithium.

Cunningham [A.8], in iron crucible capsule tests with various alloys and metallic elements at 600, 800 and 1000 °C, reported significant concentration gradient mass transfer as well as intergranular penetration in test periods up to 400 hours. It is evident in light of these and other results, that carbon and metal carbides in the steel must play a significant role in the corrosion processes of lithium/steel systems.

Elrod et al. [A.9] investigated corrosion in forced convection lithium loops at temperatures up to 871 °C and exposure times up to 1000 hours. Seven "isothermal" (ΔT = 10 °C; v = 6-18 m/s) and one thermal gradient loop (T_{max} = 871 °C; T_{min} = 643 °C) were operated. The "isothermal" loops plugged after 369 and 550 hours of operation at 871 °C, while the thermal gradient loop plugged in less than 250 hours. Dana et al. [A.10] as cited by DeVan [A.1], measured weight changes in 310 SS for nearly isothermal conditions at 524, 760, 816, 871 and 874 °C, at velocities between 7.5 and 15.5 m/s. The weight change of the 816 °C sample was -8.2 %, for the 871 °C, -0.7 %, and the 874 °C sample changed -8.6 %. Analysis of the lithium showed great variation in the lithium chemistry used in the experimental runs.

Dana et al. [A.11] in another series of experiments, measured deposition rates in 310 SS. They observed initial deposition rates two to three times larger than later in the test sequence. Additionally, a thick porous ferrite layer had formed on the surface of the hot leg where material had been lost. The formation of a ferrite layer on lithium corroded surfaces is characteristic of austenitic stainless steels. The initial stage of large weight loss (and corresponding high deposition rates) in austenitic stainless steels corresponds to the formation of this ferrite layer from preferential leaching of nickel and, to a less extent, chromium from the surface due to higher solubilities and diffusivities as compared to iron. Depletion of nickel causes the austenite phase to transform to ferrite at nickel concentration below about 8 w/o. Typical ferrite layers on austenitic steels exposed to lithium contain less that 2 w/o nickel. The nature of the porosity is complicated and still not well understood even some 30 years later.

Brush [A.12] established that lithium is more corrosive than sodium. High nickel content austenitic stainless steels and high-chromium/high-carbon ferritic steels are more vulnerable to attack by lithium. McKee [A.13] showed the importance of nitrogen as an impurity in lithium to the corrosion and mass transport of 316 SS. Static capsule tests at 871 °C established that nitrogen is easily transferred to the lithium in a short time (< 100 hours). In TCL experiments between 593 °C and 871 °C (35 mm/s), McKee [A.13] found that an increase in nitrogen content of lithium from 125 to 370 wppm gave rise to a 42% increase in mass transport.

Correspondingly, a reduction to 20 wppm nitrogen via titanium and zirconium gettering reduced the mass transport by 28% from that in the 125 wppm run. Analysis of the lithium cut from the center of the tube showed the nitrogen concentration highest near the walls and decreasing radially inward. This was the first evidence of the importance of nitrogen in corrosion behavior in lithium.

Earlier work by Parkinson [A.14], and later by Parkinson and Sisman [A.15], found no effect of irradiation up to 910 °C and 160 hours on the corrosion rate of stainless steels in lithium. There is apparently no strong synergism between irradiation and liquid metal corrosion. However, long term irradiation may cause changes in grain boundary chemistry which may significantly affect the corrosion behavior of steel in liquid lithium.

One of the most extensive investigations in general lithium compatibility with materials was completed, in 1959, by Hoffman [A.16], at Oak Ridge National Laboratory (ORNL). The compatibility of various materials (rare metals, alloys, ceramics) with lithium was evaluated in static and agitated capsule tests and thermal convection loops at temperatures between 538 °C and 1000 °C for up to 3000 hours of exposure. However, it is difficult to summarize concisely the results of this extensive, largely experimental program. The following observations can be made:

1. Mass transport of chromium around the loop seems to be associated with carbon.

2. Grain boundary and mass transport data at high temperatures varied from loop to loop and are inconsistent.

3. All austenitic steel examined exhibited formation of a ferrite layer.

4. Data for 316 SS weight loss in hot leg were well-fit by log (weight loss) = A+B/T, suggesting a chemically controlled process

5. Elimination of a diffusion cold trap from a loop experiment increased corrosion rates by a factor of five.

6. Increasing flow velocity increased corrosion and mass transport.

The processes by which a liquid metal can interact with, or corrode, a material were outlined by Manly [A.17] as:

1) Simple dissolution
2) Interalloying between liquid and solid metal
3) Intergranular penetration
4) Impurity (solid or liquid) chemical reactions
5) Temperature gradient mass transfer (TGMT)
6) Concentration gradient mass transfer (CGMT)

Simple dissolution is a solubility phenomenon: the solid material is dissolved by the liquid metal. Interalloying is the combination of lithium alloy components to form a separate, distinct phase. Intergranular penetration occurs when the liquid metal penetrates the solid along grain boundaries into the bulk material. The intrusion can be the result of surface tension and/or chemical reactions and has a profound effect on the mechanical properties of the material by providing crack initiating points on the surface of the steel. Impurities in the solid or liquid, such as carbon and nitrogen for lithium/ferrous alloy systems, can affect the corrosion of solid metals by liquid metals by the formation of corrosion products and other chemical compounds. This effect may be either thermodynamic, by changing the chemical activity of the system, or kinetic (catalytic), by changing the reaction rates, or both. Temperature and concentration gradient mass transfer occur because the chemical potential of the phase is a function of temperature and composition.

Some of the results of an extensive experimental program at Pratt and Whitney Aircraft Company (PWAC) for austenitic steel in lithium can be found in Bunker [A.18] and Shaw et al. [A.19-21]. This program is significant because of the wide range of parameters investigated and the analysis of deposited material. However, as DeVan [A.1] indicates, the data are quite inconsistent, probably because of the number of variations in the experimental parameters in the loop systems during operation.

Results of Soviet experiments in lithium corrosion and material compatibility began to appear in the open literature in about 1958. Lyashenko et al. [A.22] discussed the resistance of materials to both sodium and lithium. Changes in material mechanical properties were used to evaluate the extent of corrosion. Corrosion and mass transport were not due to the "inherent" solubility of the alloy constituents in the liquid metal. It was concluded that impurities in lithium, sodium, nitrogen and oxygen, respectively, were to blame for the corrosion behavior. Improved corrosion resistance was obtained by adding niobium and tungsten to the steel alloys.

The 1950's brought about a great deal of understanding to the field of lithium corrosion. Weight loss and compositional analysis of corrosion samples was begun. Many alloys had been screened and effects of alloy composition had been established. The importance of impurities both in the lithium and in the alloy were recognized by most investigators in the field. Velocity effects were established. The following 20 year period saw refinement of these early results and the beginning of analytical and mechanistic approaches to understanding the results of experiments with more concern for impurity effects.

A.2 Corrosion Experiments Between 1960 and 1979

While work in the 1950's was driven by ANP applications, many liquid metal corrosion studies in the 1960's and 1970's were motivated by the fast breeder fission reactor and MHD energy conversion programs. The ANP related programs had been concerned with characterizing the corrosion over short intervals at relatively

high temperatures. The prospect of large-scale energy systems meant longer lifetime requirements at lower average temperatures. Austenitic stainless steels were of primary interest because of their fabricability and thus the bulk of the research was aimed at austenitic steel systems.

Gill et al. [A.23-24] conducted FCL experiments in lithium with 304SS. Both flat and circular exposure geometries were used and inserted in both the hot and cold legs of the loops. Temperatures between 421 and 612 °C, 10 °C < ΔT < 212 °C, and velocities up to about 90 cm/s were investigated at a nitrogen concentration of 600 wppm for periods up to 100 hours. Dissolution in the hot leg was found to be independent of ΔT and velocity, thereby indicating a solid-phase or interface controlled process. Deposition in the cold leg was found to be linear in Reynold's number to the 0.8 power indicating boundary layer diffusion control of the mass transport.

Seebold et al. [A.25] filled 304 SS tubes with pure and air-contaminated lithium and observed mass transfer due to thermal convection between 815 °C and 427 °C. Slight mass transfer was reported for "pure" lithium (less than 10 wppm nitrogen and 100 wppm oxygen) for 720 hours. Large mass transfer rates were recorded in just 72 hours with 0.36 w/o air-contamination of the lithium. All mass transfer deposits were found in the region between 426 °C and 537 °C. This was not the coldest temperature in the system. Analysis of the air-contaminated lithium showed it had between 12 w/o and 25 w/o chromium dissolved in it, while the

deposited material was low in chromium as compared to the original alloy.

Solubility of steel alloy components and the effects of impurities in the lithium on solubilities were studied by Bychkov [A.26], Beskorovaynyy et al. [A.27], Minushkin [A.28,29], Strauss et al [A.30], and Leavenworth and Cleary [A.31]. Bychkov [A.26] indicated that oxygen and nitrogen increased the solubility of nickel and chromium, but had little effect on iron. Beskorovaynyy et al. [A.27] found that corrosion and the solubility of iron-chromium alloys were increased by additions of sulfur and phosphorus. Minushkin performed solubility experiments on 304 SS and other materials at 871 °C with additions of titanium, barium, aluminum, tantalum, nitrogen , oxygen chlorine, and phosphorus. Additions of nitrogen, oxygen and titanium increased the solution rates while phosphorus and chlorine had no effect. Stirring of the samples greatly increased the solution rate. Anthrop's [A.32] review gives a good summary of the solubility work up to about 1967. The data of Leavenworth and Cleary [A.31] are generally accepted as being the most accurate and complete. The data of Leavenworth and Cleary were adopted for use in this work.

Work in lithium compatibility with carbon steels by Popovich [A.33,34] showed that penetration was worse at intermediate temperatures (< 700 °C) than at high temperatures. Carbon-lithium liquid solution is formed by lithium intruding along the carbon rich pearlite grain boundaries, which eventually saturates and a lithium carbon compound is formed. The corrosion product has a larger

specific volume than the cementite and the increase in local volume causes cracking along the grain boundaries. At temperatures above 725 °C, the carbon goes into solution with the steel and no longer resides at the penetrated grain boundaries.

Capsule compatibility tests by Slatter and Howat [A.35] for lithium and uranium carbide were performed in 304 SS containers. General dissolution of the steel began at about 900 °C along with growth of chromium-rich nodules on the uranium carbide pellets. Lithium nitride was thought to promote the attack by releasing carbon from uranium monocarbide and then forming a uranium-carbon-nitrogen mixture. Elimination of nitrogen from the system was postulated as a method for reducing the attack.

Shatinskii and Goikam [A.36] and Shatinskii and Zbozhnaya [A.37] investigated the role of carbon on the corrosion of a titanium stabilized high chromium (18Cr-9Ni) stainless steel. The weight loss was found to obey a log (wt. loss) = A-B/T relation similar to Hoffman's [A.16] earlier data, indicating a solid phase or interfacial chemical reaction controlled process. It was concluded that precipitation of carbides intensifies corrosion in austenitic steels and that no heat treatment can improve the corrosion resistance in the range of 500-700 °C because of the precipitation of carbides. Low carbon content steels were seen as the only recourse. Later, Shatinskii and Zbozhnaya [A.38] experimented with beryllium coatings for steels with limited success. The Fe-Be coating was found acceptable for short duration exposures (< 500 hours) at 900 °C.

Although much of this early work was fragmented and incomplete, it provided a strong experience base for lithium compatibility research in the 1960's and 1970's.

A good summary and an annotated bibliography of the literature on lithium interaction with ferrous alloys is given by DeVan et al. [A.1].

A.3 Liquid Metal Corrosion Models

Epstein [A.39] formulated a method for modeling mass transport in liquid metal systems and compared the analytical predictions with experimental data. Models for both static capsule and dynamic flow systems were developed. In the model formulation, liquid metal/containment alloy systems were divided into diffusion-limited (e.g., Hg/Fe) and rate-limited (e.g. Fe/Na) categories. Mass transport and corrosion in diffusion-limited loop systems are governed by the mass diffusion rate throughout the boundary layer adjacent to the solid/liquid interface (reaction step is fast compared to diffusion step). In a reaction-limited loop system, mass transport and corrosion are limited by the rate at which material is released into the boundary layer from the surface (diffusion step is fast compared to the reaction step). The models are developed in terms of a solution rate parameter, α, which characterizes each of the different systems. For the diffusion-limited system, α is a function of the diffusion coefficient and flow parameters (velocity, geometry). For the reaction-limited system, α is a function of temperature only. Mass transport in loop systems is described by,

$$\frac{dS}{dx} = \frac{4 \quad \alpha}{D_h \; V} \; (S^\circ - S)$$

where S is the local concentration in the fluid, S° is the solubility at the local temperature, α is the solution rate parameter for the system, D_h is the hydraulic diameter of the loop tubing, V is average velocity of the liquid metal, and x is the coordinate along the fluid flow path. Epstein derives an expression for the average corrosion rate in the hot leg of a diffusion-limited system as,

$$R_{T+\frac{\Delta T}{2}} = -0.023 \left(\frac{D_{LM}}{D_h}\right)\left(\frac{V \; D_h}{\nu}\right)^{0.8}\left(\frac{\nu}{D_{LM}}\right)^{0.4} \frac{dS^\circ}{dT} \Delta T$$

where $R_{T+\frac{\Delta T}{2}}$ is the corrosion rate, D_h is the loop hydraulic diameter, D_{LM} is the diffusion coefficient in the liquid metal, V is the bulk average velocity, ν is the viscosity of the liquid metal, S° is the solubility of the wall solute species in the liquid metal, and ΔT is the overall loop temperature differential. The corresponding average solution rate constant, α, is given by:

$$\alpha = \frac{R_{T+\frac{\Delta T}{2}}}{\left(\frac{dS^\circ}{dT}\right)_{T+\Delta T/2} \Delta T} \quad \left(\frac{V_L}{A_s}\right)$$

where V_L is the volume of the loop and A_S is the corroding surface area. The same differential equation describes the mass transport, but the solution rate parameter is a function of temperature only. The average corrosion rate for a reaction-limited loop system is given by:

$$R_{T+\frac{\Delta T}{2}} = -\frac{\alpha}{2}\ \frac{dS^\circ}{dT}\ \Delta T$$

where we note that the corrosion rate in a reaction-limited system is independent of the flow system geometry and configuration. Note also that the slope of the average corrosion rate, for either type of solution rate, versus temperature should have the same slope as the solubility curve, $\frac{dS^\circ}{dT}$, the enthalpy of solution. The models are used to predict the behavior in Na/Fe systems. Order-of-magnitude agreement is obtained for the average corrosion rate. Deposition was not modeled. Epstein incorporates the effects of impurities by changes in α . For example, Na/Fe systems are quite sensitive to oxygen concentration in the sodium. The corrosion rate is known to be a strong function of oxygen partial pressure. Epstein asserts that the expression for α is given by:

$$\alpha = \alpha_o + k\,p + \ldots$$

where α_o is the solution rate constant for the "inherent" solubility (no impurities), p is the partial pressure of oxygen dissolved in the sodium, and k is the impurity solubility of the reaction rate constant for the overall Na/O/Fe solubility reaction set. Hildebrand [A.40] also described a quantity similar to the inherent solubility which is a function of the fluid viscosity and the specific volume of the solute atoms. The inherent solubility is usually much smaller than that due to impurities [A.41]. Thus, the effects of impurities could be included in Epstein's model. This is demonstrated for Na/Fe system but no calculations or comparisons are made between analytical and experimental results. Epstein's models are simple and the basic methodology has been applied by many authors in various forms, with and without modifications [A.23, 24, 42], with varying degrees of success. The models for diffusion-limited solution rate parameters are usually taken from heat transfer analogies. The success relies on the validity of an assumed single controlling mechanism which characterizes the system as a whole and that the same mechanism is always the controlling process. Good solubility and diffusivity data, and luck, are also helpful. Epstein's model also ignores the solid phase transport (diffusion) and assumes that the solute remains in solution (no particulates), although he mentions their possible formation and existence.

Gill et al. [A.23] compared experimental results for mass transport and deposition in a forced convection loop experiment with flat-plate exposure coupons geometry. An integrated form of

Epstein's [A.39] model was used to make a qualitative comparison (scaling) of experimental data to determine the rate controlling mechanism for a lithium/304 SS system. Mass transfer (removal) in the hot zone was determined to be reaction-rate controlled (612-510 °C), while deposition was deemed diffusion-rate controlled (490-328 °C). Later investigations in circular cross sectional conduits [A.24] in the same loop indicated the controlling mechanism in the hot and cold zones may change as a function of temperature. These data supported previous findings on flat coupons [A.23].

Brush [A.43] analytically and experimentally investigated mass removal in sodium/316 SS systems. Brush's experimental data consisted of microprobe concentration profiles in the solid material from coupons exposed to flowing sodium. Brush split the species mass fluxes into selective and non-selective components with the total being the sum of the two. The selective component of mass flux is transient. The non-selective component is the steady-state component and corresponds to stoichiometric corrosion. At steady-state, the selective component of all species vanishes. Further, solid species were categorized as being active noble or neutral, depending on the relative magnitude of their selective and non-selective mass fluxes. A species was said to be active if its selective mass flux was larger than the eventual steady-state species mass flux. A noble component's selective mass flux is less than the eventual steady-state species mass flux. A neutral species always corrodes at its steady-state mass flux. Brush's analytical work was primarily in modeling the solid phase. A closed form, semi-infinite solid moving

boundary model for diffusion in the solid was evaluated. Brush can be credited with defining the term "stoichiometric corrosion" which refers to the steady-state mass flux in a multi-component solid/liquid metal system. The onset of steady-state or stoichiometric corrosion is defined as when the ratio of mass fluxes of the constituents across the solid/liquid interface is the same as their concentration ratios in the bulk solid material. This also corresponds to a linear total mass loss rate from the material. The model allowed estimates of the diffusion coefficient to be made from the concentration profile data. Agreement between the analytical local and the experimental averaged corrosion rates was good for most of the data. The inability of the microprobe to accurately resolve the concentration profile near the sample surface made complete agreement difficult and dependent on a data extrapolation technique. Brush's model is a local model of the solid paths and boundary regions. The effects of loop geometry are not included.

Evans et al. [A.44,45] investigated analytical modeling of sodium/nickel-based alloys and molten salts/Hastelloy systems. A quasi-steady-state analysis of the mass transfer from the solid was performed. The solid was modeled as semi-infinite. The bulk concentration around the loop was assumed to be constant with position and time. The driving force for mass transfer to the liquid was the change in saturation concentration at the wall as a function of temperature along the flow path length. Agreement for the molten salt/Hastelloy system was good where the reactions and chemical information are well characterized. Results from the same

model applied to sodium/Inconel were in error by more than a factor of 70. The discrepancy was blamed on lack of good diffusion coefficient data and chemical information.

Weeks and Isaacs [A.46] developed an empirical model (correlation) for corrosion in sodium/stainless steel based on experimental observations and qualitative analytical formalism. The model reflects the catalysis effect of oxygen in sodium corrosion and can be taken as a statement of the chemical behavior of the sodium/316 SS system. Transport and diffusive processes are not included in the model. Their corrosion rate, R [mils/year], was expressed as,

$$R = \frac{7.93 \times 10^{11}}{X_{Fe}} \frac{[O]^{2x_{Fe}}}{[O]_{sat}} \exp\left(\frac{-50300}{RT}\right)\left(1 - \varepsilon \left(\frac{L}{D}\right)^2\right)$$

where X_{Fe} and $[O]_{sat}$ are the saturation concentration of iron and oxygen in sodium, and [O] is the actual concentration of oxygen in the system. The "downstream effect" (L/D dependence) included in the model is a chemical poisoning effect of the "active corrosion" sites on the surface of the alloy and not a boundary layer approach to saturation that would result from a mass transport model. The correlation (model) agrees well with most of the available data for sodium with velocities above 4 m/s and oxygen concentrations greater than 3 wppm for temperatures up to about 650 °C. The model does not (cannot) predict the transition from a diffusion to a

reaction rate controlled system. Neither deposition nor particulate forms are included in the model.

DeVan and Bagnall [A.47] suggest that it may not be possible to obtain a model/correlation for lithium/ferrous alloy systems such as Weeks and Isaacs obtained for sodium/ferrous alloys because, at present, the system parameters affecting the corrosion process in the temperature range of interest to fusion are less well understood. They note that for sodium in the temperature range applicable to LMFBR's, corrosion of ferrous alloys is only a function of three principal variables (temperature, oxygen content of the sodium, and velocity). Lithium corrosion, on the other hand, is a function of temperature, temperature gradient, nitrogen content, velocity, and system geometry and configuration. Thus, it is difficult to collapse all of the data into a single relation which can be expected to predict the corrosion behavior very well over a large parameter range.

Olander [A.48] presents an excellent analytical formulation of the general mass transport by diffusion only in sodium and stainless steel systems. In the development of the methodology, it is shown that errors of two to three orders of magnitude in the corrosion rate can be made if only either the hot or cold leg region is modeled. The general method is presented but no attempt is made to use the model to predict system mass transfer behavior.

Roy and Schad [A.49], and Schad [A.50], showed that velocity effects for sodium mass transfer could be correlated to turbulent velocity boundary layer thickness. Schad's later work [A.51-53] is the most extensive computational effort in diffusional mass transport

modeling in liquid sodium. The mass diffusion equations in the solid and liquid were solved together. The solid was modeled as a receding boundary, semi-infinite solid and the combined diffusion convection in the liquid sodium was modeled. The model assumed that the interface between the solid and liquid was saturated at the local temperature (diffusion controlled model). The kinetics of the surface reaction were not included. In these works, Schad modeled mass removal (corrosion) only and did not model deposition or particulate behavior. Transient surface recession rates and solid phase constituent concentration profiles were modeled ignoring chemical reaction rates. Comparison is made between model prediction and microprobe data collected for a rotating disk experiment for 316 SS in sodium [A.52] as well as predictions for mass transport from a LMFBR fuel rod assembly. Numerically predicted mass loss rates for the rotating disk experiment were two orders-of-magnitude higher than the measured corrosion rate. The model results were shown to be sensitive to diffusivity and solubility data input. It was necessary to divide the available chromium solubility relation by 100 to obtain agreement between the model and attain overall total mass loss. The predicted chromium spatial distributions did not agree with available microprobe data. Schad's work is significant as the first computationally intensive study of the mass transport problem in liquid metals.

Clement [A.54-55] and Clement and Hawtin [A.41] qualitatively developed a general methodology for describing mass transport in liquid circuits. The equations are derived from transport of a single

species and are similar to Epstein [A.39]. In this model, the effects of solid phase processes, surface reactions, liquid phase diffusion and transport, and particulate dynamics are separately considered. The system of equations are not solved, evaluated or integrated into a single system model of mass transport. The model parameters are used to qualitatively describe the observed behavior in sodium systems. Correlations for use in heat transfer analogies of the mass transfer are suggested. The effects of a mixed corrosion product scale and base metal surface are qualitatively described. It is concluded that particulate effects will be most pronounced in systems with large residence times as compared to particulate growth rate time constants. Clement mentions that more accurate information (diffusivities, solubilities) is required in order to properly evaluate the models for mass transport of any system.

Bauer [A.42] sought to model the mass transport results of his FCL experiment in a lithium/316 SS system using Epstein's model [A.39]. Calculated mass fluxes were between 5 and 15 times higher than those measured in the experiment. Mass transfer coefficients based on heat transfer analogies and experimentally measured values in the hot leg section were both used in the modeling. Simple solubility relations were used to describe the chemical release of material from the surface assuming the interface was saturated at the local temperature. The discrepancy between the calculated and measured results could not be reasonably resolved on the basis of surface reaction kinetics, particulate behavior or errors in solubility data. However, based on Clement and Hawtin's analyses [A.41],

Bauer's apparatus would tend to mask particulate effects in the test sections.

Bjorndahl and Gordon [A.56] developed a computer model for mass transport with lithium-lead/HT9 in the MARS reactor design configuration. The model was similar to that of Epstein [A.39], but included a radioactive decay term in the material balance because determination of the radioactive component activation was of primary interest. The radioactive decay term was proportional to the local concentration and was considered a loss term in the analysis. The model is best summarized by the following equations:

$$\frac{dS}{dx} - \left(\frac{4\ \alpha}{D_h\ V}\right)(S^\circ - S) + \left(\frac{\lambda}{V}\right)S = 0$$

Epstein's Transport Terms Radioactive Decay

λ = Radioactive Decay Constant [A.1/s]

Mass transfer coefficients were based on heat transfer analogies for calculations of the solution rate parameters (diffusion controlled) α. No data were available for comparison.

Klein and Vogelsang [A.57-58] produced a more extensive model for radioactive transport in many different reactor systems. Mass transport and deposition rates were taken from experimental data (mass flux) for corrosion or deposition. If necessary, mass transfer coefficients were taken from heat transfer analogies or experimental data where available. The calculation of radioactive dose rate due to deposition of activated corrosion products was of

primary interest rather than the modeling of mass transport release mechanisms. Radioactive decay loss components were also included, similar to [A.56]. No data were available for comparison.

Malang [A.59], and Malang and Smith [A.60] developed a mass transfer model based on boundary layer diffusion. The effect of velocity profile (laminar, turbulent, MHD boundary layer thinning) on the mass transfer rate in a circular cross-sectional duct for lithium-lead and HT9 systems was evaluated. The mass diffusion equation was solved with a variety of assumed velocity profiles. Solubility data for lead was used to model material release. The solid/liquid interface was assumed saturated at the local temperature. Diffusion in the solid, chemical reactions and particulate behavior were not considered. The mass transfer coefficient was seen to increase in order of laminar, MHD (Hartmann) and turbulent velocity profiles. Comparison is made between the model and the ANL experiment in lithium-lead. Order of magnitude agreement is obtained, although the modeled geometry did not agree with the experimental apparatus and only mass release was modeled. Similar modeling was performed by Bjorndahl and Gordon for [A.56].

A model similar to Malang's was reported by Abdou, et al. [A.61], for lithium/austenitic systems. Results were presented which showed the mass transfer rate increasing as a function of Hartmann number up to a critical value beyond which no more increase in mass transfer was observed due to MHD thinning of the velocity boundary layer. The interaction of a magnetic field with a perpendicularly

flowing fluid causes a body force which augments the velocity profiles from those in regular laminar flow. The Hartmann number is the dimensionless ratio of magnetic to viscous forces in the flow of a conducting fluid in the presence of a magnetic field. The critical value of the Hartmann number is dependent on the Schmidt number of the fluid (viscosity/diffusion coefficient). Predicted corrosion rates were 50 to 100 times larger than those measured in experiments. However, only the mass release in the hot leg was modeled and loop effects, such as mentioned by Olander [A.48], would tend to reduce this error.

A.4 References for Appendix A

[A.1] J.H. DeVan, J.E. Selle, and A.E. Morris, A Review of Lithium Iron-based Alloy Corrosion Studies," ORNL/TM-4927 (1976).

[A.2] E.C. Miller, "Corrosion of Materials by Liquid Metals, Liquid Metals Handbook, Second Edition, Lyon, R.N., Ed. (1952).

[A.3] W.N. Burton, S.W. Coffman and C.L. Randolph, A Compendium of Information Concerning Lithium, RTM-57, Aerojet Engineering Corp. (Classified) (1949).

[A.4] R.B. Day and A.D. Brasunas, Testing and Examination of Thermal Convection Loops Operated with Lithium and Lead," Y-F31-4 (1951).

[A.5] R. Anderson and H. Stephen, Progress Report on Materials Tested in Lithium, NEPA-1652 (1950).

[A.6] W.D. Wilkinson and F.L. Yagee, Attack of Metals by Lithium, ANL-4990, Argonne National Laboratory (1950).

[A.7] D.S. Jessman et al., Preliminary Investigations of Metallic Elements in Molten Lithium, NEPA-1465 (1950).

[A.8] J.E. Cunningham, Resistance of Metallic Materials to Corrosion Attack by High Temperature Lithium, CF-51-7-135 (1951).

[A.9] H.G. Elrod Jr., R.R. Fouse and P.B.Richards, Erosion and Heat Transfer with Molten Lithium, NEPA-1837 (1951).

[A.10] A.W. Dana Jr. et al., Erosion and Corrosion Studies of Liquid Metal Systems: Investigations of Constant Temperature, Forced Circulation Liquid Lithium Systems, Tech Report III, B&W Rep. 5228, DC-52-5-19 (1952).

[A.11] A.W. Dana Jr., O.H. Baker and M. Ferguson, Investigations of Large Scale Dynamic Liquid Lithium Corrosion Apparatus, Tech. Rep.IV, B&W Rep. 5229, DC-52-25-66 (1952).

[A.12] E.G. Brush, Corrosion Resistance of Ferritic and Austenitic Steels in Lithium at 500 °C, KAPL-5239

[A.13] J.M. McKee, Effect of Nitrogen on Corrosion by Lithium, NDA-40, (1957).

[A.14] W.W. Parkinson Jr., Stability of Iron Toward Lithium at Elevated Temperature Under Cyclotron Radiation, NAA-SR-73, (1952).

[A.15] W.W. Parkinson Jr. and O. Sisman, Liquid Metal Loops Irradiated in the ORNL Graphite Reactor and the LITR, ORNL-2630, (1959).

[A.16] E.E. Hoffman, Corrosion of Materials by Lithium at Elevated Temperatures, ORNL-2674 (1959).

[A.17] W.D. Manly, "Fundamentals of Liquid Metal Corrosion," Corrosion , v.12, #.7, (1956) 46-52.

[A.18] C.E. Bunker, Test Results of Lithium Mass Transfer Loop LPL-1, TIM-405 (1957).

[A.19] R.C. Shaw and G.E. Coyle, Type 316 Stainless Steel Forced Convection Lithium Corrosion Loop Test LSSA-1A1, TIM-434 (1958).

[A.20] R.C. Shaw, Type 316 Stainless Steel Forced Convection Lithium Corrosion Loop Test LSSA-3B1," TIM-465 (1958).

[A.21] R.C. Shaw, Type 316 Stainless Steel Forced Convection Lithium Corrosion Loop Test LSSA-4A2, TIM-466(1958).

[A.22] V.K. Lyashenko et al., "On the Corrosion Resistance of Some Materials in Sodium and Lithium," Proceedings of the United Nations International Conference on Peaceful Uses of Atomic Energy, 2nd, Geneva, 1958 , v.7, United Nations Press, N.Y. (1958).

[A.23] W.N. Gill, R.P. Vanek, R.V. Jalinek and C.S. Grove Jr., "Mass Transfer in Liquid Lithium Systems," A.I.Ch.E.J., v.6, #1, (1960) 139-144.

[A.24] W.N. Gill, R.P. Vanek and C.S. Grove Jr., "Mass Transfer with Liquid Lithium in Circular Conduits," A.I.Ch.E.J., v.7, #2, (1961) 216-220.

[A.25] R.E. Seebold, L.S. Birks and E.J. Brooks, "Selective Removal of Chromium from Type 304 Stainless Steel by Air-Contaminated Lithium," Corrosion , 16 (1960) 140-142.

[A.26] Y.F. Bychkov et al., "Corrosion Resistance of TA-1-T (Cr-Ni) Stainless Steel in Lithium with Oxygen and Nitrogen Impurities," Metallurgy and Metallography of Pure Metals , Yemel'yanov, V.S. and Yevstyukhin, A.I., Eds., Atomizdat, Moscow, 1960; English translation by Gordon and Breach, New York, (1962) 76-90.

[A.27] N.M. Beskoroaynyy and Y.I. Yakovlev, "Study of Corrosion of Iron and Chromium Steels in Liquid Lithium," Metallurgy and Metallography of Pure Metals , V.S.Yemel'yanov and A.I. Yevstyukhin, Eds., Atomizdat, Moscow, 1960; English translation by Gordon and Breach, New York, (1962) 190-210.

[A.28] B. Minushkin, Determination of the Solution Rates of Metals in Lithium, NDA-44(Del.) (1958).

[A.29] B. Minushkin, Solution Rates and Equilibrium Solubility of Nickel and Iron in Liquid Lithium, NDA-2141-1 (1961).

[A.30] S.W. Strauss, J.L.White and B.F.Brown, "The Atomic Size Effect and Alloying Behavior in Liquid Metals," Acta Metallurgica , 6 (1958) 604-606.

[A.31] H.W. Leavenworth and R.E. Cleary, "The Solubility of Ni, Cr, Fe, Ti and Mo in Liquid Lithium," Acta Metallurgica , 9 (1961) 519-520.

[A.32] E.F. Anthrop, The Solubility of Transition Metals in Liquid Alkali Metal and Alkaline Earth Metals, Lathanum and Cerium: A Critical Review of the Literature, UCRL-50315 (1967).

[A.33] V.V. Popovich et al., "Corrosion Resistance of Armco Iron in Liquid Lithium," Soviet Material Science, (English translation) v.3, #1 (1967).17-23

[A.34] V.V. Popovich, I.G. Shtyklo and M.I.Chaevski, "Effect of Lithium on the Mechanical Properties of Armco Iron," Soviet Material Science , (English translation), v.3, #2 (1967).

[A.35] D.L. Slatter and D.D. Howat, "Mass Transfer Effects in Stainless Steel-Liquid Lithium Uranium Carbide System," Journal of Iron and Steel Institute , (London), 208 (1970).282-288

[A.36] V.F. Shatinskii and M.S. Goikham, "Mechanism of Corrosion of Steel (1Kh18N9T) in Lithium Involving the Precipitation of Second Phases," Soviet Material Science , (English translation), v.7, #5 (1971) 718-721.

[A.37] V.F. Shatinskii and O.M. Zbozhanaya, "Saturation of (1Kh18N9T) Steel with Beryllium and the Corrosion Rate of the Coating in a Lithium Melt," Soviet Material Science , (English translation), v.8, #5 (1972) 59-61.

[A.38] O.M. Zbozhanaya and E.V. Borisov, "On the Redistribution of Main Components in (1Kh18N9T) Steel After Beryllium Plating and Testing in Lithium Flow," Soviet Material Science , (English translation), v.10, #3 (1974) 64-67.

[A.39] L.F. Epstein, "Static and Dynamic Corrosion and Mass Transfer in Liquid Metal Systems," Liquid Metal Technology--Chemical Engineering Progress Symposium Series , No. 20, v.53 (1957).

[A.40] J.H. Hildebrand, Solubility , Chemical Catalog Co., New York (1929).

[A.41] C.F. Clement and P. Hawtin, "The Corrosion of Steels in Liquid Sodium," Proc. Int. Conf. on Liquid Metal Technology in Energy Production , Cooper, M.H., Ed., CONF-760503-P1 (1976).

[A.42] D.G. Bauer, Kinetics of the Degradation of 316 Stainless Steel by Lithium, Ph.D. Thesis, University of Wisconsin-Madison (1980).

[A.43] E.G. Brush, Sodium Mass Transfer XVI: The Selective Corrosion Component of Steel Exposed to Flowing Sodium, GEAP-4832 (1965).

[A.44] R.B. Evans III and P. Nelson Jr., Corrosion in Polythermal Loop Systems, I. Mass Transfer Limited by Surface and Interface Resistances as Compared with Sodium Inconel Behavior, ORNL-4575, 1 (1971).

[A.45] R.B. Evans III, J.W. Kogar, and J.H. DeVan, Corrosion in Polythermal Loop Systems, II. A Solid-State Diffusion Mechanism With and Without Film Effects, ORNL-4575, 2 (1971).

[A.46] J.R. Weeks and J.W. Isaacs, "Corrosion and Deposition of Steels and Nickel-Based Alloys in Liquid Sodium," Advances in Corrosion Science and Technology ,M.G. Fontana and R.W. Straehle Eds., Plenum, 3 (1973) 1-66.

[A.47] J.H. DeVan and C. Bagnall, "A Perspective of the Corrosion Behavior of Lithium and Sodium," Liquid Metal Engineering and Technology , BNES, London, 3 (1985) 65-72.

[A.48] Olander, D.R., Fundamental Aspects of Nuclear Reactor Fuel Elements, NTIS (1976).

[A.49] P. Roy and M. Schad, "An Analysis of Corrosion of Steels by Liquid Sodium," Journal of Nuclear Materials , 47 (1973) 129-131.

[A.50] M. Schad, The Impact of Diffusion on Sodium Mass Transfer, MS Thesis, University of California, Santa Cruz (1972).

[A.51] M. Schad, "Corrosion of Austenitic Steel in Sodium," Material Behavior and Physical Chemistry in Liquid Metal Systems , Borgstedt, H.U., Ed., Plenum (1982).

[A.52] M. Schad, "Application of a Sodium Austenitic Corrosion Model to a Fuel Rod," Nuclear Technology , 50 (1980) 289-297.

[A.53] M. Schad, "To the Corrosion of Steel in Sodium Loops," Nuclear Technology , 50 (1980) 267-288.

[A.54] C.F. Clement, Theory of Mass Transport in Liquid Circuits, AERE-TP-606 (1975).

[A.55] C.F. Clement, Models for the Growth and Dissolution of Small Particles in Liquids, AERE-TP-605 (1974).

[A.56] W.D. Bjorndahl and J.D. Gordon, "MHD Effects on Liquid Metal Corrosion Product Transport," Proc. of ANS Annual Meeting, New Orleans (1983).

[A.57] A.C. Klein and W.F. Vogelsang, "Activation Product Transport in Fusion Reactors," Journal of Nuclear Materials, 122 & 123 (1984) 1236-1240.

[A.58] A.C. Klein and W.F. Vogelsang, "RAPTOR: A Computer Code to Calculate the Transport of Activation Products in Fusion Reactors," UWFDM-5671 (1984).

[A.59] S. Malang, "Influence of a Magnetic Field on Liquid Metal Corrosion," Proc. of the 13th Symposium of Fusion Technology, Varese, Italy (1984).

[A.60] S. Malang and D.L. Smith, "Modeling of Liquid Metal Corrosion/Deposition in a Fusion Reactor Blanket," ANL/FPP/TM-192, Argonne National Laboratory (1984).

[A.61] M.A. Abdou et al., "A Study of the Issues and Experiments for Fusion Nuclear Technology," Fusion Technology, 8, #3 (1985) 2595-2645.

APPENDIX B ELEMENTAL DISSOLUTION AND DEPOSITION MODELING OF MASS TRANSFER IN LITHIUM/Fe-Cr SYSTEMS

The solubilities of iron and chromium are very similar in magnitude and temperature dependence (see Figure 1.3 and Table 1.3). If we assume that the mass transfer behavior of iron-chromium alloys is governed by the solubility of iron and chromium in lithium, then at steady-state we can write the following equation for conservation of a generic metal constituent (Fe or Cr)

$$\frac{dM^{bulk}}{dx} = \frac{K^M(x)}{D_h(x)\ V_{bulk}(x)}\ (M^{sat} - M^{bulk})$$

where

M^{bulk} = Bulk mass fraction of metal species in liquid [1]

x = Axial coordinate [m]

M^{sat} = Saturation mass fraction of metal species in liquid [1]

$K^M(x)$ = Mass transfer coefficient based on mass fraction for species M as a function of x [m/s]

$$= \frac{1}{\left(\frac{1}{k_{bl}} + \frac{\delta}{D_{M\ scale}} + \frac{1}{k_r}\right)}$$

k_{bl} = Boundary layer mass transfer coefficient

$= \frac{D_M}{D_h} Nu_m(Gr_D, Sc)$ for free-convection (see Chapter 4) or $\backslash F(D_{M,liquid}, D_h)\ Nu_m(Re_D, Sc)$ for forced-convection

δ = Surface scale thickness [m] = 0

$D_{M,\ scale}$= Mass diffusivity of species M in scale [m^2/s]

k_r = Surface reaction mass transfer coefficient [m/s]

$D_{M,\ liquid}$= Mass diffusivity of species M in liquid [m^2/s]

$$= \frac{kT}{6\pi\mu R_a^i} \quad \text{(Stokes-Einstein model)}$$

k = Boltzmann's constant

μ = Dynamic viscosity [kg/m^2-s]

R_a^i = Atomic radius of species i (~ 1-2 x 10^{-10} m)

T = Absolute temperature [K]

Gr_D = Grashof number [1] $= \left(\frac{g\beta\Delta T D_h^3}{\nu^2}\right)$

Re_D = Reynolds number [1] $= \frac{V_{bulk} D_h}{\nu}$

Sc = Schmidt number [1] $= \frac{\nu}{D_M}$

ν = kinematic viscosity [m^2/s]

$D_h(x)$ = Hydraulic diameter of system as a function x [m]

$V_{bulk}(x)$= Bulk velocity of liquid as a function of x [m/s]

The experiments performed were in a rectangular loop configuration. The boundary condition for the above equation can be expressed in two different ways. The first reflects the fact that the two points x= 0 and x=L are the same material point and we write that

$$M^{bulk}(0) - M^{bulk}(L) = 0$$

or we can impose mass conservation as,

$$\int_0^L \frac{K^M(x)}{D_h(x)\ V_{bulk}(x)} (M^{sat} - M^{bulk})\, dx = 0$$

Equation B.1 was integrated to x=L with a stepwise fourth-order Runge-Kutta method assuming an initial guess, $M^{bulk,Guess,0}$, of the bulk concentration at x=0. A simplex technique [B.1] was used to adjust (determine) the concentration profile which gave the least error in either condition the continuity of concentration or the conservation of mass to a tolerance less than 10^{-6}. Once the resulting profile for $M^{bulk}(x)$ was known, then the mass flux of generic metal atoms was calculated from,

$$j_M = \rho_{Li}\, K^M(x)\, (\, M^{sat}(T) - M^{bulk}(x))$$

and the mass fluxes of the individual species could be related to their mass fraction in the bulk of the alloy as

$$j_{Cr} = X^{\circ}_{Cr}\, j_M$$

$$j_{Fe} = X^{\circ}_{Fe}\, j_M$$

where X°_{Cr} and X°_{Fe} are the mass fractions of chromium and iron in the bulk of the alloy, 0.12 and 0.85, respectively.

The results for such modeling for the experiments GEB-1 and GEB-2 are shown in Figures B.1 and B.2, respectively. It was

assumed that 1) there was no surface scale and 2) the surface reaction mass transfer coefficient was much larger than the boundary layer mass transfer coefficient and therefore boundary layer transport was controlling the mass transfer. The correlations given in chapter 4 were used to estimate the mass transfer coefficients at with Grashof number of 10^7. In general, the predictions from such models were larger, by more than two orders of magnitude, than the experimentally measured mass fluxes. Similar models for austenitic steel in both sodium and lithium have yielded similar results. The source of the error in such modeling is not apparent. However, from the experimental results, which showed that carbon controls the deposition of iron and chromium, we would not expect an elemental depositon model to correctly predict deposition behavior. The temperature dependence (63.7 kJ/mole) of the weight losses of the cobblestoned specimens in the heated leg of GEB-2 suggests that solubility may indeed be the controlling mechanism for mass release (corrosion) at these high temperatures. However, the magnitude of the transport properties (in particular, mass diffusivity) maybe in error or that the dissolution of an alloy may be different than the dissolution of the pure elements.

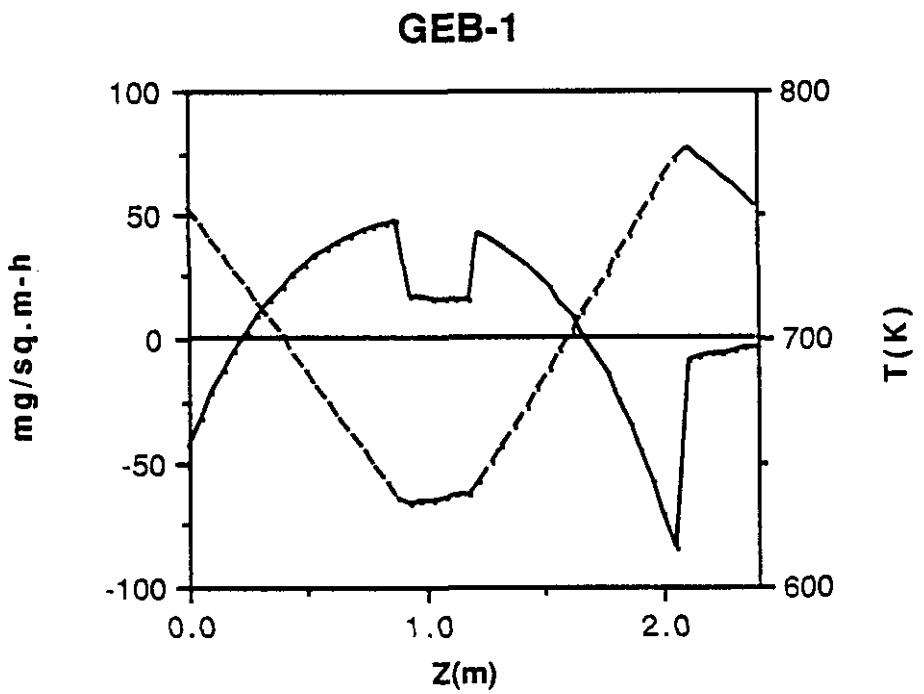

Figure B.1 Predictions of an Elemental Mass Transport Model for GEB-1

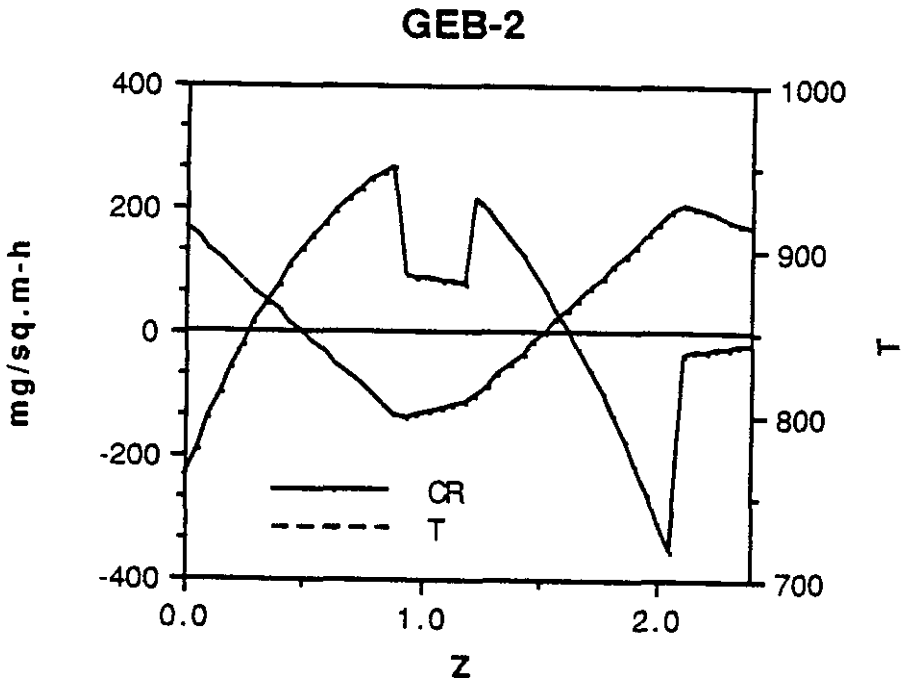

Figure B.2 Predictions of an Elemental Mass Transport Model for GEB-2

APPENDIX C RAW DATA

The raw weighing and EDX data are shown for GEB-1 and GEB-2 in Tables C.1 through C.4 which were generated from Microsoft Excel spreadsheet program for the Apple Macintosh computer. The spreadsheet allows simple manipulation of the data and a convenient data storage method.

The Tables C.1 and C.2 show physical and experimental data for the specimens used for GEB-1 and GEB-2, respectively. After heat treatment, polishing and cleaning prior to operation, each specimen was measured in order to accurately calculate the surface area. The specimens were identified as either L or H for GEB-1 and GEB-2, respectively. The numbering of the specimens begins at the bottom of (inlet to) the hot leg with specimen -01 and up through specimen 20 at the top of the hot leg. The numbering continues in the cold leg beginning with specimen 21 at the bottom of the cold leg and continues consecutively to 42 at the top of the cold leg. Weights for each specimen at each of the pulls were recorded. Four specimens in GEB-1 and two in GEB-2 were exchanged at various points during the experimental period as indicated by OUT on the data sheets. Replacement specimens were given the same number as the one being replaced with a decimal designation as a differentiator. For example, L-42.1 replaced L-42 at 2500 hours.

Tables C.3 and C.4 show the condensed data from the EDX analysis performed for GEB-1 and GEB-2, respectively. The data

sheets show the semi-quantitative analysis results for iron, chromium, nickel, molybdenum, and silicon along with the data file (Q-file) numbers for the specimen and associated SEM photos.

SPECIMEN ID#		OA LENGTH INCHES	ACTIVE LNTH METERS	POSITION METERS	ID-MALE INCHES	OD-MALE INCHES	ID-FEMALE INCHES	OD-FEMALE INCHES	INNER AREA SQ. METERS
L-01	BHL	1.4310	0.0332	0.0332	0.6352	0.6700	0.6738	0.7522	1.681E-03
L-02	HL	1.4878	0.0346	0.0678	0.6356	0.6714	0.6776	0.7520	1.756E-03
L-02.1	HL	1.5045	0.0350	0.0682	0.6330	0.6690	0.6630	0.7500	1.770E-03
L-03	HL	1.4944	0.0348	0.1026	0.6328	0.6708	0.6786	0.7538	1.756E-03
L-04	HL	1.4814	0.0345	0.1370	0.6334	0.6702	0.6768	0.7522	1.741E-03
L-05	HL	1.5596	0.0364	0.1735	0.6334	0.6708	0.6774	0.7522	1.842E-03
L-06	HL	1.4944	0.0348	0.2082	0.6330	0.6710	0.6704	0.7518	1.757E-03
L-07	HL	1.4828	0.0345	0.2427	0.6312	0.6698	0.6774	0.7520	1.737E-03
L-08	HL	1.5080	0.0351	0.2779	0.6328	0.6710	0.6772	0.7526	1.774E-03
L-09	HL	1.4808	0.0344	0.3123	0.6330	0.6700	0.6764	0.7518	1.739E-03
L-10	HL	1.4628	0.0340	0.3463	0.6332	0.6702	0.6772	0.7520	1.717E-03
L-11	HL	1.4842	0.0345	0.3808	0.6350	0.6712	0.6772	0.7520	1.749E-03
L-12	HL	1.4902	0.0347	0.4155	0.6328	0.6704	0.6784	0.7522	1.751E-03
L-13	HL	1.5000	0.0349	0.4504	0.6352	0.6702	0.6766	0.7524	1.770E-03
L-14	HL	1.4590	0.0339	0.4843	0.6352	0.6704	0.6756	0.7524	1.717E-03
L-15	HL	1.4958	0.0348	0.5191	0.6328	0.6692	0.6770	0.7522	1.758E-03
L-16	HL	1.4820	0.0345	0.5536	0.6324	0.6708	0.6780	0.7522	1.739E-03
L-17	HL	1.4818	0.0345	0.5880	0.6342	0.6712	0.6762	0.7520	1.744E-03
L-17.1	HL	1.5022	0.0350	0.5886	0.6332	0.6702	0.6790	0.7520	1.767E-03
L-18	HL	1.5128	0.0353	0.6233	0.6336	0.6700	0.6782	0.7520	1.782E-03
L-20	HL	1.4792	0.0344	0.6577	0.6330	0.6700	0.6772	0.7522	1.737E-03
L-21	THL	1.5258	0.0356	0.6933	0.6342	0.6710	0.6782	0.7520	1.801E-03
L-22	BCL	1.4742	0.0343	0.0343	0.6342	0.6708	0.6782	0.7522	1.734E-03
L-23	CL	1.4696	0.0342	0.0684	0.6328	0.6704	0.6776	0.7524	1.725E-03
L-23.1	CL	1.4856	0.0346	0.0688	0.6334	0.6710	0.6790	0.7520	1.747E-03
L-24	CL	1.4554	0.0338	0.1022	0.6348	0.6710	0.6740	0.7522	1.712E-03
L-25	CL	1.4682	0.0341	0.1363	0.6338	0.6700	0.6782	0.7518	1.725E-03
L-26	CL	1.4662	0.0341	0.1704	0.6348	0.6712	0.6754	0.7522	1.728E-03
L-27	CL	1.4928	0.0347	0.2051	0.6324	0.6702	0.6778	0.7522	1.753E-03
L-28	CL	1.4618	0.0340	0.2391	0.6330	0.6710	0.6724	0.7520	1.715E-03
L-29	CL	1.4978	0.0349	0.2740	0.6350	0.6700	0.6778	0.7520	1.767E-03
L-30	CL	1.4952	0.0348	0.3088	0.6322	0.6710	0.6742	0.7520	1.756E-03
L-31	CL	1.4852	0.0345	0.3433	0.6332	0.6710	0.6782	0.7524	1.746E-03
L-32	CL	1.5378	0.0359	0.3792	0.6332	0.6710	0.6780	0.7522	1.813E-03
L-33	CL	1.4980	0.0349	0.4141	0.6344	0.6710	0.6758	0.7520	1.765E-03
L-34	CL	1.4712	0.0342	0.4483	0.6340	0.6712	0.6782	0.7520	1.730E-03
L-35	CL	1.4778	0.0344	0.4826	0.6340	0.6700	0.6782	0.7520	1.738E-03
L-36	CL	1.4678	0.0341	0.5187	0.6334	0.6702	0.6760	0.7518	1.724E-03
L-37	CL	1.4738	0.0343	0.5510	0.6344	0.6712	0.6792	0.7524	1.734E-03
L-38	CL	1.4964	0.0348	0.5858	0.6340	0.6710	0.6782	0.7520	1.762E-03
L-39	CL	1.5152	0.0353	0.6211	0.6338	0.6714	0.6762	0.7522	1.786E-03
L-40	CL	1.5300	0.0357	0.6568	0.6332	0.6710	0.6782	0.7528	1.803E-03
L-41	CL	1.7434	0.0411	0.6979	0.6302	0.6712	0.6788	0.7522	2.067E-03
L-42	CL	1.4990	0.0349	0.7328	0.6352	0.6700	0.6788	0.7522	1.769E-03
L-42.1	CL	1.5365	0.0359	0.7338	0.6335	0.6690	0.6615	0.7500	1.812E-03
L-43	TCL	1.4764	0.0343	0.7672	0.6324	0.6702	0.6788	0.7522	1.732E-03

Table C.1 Raw Weighing Data for GEB-1

				DATE	3-May-87	7-May-87	7-May-87	7-May-87	7-May-87
				HOURS	0.0	97.0	97.0	97.0	97.0
OUTER AREA SQ. METERS	TOTAL AREA SQ. METERS	WALL THKNS M	TEMP K	TEMP C	INITIAL WEIGHT GRAMS(4)	PULL #1 GRAMS(4)	INSTANT WT. CHANGE GRAMS(4)	INSTANT MASS,I FLUX mG/SQM-h	INSTANT MASS,I FLUX mG/SQM-h
1.991E-03	4.326E-03	1.486E-03	632.3	359.3	20.7436	20.7441	5.00E-04	3.0657	1.1916
2.077E-03	4.486E-03	1.478E-03	639.9	366.9	22.0588	22.0593	5.00E-04	2.9361	1.1491
2.097E-03	4.516E-03	1.486E-03	640.0	367.0	22.5920	OUT	OUT	OUT	OUT
2.092E-03	4.513E-03	1.537E-03	647.5	374.5	22.2177	22.2195	1.80E-03	10.5654	4.1114
2.068E-03	4.468E-03	1.509E-03	655.0	382.0	21.8137	21.8148	1.10E-03	6.5124	2.5383
2.187E-03	4.688E-03	1.509E-03	663.0	390.0	22.9445	22.9450	5.00E-04	2.7988	1.0996
2.087E-03	4.501E-03	1.509E-03	670.7	397.7	22.2455	22.2455	0.00E+00	0.0000	0.0000
2.070E-03	4.470E-03	1.534E-03	678.2	405.2	21.7898	21.7896	-2.00E-04	-1.1870	-0.4613
2.110E-03	4.545E-03	1.521E-03	685.9	412.9	22.3936	22.3941	5.00E-04	2.9060	1.1342
2.066E-03	4.463E-03	1.509E-03	693.5	420.5	21.8793	21.8815	2.20E-03	13.0387	5.0814
2.039E-03	4.414E-03	1.509E-03	700.9	427.9	21.0717	21.0719	2.00E-04	1.2009	0.4671
2.072E-03	4.475E-03	1.486E-03	708.5	435.5	21.8382	21.8384	2.00E-04	1.1786	0.4607
2.081E-03	4.493E-03	1.516E-03	716.1	443.1	22.1976	22.1987	1.10E-03	6.4765	2.5242
2.097E-03	4.522E-03	1.488E-03	723.8	450.8	22.0504	22.0505	1.00E-04	0.5824	0.2280
2.034E-03	4.406E-03	1.488E-03	731.2	458.2	21.6267	21.6276	9.00E-04	5.4024	2.1058
2.090E-03	4.507E-03	1.516E-03	738.8	465.8	22.2494	22.2493	-1.00E-04	-0.5864	-0.2287
2.069E-03	4.470E-03	1.521E-03	746.4	473.4	22.2625	22.2621	-4.00E-04	-2.3708	-0.9226
2.068E-03	4.468E-03	1.496E-03	753.9	480.9	21.8542	21.8543	1.00E-04	0.5911	0.2307
2.099E-03	4.525E-03	1.509E-03	754.0	481.0	22.2844	OUT	OUT	OUT	OUT
2.115E-03	4.555E-03	1.504E-03	761.7	488.7	22.5735	22.5728	-7.00E-04	-4.0492	-1.5843
2.065E-03	4.461E-03	1.514E-03	769.2	496.2	22.1635	22.1627	-8.00E-04	-4.7470	-1.8486
2.135E-03	4.592E-03	1.496E-03	777.0	504.0	22.6785	22.6782	-3.00E-04	-1.7176	-0.6735
2.057E-03	4.448E-03	1.499E-03	630.8	357.8	21.7688	21.7698	1.00E-03	5.9444	2.3178
2.050E-03	4.436E-03	1.519E-03	636.6	363.6	22.1281	22.1288	7.00E-04	4.1846	1.6269
2.074E-03	4.479E-03	1.506E-03	636.7	363.7	21.9486	OUT	OUT	OUT	OUT
2.028E-03	4.395E-03	1.491E-03	642.3	369.3	21.5015	21.5020	5.00E-04	3.0114	1.1729
2.047E-03	4.429E-03	1.499E-03	648.1	375.1	21.8667	21.8673	6.00E-04	3.5848	1.3967
2.045E-03	4.425E-03	1.491E-03	653.9	380.9	21.7188	21.7197	9.00E-04	5.3768	2.0966
2.085E-03	4.500E-03	1.521E-03	659.8	386.8	22.0686	22.0692	6.00E-04	3.5282	1.3747
2.038E-03	4.411E-03	1.511E-03	665.5	392.5	21.7220	21.7231	1.10E-03	6.6120	2.5711
2.092E-03	4.513E-03	1.486E-03	671.4	398.4	21.9369	21.9387	1.80E-03	10.5027	4.1115
2.088E-03	4.505E-03	1.521E-03	677.3	404.3	22.3347	22.3360	1.30E-03	7.8334	2.9752
2.074E-03	4.480E-03	1.514E-03	683.2	410.2	22.0466	22.0467	1.00E-04	0.5906	0.2301
2.154E-03	4.627E-03	1.511E-03	689.3	416.3	22.9382	22.9388	6.00E-04	3.4115	1.3370
2.093E-03	4.514E-03	1.494E-03	695.2	422.2	22.1542	22.1547	5.00E-04	2.9198	1.1420
2.052E-03	4.439E-03	1.499E-03	701.0	428.0	21.8186	21.8205	1.90E-03	11.3231	4.4127
2.062E-03	4.457E-03	1.499E-03	706.8	433.8	21.9505	21.9505	0.00E+00	0.0000	0.0000
2.046E-03	4.427E-03	1.504E-03	712.6	439.6	21.9848	21.9851	3.00E-04	1.7941	0.6986
2.057E-03	4.449E-03	1.499E-03	718.4	445.4	21.7710	21.7712	2.00E-04	1.1889	0.4635
2.090E-03	4.510E-03	1.499E-03	724.3	451.3	22.3220	22.3231	1.10E-03	6.4350	2.5147
2.119E-03	4.563E-03	1.504E-03	730.3	457.3	22.5000	22.5007	7.00E-04	4.0409	1.5815
2.144E-03	4.608E-03	1.519E-03	736.3	463.3	22.8332	22.8334	2.00E-04	1.1435	0.4474
2.467E-03	5.202E-03	1.549E-03	743.3	470.3	26.5230	26.5233	3.00E-04	1.4961	0.5946
2.095E-03	4.518E-03	1.486E-03	749.2	476.2	21.9404	21.9445	4.10E-03	23.8945	9.3552
2.146E-03	4.608E-03	1.480E-03	749.3	476.3	23.0611	OUT	OUT	OUT	OUT
2.060E-03	4.454E-03	1.521E-03	755.0	482.0	21.9736	21.9766	3.00E-03	17.8549	6.9442

Table C.1 Raw Weighing Data for GEB-1 (continued)

19MAY87	19-May-87	19-May-87	19-May-87	19-May-87	19-May-87	19-May-87	29-May-87	29-May-87
292.0	292.0	292.0	292.0	292.0	292.0	292.0	460.0	460.0
PULL #2	INSTANT WT. CHANGE	OVERALL WT. CHANGE	INSTANT(4) MASS,I FLUX	OVERALL(4) MASS,I FLUX	INSTANT(4) MASS,I FLUX	OVERALL(4) MASS,I FLUX	PULL #3	PULL #3
GRAMS(4)	GRAMS(4)	GRAMS(4)	mG/SQM-h	mG/SQM-h	mG/SQM-h	mG/SQM-h	GRAMS(4)	GRAMS(5)
20.7435	-6.00E-04	-1.00E-04	-1.8300	-0.2037	-0.7113	-0.0792	20.7431	20.74365
22.0586	-7.00E-04	-2.00E-04	-2.0447	-0.3901	-0.8002	-0.1527	22.0586	22.05862
OUT	OUT	OUT	OUT	OUT	OUT	OUT	OUT	OUT
22.2181	-1.40E-03	4.00E-04	-4.0877	0.7799	-1.5907	0.3035	22.2183	22.21841
21.8140	-8.00E-04	3.00E-04	-2.3560	0.5900	-0.9183	0.2300	21.8141	21.81404
22.9439	-1.10E-03	-6.00E-04	-3.0629	-1.1157	-1.2034	-0.4383	22.9437	22.94393
22.2450	-5.00E-04	-5.00E-04	-1.4594	-0.9746	-0.5697	-0.3805	22.2448	22.24481
21.7890	-6.00E-04	-8.00E-04	-1.7713	-1.5772	-0.6884	-0.6130	21.7891	21.78921
22.3930	-1.10E-03	-8.00E-04	-3.1802	-1.1584	-1.2412	-0.4521	22.3927	22.39332
21.8808	-7.00E-04	1.50E-03	-2.0637	2.9532	-0.8043	1.1509	21.8804	21.88098
21.0708	-1.10E-03	-9.00E-04	-3.2856	-1.7952	-1.2779	-0.6982	21.0710	21.07093
21.8372	-1.20E-03	-1.00E-03	-3.5178	-1.9577	-1.3750	-0.7652	21.8372	21.83761
22.1976	-1.10E-03	0.00E+00	-3.2217	0.0000	-1.2556	0.0000	22.1979	22.19784
22.0496	-9.00E-04	-8.00E-04	-2.6072	-1.5477	-1.0207	-0.6059	22.0498	22.05038
21.6270	-8.00E-04	3.00E-04	-1.7916	0.5982	-0.6983	0.2332	21.6273	21.62727
22.2489	-4.00E-04	-5.00E-04	-1.1667	-0.9739	-0.4551	-0.3799	22.2493	22.24934
22.2618	-3.00E-04	-7.00E-04	-0.8845	-1.3782	-0.3442	-0.5364	22.2625	22.26249
21.8540	-3.00E-04	-2.00E-04	-0.8821	-0.3927	-0.3443	-0.1533	21.8540	21.85454
OUT	OUT	OUT	OUT	OUT	OUT	OUT	OUT	OUT
22.5725	-3.00E-04	-1.00E-03	-0.8632	-1.9216	-0.3377	-0.7518	22.5729	22.57350
22.1620	-7.00E-04	-1.50E-03	-2.0661	-2.9567	-0.8046	-1.1514	22.1628	22.16308
22.6781	-1.00E-04	-4.00E-04	-0.2848	-0.7608	-0.1117	-0.2983	22.6787	22.67942
21.7692	-8.00E-04	4.00E-04	-1.7742	0.7899	-0.6918	0.3080	21.7688	21.76890
22.1281	-7.00E-04	0.00E+00	-2.0816	0.0000	-0.8093	0.0000	22.1279	22.12799
OUT	OUT	OUT	OUT	OUT	OUT	OUT	OUT	OUT
21.5011	-9.00E-04	-4.00E-04	-2.6963	-0.8003	-1.0502	-0.3117	21.5003	21.50095
21.8665	-8.00E-04	-2.00E-04	-2.3776	-0.3970	-0.9263	-0.1547	21.8664	21.86635
21.7190	-7.00E-04	2.00E-04	-2.0803	0.3969	-0.8112	0.1548	21.7187	21.71858
22.0685	-7.00E-04	-1.00E-04	-2.0475	-0.1953	-0.7978	-0.0761	22.0680	22.06824
21.7223	-8.00E-04	3.00E-04	-2.3920	0.5990	-0.9302	0.2329	21.7219	21.72208
21.9375	-1.20E-03	6.00E-04	-3.4830	1.1630	-1.3635	0.4553	21.9366	21.93741
22.3350	-1.00E-03	3.00E-04	-2.9209	0.5852	-1.1385	0.2281	22.3347	22.33471
22.0457	-1.00E-03	-9.00E-04	-2.9377	-1.7656	-1.1447	-0.6880	22.0456	22.04557
22.9375	-1.30E-03	-7.00E-04	-3.6768	-1.3221	-1.4409	-0.5181	22.9369	22.93723
22.1537	-1.00E-03	-5.00E-04	-2.9048	-0.9699	-1.1362	-0.3794	22.1531	22.15338
21.8194	-1.10E-03	8.00E-04	-3.2609	1.5838	-1.2708	0.6172	21.8190	21.81885
21.9500	-5.00E-04	-5.00E-04	-1.4750	-0.9850	-0.5753	-0.3842	21.9491	21.94959
21.9841	-1.00E-03	-7.00E-04	-2.9748	-1.3906	-1.1584	-0.5415	21.9836	21.98407
21.7704	-8.00E-04	-6.00E-04	-2.3655	-1.1848	-0.9222	-0.4619	21.7693	21.76984
22.3221	-1.00E-03	1.00E-04	-2.9100	0.1943	-1.1372	0.0759	22.3213	22.32153
22.4995	-1.20E-03	-5.00E-04	-3.4459	-0.9588	-1.3486	-0.3753	22.4988	22.49929
22.8328	-6.00E-04	-4.00E-04	-1.7064	-0.7597	-0.6677	-0.2973	22.8323	22.83247
26.5224	-9.00E-04	-6.00E-04	-2.2327	-0.9940	-0.8873	-0.3950	26.5216	26.52217
21.9444	-1.00E-04	4.00E-03	-0.2899	7.7440	-0.1135	3.0319	21.9437	21.94383
OUT	OUT	OUT	OUT	OUT	OUT	OUT	OUT	OUT
21.9766	0.00E+00	3.00E-03	0.0000	5.9312	0.0000	2.3068	21.9756	21.97611

Table C.1 Raw Weighing Data for GEB-1 (continued)

29-May-87 460.0	29-May-87 460.0	29-May-87 460.0	29-May-87 460.0	29-May-87 460.0	29-May-87 460.0	30-Jun-87 984.0	30-Jun-87 984.0	30-Jun-87 984.0	
INSTANT WT. CHANGE GRAMS(4)	OVERALL(4) WT. CHANGE GRAMS(4)	INSTANT(4) MASS,↓ FLUX mG/SQM-h	OVERALL(4) MASS,↓ FLUX mG/SQM-h	INSTANT(4) MASS,↑ FLUX mG/SQM-h	OVERALL(4) MASS,↑ FLUX mG/SQM-h	PULL #4 GRAMS (4)	PULL #4 GRAMS(5)	INSTANT(4) WT. CHANGE GRAMS(4)	
-4.00E-04	-5.00E-04	-1.4161	-0.6465	-0.5504	-0.2513	20.7432	20.74355	1.00E-04	
0.00E+00	-2.00E-04	0.0000	-0.2477	0.0000	-0.0969	22.0581	22.05840	-5.00E-04	
OUT	OUT	OUT	OUT	OUT	OUT	OUT	OUT	OUT	
2.00E-04	6.00E-04	0.6778	0.7426	0.2638	0.2890	22.2173	22.21803	-1.00E-03	
1.00E-04	4.00E-04	0.3418	0.4994	0.1332	0.1946	21.8132	21.81364	-9.00E-04	
-2.00E-04	-8.00E-04	-0.6464	-0.9443	-0.2540	-0.3710	22.9428	22.94344	-9.00E-04	
-2.00E-04	-7.00E-04	-0.6776	-0.8661	-0.2645	-0.3381	22.2441	22.24455	-7.00E-04	
1.00E-04	-7.00E-04	0.3427	-0.8760	0.1332	-0.3405	21.7877	21.78883	-1.40E-03	
-3.00E-04	-9.00E-04	-1.0067	-1.1030	-0.3929	-0.4305	22.3921	22.39258	-6.00E-04	
-4.00E-04	1.10E-03	-1.3688	1.3747	-0.5334	0.5358	21.8800	21.88045	-4.00E-04	
2.00E-04	-7.00E-04	0.6934	-0.8863	0.2697	-0.3447	21.0698	21.07040	-1.20E-03	
0.00E+00	-1.00E-03	0.0000	-1.2427	0.0000	-0.4857	21.8362	21.83715	-1.00E-03	
3.00E-04	3.00E-04	1.0198	0.3725	0.3975	0.1452	22.1969	22.19743	-1.00E-03	
2.00E-04	-6.00E-04	0.6725	-0.7368	0.2633	-0.2885	22.0495	22.05007	-3.00E-04	
3.00E-04	6.00E-04	1.0397	0.7595	0.4053	0.2960	21.6271	21.62719	-2.00E-04	
4.00E-04	-1.00E-04	1.3542	-0.1236	0.5282	-0.0482	22.2488	22.24934	-5.00E-04	
7.00E-04	0.00E+00	2.3955	0.0000	0.9322	0.0000	22.2621	22.26270	-4.00E-04	
0.00E+00	-2.00E-04	0.0000	-0.2493	0.0000	-0.0973	21.8541	21.85486	1.00E-04	
OUT	OUT	OUT	OUT	OUT	OUT	22.2644	22.28627	IN	
4.00E-04	-6.00E-04	1.3360	-0.7319	0.5227	-0.2864	22.5733	22.57396	4.00E-04	
8.00E-04	-7.00E-04	2.7408	-0.8759	1.0674	-0.3411	22.1628	22.16343	0.00E+00	
6.00E-04	2.00E-04	1.9835	0.2415	0.7777	0.0947	22.6795	22.68003	8.00E-04	
-4.00E-04	0.00E+00	-1.3729	0.0000	-0.5353	0.0000	21.7682	21.76865	-6.00E-04	
-2.00E-04	-2.00E-04	-0.6903	-0.2521	-0.2684	-0.0980	22.1269	22.12752	-1.00E-03	
OUT	OUT	OUT	OUT	OUT	OUT	21.9486	21.94989	IN	
-8.00E-04	-1.20E-03	-2.7819	-1.5240	-1.0836	-0.5936	21.5000	21.50056	-3.00E-04	
-1.00E-04	-3.00E-04	-0.3450	-0.3780	-0.1344	-0.1473	21.8656	21.86605	-8.00E-04	
-3.00E-04	-1.00E-04	-1.0348	-0.1260	-0.4035	-0.0491	21.7177	21.71825	-1.00E-03	
-5.00E-04	-6.00E-04	-1.6976	-0.7440	-0.6614	-0.2899	22.0673	22.06759	-7.00E-04	
-4.00E-04	-1.00E-04	-1.3882	-0.1268	-0.5398	-0.0493	21.7211	21.72149	-8.00E-04	
-9.00E-04	-3.00E-04	-3.0320	-0.3691	-1.1870	-0.1445	21.9361	21.93680	-5.00E-04	
-3.00E-04	0.00E+00	-1.0171	0.0000	-0.3964	0.0000	22.3337	22.33422	-1.00E-03	
-1.00E-04	-1.00E-03	-0.3410	-1.2453	-0.1329	-0.4852	22.0445	22.04508	-1.10E-03	
-6.00E-04	-1.30E-03	-1.9697	-1.5586	-0.7719	-0.6108	22.9360	22.93660	-9.00E-04	
-6.00E-04	-1.10E-03	-2.0230	-1.3545	-0.7913	-0.5298	22.1522	22.15275	-9.00E-04	
-4.00E-04	4.00E-04	-1.3764	0.5027	-0.5364	0.1959	21.8179	21.81839	-1.10E-03	
-9.00E-04	-1.40E-03	-3.0817	-1.7508	-1.2020	-0.6829	21.9485	21.94893	-6.00E-04	
-5.00E-04	-1.20E-03	-1.7265	-1.5133	-0.6723	-0.5893	21.9827	21.98340	-9.00E-04	
-1.10E-03	-1.70E-03	-3.7753	-2.1309	-1.4718	-0.8307	21.7688	21.76926	-5.00E-04	
-8.00E-04	-7.00E-04	-2.7022	-0.8635	-1.0560	-0.3374	22.3203	22.32090	-1.00E-03	
-7.00E-04	-1.20E-03	-2.3331	-1.4608	-0.9131	-0.5717	22.4985	22.49872	-3.00E-04	
-5.00E-04	-9.00E-04	-1.6505	-1.0851	-0.6459	-0.4246	22.8312	22.83199	-1.10E-03	
-8.00E-04	-1.40E-03	-2.3036	-1.4723	-0.9155	-0.5851	26.5211	26.52169	-5.00E-04	
-7.00E-04	3.30E-03	-2.3555	4.0555	-0.9222	1.5878	21.9436	21.94378	-1.00E-04	
OUT	OUT	OUT	OUT	OUT	OUT	OUT	OUT	OUT	
-1.00E-03	2.00E-03	-3.4364	2.5100	-1.3365	0.9762	21.9756	21.97604	0.00E+00	

Table C.1 Raw Weighing Data for GEB-1 (continued)

30-Jun-87	30-Jun-87	30-Jun-87	30-Jun-87	30-Jun-87	30-Jun-87	30-Jun-87	30-Jun-87	23-Jul-87
984.0	984.0	984.0	984.0	984.0	984.0	984.0	984.0	1496.0
OVERALL(4) WT. CHANGE GRAMS(4)	INSTANT(5) WT. CHANGE GRAMS(5)	INSTANT(4) MASS,I FLUX mG/SQM-h	OVERALL(4) MASS,I FLUX mG/SQM-h	OVERALL(4) MASS,t FLUX mG/SQM-h	INSTANT(5) MASS,I FLUX mG/SQM-h	INSTANT(5) MASS,t FLUX mG/SQM-h	INSTANT(4) MASS,t FLUX mG/SQM-h	PULL #5 GRAMS (4)
-4.00E-04	-1.00E-04	0.1135	-0.2418	-0.0940	-0.1135	-0.0441	0.0441	20.7432
-7.00E-04	-2.20E-04	-0.5435	-0.4052	-0.1586	-0.2391	-0.0936	-0.2127	22.0578
OUT	OUT	OUT	OUT	OUT	OUT	OUT	OUT	OUT
-4.00E-04	-3.80E-04	-1.0866	-0.2314	-0.0901	-0.4129	-0.1607	-0.4228	22.2173
-5.00E-04	-4.00E-04	-0.9863	-0.2918	-0.1137	-0.4384	-0.1709	-0.3844	21.8130
-1.70E-03	-4.90E-04	-0.9326	-0.9381	-0.3686	-0.5077	-0.1995	-0.3664	22.9427
-1.40E-03	-2.60E-04	-0.7604	-0.8098	-0.3161	-0.2824	-0.1102	-0.2968	22.2439
-2.10E-03	-3.80E-04	-1.5381	-1.2286	-0.4775	-0.4175	-0.1622	-0.5977	21.7882
-1.50E-03	-7.40E-04	-0.6455	-0.8594	-0.3354	-0.7961	-0.3107	-0.2519	22.3919
7.00E-04	-5.30E-04	-0.4388	0.4090	0.1594	-0.5815	-0.2266	-0.1710	21.8798
-1.90E-03	-5.30E-04	-1.3338	-1.1246	-0.4374	-0.5891	-0.2291	-0.5188	21.0698
-2.00E-03	-4.60E-04	-1.0909	-1.1619	-0.4541	-0.5018	-0.1961	-0.4264	21.8364
-7.00E-04	-4.10E-04	-1.0899	-0.4063	-0.1583	-0.4469	-0.1742	-0.4248	22.1969
-9.00E-04	-3.10E-04	-0.3234	-0.5167	-0.2023	-0.3342	-0.1308	-0.1266	22.0495
4.00E-04	-8.00E-05	-0.2222	0.2367	0.0923	-0.0889	-0.0347	-0.0866	21.6268
-6.00E-04	0.00E+00	-0.5427	-0.3468	-0.1353	0.0000	0.0000	-0.2117	22.2491
-4.00E-04	2.10E-04	-0.4389	-0.2337	-0.0909	0.2304	0.0897	-0.1708	22.2628
-1.00E-04	3.20E-04	0.1094	-0.0583	-0.0227	0.3502	0.1367	0.0427	OUT
IN	IN	IN	IN	IN	IN	IN	IN	22.2850
-2.00E-04	4.60E-04	0.4283	-0.1140	-0.0446	0.4926	0.1927	0.1676	22.5743
-7.00E-04	3.50E-04	0.0000	-0.4094	-0.1595	0.3844	0.1497	0.0000	22.1630
1.00E-03	6.10E-04	0.8479	0.5644	0.2213	0.6465	0.2535	0.3325	22.6798
-6.00E-04	-2.50E-04	-0.6602	-0.3516	-0.1371	-0.2751	-0.1073	-0.2574	21.7682
-1.20E-03	-4.70E-04	-1.1066	-0.7071	-0.2749	-0.5201	-0.2022	-0.4302	OUT
IN	IN	IN	IN	IN	IN	IN	IN	21.9484
-1.50E-03	-3.90E-04	-0.3345	-0.8906	-0.3469	-0.4348	-0.1694	-0.1303	21.5000
-1.10E-03	-3.00E-04	-0.8848	-0.6479	-0.2524	-0.3318	-0.1293	-0.3447	21.8655
-1.10E-03	-3.10E-04	-1.1059	-0.6478	-0.2526	-0.3428	-0.1337	-0.4312	21.7176
-1.30E-03	-6.50E-04	-0.7620	-0.7536	-0.2936	-0.7075	-0.2757	-0.2969	22.0670
-9.00E-04	-5.90E-04	-0.8902	-0.5333	-0.2074	-0.6565	-0.2553	-0.3461	21.7207
-8.00E-04	-6.10E-04	-0.5401	-0.4601	-0.1801	-0.6589	-0.2579	-0.2114	21.9363
-1.00E-03	-4.90E-04	-1.0870	-0.5788	-0.2256	-0.5326	-0.2076	-0.4237	22.3337
-2.10E-03	-4.90E-04	-1.2025	-1.2225	-0.4764	-0.5357	-0.2087	-0.4686	22.0446
-2.20E-03	-6.30E-04	-0.9473	-1.2331	-0.4832	-0.6631	-0.2599	-0.3712	22.9363
-2.00E-03	-6.30E-04	-0.9729	-1.1513	-0.4503	-0.6810	-0.2664	-0.3805	22.1520
-7.00E-04	-4.60E-04	-1.2135	-0.4112	-0.1603	-0.5075	-0.1978	-0.4729	21.8177
-2.00E-03	-6.60E-04	-0.6587	-1.1692	-0.4560	-0.7246	-0.2826	-0.2569	21.9484
-2.10E-03	-6.70E-04	-0.9963	-1.2360	-0.4821	-0.7417	-0.2888	-0.3880	21.9827
-2.20E-03	-5.80E-04	-0.5502	-1.2891	-0.5026	-0.6382	-0.2488	-0.2145	21.7685
-1.70E-03	-6.30E-04	-1.0829	-0.9804	-0.3831	-0.6822	-0.2666	-0.4232	22.3202
-1.50E-03	-5.70E-04	-0.3206	-0.8536	-0.3341	-0.6091	-0.2384	-0.1255	22.4980
-2.00E-03	-4.80E-04	-1.1642	-1.1272	-0.4411	-0.5080	-0.1988	-0.4556	22.8313
-1.90E-03	-4.80E-04	-0.4616	-0.9341	-0.3712	-0.4431	-0.1761	-0.1834	26.5212
3.20E-03	-5.00E-05	-0.1079	1.8384	0.7198	-0.0539	-0.0211	-0.0422	21.9431
OUT	OUT	OUT	OUT	OUT	OUT	OUT	OUT	OUT
2.00E-03	-7.00E-05	0.0000	1.1734	0.4564	-0.0771	-0.0300	0.0000	21.9756

Table C.1 Raw Weighing Data for GEB-1 (continued)

23-Jul-87 1496.0	23-Jul-87 1496.0	23-Jul-87 1496.0	23-Jul-87 1496.0	23-Jul-87 1496.0	23-Jul-87 1496.0	23-Jul-87 1496.0	23-Jul-87 1496.0	23-Jul-87 1496.0
PULL #5 GRAMS (5)	INSTANT(4) WT. CHANGE GRAMS (4)	OVERALL(4) WT. CHANGE GRAMS (4)	INSTANT(5) WT. CHANGE GRAMS (5)	INSTANT(4) MASS,I FLUX mG/SQM-h	OVERALL(4) MASS,I FLUX mG/SQM-h	OVERALL(4) MASS,t FLUX mG/SQM-h	INSTANT(5) MASS,I FLUX mG/SQM-h	INSTANT(5) MASS,t FLUX mG/SQM-h
20.74352	0.00E+00	-4.00E-04	-3.00E-05	0	-0.1590222	-0.0618126	-0.0348482	-0.0135456
22.05824	-3.00E-04	-1.00E-03	-1.60E-04	-0.3337	-0.3807	-0.1490	-0.1780	-0.0697
OUT	OUT	OUT	OUT	OUT	OUT	OUT	OUT	OUT
22.21784	0.00E+00	-4.00E-04	-1.90E-04	0.0000	-0.1522	-0.0592	-0.2113	-0.0822
21.81340	-2.00E-04	-7.00E-04	-2.40E-04	-0.2243	-0.2687	-0.1047	-0.2692	-0.1049
22.94318	-1.00E-04	-1.80E-03	-2.60E-04	-0.1060	-0.6533	-0.2567	-0.2757	-0.1083
22.24432	-2.00E-04	-1.60E-03	-2.30E-04	-0.2223	-0.6087	-0.2376	-0.2557	-0.0998
21.78854	5.00E-04	-1.60E-03	-2.90E-04	0.5622	-0.6157	-0.2393	-0.3261	-0.1267
22.39235	-2.00E-04	-1.70E-03	-2.30E-04	-0.2202	-0.6406	-0.2500	-0.2533	-0.0988
21.88014	-2.00E-04	5.00E-04	-3.10E-04	-0.2246	0.1921	0.0749	-0.3481	-0.1357
21.07007	0.00E+00	-1.90E-03	-3.30E-04	0.0000	-0.7397	-0.2877	-0.3754	-0.1460
21.83690	2.00E-04	-1.80E-03	-2.50E-04	0.2233	-0.6878	-0.2688	-0.2791	-0.1091
22.19728	0.00E+00	-7.00E-04	-1.70E-04	0.0000	-0.2672	-0.1042	-0.1896	-0.0739
22.05000	0.00E+00	-9.00E-04	-7.00E-05	0.0000	-0.3398	-0.1331	-0.0772	-0.0302
21.82716	-3.00E-04	1.00E-04	-3.00E-05	-0.3412	0.0389	0.0152	-0.0341	-0.0133
22.24952	3.00E-04	-3.00E-04	1.80E-04	0.3333	-0.1141	-0.0445	0.2000	0.0780
22.26309	7.00E-04	3.00E-04	3.90E-04	0.7860	0.1153	0.0449	0.4379	0.1704
OUT	OUT	OUT	OUT	OUT	OUT	OUT	OUT	OUT
22.28515	6.00E-04	6.00E-04	-1.12E-03	0.6630	0.6630	0.2590	-1.2376	-0.4834
22.57468	1.00E-03	8.00E-04	7.20E-04	1.0959	0.3001	0.1174	0.7890	0.3087
22.16347	2.00E-04	-5.00E-04	4.00E-05	0.2248	-0.1924	-0.0749	0.0450	0.0175
22.68028	3.00E-04	1.30E-03	2.50E-04	0.3254	0.4826	0.1892	0.2712	0.1063
21.76862	0.00E+00	-6.00E-04	-3.00E-05	0.0000	-0.2313	-0.0902	-0.0338	-0.0132
OUT	OUT	OUT	OUT	OUT	OUT	OUT	OUT	OUT
21.94888	-2.00E-04	-2.00E-04	-1.01E-03	-0.2236	-0.2236	-0.0872	-1.1293	-0.4404
21.50035	0.00E+00	-1.50E-03	-2.10E-04	0.0000	-0.5858	-0.2282	-0.2396	-0.0933
21.86581	-1.00E-04	-1.20E-03	-2.40E-04	-0.1132	-0.4649	-0.1811	-0.2717	-0.1058
21.71797	-1.00E-04	-1.20E-03	-2.80E-04	-0.1132	-0.4648	-0.1813	-0.3169	-0.1236
22.06742	-3.00E-04	-1.60E-03	-1.70E-04	-0.3342	-0.6100	-0.2377	-0.1894	-0.0738
21.72123	-4.00E-04	-1.30E-03	-2.60E-04	-0.4555	-0.5067	-0.1970	-0.2961	-0.1151
21.93654	2.00E-04	-6.00E-04	-2.60E-04	0.2211	-0.2270	-0.0889	-0.2874	-0.1125
22.33399	0.00E+00	-1.00E-03	-2.30E-04	0.0000	-0.3807	-0.1484	-0.2559	-0.0997
22.04496	1.00E-04	-2.00E-03	-1.20E-04	0.1119	-0.7658	-0.2984	-0.1343	-0.0523
22.93637	3.00E-04	-1.90E-03	-2.30E-04	0.3232	-0.7005	-0.2745	-0.2478	-0.0971
22.15246	-2.00E-04	-2.20E-03	-2.90E-04	-0.2213	-0.8330	-0.3258	-0.3208	-0.1255
21.81813	-2.00E-04	-9.00E-04	-2.60E-04	-0.2258	-0.3478	-0.1355	-0.2936	-0.1144
21.94884	-1.00E-04	-2.10E-03	-9.00E-05	-0.1124	-0.8075	-0.3150	-0.1011	-0.0394
21.98316	0.00E+00	-2.10E-03	-2.40E-04	0.0000	-0.8143	-0.3171	-0.2719	-0.1059
21.76892	-3.00E-04	-2.50E-03	-3.40E-04	-0.3378	-0.9636	-0.3756	-0.3829	-0.1493
22.32062	-1.00E-04	-1.80E-03	-2.80E-04	-0.1108	-0.6828	-0.2668	-0.3103	-0.1213
22.49844	-5.00E-04	-2.00E-03	-2.80E-04	-0.5468	-0.7486	-0.2930	-0.3062	-0.1198
22.83170	1.00E-04	-1.90E-03	-2.90E-04	0.1083	-0.7043	-0.2756	-0.3141	-0.1229
26.52153	1.00E-04	-1.80E-03	-1.60E-04	0.0945	-0.5820	-0.2313	-0.1512	-0.0601
21.94344	-5.00E-04	2.70E-03	-3.40E-04	-0.5521	1.0203	0.3995	-0.3754	-0.1470
OUT	OUT	OUT	OUT	OUT	OUT	OUT	OUT	OUT
21.97595	0.00E+00	2.00E-03	-9.00E-05	0.0000	0.7718	0.3002	-0.1015	-0.0395

Table C.1 Raw Weighing Data for GEB-1 (continued)

23-Jul-87 1496.0	25-Aug-87 1996.0	25-Aug-87 1996.0	25-Aug-87 1996.0	25-Aug-87 1996.0	25-Aug-87 1996.0	25-Aug-87 1996.0	25-Aug-87 1996.0	25-Aug-87 1996.0
INSTANT(4) MASS,t FLUX mG/SQM-h	PULL #6 GRAMS(4)	PULL #6 GRAMS (5)	INSTANT(4) WT. CHANGE GRAMS (4)	OVERALL(4) WT. CHANGE GRAMS (4)	INSTANT(5) WT. CHANGE GRAMS (5)	INSTANT(4) MASS,I FLUX mG/SQM-h	OVERALL(4) MASS,I FLUX mG/SQM-h	OVERALL(4) MASS,t FLUX mG/SQM-h
0	20.7433	20.74377	1.00E-04	-3.00E-04	2.50E-04	0.1189	-0.0894	-0.0347
-0.1306	22.0575	22.05800	-3.00E-04	-1.30E-03	-2.40E-04	-0.3418	-0.3710	-0.1452
OUT	OUT	OUT	OUT	OUT	OUT	OUT	OUT	OUT
0.0000	22.2176	22.21795	3.00E-04	-1.00E-04	1.10E-04	0.3416	-0.0285	-0.0111
-0.0874	21.8124	21.81273	-6.00E-04	-1.30E-03	-6.70E-04	-0.6891	-0.3740	-0.1458
-0.0417	22.9430	22.94337	3.00E-04	-1.50E-03	1.90E-04	0.3258	-0.4080	-0.1603
-0.0868	22.2433	22.24378	-6.00E-04	-2.20E-03	-5.40E-04	-0.6830	-0.6274	-0.2449
0.2185	21.7879	21.78818	-3.00E-04	-1.90E-03	-3.60E-04	-0.3454	-0.5480	-0.2130
-0.0860	22.3919	22.39228	0.00E+00	-1.70E-03	-7.00E-05	0.0000	-0.4802	-0.1874
-0.0875	21.8792	21.87970	-6.00E-04	-1.00E-04	-4.40E-04	-0.6899	-0.0288	-0.0112
0.0000	21.0694	21.06942	-4.00E-04	-2.30E-03	-6.50E-04	-0.4660	-0.6711	-0.2610
0.0873	21.8354	21.83586	-1.00E-03	-2.80E-03	-1.04E-03	-1.1433	-0.8019	-0.3134
0.0000	22.1959	22.19638	-1.00E-03	-1.70E-03	-8.80E-04	-1.1422	-0.4864	-0.1898
0.0000	22.0486	22.04889	-9.00E-04	-1.80E-03	-1.11E-03	-1.0168	-0.5094	-0.1994
-0.1330	21.6268	21.62723	0.00E+00	1.00E-04	7.00E-05	0.0000	0.0292	0.0114
0.1300	22.2493	22.24969	2.00E-04	-1.00E-04	1.70E-04	0.2275	-0.0285	-0.0111
0.3059	22.2634	22.26371	6.00E-04	9.00E-04	6.20E-04	0.6899	0.2592	0.1009
OUT	OUT	OUT	OUT	OUT	OUT	OUT	OUT	OUT
0.2590	22.2849	22.28532	-1.00E-04	5.00E-04	1.70E-04	-0.1132	0.2795	0.1092
0.4288	22.5747	22.57493	4.00E-04	1.20E-03	2.50E-04	0.4469	0.3373	0.1320
0.0876	22.1633	22.16360	3.00E-04	-2.00E-04	1.30E-04	0.3453	-0.0577	-0.0225
0.1276	22.6800	22.68043	2.00E-04	1.50E-03	1.50E-04	0.2221	0.4174	0.1636
0.0000	21.7672	21.76746	-1.00E-03	-1.60E-03	-1.16E-03	-1.1532	-0.4622	-0.1802
OUT	OUT	OUT	OUT	OUT	OUT	OUT	OUT	OUT
-0.0872	21.9480	21.94831	-4.00E-04	-6.00E-04	-5.70E-04	-0.4580	-0.3394	-0.1324
0.0000	21.4994	21.49976	-6.00E-04	-2.10E-03	-5.90E-04	-0.7010	-0.6146	-0.2394
-0.0441	21.8647	21.86511	-8.00E-04	-2.00E-03	-7.00E-04	-0.9273	-0.5807	-0.2262
-0.0441	21.7172	21.71766	-4.00E-04	-1.60E-03	-3.10E-04	-0.4636	-0.4645	-0.1811
-0.1302	22.0665	22.06679	-5.00E-04	-2.10E-03	-6.30E-04	-0.5704	-0.6001	-0.2338
-0.1771	21.7199	21.72002	-8.00E-04	-2.10E-03	-1.21E-03	-0.9329	-0.6134	-0.2385
0.0865	21.9349	21.93530	-1.40E-03	-2.00E-03	-1.24E-03	-1.5847	-0.5671	-0.2220
0.0000	22.3326	22.33290	-1.10E-03	-2.10E-03	-1.09E-03	-1.2530	-0.5992	-0.2336
0.0436	22.0444	22.04472	-2.00E-04	-2.20E-03	-2.40E-04	-0.2291	-0.6314	-0.2460
0.1266	22.9354	22.93587	-9.00E-04	-2.80E-03	-5.00E-04	-0.9927	-0.7737	-0.3032
-0.0865	22.1518	22.15219	-2.00E-04	-2.40E-03	-2.70E-04	-0.2266	-0.6811	-0.2664
-0.0880	21.8171	21.81756	-6.00E-04	-1.50E-03	-5.70E-04	-0.6937	-0.4344	-0.1693
-0.0438	21.9479	21.94825	-5.00E-04	-2.60E-03	-5.90E-04	-0.5753	-0.7493	-0.2923
0.0000	21.9823	21.98259	-4.00E-04	-2.50E-03	-5.70E-04	-0.4641	-0.7266	-0.2829
-0.1317	21.7682	21.76861	-3.00E-04	-2.80E-03	-3.10E-04	-0.3460	-0.8089	-0.3153
-0.0433	22.3200	22.32055	-2.00E-04	-2.00E-03	-7.00E-05	-0.2270	-0.5686	-0.2222
-0.2140	22.4976	22.49767	-4.00E-04	-2.40E-03	-7.70E-04	-0.4480	-0.6733	-0.2635
0.0424	22.8311	22.83149	-2.00E-04	-2.10E-03	-2.10E-04	-0.2218	-0.5835	-0.2283
0.0375	26.5212	26.52164	0.00E+00	-1.80E-03	1.10E-04	0.0000	-0.4362	-0.1734
-0.2161	21.9428	21.94321	-3.00E-04	2.40E-03	-2.30E-04	-0.3392	0.6797	0.2661
OUT	OUT	OUT	OUT	OUT	OUT	OUT	OUT	OUT
0.0000	21.9758	21.97623	2.00E-04	2.20E-03	2.80E-04	0.2309	0.6363	0.2475

Table C.1 Raw Weighing Data for GEB-1 (continued)

25-Aug-87 1996.0	25-Aug-87 1996.0	25-Aug-87 1996.0	21-Sep-87 2505.0	21-Sep-87 2505.0	21-Sep-87 2505.0	21-Sep-87 2505.0	21-Sep-87 2505.0	21-Sep-87 2505.0
INSTANT(5) MASS,I FLUX mG/SQM-h	INSTANT(5) MASS,t FLUX mG/SQM-h	INSTANT(4) MASS,t FLUX mG/SQM-h	PULL #7 GRAMS(4)	PULL #7 GRAMS(5)	INSTANT(4) WT. CHANGE GRAMS (4)	OVERALL(4) WT. CHANGE GRAMS (4)	INSTANT(5) WT. CHANGE GRAMS (5)	INSTANT(4) MASS,I FLUX mG/SQM-h
0.2974	0.1156	0.0462	20.7426	20.74264	-7.00E-04	-1.00E-03	-1.13E-03	-0.8179
-0.2734	-0.1070	-0.1337	22.0572	22.05730	-3.00E-04	-1.60E-03	-7.00E-04	-0.3357
OUT	OUT	OUT	22.5920	22.59147	IN	IN	IN	IN
0.1253	0.0487	0.1329	22.2171	22.21720	-5.00E-04	-6.00E-04	-7.50E-04	-0.5593
-0.7695	-0.2999	-0.2686	21.8120	21.81212	-4.00E-04	-1.70E-03	-6.10E-04	-0.4513
0.2063	0.0811	0.1280	22.9419	22.94224	-1.10E-03	-2.60E-03	-1.13E-03	-1.1734
-0.6147	-0.2400	-0.2666	22.2434	22.24351	1.00E-04	-2.10E-03	-2.70E-04	0.1118
-0.4145	-0.1611	-0.1342	21.7875	21.78759	-4.00E-04	-2.30E-03	-5.90E-04	-0.4524
-0.0789	-0.0308	0.0000	22.3913	22.39150	-6.00E-04	-2.30E-03	-7.80E-04	-0.6646
-0.5059	-0.1972	-0.2689	21.8785	21.87868	-7.00E-04	-8.00E-04	-1.02E-03	-0.7906
-0.7572	-0.2945	-0.1812	21.0680	21.06830	-1.40E-03	-3.70E-03	-1.12E-03	-1.6020
-1.1890	-0.4648	-0.4469	21.8347	21.83480	-7.00E-04	-3.50E-03	-1.06E-03	-0.7862
-1.0052	-0.3918	-0.4452	22.1951	22.19530	-8.00E-04	-2.50E-03	-1.08E-03	-0.8976
-1.2541	-0.4910	-0.3981	22.0477	22.04780	-9.00E-04	-2.70E-03	-1.09E-03	-0.9988
0.0815	0.0318	0.0000	21.6265	21.62666	-3.00E-04	-2.00E-04	-5.70E-04	-0.3432
0.1934	0.0754	0.0887	22.2491	22.24932	-2.00E-04	-3.00E-04	-3.70E-04	-0.2235
0.7129	0.2774	0.2685	22.2633	22.26333	-1.00E-04	8.00E-04	-3.80E-04	-0.1130
OUT	OUT	OUT	OUT	OUT	OUT	OUT	OUT	OUT
0.1924	0.0751	-0.0442	22.2852	22.28505	3.00E-04	8.00E-04	-2.70E-04	0.3335
0.2806	0.1098	0.1756	22.5749	22.57513	2.00E-04	1.40E-03	2.00E-04	0.2205
0.1496	0.0583	0.1345	22.1635	22.16359	2.00E-04	0.00E+00	-1.00E-05	0.2262
0.1666	0.0653	0.0871	22.6805	22.68079	5.00E-04	2.00E-03	3.60E-04	0.5455
-1.3377	-0.5216	-0.4497	21.7662	21.76642	-1.00E-03	-2.60E-03	-1.04E-03	-1.1328
OUT	OUT	OUT	OUT	OUT	OUT	OUT	OUT	OUT
-0.6526	-0.2545	-0.1786	21.9468	21.94691	-1.20E-03	-1.80E-03	-1.40E-03	-1.3497
-0.6894	-0.2685	-0.2731	21.4988	21.49877	-6.00E-04	-2.70E-03	-9.90E-04	-0.6886
-0.8114	-0.3161	-0.3613	21.8643	21.86458	-4.00E-04	-2.40E-03	-5.30E-04	-0.4554
-0.3593	-0.1401	-0.1808	21.7167	21.71677	-5.00E-04	-2.10E-03	-8.90E-04	-0.5693
-0.7187	-0.2800	-0.2222	22.0662	22.06625	-3.00E-04	-2.40E-03	-5.40E-04	-0.3362
-1.4110	-0.5487	-0.3628	21.7190	21.71932	-9.00E-04	-3.00E-03	-7.00E-04	-1.0310
-1.4036	-0.5495	-0.8204	21.9344	21.93463	-5.00E-04	-2.50E-03	-6.70E-04	-0.5560
-1.2417	-0.4840	-0.4884	22.3315	22.33156	-1.10E-03	-3.20E-03	-1.34E-03	-1.2309
-0.2750	-0.1071	-0.0893	22.0442	22.04433	-2.00E-04	-2.40E-03	-3.90E-04	-0.2251
-0.5515	-0.2161	-0.3891	22.9353	22.93562	-1.00E-04	-2.90E-03	-2.50E-04	-0.1084
-0.3059	-0.1196	-0.0886	22.1517	22.15194	-1.00E-04	-2.50E-03	-2.50E-04	-0.1113
-0.6590	-0.2568	-0.2703	21.8169	21.81706	-2.00E-04	-1.70E-03	-5.00E-04	-0.2271
-0.6788	-0.2648	-0.2244	21.9474	21.94749	-5.00E-04	-3.10E-03	-7.60E-04	-0.5651
-0.6613	-0.2575	-0.1807	21.9818	21.98202	-5.00E-04	-3.00E-03	-5.70E-04	-0.5698
-0.3575	-0.1394	-0.1349	21.7678	21.76786	-4.00E-04	-3.20E-03	-7.50E-04	-0.4531
-0.0794	-0.0310	-0.0887	22.3198	22.31974	-2.00E-04	-2.20E-03	-8.10E-04	-0.2230
-0.8623	-0.3375	-0.1753	22.4968	22.49692	-8.00E-04	-3.20E-03	-7.50E-04	-0.8801
-0.2329	-0.0911	-0.0868	22.8306	22.83076	-5.00E-04	-2.60E-03	-7.30E-04	-0.5448
0.1064	0.0423	0.0000	26.5205	26.52084	-7.00E-04	-2.50E-03	-8.00E-04	-0.6653
-0.2600	-0.1018	-0.1328	21.9427	21.94260	-1.00E-04	2.30E-03	-4.10E-04	-0.1111
OUT	OUT	OUT	23.0611	23.06104	IN	IN	IN	IN
0.3233	0.1257	0.0898	21.9755	21.97569	-3.00E-04	1.90E-03	-5.40E-04	-0.3403

Table C.1 Raw Weighing Data for GEB-1 (continued)

21-Sep-87 2505.0	21-Sep-87 2505.0	21-Sep-87 2505.0	21-Sep-87 2505.0	21-Sep-87 2505.0	17-Oct-87 3040.0	17-Oct-87 3040.0	17-Oct-87 3040.0	17-Oct-87 3040.0
OVERALL(4) MASS,I FLUX mG/SQM-h	OVERALL(4) MASS,t FLUX mG/SQM-h	INSTANT(5) MASS,I FLUX mG/SQM-h	INSTANT(5) MASS,t FLUX mG/SQM-h	INSTANT(4) MASS,t FLUX mG/SQM-h	PULL#8 GRAMS(4)	PULL#8 GRAMS(5)	INSTANT(4) WT. CHANGE GRAMS (4)	OVERALL(4) WT. CHANGE GRAMS (4)
-0.2374	-0.0923	-1.3204	-0.5132	-0.3179	20.7428	20.74264	2.00E-04	-8.00E-04
-0.3638	-0.1424	-0.7833	-0.3066	-0.1314	OUT	OUT	OUT	OUT
IN	IN	IN	IN	IN	22.5908	22.59076	-1.20E-03	-1.20E-03
-0.1364	-0.0531	-0.8389	-0.3265	-0.2176	22.2175	22.21740	4.00E-04	-2.00E-04
-0.3897	-0.1519	-0.6882	-0.2682	-0.1759	21.8124	21.81218	4.00E-04	-1.30E-03
-0.5836	-0.2214	-1.2054	-0.4736	-0.4610	22.9424	22.94237	5.00E-04	-2.10E-03
-0.4772	-0.1863	-0.3019	-0.1179	0.0437	22.2434	22.24351	0.00E+00	-2.10E-03
-0.5286	-0.2054	-0.6673	-0.2593	-0.1758	21.7876	21.78738	1.00E-04	-2.20E-03
-0.5176	-0.2020	-0.8639	-0.3372	-0.2594	22.3912	22.39140	-1.00E-04	-2.40E-03
-0.1836	-0.0716	-1.1520	-0.4490	-0.3081	21.8794	21.87915	9.00E-04	1.00E-04
-0.8603	-0.3346	-1.2816	-0.4985	-0.6231	21.0691	21.06888	1.10E-03	-2.60E-03
-0.7987	-0.3122	-1.1905	-0.4653	-0.3073	21.8358	21.83561	1.10E-03	-2.40E-03
-0.5700	-0.2221	-1.2118	-0.4723	-0.3498	22.1962	22.19608	1.10E-03	-1.40E-03
-0.6089	-0.2384	-1.2097	-0.4736	-0.3911	22.0490	22.04879	1.30E-03	-1.40E-03
-0.0465	-0.0181	-0.6520	-0.2542	-0.1338	21.6276	21.62746	1.10E-03	9.00E-04
-0.0681	-0.0266	-0.4135	-0.1613	-0.0872	22.2500	22.25000	9.00E-04	6.00E-04
0.1836	0.0715	-0.4292	-0.1670	-0.0440	22.2644	22.26453	1.10E-03	1.90E-03
OUT	OUT	OUT	OUT	OUT	OUT	OUT	OUT	OUT
0.2976	0.1162	-0.3001	-0.1172	0.1302	22.2860	22.28575	8.00E-04	1.60E-03
0.3136	0.1227	0.2205	0.0863	0.0863	22.5754	22.57545	5.00E-04	1.90E-03
0.0000	0.0000	-0.0113	-0.0044	0.0881	22.1639	22.16377	4.00E-04	4.00E-04
0.4434	0.1739	0.3928	0.1540	0.2139	22.6812	22.68125	7.00E-04	2.70E-03
-0.5985	-0.2334	-1.1781	-0.4594	-0.4417	21.7666	21.76660	4.00E-04	-2.20E-03
OUT	OUT	OUT	OUT	OUT	OUT	OUT	OUT	OUT
-0.6775	-0.2642	-1.5747	-0.6141	-0.5263	21.9474	21.94728	6.00E-04	-1.20E-03
-0.6297	-0.2453	-1.1363	-0.4426	-0.2682	21.4995	21.49953	7.00E-04	-2.00E-03
-0.5553	-0.2163	-0.6035	-0.2351	-0.1774	21.8651	21.86503	8.00E-04	-1.80E-03
-0.4858	-0.1894	-1.0133	-0.3951	-0.2220	21.7170	21.71708	3.00E-04	-1.80E-03
-0.5465	-0.2129	-0.6051	-0.2358	-0.1310	22.0666	22.06648	4.00E-04	-2.00E-03
-0.6983	-0.2715	-0.8019	-0.3118	-0.4009	21.7198	21.71954	8.00E-04	-2.20E-03
-0.5649	-0.2211	-0.7450	-0.2916	-0.2176	21.9347	21.93466	3.00E-04	-2.20E-03
-0.7276	-0.2836	-1.4994	-0.5844	-0.4798	22.3317	22.33166	2.00E-04	-3.00E-03
-0.5488	-0.2139	-0.4389	-0.1710	-0.0877	22.0445	22.04445	3.00E-04	-2.10E-03
-0.6385	-0.2502	-0.2709	-0.1062	-0.0425	22.9356	22.93550	3.00E-04	-2.60E-03
-0.5653	-0.2211	-0.2782	-0.1088	-0.0435	22.1518	22.15174	1.00E-04	-2.40E-03
-0.3923	-0.1529	-0.5679	-0.2213	-0.0885	21.8171	21.81716	2.00E-04	-1.50E-03
-0.7119	-0.2777	-0.8589	-0.3350	-0.2204	21.9478	21.94778	4.00E-04	-2.70E-03
-0.6947	-0.2705	-0.6496	-0.2530	-0.2219	21.9826	21.98254	8.00E-04	-2.20E-03
-0.7366	-0.2871	-0.8496	-0.3312	-0.1766	21.7685	21.76835	7.00E-04	-2.50E-03
-0.4984	-0.1948	-0.9030	-0.3529	-0.0871	22.3204	22.32037	6.00E-04	-1.60E-03
-0.7153	-0.2800	-0.8251	-0.3229	-0.3444	22.4973	22.49728	5.00E-04	-2.70E-03
-0.5756	-0.2252	-0.7954	-0.3112	-0.2132	22.8315	22.83131	9.00E-04	-1.70E-03
-0.4828	-0.1919	-0.7603	-0.3022	-0.2644	26.5214	26.52142	9.00E-04	-1.60E-03
0.5190	0.2032	-0.4554	-0.1783	-0.0435	OUT	OUT	OUT	OUT
IN	IN	IN	IN	IN	23.0606	23.06040	-5.00E-04	-5.00E-04
0.4379	0.1703	-0.6125	-0.2382	-0.1323	21.9756	21.97550	1.00E-04	2.00E-03

Table C.1 Raw Weighing Data for GEB-1 (continued)

17-Oct-87	17-Oct-87	17-Oct-87	17-Oct-87	17-Oct-87	17-Oct-87	17-Oct-87
3040.0	3040.0	3040.0	3040.0	3040.0	3040.0	3040.0
INSTANT(5) WT. CHANGE GRAMS (5)	INSTANT(4) MASS,I FLUX mG/SQM-h	OVERALL(4) MASS,I FLUX mG/SQM-h	OVERALL(4) MASS,t FLUX mG/SQM-h	INSTANT(5) MASS,I FLUX mG/SQM-h	INSTANT(5) MASS,t FLUX mG/SQM-h	INSTANT(4) MASS,t FLUX mG/SQM-h
0.00E+00	0.2223	-0.1565	-0.0608	0.0000	0.0000	0.0864
OUT	OUT	OUT	OUT	OUT	OUT	OUT
-7.10E-04	-1.2673	-1.2673	-0.4967	-0.7498	-0.2939	-0.4967
2.00E-04	0.4257	-0.0375	-0.0146	0.2128	0.0828	0.1657
6.00E-05	0.4294	-0.2456	-0.0957	0.0644	0.0251	0.1674
1.30E-04	0.5074	-0.3751	-0.1474	0.1319	0.0518	0.1994
0.00E+00	0.0000	-0.3932	-0.1535	0.0000	0.0000	0.0000
-2.10E-04	0.1076	-0.4166	-0.1619	-0.2260	-0.0878	0.0418
-1.00E-04	-0.1054	-0.4451	-0.1737	-0.1054	-0.0411	-0.0411
4.70E-04	0.9671	0.0189	0.0074	0.5050	0.1968	0.3769
5.80E-04	1.1975	-0.4981	-0.1937	0.6314	0.2456	0.4658
8.10E-04	1.1753	-0.4513	-0.1764	0.8655	0.3383	0.4594
7.80E-04	1.1742	-0.2630	-0.1025	0.8326	0.3245	0.4577
9.90E-04	1.3726	-0.2602	-0.1019	1.0453	0.4093	0.5374
8.00E-04	1.1972	0.1724	0.0672	0.8707	0.3394	0.4666
6.80E-04	0.9568	0.1123	0.0438	0.7229	0.2820	0.3732
1.20E-03	1.1821	0.3593	0.1398	1.2896	0.5018	0.4600
OUT	OUT	OUT	OUT	OUT	OUT	OUT
7.00E-04	0.8460	0.4403	0.1720	0.7403	0.2891	0.3304
3.20E-04	0.5244	0.3507	0.1372	0.3356	0.1313	0.2052
1.80E-04	0.4303	0.0757	0.0295	0.1936	0.0754	0.1676
4.60E-04	0.7266	0.4933	0.1934	0.4775	0.1872	0.2849
1.80E-04	0.4311	-0.4173	-0.1627	0.1940	0.0756	0.1681
OUT	OUT	OUT	OUT	OUT	OUT	OUT
3.70E-04	0.6421	-0.3341	-0.1303	0.3959	0.1544	0.2504
7.60E-04	0.7644	-0.3843	-0.1497	0.8299	0.3232	0.2977
4.50E-04	0.8666	-0.3050	-0.1188	0.4875	0.1899	0.3376
2.90E-04	0.3250	-0.3431	-0.1338	0.3141	0.1225	0.1267
2.30E-04	0.4265	-0.3753	-0.1462	0.2452	0.0955	0.1662
2.20E-04	0.8719	-0.4220	-0.1641	0.2398	0.0932	0.3390
3.00E-05	0.3174	-0.4096	-0.1603	0.0317	0.0124	0.1242
1.00E-04	0.2129	-0.5621	-0.2191	0.1065	0.0415	0.0830
1.20E-04	0.3212	-0.3957	-0.1542	0.1285	0.0501	0.1252
-1.20E-04	0.3093	-0.4717	-0.1849	-0.1237	-0.0485	0.1212
-2.00E-04	0.1059	-0.4472	-0.1749	-0.2118	-0.0828	0.0414
1.00E-04	0.2161	-0.2852	-0.1112	0.1081	0.0421	0.0842
2.90E-04	0.4301	-0.5109	-0.1993	0.3118	0.1216	0.1678
5.20E-04	0.8674	-0.4198	-0.1635	0.5638	0.2195	0.3378
4.90E-04	0.7544	-0.4742	-0.1849	0.5281	0.2059	0.2941
6.30E-04	0.6364	-0.2987	-0.1167	0.6682	0.2611	0.2487
3.60E-04	0.5233	-0.4973	-0.1946	0.3768	0.1475	0.2048
5.50E-04	0.9329	-0.3101	-0.1214	0.5701	0.2231	0.3651
5.80E-04	0.8138	-0.2546	-0.1012	0.5244	0.2084	0.3234
OUT	OUT	OUT	OUT	OUT	OUT	OUT
-6.40E-04	-0.5157	-0.5157	-0.2029	-0.6601	-0.2597	-0.2029
-1.90E-04	0.1079	0.3798	0.1477	-0.2050		

Table C.1 Raw Weighing Data for GEB-1 (continued)

SPECIMEN ID#		OA LENGTH INCHES	ACTIVE LNTH METERS	POSITION METERS	ID-MALE INCHES	OD-MALE INCHES	ID-FEMALE INCHES	OD-FEMALE INCHES	INNER AREA SQ. METERS
H-01	BHL	1.4932	0.0348	0.0348	0.6330	0.6710	0.6794	0.7528	1.755E-03
H-02	HL	1.4956	0.0348	0.0696	0.6328	0.6710	0.6790	0.7524	1.758E-03
H-03	HL	1.4702	0.0342	0.1037	0.6330	0.6700	0.6800	0.7520	1.726E-03
H-04	HL	1.4868	0.0346	0.1383	0.6330	0.6710	0.6790	0.7530	1.747E-03
H-05	HL	1.4700	0.0342	0.1725	0.6336	0.6700	0.6792	0.7530	1.727E-03
H-06	HL	1.4690	0.0341	0.2066	0.6328	0.6700	0.6790	0.7534	1.724E-03
H-07	HL	1.4366	0.0333	0.2399	0.6332	0.6712	0.6788	0.7520	1.683E-03
H-08	HL	1.4722	0.0342	0.2742	0.6330	0.6702	0.6790	0.7524	1.728E-03
H-09	HL	1.4954	0.0348	0.3090	0.6332	0.6700	0.6788	0.7526	1.759E-03
H-10	HL	1.4970	0.0348	0.3438	0.6324	0.6708	0.6794	0.7518	1.759E-03
H-11	HL	1.6244	0.0381	0.3819	0.6330	0.6704	0.6782	0.7522	1.924E-03
H-12	HL	1.4946	0.0348	0.4167	0.6330	0.6710	0.6784	0.7530	1.757E-03
H-13	HL	1.4000	0.0324	0.4491	0.6336	0.6710	0.6786	0.7524	1.637E-03
H-14	HL	1.2680	0.0290	0.4781	0.6320	0.6718	0.6808	0.7526	1.464E-03
H-15	HL	1.4684	0.0341	0.5122	0.6336	0.6700	0.6790	0.7522	1.725E-03
H-16	HL	1.4772	0.0343	0.5466	0.6338	0.6710	0.6790	0.7520	1.737E-03
H-17	HL	1.5004	0.0349	0.5815	0.6320	0.6720	0.6788	0.7522	1.762E-03
H-18	HL	1.5004	0.0349	0.6164	0.6332	0.6708	0.6808	0.7522	1.765E-03
H-18.1	HL	1.5048	0.0350	0.6166	0.6320	0.6702	0.6780	0.7500	1.767E-03
H-19	HL	1.4682	0.0341	0.6507	0.6330	0.6714	0.6786	0.7520	1.723E-03
H-20	THL	1.4666	0.0341	0.6847	0.6322	0.6718	0.6780	0.7530	1.719E-03
H-21	BCL	1.4940	0.0348	0.0348	0.6338	0.6708	0.6808	0.7520	1.759E-03
H-22	CL	1.4582	0.0339	0.0686	0.6334	0.6710	0.6780	0.7520	1.712E-03
H-22.1	CL	1.4652	0.0340	0.0688	0.6342	0.6701	0.6782	0.7501	1.723E-03
H-23	CL	1.5266	0.0356	0.1044	0.6332	0.6710	0.6800	0.7522	1.799E-03
H-24	CL	1.5020	0.0350	0.1394	0.6332	0.6710	0.6788	0.7530	1.767E-03
H-25	CL	1.5094	0.0352	0.1746	0.6332	0.6710	0.6784	0.7522	1.777E-03
H-26	CL	1.4682	0.0341	0.2087	0.6330	0.6710	0.6780	0.7530	1.723E-03
H-27	CL	1.4778	0.0344	0.2430	0.6346	0.6710	0.6790	0.7520	1.740E-03
H-28	CL	1.4632	0.0340	0.2770	0.6336	0.6710	0.6804	0.7518	1.719E-03
H-29	CL	1.4984	0.0349	0.3119	0.6332	0.6708	0.6802	0.7526	1.763E-03
H-30	CL	1.4956	0.0348	0.3467	0.6330	0.6710	0.6790	0.7522	1.758E-03
H-31	CL	1.4730	0.0342	0.3810	0.6340	0.6718	0.6800	0.7520	1.732E-03
H-32	CL	1.4978	0.0349	0.4158	0.6338	0.6718	0.6790	0.7522	1.764E-03
H-33	CL	1.4886	0.0346	0.4505	0.6330	0.6702	0.6790	0.7528	1.750E-03
H-34	CL	1.4850	0.0345	0.4850	0.6330	0.6710	0.6784	0.7528	1.745E-03
H-35	CL	1.4292	0.0331	0.5181	0.6330	0.6710	0.6790	0.7522	1.673E-03
H-36	CL	1.5008	0.0349	0.5531	0.6330	0.6714	0.6804	0.7528	1.765E-03
H-37	CL	1.5022	0.0350	0.5881	0.6330	0.6700	0.6784	0.7522	1.767E-03
H-38	CL	1.4812	0.0344	0.6225	0.6320	0.6710	0.6790	0.7520	1.737E-03
H-39	CL	1.5152	0.0353	0.6578	0.6328	0.6706	0.6780	0.7528	1.783E-03
H-40	CL	1.4828	0.0345	0.6923	0.6330	0.6718	0.6790	0.7526	1.742E-03
H-41	CL	1.5010	0.0350	0.7273	0.6330	0.6710	0.6788	0.7522	1.765E-03
H-42	TCL	1.4750	0.0343	0.7616	0.6334	0.6700	0.6782	0.7532	1.733E-03

Table C.2 Raw Weighing Data for GEB-2

				DATE	28-Jun-87	28-Jun-87	30-Jun-87	30-Jun-87	30-Jun-87
				HOURS	0.0	0.0	95.0	95.0	95.0
OUTER AREA SQ. METERS	TOTAL AREA SQ. METERS	WALL THKNS M	TEMP K	TEMP C	INITIAL WEIGHT GRAMS(4)	INITIAL WEIGHT GRAMS(5)	PULL#1 GRAMS(4)	PULL#1 GRAMS(5)	INSTANT WT. CHANGE GRAMS(4)
2.088E-03	4.505E-03	1.521E-03	801.6	528.6	22.3026	22.30324	22.3076	22.30885	5.00E-03
2.090E-03	4.509E-03	1.519E-03	808.2	535.2	22.4562	22.45670	22.4566	22.45825	4.00E-04
2.050E-03	4.438E-03	1.511E-03	814.7	541.7	21.9307	21.93118	21.9307	21.93160	0.00E+00
2.078E-03	4.488E-03	1.524E-03	821.3	548.3	22.2448	22.24542	22.2446	22.24516	-2.00E-04
2.053E-03	4.441E-03	1.516E-03	827.7	554.7	21.8780	21.87865	21.8772	21.87797	-8.00E-04
2.052E-03	4.440E-03	1.532E-03	834.2	561.2	22.0560	22.05665	22.0545	22.05558	-1.50E-03
1.999E-03	4.342E-03	1.509E-03	840.6	567.6	21.2751	21.27560	21.2735	21.27451	-1.60E-03
2.054E-03	4.443E-03	1.516E-03	847.0	574.0	21.9888	21.98974	21.9871	21.98844	-1.70E-03
2.090E-03	4.510E-03	1.516E-03	853.7	580.7	22.3651	22.36565	22.3633	22.36394	-1.80E-03
2.091E-03	4.510E-03	1.516E-03	860.3	587.3	22.4776	22.47805	22.4754	22.47613	-2.20E-03
2.286E-03	4.869E-03	1.514E-03	867.5	594.5	24.4438	24.44436	24.4390	24.44170	-4.80E-03
2.090E-03	4.510E-03	1.524E-03	874.1	601.1	22.3170	22.31778	22.3148	22.31535	-2.20E-03
1.944E-03	4.241E-03	1.509E-03	880.3	607.3	20.6384	20.63881	20.6357	20.63633	-2.70E-03
1.744E-03	3.872E-03	1.532E-03	885.8	612.8	18.5854	18.58625	18.5834	18.58416	-2.00E-03
2.048E-03	4.432E-03	1.506E-03	892.2	619.2	21.7257	21.72594	21.7224	21.72310	-3.30E-03
2.061E-03	4.456E-03	1.501E-03	898.8	625.8	21.8742	21.87493	21.8706	21.87149	-3.60E-03
2.097E-03	4.522E-03	1.527E-03	905.4	632.4	22.5750	22.57561	22.5709	22.57171	-4.10E-03
2.097E-03	4.522E-03	1.511E-03	912.0	639.0	22.3699	22.37058	22.3648	22.36558	-5.10E-03
2.097E-03	4.521E-03	1.499E-03	912.1	639.1	22.5447	N/A	OUT	OUT	OUT
2.047E-03	4.430E-03	1.511E-03	918.5	645.5	21.9418	21.94233	21.9357	21.93648	-6.10E-03
2.048E-03	4.431E-03	1.534E-03	925.0	652.0	22.1787	22.17913	22.1702	22.17088	-8.50E-03
2.087E-03	4.503E-03	1.501E-03	803.0	530.0	22.2013	22.20208	22.2036	22.20414	2.30E-03
2.032E-03	4.402E-03	1.506E-03	807.9	534.9	22.5518	22.55220	22.5530	22.55418	1.20E-03
2.038E-03	4.411E-03	1.472E-03	807.9	534.9	21.6435	N/A	OUT	OUT	OUT
2.137E-03	4.596E-03	1.511E-03	813.1	540.1	22.2951	22.29632	22.2975	22.29824	2.40E-03
2.102E-03	4.531E-03	1.521E-03	818.1	545.1	22.5501	22.55093	22.5522	22.55268	2.10E-03
2.111E-03	4.547E-03	1.511E-03	823.2	550.2	21.7192	21.71980	21.7200	21.72151	8.00E-04
2.050E-03	4.435E-03	1.524E-03	828.1	555.1	21.9943	21.99522	21.9951	21.99678	8.00E-04
2.062E-03	4.458E-03	1.491E-03	833.1	560.1	21.7166	21.71712	21.7170	21.71869	4.00E-04
2.039E-03	4.415E-03	1.499E-03	838.0	565.0	21.8783	21.87897	21.8796	21.88040	1.30E-03
2.095E-03	4.519E-03	1.516E-03	843.1	570.1	22.3310	22.33211	22.3328	22.33357	1.80E-03
2.090E-03	4.508E-03	1.514E-03	848.1	575.1	22.4261	22.42661	22.4271	22.42808	1.00E-03
2.055E-03	4.445E-03	1.499E-03	853.0	580.0	21.7288	21.72951	21.7303	21.73102	1.50E-03
2.093E-03	4.515E-03	1.504E-03	858.1	585.1	22.1942	22.19483	22.1957	22.19647	1.50E-03
2.081E-03	4.492E-03	1.521E-03	863.1	590.1	22.2028	22.20339	22.2035	22.20502	7.00E-04
2.075E-03	4.482E-03	1.521E-03	868.1	595.1	22.1573	22.15756	22.1578	22.15906	5.00E-04
1.988E-03	4.322E-03	1.514E-03	872.8	599.8	21.3089	21.30976	21.3105	21.31128	1.60E-03
2.099E-03	4.527E-03	1.521E-03	877.9	604.9	22.4128	22.41342	22.4127	22.41458	-1.00E-04
2.100E-03	4.526E-03	1.514E-03	882.9	609.9	22.3953	22.39579	22.3957	22.39653	4.00E-04
2.067E-03	4.466E-03	1.524E-03	887.9	614.9	22.1140	22.11449	22.1133	22.11459	-7.00E-04
2.121E-03	4.566E-03	1.524E-03	893.0	620.0	22.6098	22.61057	22.6090	22.61018	-8.00E-04
2.071E-03	4.475E-03	1.519E-03	898.0	625.0	22.1366	22.13729	22.1352	22.13631	-1.40E-03
2.098E-03	4.523E-03	1.514E-03	903.0	630.0	22.5488	22.54935	22.5466	22.54761	-2.20E-03
2.061E-03	4.455E-03	1.521E-03	908.0	635.0	22.0725	22.07336	22.0698	22.07072	-2.70E-03

Table C.2 Raw Weighing Data for GEB-2 (continued)

30-Jun-87	30-Jun-87	10-Jul-87	10-Jul-87	10-Jul-87	10-Jul-87	10-Jul-87	10-Jul-87	10-Jul-87
95.0	95.0	292.0	292.0	292.0	292.0	292.0	292.0	292.0
INSTANT(4) MASS,I FLUX mG/SQM-h	INSTANT MASS,I FLUX mG/SQM-h	PULL #2 GRAMS(4)	INSTANT WT. CHANGE GRAMS	INSTANT(4) MASS,I FLUX mG/SQM-h	INSTANT(4) MASS,I FLUX mG/SQM-h	OVERALL WT. CHANGE GRAMS(4)	OVERALL(4) MASS,I FLUX mG/SQM-h	OVERALL(4) MASS,I FLUX mG/SQM-h
29.9831	11.6831	22.3140	6.40E-03	18.5073	7.2115	1.14E-02	22.2409	8.6663
2.3952	0.9337	22.4591	2.50E-03	7.2190	2.8143	2.90E-03	5.6496	2.2024
0.0000	0.0000	21.9314	7.00E-04	2.0588	0.8011	7.00E-04	1.3890	0.5404
-1.2050	-0.4691	22.2447	1.00E-04	0.2905	0.1131	-1.00E-04	-0.1960	-0.0763
-4.8754	-1.8964	21.8768	-4.00E-04	-1.1755	-0.4573	-1.20E-03	-2.3793	-0.9255
-9.1598	-3.5565	22.0535	-1.00E-03	-2.9448	-1.1434	-2.50E-03	-4.9668	-1.9285
-10.0055	-3.8792	21.2727	-8.00E-04	-2.4125	-0.9353	-2.40E-03	-4.8828	-1.8931
-10.3532	-4.0273	21.9863	-8.00E-04	-2.3495	-0.9139	-2.50E-03	-4.9534	-1.9269
-10.7732	-4.2017	22.3614	-1.90E-03	-5.4838	-2.1387	-3.70E-03	-7.2047	-2.8099
-13.1685	-5.1350	22.4735	-1.90E-03	-5.4843	-2.1386	-4.10E-03	-7.9843	-3.1135
-26.2651	-10.3762	24.4387	-3.00E-04	-0.7916	-0.3127	-5.10E-03	-9.0792	-3.5868
-13.1791	-5.1351	22.3124	-2.40E-03	-6.9332	-2.7014	-4.60E-03	-8.9652	-3.4932
-17.3579	-6.7016	20.6333	-2.40E-03	-7.4405	-2.8727	-5.10E-03	-10.6671	-4.1184
-14.3789	-5.4369	18.5816	-1.80E-03	-6.2406	-2.3597	-3.80E-03	-8.8883	-3.3608
-20.1351	-7.8383	21.7193	-3.10E-03	-9.1213	-3.5508	-6.40E-03	-12.7046	-4.9457
-21.8157	-8.5046	21.8664	-4.20E-03	-12.2736	-4.7847	-7.80E-03	-15.3781	-5.9950
-24.4961	-9.5445	22.5663	-4.60E-03	-13.2534	-5.1640	-8.70E-03	-16.9112	-6.5892
-30.4130	-11.8713	22.3582	-6.60E-03	-18.9798	-7.4085	-1.17E-02	-22.6995	-8.8604
OUT	OUT	OUT	OUT	OUT	OUT	OUT	OUT	OUT
-37.2602	-14.4934	21.9292	-6.50E-03	-19.1463	-7.4475	-1.26E-02	-25.0395	-9.7398
-52.0476	-20.1924	22.1622	-8.00E-03	-23.6227	-9.1647	-1.65E-02	-32.8705	-12.7525
13.7668	5.3761	22.2078	4.20E-03	12.1230	4.7342	6.50E-03	12.6578	4.9431
7.3802	2.8695	22.5580	5.00E-03	14.8291	5.7657	6.20E-03	12.4056	4.8234
OUT	OUT	OUT	OUT	OUT	OUT	OUT	OUT	OUT
14.0445	5.4972	22.3016	4.10E-03	11.5701	4.5287	6.50E-03	12.3751	4.8438
12.5085	4.8790	22.5556	3.40E-03	9.7661	3.8093	5.50E-03	10.6583	4.1573
4.7397	1.8520	21.7242	4.20E-03	11.9995	4.6888	5.00E-03	9.6376	3.7659
4.8866	1.8986	21.9998	4.70E-03	13.8443	5.3789	5.50E-03	10.9300	4.2466
2.4198	0.9445	21.7216	4.60E-03	13.4196	5.2381	5.00E-03	9.8409	3.8413
7.9628	3.0998	21.8827	3.10E-03	9.1568	3.5646	4.40E-03	8.7683	3.4133
10.7496	4.1932	22.3356	2.80E-03	8.0637	3.1455	4.60E-03	8.9376	3.4863
5.9861	2.3349	22.4300	2.90E-03	8.3714	3.2653	3.90E-03	7.5954	2.9626
9.1153	3.5525	21.7330	2.70E-03	7.9123	3.0836	4.20E-03	8.3037	3.2362
8.9535	3.4970	22.1981	2.40E-03	6.9083	2.8982	3.90E-03	7.5737	2.9581
4.2112	1.6403	22.2065	3.00E-03	8.7033	3.3900	3.70E-03	7.2418	2.8208
3.0164	1.1744	22.1600	2.20E-03	6.4002	2.4918	2.70E-03	5.2993	2.0632
10.0654	3.8970	21.3120	1.50E-03	4.5505	1.7618	3.10E-03	6.3447	2.4565
-0.5963	-0.2325	22.4147	2.00E-03	5.7516	2.2428	1.90E-03	3.6863	1.4374
2.3830	0.9303	22.3963	6.00E-04	1.7237	0.6729	1.00E-03	1.9382	0.7566
-4.2415	-1.6497	22.1136	3.00E-04	0.8766	0.3410	-4.00E-04	-0.7885	-0.3067
-4.7229	-1.8442	22.6083	-7.00E-04	-1.9928	-0.7782	-1.50E-03	-2.8810	-1.1250
-8.4596	-3.2932	22.1344	-8.00E-04	-2.3311	-0.9075	-2.20E-03	-4.3250	-1.6837
-13.1178	-5.1196	22.5451	-1.50E-03	-4.3131	-1.6833	-3.70E-03	-7.1776	-2.8013
-16.3988	-6.3790	22.0677	-2.10E-03	-6.1507	-2.3926	-4.80E-03	-9.4848	-3.6895

Table C.2 Raw Weighing Data for GEB-2 (continued)

21-Jul-87 459.0	21-Jul-87 459.0	21-Jul-87 459.0	21-Jul-87 459.0	21-Jul-87 459.0	21-Jul-87 459.0	21-Jul-87 459.0	28-Aug-87 1014.0	28-Aug-87 1014.0
PULL#3 GRAMS(4)	INSTANT WT. CHANGE GRAMS(4)	INSTANT(4) MASS,I FLUX mG/SQM-h	INSTANT(4) MASS,t FLUX mG/SQM-h	OVERALL WT. CHANGE GRAMS(4)	OVERALL(4) MASS,I FLUX mG/SQM-h	OVERALL(4) MASS,t FLUX mG/SQM-h	PULL #4 GRAMS(4)	INSTANT WT. CHANGE GRAMS(4)
22.3166	2.60E-03	8.8692	3.4560	1.40E-02	1.74E+01	6.77E+00	22.3276	1.10E-02
22.4616	2.50E-03	8.5159	3.3198	5.40E-03	6.69E+00	2.61E+00	22.4643	2.70E-03
21.9337	2.30E-03	7.9800	3.1049	3.00E-03	3.79E+00	1.47E+00	21.9340	3.00E-04
22.2468	2.10E-03	7.1973	2.8019	2.00E-03	2.49E+00	9.71E-01	22.2454	-1.40E-03
21.8787	1.90E-03	6.5869	2.5621	7.00E-04	8.83E-01	3.43E-01	21.8764	-2.30E-03
22.0553	1.80E-03	6.2528	2.4278	-7.00E-04	-8.85E-01	-3.44E-01	22.0527	-2.60E-03
21.2736	9.00E-04	3.2016	1.2413	-1.50E-03	-1.94E+00	-7.53E-01	21.2709	-2.70E-03
21.9870	7.00E-04	2.4251	0.9434	-1.80E-03	-2.27E+00	-8.83E-01	21.9848	-2.20E-03
22.3623	9.00E-04	3.0642	1.1951	-2.80E-03	-3.47E+00	-1.35E+00	22.3584	-3.90E-03
22.4743	8.00E-04	2.7240	1.0622	-3.30E-03	-4.09E+00	-1.59E+00	22.4700	-4.30E-03
24.4397	1.00E-03	3.1128	1.2297	-4.10E-03	-4.64E+00	-1.83E+00	24.4340	-5.70E-03
22.3124	0.00E+00	0.0000	0.0000	-4.60E-03	-5.70E+00	-2.22E+00	22.3068	-5.60E-03
20.6334	1.00E-04	0.3657	0.1412	-5.00E-03	-6.65E+00	-2.57E+00	20.6277	-5.70E-03
18.5815	-1.00E-04	-0.4090	-0.1546	-3.90E-03	-5.80E+00	-2.19E+00	18.5770	-4.50E-03
21.7193	0.00E+00	0.0000	0.0000	-6.40E-03	-8.08E+00	-3.15E+00	21.7116	-7.70E-03
21.8666	2.00E-04	0.6895	0.2688	-7.60E-03	-9.53E+00	-3.72E+00	21.8571	-9.50E-03
22.5660	-3.00E-04	-1.0196	-0.3973	-9.00E-03	-1.11E+01	-4.34E+00	22.5555	-1.05E-02
22.3581	-1.00E-04	-0.3392	-0.1324	-1.18E-02	-1.46E+01	-5.68E+00	22.3431	-1.50E-02
OUT	OUT	OUT	OUT	OUT	OUT	OUT	OUT	OUT
21.9288	-4.00E-04	-1.3899	-0.5406	-1.30E-02	-1.64E+01	-6.39E+00	21.9152	-1.36E-02
22.1612	-1.00E-03	-3.4833	-1.3514	-1.75E-02	-2.22E+01	-8.60E+00	22.1439	-1.73E-02
22.2139	6.10E-03	20.7702	8.1111	1.26E-02	1.56E+01	6.10E+00	22.2225	8.60E-03
22.5622	4.20E-03	14.6941	5.7132	1.04E-02	1.32E+01	5.15E+00	22.5719	9.70E-03
OUT	OUT	OUT	OUT	OUT	OUT	OUT	OUT	OUT
22.3044	2.80E-03	9.3209	3.6483	9.30E-03	1.13E+01	4.41E+00	22.3131	8.70E-03
22.5567	1.10E-03	3.7272	1.4538	6.60E-03	8.14E+00	3.17E+00	22.5649	8.20E-03
21.7234	-8.00E-04	-2.6962	-1.0535	4.20E-03	5.15E+00	2.01E+00	21.7309	7.50E-03
21.9974	-2.40E-03	-8.3394	-3.2401	3.10E-03	3.92E+00	1.52E+00	22.0031	5.70E-03
21.7199	-1.70E-03	-5.8504	-2.2836	3.30E-03	4.13E+00	1.61E+00	21.7256	5.70E-03
21.8810	-1.70E-03	-5.9235	-2.3059	2.70E-03	3.42E+00	1.33E+00	21.8866	5.60E-03
22.3328	-2.80E-03	-9.5123	-3.7105	1.80E-03	2.22E+00	8.68E-01	22.3371	4.30E-03
22.4259	-4.10E-03	-13.9616	-5.4457	-2.00E-04	-2.48E-01	-9.67E-02	22.4290	3.10E-03
21.7288	-4.20E-03	-14.5190	-5.6584	0.00E+00	0.00E+00	0.00E+00	21.7318	3.00E-03
22.1939	-4.20E-03	-14.2612	-5.5701	-3.00E-04	-3.71E-01	-1.45E-01	22.1957	1.80E-03
22.2020	-4.50E-03	-15.4001	-5.9985	-8.00E-04	-9.96E-01	-3.88E-01	22.2038	1.80E-03
22.1560	-4.00E-03	-13.7273	-5.3445	-1.30E-03	-1.62E+00	-6.32E-01	22.1573	1.30E-03
21.3073	-4.70E-03	-16.8196	-6.5119	-1.60E-03	-2.08E+00	-8.07E-01	21.3079	6.00E-04
22.4099	-4.80E-03	-16.2835	-6.3495	-2.90E-03	-3.58E+00	-1.40E+00	22.4101	2.00E-04
22.3909	-5.40E-03	-18.3004	-7.1440	-4.40E-03	-5.43E+00	-2.12E+00	22.3908	-1.00E-04
22.1083	-5.30E-03	-18.2684	-7.1056	-5.70E-03	-7.15E+00	-2.78E+00	22.1079	-4.00E-04
22.6022	-6.10E-03	-20.4858	-7.9998	-7.60E-03	-9.29E+00	-3.63E+00	22.6015	-7.00E-04
22.1295	-4.90E-03	-16.8431	-6.5569	-7.10E-03	-8.88E+00	-3.46E+00	22.1281	-1.40E-03
22.5421	-3.00E-03	-10.1757	-3.9714	-6.70E-03	-8.27E+00	-3.23E+00	22.5390	-3.10E-03
22.0646	-3.10E-03	-10.7107	-4.1664	-7.90E-03	-9.93E+00	-3.86E+00	22.0594	-5.20E-03

Table C.2 Raw Weighing Data for GEB-2 (continued)

28-Aug-87 1014.0	28-Aug-87 1014.0	28-Aug-87 1014.0	28-Aug-87 1014.0	28-Aug-87 1014.0	11-Sep-87 1235.0	11-Sep-87 1235.0	11-Sep-87 1235.0	11-Sep-87 1235.0
INSTANT(4) MASS,I FLUX mG/SQM-h	INSTANT(4) MASS,t FLUX mG/SQM-h	OVERALL WT. CHANGE GRAMS(4)	OVERALL(4) MASS,I FLUX mG/SQM-h	OVERALL(4) MASS,t FLUX mG/SQM-h	PULL #5 GRAMS(4)	INSTANT WT. CHANGE GRAMS(4)	INSTANT(4) MASS,I FLUX mG/SQM-h	INSTANT(4) MASS,t FLUX mG/SQM-h
11.2909	4.3996	2.50E-02	14.0453	5.4728	22.3302	2.60E-03	8.7021	2.6115
2.7674	1.0789	8.10E-03	4.5442	1.7715	22.4647	4.00E-04	1.0296	0.4014
0.3132	0.1219	3.30E-03	1.8857	0.7337	21.9336	-4.00E-04	-1.0487	-0.4080
-1.4438	-0.5621	6.00E-04	0.3387	0.1318	22.2443	-1.10E-03	-2.8488	-1.1091
-2.3993	-0.9332	-1.60E-03	-0.9135	-0.3553	21.8759	-5.00E-04	-1.3099	-0.5095
-2.7177	-1.0552	-3.30E-03	-1.8880	-0.7330	22.0522	-5.00E-04	-1.3125	-0.5096
-2.8901	-1.1205	-4.20E-03	-2.4607	-0.9540	21.2704	-5.00E-04	-1.3441	-0.5211
-2.2934	-0.8921	-4.00E-03	-2.2823	-0.8878	21.9832	-1.60E-03	-4.1887	-1.6294
-3.9955	-1.5583	-6.70E-03	-3.7569	-1.4652	22.3575	-9.00E-04	-2.3155	-0.9031
-4.4057	-1.7180	-7.60E-03	-4.2620	-1.6620	22.4683	-1.70E-03	-4.3742	-1.7057
-5.3388	-2.1091	-9.80E-03	-5.0240	-1.9848	24.4324	-1.60E-03	-3.7635	-1.4868
-5.7422	-2.2374	-1.02E-02	-5.7246	-2.2306	22.3053	-1.50E-03	-3.8626	-1.5050
-6.2725	-2.4217	-1.07E-02	-6.4447	-2.4882	20.6255	-2.20E-03	-6.0798	-2.3473
-5.5378	-2.0939	-8.40E-03	-5.6580	-2.1394	18.5746	-2.40E-03	-7.4172	-2.8046
-8.0419	-3.1306	-1.41E-02	-8.0602	-3.1377	21.7092	-2.40E-03	-6.2948	-2.4505
-9.8542	-3.8415	-1.71E-02	-9.7084	-3.7847	21.8545	-2.60E-03	-6.7728	-2.6403
-10.7382	-4.1840	-1.95E-02	-10.9152	-4.2530	22.5524	-3.10E-03	-7.9617	-3.1022
-15.3113	-5.9765	-2.68E-02	-14.9730	-5.8445	22.3396	-3.50E-03	-8.9720	-3.5021
OUT	OUT	OUT	OUT	OUT	22.5447	IN	IN	IN
-14.2195	-5.5311	-2.66E-02	-15.2224	-5.9212	21.911	-4.20E-03	-11.0280	-4.2896
-18.1325	-7.0347	-3.48E-02	-19.9640	-7.7452	22.1383	-5.60E-03	-14.7401	-5.7186
8.8112	3.4409	2.12E-02	11.8885	4.6426	22.2273	4.80E-03	12.3503	4.8230
10.2115	3.9703	2.01E-02	11.5816	4.5030	22.5756	3.70E-03	9.7818	3.8032
OUT	OUT	OUT	OUT	OUT	21.6435	IN	IN	IN
8.7145	3.4110	1.80E-02	9.8685	3.8627	22.3161	3.00E-03	7.5485	2.9538
8.3604	3.2610	1.48E-02	8.2591	3.2215	22.5682	3.30E-03	8.4495	3.2958
7.6059	2.9720	1.17E-02	6.4942	2.5376	21.7335	2.60E-03	6.6216	2.5874
5.9596	2.3155	8.80E-03	5.0360	1.9566	22.0064	3.30E-03	8.6648	3.3665
5.9024	2.3039	9.00E-03	5.1010	1.9911	21.7283	2.70E-03	7.0214	2.7407
5.8714	2.2856	8.30E-03	4.7631	1.8542	21.8884	1.80E-03	4.7394	1.8450
4.3956	1.7146	6.10E-03	3.4130	1.3313	22.3386	1.50E-03	3.8507	1.5021
3.1764	1.2390	2.90E-03	1.6264	0.6344	22.43	1.00E-03	2.5732	1.0037
3.1206	1.2162	3.00E-03	1.7080	0.6656	21.7324	6.00E-04	1.5673	0.6108
1.8391	0.7183	1.50E-03	0.8388	0.3276	22.1971	1.40E-03	3.5922	1.4030
1.8536	0.7220	1.00E-03	0.5638	0.2195	22.2045	7.00E-04	1.8102	0.7051
1.3424	0.5227	0.00E+00	0.0000	0.0000	22.1576	3.00E-04	0.7780	0.3029
0.8461	0.2501	-1.00E-03	-0.5894	-0.2282	21.3079	0.00E+00	0.0000	0.0000
0.2042	0.0796	-2.70E-03	-1.5085	-0.5882	22.4103	2.00E-04	0.5127	0.1999
-0.1020	-0.0398	-4.50E-03	-2.5116	-0.9805	22.3908	0.00E+00	0.0000	0.0000
-0.4149	-0.1614	-6.10E-03	-3.4629	-1.3469	22.1078	-1.00E-04	-0.2605	-0.1013
-0.7074	-0.2762	-8.30E-03	-4.5907	-1.7926	22.6017	2.00E-04	0.5075	0.1982
-1.4480	-0.5637	-8.50E-03	-4.8120	-1.8733	22.1274	-7.00E-04	-1.8182	-0.7078
-3.1640	-1.2348	-9.80E-03	-5.4746	-2.1366	22.5379	-1.10E-03	-2.8194	-1.1004
-5.4061	-2.1029	-1.31E-02	-7.4543	-2.8997	22.0576	-1.80E-03	-4.6995	-1.8281

Table C.2 Raw Weighing Data for GEB-2 (continued)

11-Sep-87 1235.0	11-Sep-87 1235.0	11-Sep-87 1235.0	22-Sep-87 1497.0	22-Sep-87 1497.0	22-Sep-87 1497.0	22-Sep-87 1497.0	22-Sep-87 1497.0	22-Sep-87 1497.0
OVERALL WT. CHANGE GRAMS(4)	OVERALL MASS,I FLUX mG/SQM-h	OVERALL MASS,t FLUX mG/SQM-h	PULL #6 GRAMS(4)	PULL #6 GRAMS(5)	INSTANT WT. CHANGE GRAMS(4)	INSTANT(4) MASS,I FLUX mG/SQM-h	INSTANT(4) MASS,t FLUX mG/SQM-h	OVERALL WT. CHANGE GRAMS(4)
2.78E-02	12.7313	4.9608	22.3345	22.33488	4.30E-03	9.3497	3.6432	3.19E-02
8.50E-03	3.9152	1.5263	22.4660	22.46622	1.30E-03	2.8226	1.1004	9.80E-03
2.90E-03	1.3606	0.5294	21.9335	21.93398	-1.00E-04	-0.2212	-0.0860	2.80E-03
-5.00E-04	-0.2317	-0.0902	22.2441	22.24417	-2.00E-04	-0.4369	-0.1701	-7.00E-04
-2.10E-03	-0.9845	-0.3829	21.8755	21.87523	-4.00E-04	-0.8839	-0.3438	-2.50E-03
-3.80E-03	-1.7850	-0.6931	22.0510	22.05129	-1.20E-03	-2.6570	-1.0317	-5.00E-03
-4.70E-03	-2.2608	-0.8766	21.2693	21.26964	-1.10E-03	-2.4942	-0.9670	-5.80E-03
-5.60E-03	-2.6234	-1.0205	21.9821	21.98241	-1.10E-03	-2.4291	-0.9449	-6.70E-03
-7.60E-03	-3.4990	-1.3646	22.3558	22.35599	-1.70E-03	-3.6893	-1.4389	-9.30E-03
-9.30E-03	-4.2821	-1.6698	22.4662	22.46649	-2.10E-03	-4.5578	-1.7773	-1.14E-02
-1.14E-02	-4.7984	-1.8957	24.4292	24.42952	-3.20E-03	-6.3491	-2.5082	-1.46E-02
-1.17E-02	-5.3914	-2.1007	22.3021	22.30242	-3.20E-03	-6.9508	-2.7083	-1.49E-02
-1.29E-02	-6.3794	-2.4630	20.6224	20.6228	-3.10E-03	-7.2263	-2.7900	-1.60E-02
-1.08E-02	-5.9728	-2.2584	18.5721	18.57233	-2.50E-03	-6.5172	-2.4642	-1.33E-02
-1.65E-02	-7.7443	-3.0147	21.7056	21.70577	-3.60E-03	-7.9646	-3.1005	-2.01E-02
-1.97E-02	-9.1831	-3.5799	21.8498	21.85001	-4.70E-03	-10.3273	-4.0260	-2.44E-02
-2.26E-02	-10.3867	-4.0470	22.5470	22.54731	-5.40E-03	-11.6985	-4.5581	-2.80E-02
-3.03E-02	-13.8992	-5.4253	OUT	OUT	OUT	OUT	OUT	OUT
IN	IN	IN	22.5260	22.52602	-1.87E-02	-40.3822	-15.7872	-1.87E-02
-3.08E-02	-14.4718	-5.6292	21.8999	21.90021	-1.11E-02	-24.5844	-9.5628	-4.19E-02
-4.04E-02	-19.0292	-7.3826	22.1254	22.12564	-1.29E-02	-28.8414	-11.1117	-5.33E-02
2.60E-02	11.9711	4.6749	22.2321	22.23237	4.80E-03	10.4176	4.0682	3.08E-02
2.38E-02	11.2595	4.3778	OUT	OUT	OUT	OUT	OUT	OUT
IN	IN	IN	21.6472	21.64733	3.70E-03	8.1976	3.2014	3.70E-03
2.10E-02	9.4530	3.7000	22.3208	22.32112	4.70E-03	9.9727	3.9035	2.57E-02
1.81E-02	8.2932	3.2348	22.5725	22.5729	4.30E-03	9.2870	3.6225	2.24E-02
1.43E-02	6.5170	2.5465	21.7371	21.73743	3.60E-03	7.7336	3.0219	1.79E-02
1.21E-02	5.6853	2.2089	22.0101	22.01027	3.70E-03	8.1948	3.1839	1.58E-02
1.17E-02	5.4446	2.1252	21.7310	21.73106	2.70E-03	5.9226	2.3118	1.44E-02
1.01E-02	4.7588	1.8525	21.8906	21.89066	2.20E-03	4.8862	1.9021	1.23E-02
7.60E-03	3.4913	1.3619	22.3400	22.34032	1.40E-03	3.0316	1.1826	9.00E-03
3.90E-03	1.7958	0.7005	22.4306	22.43147	6.00E-04	1.3023	0.5080	4.50E-03
3.60E-03	1.6828	0.6558	21.7336	21.73388	1.20E-03	2.6441	1.0305	4.80E-03
2.90E-03	1.3315	0.5201	22.1980	22.19828	9.00E-04	1.9479	0.7608	3.80E-03
1.70E-03	0.7867	0.3064	22.2055	22.20554	1.00E-03	2.1814	0.8497	2.70E-03
3.00E-04	0.1392	0.0542	22.1580	22.15824	4.00E-04	0.8750	0.3407	7.00E-04
-1.00E-03	-0.4839	-0.1874	21.3081	21.30834	2.00E-04	0.4562	0.1766	-8.00E-04
-2.50E-03	-1.1468	-0.4472	22.4106	22.41098	3.00E-04	0.6487	0.2530	-2.20E-03
-4.50E-03	-2.0622	-0.8050	22.3912	22.39144	4.00E-04	0.8641	0.3373	-4.10E-03
-6.20E-03	-2.8898	-1.1240	22.1076	22.10777	-2.00E-04	-0.4394	-0.1709	-6.40E-03
-8.10E-03	-3.6784	-1.4364	22.6011	22.60138	-6.00E-04	-1.2844	-0.5015	-8.70E-03
-9.20E-03	-4.2763	-1.6647	22.1268	22.12687	-6.00E-04	-1.3146	-0.5118	-9.80E-03
-1.09E-02	-4.9994	-1.9512	22.5365	22.53662	-1.40E-03	-3.0268	-1.1813	-1.23E-02
-1.49E-02	-6.9613	-2.7079	22.0556	22.05578	-2.00E-03	-4.4045	-1.7133	-1.69E-02

Table C.2 Raw Weighing Data for GEB-2 (continued)

22-Sep-87 1497.0	22-Sep-87 1497.0	16-Oct-87 1840.0	16-Oct-87 1840.0	16-Oct-87 1840.0	16-Oct-87 1840.0	16-Oct-87 1840.0	16-Oct-87 1840.0	16-Oct-87 1840.0
OVERALL MASS,I FLUX mG/SQM-h	OVERALL MASS,t FLUX mG/SQM-h	PULL #7 GRAMS(4)	PULL #7 GRAMS(5)	INSTANT WT. CHANGE GRAMS(4)	INSTANT WT. CHANGE GRAMS(5)	INSTANT(4) MASS,I FLUX mG/SQM-h	INSTANT(4) MASS,t FLUX mG/SQM-h	OVERALL WT. CHANGE GRAMS(4)
12.1394	4.7302	22.3379	22.33771	3.40E-03	2.83E-03	5.6470	2.2004	3.53E-02
3.7240	1.4518	22.4661	22.46624	1.00E-04	2.00E-05	0.1658	0.0647	9.90E-03
1.0837	0.4217	21.9326	21.93253	-9.00E-04	-1.45E-03	-1.5203	-0.5915	1.90E-03
-0.2676	-0.1042	22.2430	22.24294	-1.10E-03	-1.23E-03	-1.8355	-0.7146	-1.80E-03
-0.9669	-0.3761	21.8738	21.87380	-1.70E-03	-1.43E-03	-2.8695	-1.1161	-4.20E-03
-1.9376	-0.7523	22.0496	22.04965	-1.40E-03	-1.64E-03	-2.3678	-0.9194	-6.40E-03
-2.3017	-0.8924	21.2683	21.26816	-1.00E-03	-1.48E-03	-1.7320	-0.6715	-6.80E-03
-2.5894	-1.0073	21.9808	21.98045	-1.30E-03	-1.96E-03	-2.1928	-0.8530	-8.00E-03
-3.5323	-1.3776	22.3539	22.35392	-1.90E-03	-2.07E-03	-3.1496	-1.2284	-1.12E-02
-4.3303	-1.6886	22.4642	22.46399	-2.00E-03	-2.50E-03	-3.3157	-1.2929	-1.34E-02
-5.0696	-2.0029	24.4268	24.42669	-2.40E-03	-2.83E-03	-3.6373	-1.4369	-1.70E-02
-5.6643	-2.2071	22.2993	22.29912	-2.80E-03	-3.30E-03	-4.6457	-1.8102	-1.77E-02
-6.5276	-2.5202	20.6195	20.61956	-2.90E-03	-3.24E-03	-5.1637	-1.9936	-1.89E-02
-6.0681	-2.2944	18.5695	18.56948	-2.60E-03	-2.85E-03	-5.1772	-1.9576	-1.59E-02
-7.7828	-3.0298	21.7015	21.70138	-4.10E-03	-4.39E-03	-6.9287	-2.6973	-2.42E-02
-9.3834	-3.6580	21.8459	21.84568	-3.90E-03	-4.33E-03	-6.5458	-2.5518	-2.83E-02
-10.6163	-4.1365	22.5427	22.54269	-4.30E-03	-4.62E-03	-7.1156	-2.7725	-3.23E-02
OUT	OUT	OUT	OUT	OUT		OUT	OUT	OUT
-40.3822	-15.7872	22.5183	22.51808	-7.70E-03	-7.94E-03	-12.7012	-4.9655	-2.64E-02
-16.2417	-6.3177	21.8940	21.89390	-5.90E-03	-6.31E-03	-9.9815	-3.8826	-4.78E-02
-20.7115	-8.0352	22.1172	22.11720	-8.20E-03	-8.44E-03	-13.9087	-5.3953	-6.15E-02
11.6992	4.5687	22.2375	22.23743	5.40E-03	5.06E-03	8.9521	3.4959	3.62E-02
OUT	OUT	OUT	OUT	OUT		OUT	OUT	OUT
8.1976	3.2014	21.6512	21.65149	4.00E-03	4.16E-03	6.7694	2.6436	7.70E-03
9.5440	3.7356	22.3255	22.32561	4.70E-03	4.49E-03	7.6177	2.9816	3.04E-02
8.4671	3.3027	22.5769	22.57691	4.40E-03	4.01E-03	7.2588	2.8314	2.68E-02
6.7299	2.6297	21.7413	21.74097	4.20E-03	3.54E-03	6.8918	2.6930	2.21E-02
6.1245	2.3796	22.0130	22.01309	2.90E-03	2.82E-03	4.9062	1.9062	1.87E-02
5.5283	2.1579	21.7336	21.73339	2.60E-03	2.33E-03	4.3564	1.7005	1.70E-02
4.7811	1.8612	21.8924	21.89223	1.80E-03	1.57E-03	3.0537	1.1887	1.41E-02
3.4109	1.3305	22.3417	22.34147	1.70E-03	1.15E-03	2.8119	1.0969	1.07E-02
1.7095	0.6668	22.4322	22.43211	1.60E-03	6.40E-04	2.6527	1.0347	6.10E-03
1.8511	0.7214	21.7345	21.73454	9.00E-04	6.60E-04	1.5148	0.5904	5.70E-03
1.4394	0.5622	22.1989	22.19884	9.00E-04	5.60E-04	1.4879	0.5811	4.70E-03
1.0308	0.4015	22.2056	22.20576	1.00E-04	2.20E-04	0.1666	0.0649	2.80E-03
0.2680	0.1043	22.1580	22.15799	0.00E+00	-2.50E-04	0.0000	0.0000	7.00E-04
-0.3194	-0.1237	21.3081	21.30802	0.00E+00	-3.20E-04	0.0000	0.0000	-8.00E-04
-0.8326	-0.3247	22.4109	22.41060	3.00E-04	-3.80E-04	0.4955	0.1932	-1.90E-03
-1.5500	-0.6051	22.3912	22.39106	0.00E+00	-3.80E-04	0.0000	0.0000	-4.10E-03
-2.4609	-0.9572	22.1074	22.10720	-2.00E-04	-5.70E-04	-0.3356	-0.1305	-6.60E-03
-3.2594	-1.2728	22.6005	22.60039	-6.00E-04	-9.90E-04	-0.9811	-0.3831	-9.30E-03
-3.7579	-1.4629	22.1259	22.12567	-9.00E-04	-1.20E-03	-1.5062	-0.5864	-1.07E-02
-4.6542	-1.8164	22.5350	22.53482	-1.50E-03	-1.80E-03	-2.4772	-0.9668	-1.38E-02
-6.5138	-2.5338	22.0524	22.05250	-3.20E-03	-3.28E-03	-5.3830	-2.0940	-2.01E-02

Table C.2 Raw Weighing Data for GEB-2 (continued)

16-Oct-87 1840.0	16-Oct-87 1840.0	13-Nov-87 2510.0	13-Nov-87 2510.0	13-Nov-87 2510.0	13-Nov-87 2510.0	13-Nov-87 2510.0	13-Nov-87 2510.0	13-Nov-87 2510.0
OVERALL MASS,I FLUX mG/SQM-h	OVERALL MASS,I FLUX mG/SQM-h	PULL #8 GRAMS(5)	INSTANT WT. CHANGE GRAMS(5)	INSTANT(5) MASS,I FLUX mG/SQM-h	INSTANT(5) MASS,I FLUX mG/SQM-h	OVERALL WT. CHANGE GRAMS(5)	OVERALL MASS,I FLUX mG/SQM-h	OVERALL MASS,I FLUX mG/SQM-h
10.9292	4.2586	22.34465	6.94E-03	5.9008	2.2993	4.21E-02	9.5438	3.7188
3.0607	1.1932	22.46772	1.48E-03	1.2566	0.4899	1.15E-02	2.6109	1.0178
0.5983	0.2328	21.93250	-3.00E-05	-0.0259	-0.0101	1.80E-03	0.4155	0.1617
-0.5599	-0.2180	22.24229	-6.50E-04	-0.5553	-0.2162	-2.51E-03	-0.5724	-0.2228
-1.3215	-0.5140	21.87270	-1.10E-03	-0.9505	-0.3697	-5.30E-03	-1.2225	-0.4755
-2.0178	-0.7835	22.04787	-1.78E-03	-1.5412	-0.5984	-8.13E-03	-1.8790	-0.7296
-2.1955	-0.8512	21.26626	-1.90E-03	-1.6847	-0.6532	-8.84E-03	-2.0923	-0.8112
-2.5155	-0.9785	21.97839	-2.06E-03	-1.7789	-0.6920	-1.04E-02	-2.3995	-0.9334
-3.4609	-1.3498	22.35098	-2.94E-03	-2.4950	-0.9731	-1.41E-02	-3.1986	-1.2475
-4.1412	-1.6148	22.46101	-2.98E-03	-2.5292	-0.9862	-1.66E-02	-3.7585	-1.4656
-4.8028	-1.8974	24.42247	-4.22E-03	-3.2742	-1.2935	-2.13E-02	-4.4175	-1.7452
-5.4745	-2.1331	22.29487	-4.25E-03	-3.6099	-1.4066	-2.21E-02	-5.0176	-1.9551
-6.2734	-2.4220	20.61526	-4.30E-03	-3.9197	-1.5133	-2.31E-02	-5.6305	-2.1738
-5.9020	-2.2316	18.56580	-3.68E-03	-3.7514	-1.4185	-1.96E-02	-5.3334	-2.0166
-7.6236	-2.9678	21.69582	-5.56E-03	-4.8102	-1.8725	-2.99E-02	-6.9003	-2.6862
-8.8544	-3.4518	21.83976	-5.92E-03	-5.0867	-1.9830	-3.44E-02	-7.8991	-3.0794
-9.9637	-3.8822	22.53616	-6.53E-03	-5.5319	-2.1554	-3.88E-02	-8.7830	-3.4222
OUT	OUT	OUT	OUT	OUT	OUT	OUT	OUT	OUT
-24.6887	-9.6519	22.50713	-1.10E-02	-9.2468	-3.6150	-3.76E-02	-16.6717	-6.5177
-15.0747	-5.8637	21.88542	-8.48E-03	-7.3445	-2.8568	-5.64E-02	-13.0344	-5.0701
-19.4430	-7.5431	22.10434	-1.29E-02	-11.1653	-4.3317	-7.44E-02	-17.2334	-6.6859
11.1871	4.3687	22.24628	8.85E-03	7.5110	2.9331	4.50E-02	10.1900	3.9793
OUT	OUT	OUT	OUT	OUT	OUT	OUT	OUT	OUT
7.3879	2.8852	21.65878	7.29E-03	6.3160	2.4665	1.53E-02	6.9567	2.7167
9.1849	3.5951	22.33284	7.23E-03	5.9990	2.3481	3.77E-02	8.3588	3.2718
8.2419	3.2148	22.58339	6.48E-03	5.4728	2.1347	3.33E-02	7.5050	2.9274
6.7601	2.6415	21.74599	5.02E-03	4.2171	1.6478	2.68E-02	6.0073	2.3474
5.8974	2.2913	22.01735	4.26E-03	3.6896	1.4335	2.31E-02	5.3289	2.0704
5.3098	2.0726	21.73672	3.33E-03	2.8564	1.1150	2.01E-02	4.6068	1.7982
4.4591	1.7358	21.89460	2.37E-03	2.0584	0.8013	1.63E-02	3.7789	1.4710
3.2992	1.2869	22.34340	1.93E-03	1.6343	0.6375	1.24E-02	2.8028	1.0933
1.8853	0.7354	22.43355	1.44E-03	1.2222	0.4767	7.45E-03	1.6879	0.6584
1.7884	0.6970	21.73626	1.72E-03	1.4820	0.5776	7.46E-03	1.7158	0.6687
1.4485	0.5657	22.20028	1.44E-03	1.2187	0.4760	6.08E-03	1.3738	0.5365
0.8697	0.3388	22.20629	5.30E-04	0.4521	0.1761	3.49E-03	0.7947	0.3095
0.2180	0.0849	22.15797	-2.00E-05	-0.0171	-0.0067	6.70E-04	0.1530	0.0596
-0.2598	-0.1006	21.30849	4.70E-04	0.4192	0.1623	-4.10E-04	-0.0976	-0.0378
-0.5850	-0.2281	22.41122	6.20E-04	0.5243	0.2044	-1.58E-03	-0.3566	-0.1391
-1.2611	-0.4923	22.39140	3.40E-04	0.2872	0.1121	-3.90E-03	-0.8794	-0.3433
-2.0648	-0.8031	22.10702	-1.80E-04	-0.1546	-0.0602	-6.98E-03	-1.6008	-0.6226
-2.8347	-1.1069	22.59963	-7.60E-04	-0.6362	-0.2484	-1.02E-02	-2.2724	-0.8874
-3.3382	-1.2995	22.12406	-1.61E-03	-1.3794	-0.5370	-1.25E-02	-2.8679	-1.1165
-4.2484	-1.6580	22.53212	-2.70E-03	-2.2827	-0.8909	-1.67E-02	-3.7643	-1.4691
-6.3030	-2.4518	22.04794	-4.56E-03	-3.9270	-1.5278	-2.46E-02	-5.6458	-2.1962

Table C.2 Raw Weighing Data for GEB-2 (continued)

Sample	hours	T (C)	Photo #	Disks	Spectra	Q-file	Fe	Cr	Mo	Si	Ni	Fe	Cr	Mo	Si	Ni
							SSQ Surface Composition (wt%)					SSQ Feature Composition (wt%)				
STD	0	RT		2107	1601	1601	65.90	11.50	1.10	0.90	0.50	<----------NO FEATURES---------->				
M/Fe(original)					1603		1.0E+00	1.3E-01	1.5E-02	1.0E-02	7.0E-03					
M/Fe(surface) or M/Mf(feature)							1.0E+00	1.3E-01	1.3E-02	1.0E-02	7.0E-03					
L-01ID	3040	359.3	26880	1958	1001	1001	89.50	8.80	1.00	0.70	0.00	<----------NO FEATURES---------->				
M/Fe(original)			26871		1000		1.0E+00	1.0E-01	1.2E-02	8.1E-03	0.0E+00					
M/Fe(surface) or M/Mf(feature)							1.0E+00	9.8E-02	1.1E-02	7.8E-03	0.0E+00					
L-01OD	3040	359.3	NONE	1958	1011	1011	89.50	9.80	0.70	0.40	0.50	<----------NO FEATURES---------->				
M/Fe(original)					1015		1.04E+00	1.04E-01	8.15E-03	4.66E-03	5.82E-03					
M/Fe(surface) or M/Mf(feature)							1.00E+00	9.94E-02	7.82E-03	4.47E-03	5.59E-03					
L-02ID	2505	368.9	26858	1958	801	801	88.80	8.30	0.90	1.20	0.70	<----------NO FEATURES---------->				
M/Fe(original)			26863		807		1.03E+00	9.66E-02	1.05E-02	1.40E-02	8.15E-03					
M/Fe(surface) or M/Mf(feature)							1.00E+00	9.35E-02	1.01E-02	1.35E-02	7.88E-03					
L-03.1ID	500	387.0	26875	1958	1101	1101	89.00	9.70	0.70	0.30	0.30	<----------NO FEATURES---------->				
M/Fe(original)			26875		1105		1.04E+00	1.13E-01	8.15E-03	3.49E-03	3.49E-03					
M/Fe(surface) or M/Mf(feature)							1.00E+00	1.08E-01	7.87E-03	3.37E-03	3.37E-03					
L-02.1OD	500	387.0	26875	1958	1111	1111	89.30	9.20	0.90	0.50	0.10	<----------NO FEATURES---------->				
M/Fe(original)					1118		1.04E+00	1.07E-01	1.05E-02	5.82E-03	1.16E-03					
M/Fe(surface) or M/Mf(feature)							1.00E+00	1.03E-01	1.01E-02	5.60E-03	1.12E-03					
L-03ID	3040	374.5	26971	1958	1201	1201	91.10	8.70	0.14	0.00	0.10	<----------NO FEATURES---------->				
M/Fe(original)			26972		1206		1.06E+00	1.01E-01	1.63E-03	0.00E+00	1.16E-03					
M/Fe(surface) or M/Mf(feature)							1.00E+00	9.55E-02	1.54E-03	0.00E+00	1.10E-03					
L-04ID	3040	382.0	26973	1958	1301	1301	89.80	9.40	0.80	0.00	0.20	<----------NO FEATURES---------->				
M/Fe(original)					1304		1.05E+00	1.06E-01	8.98E-03	0.00E+00	2.33E-03					
M/Fe(surface) or M/Mf(feature)							1.00E+00	1.05E-01	8.58E-03	0.00E+00	2.23E-03					
L-05ID	3040	390.0	26974	1958	1401	1401	90.70	8.40	0.40	0.00	0.40	<----------NO FEATURES---------->				
M/Fe(original)					1406		1.04E+00	9.78E-02	4.66E-03	0.00E+00	4.66E-03					
M/Fe(surface) or M/Mf(feature)							1.00E+00	9.39E-02	4.41E-03	0.00E+00	4.41E-03					
L-06ID	3040	397.7		1958	2901	2901	88.60	9.90	0.65	0.40	0.40	<----------NO FEATURES---------->				
M/Fe(original)					2909		1.03E+00	1.15E-01	7.57E-03	4.66E-03	4.66E-03					
M/Fe(surface) or M/Mf(feature)							1.00E+00	1.12E-01	7.34E-03	4.51E-03	4.51E-03					
L-07ID	3040	405.2		1958	2801	2801	90.90	8.70	0.14	0.30	0.30	<----------NO FEATURES---------->				
M/Fe(original)					2808		1.05E+00	1.01E-01	1.63E-03	3.49E-03	3.49E-03					
M/Fe(surface) or M/Mf(feature)							1.00E+00	9.61E-02	1.55E-03	3.31E-03	3.31E-03					
L-08ID	3040	412.9		1958	2701	2701	92.40	7.20	0.00	0.19	0.20	<----------NO FEATURES---------->				
M/Fe(original)					2706		1.08E+00	8.36E-02	0.00E+00	1.10E-03	2.33E-03					
M/Fe(surface) or M/Mf(feature)							1.00E+00	7.79E-02	0.00E+00	1.06E-03	2.18E-03					
L-09ID	3040	420.8		1958	2601	2601	92.40	7.20	0.00	0.20	0.20	<----------NO FEATURES---------->				
M/Fe(original)					2606		1.08E+00	8.36E-02	0.00E+00	2.33E-03	2.33E-03					
M/Fe(surface) or M/Mf(feature)							1.00E+00	7.79E-02	0.00E+00	2.18E-03	2.18E-03					
L-10ID	3040	427.9		1958	2501	2501	93.40	6.40	0.00	0.00	0.10	<----------NO FEATURES---------->				
M/Fe(original)					2508		1.09E+00	7.45E-02	0.00E+00	0.00E+00	1.16E-03					
M/Fe(surface) or M/Mf(feature)							1.00E+00	6.85E-02	0.00E+00	0.00E+00	1.07E-03					
L-11ID	3040	435.5	27079	1958	2401	2401	92.40	7.00	0.20	0.40	0.10	<----------NO FEATURES---------->				
M/Fe(original)			27071		2405		1.08E+00	8.15E-02	2.33E-03	4.66E-03	1.16E-03					
M/Fe(surface) or M/Mf(feature)							1.00E+00	7.56E-02	2.16E-03	4.33E-03	1.08E-03					
L-12ID	3040	443.1	27068	1958	2301	2301	92.50	6.70	0.20	0.40	0.20	73.90	23.50	0.50	0.90	0.10
M/Fe(original)			27068		2306		1.06E+00	7.80E-02	2.33E-03	4.66E-03	2.33E-03					
M/Fe(surface) or M/Mf(feature)							1.00E+00	7.24E-02	2.16E-03	4.32E-03	2.16E-03	7.47E-01	2.38E-01	5.06E-03	9.10E-03	1.01E-03
L-13ID	3040	450.8	27066	1959	2201	2201	90.66	6.50	0.20	0.45	0.21	43.00	55.00	0.80	0.80	2.00
M/Fe(original)			27067		2211		1.05E+00	8.90E-02	2.33E-03	5.24E-03	2.44E-03					
M/Fe(surface) or M/Mf(feature)							1.00E+00	9.38E-02	2.21E-03	4.97E-03	2.32E-03	4.23E-01	5.41E-01	7.87E-03	7.87E-03	1.97E-02
L-14ID	3040	458.2	27064	1959	2101	2101	92.80	6.80	0.10	0.20	0.15	38.00	60.40	0.80	0.70	2.20
M/Fe(original)			27065		2111		1.06E+00	7.92E-02	1.16E-03	2.33E-03	1.75E-03					
M/Fe(surface) or M/Mf(feature)							1.00E+00	7.33E-02	1.08E-03	2.16E-03	1.62E-03	3.60E-01	6.03E-01	7.99E-03	6.99E-03	2.20E-02
L-15ID	3040	465.8	27062	1959	2001	2001	92.10	7.60	0.14	0.19	0.00	33.50	63.20	0.90	0.72	1.70
M/Fe(original)			27063		2011		1.07E+00	8.85E-02	1.63E-03	2.21E-03	0.00E+00					
M/Fe(surface) or M/Mf(feature)							1.00E+00	8.23E-02	1.52E-03	2.06E-03	0.00E+00	3.35E-01	6.32E-01	9.00E-03	7.20E-03	1.70E-02
L-16ID	3040	473.4	27060	1959	1901	1901	92.70	6.50	0.20	0.42	0.10	31.30	65.70	0.86	0.44	1.60
M/Fe(original)			27061		1911		1.08E+00	7.57E-02	2.33E-03	4.89E-03	1.16E-03					
M/Fe(surface) or M/Mf(feature)							1.00E+00	7.01E-02	2.16E-03	4.53E-03	1.08E-03	3.13E-01	6.58E-01	8.61E-03	4.40E-03	1.60E-02
L-17ID	990	480.9	26974	2107	1501	1501	91.00	8.00	0.31	0.00	0.13	37.70	58.10	1.50	0.00	1.60
M/Fe(original)			26975		1508		1.06E+00	9.31E-02	3.61E-03	0.00E+00	1.51E-03					
M/Fe(surface) or M/Mf(feature)							1.00E+00	8.79E-02	3.41E-03	0.00E+00	1.43E-03	3.89E-01	5.99E-01	1.51E-02	0.00E+00	1.62E-02
L-17.1ID	2050	480.9	26980	1958	1601	1601	93.70	6.20	0.00	0.00	0.00	32.70	64.40	1.30	0.00	1.50
M/Fe(original)					1610		1.09E+00	7.23E-02	0.00E+00	0.00E+00	0.00E+00					
M/Fe(surface) or M/Mf(feature)							1.00E+00	6.62E-02	0.00E+00	0.00E+00	0.00E+00	3.27E-01	6.45E-01	1.30E-02	0.00E+00	1.50E-02
L-18ID	3040	488.7	26978	1959	1701	1701	93.30	6.60	0.10	0.00	0.10	30.20	65.80	2.90	0.00	1.20
M/Fe(original)			26979		1712		1.09E+00	7.68E-02	1.16E-03	0.00E+00	1.16E-03					
M/Fe(surface) or M/Mf(feature)							1.00E+00	7.07E-02	1.07E-03	0.00E+00	1.07E-03	3.02E-01	6.57E-01	2.90E-02	0.00E+00	1.20E-02
L-20ID	3040	496.2	26976	1959	1601	1601	92.70	7.20	0.00	0.00	0.00	32.10	63.60	2.90	0.00	1.30
M/Fe(original)			26977		1616		1.08E+00	8.38E-02	0.00E+00	0.00E+00	0.00E+00					
M/Fe(surface) or M/Mf(feature)							1.00E+00	7.77E-02	0.00E+00	0.00E+00	0.00E+00	3.21E-01	6.37E-01	2.90E-02	0.00E+00	1.30E-02

Table C.3 EDX Data for GEB-1

Sample	hours	T (C)	Photo #	Disk #	Spectra	Q-file	Fe	Cr	Mn	Si	Ni	Fe	Cr	Mn	Si	Ni
L-21ID	3040	504	26975	1959	1501	1501	93.20	6.80	0.10	0.00	0.10	34.80	61.00	3.20	0.00	1.00
M/Fe(original)					1518		1.00E+00	7.92E-02	1.16E-03	0.00E+00	1.16E-03					
M/Fe(surface) or Mi/Mf(feature)							1.00E+00	7.30E-02	1.07E-03	0.00E+00	1.07E-03	3.47E-01	6.11E-01	3.21E-02	0.00E+00	1.00E-02
L-22ID	3040	357.6		1951	3001	3001	88.70	9.80	0.70	0.80	0.40	<-------NO FEATURES------->				
M/Fe(original)					3005		1.00E+00	1.12E-01	8.15E-03	8.98E-03	4.66E-03					
M/Fe(surface) or Mi/Mf(feature)							1.00E+00	1.08E-01	7.80E-03	8.76E-03	4.51E-03					
L-23ID	996	363.6	26123	2107	1701	1701	88.90	10.10	0.30	0.00	0.40	<-------NO FEATURES------->				
M/Fe(original)			26125		1705		1.00E+00	1.18E-01	3.49E-03	0.00E+00	4.66E-03					
M/Fe(surface) or Mi/Mf(feature)							1.00E+00	1.14E-01	3.37E-03	0.00E+00	4.50E-03					
L-23.1ID	2050	363.6		1991	3101	3101	89.89	9.90	0.50	0.49	0.40	<-------NO FEATURES------->				
M/Fe(original)					3105		1.00E+00	1.04E-01	5.62E-03	4.66E-03	4.66E-03					
M/Fe(surface) or Mi/Mf(feature)							1.00E+00	9.91E-02	5.37E-03	4.45E-03	4.45E-03					
L-24ID	3040	369.3		1961	3201	3201	90.10	9.30	0.14	0.20	0.30	<-------NO FEATURES------->				
M/Fe(original)					3205		1.00E+00	1.06E-01	1.63E-03	2.33E-03	3.49E-03					
M/Fe(surface) or Mi/Mf(feature)							1.00E+00	1.03E-01	1.35E-03	2.22E-03	3.33E-03					
L-25ID	3040	375.1		1981	3301	3301	89.80	9.00	0.40	0.40	0.40	<-------NO FEATURES------->				
M/Fe(original)					3305		1.00E+00	1.05E-01	4.66E-03	4.66E-03	4.66E-03					
M/Fe(surface) or Mi/Mf(feature)							1.00E+00	1.00E-01	4.45E-03	4.45E-03	4.45E-03					
L-29ID	3040	398.1		1963	501	501	91.75	7.88	0.10	0.25	0.24	<-------NO FEATURES------->				
M/Fe(original)					505		1.07E+00	8.92E-02	1.16E-03	2.91E-03	2.79E-03					
M/Fe(surface) or Mi/Mf(feature)							1.00E+00	8.35E-02	1.09E-03	2.72E-03	2.62E-03					
L-31ID	3040	410.1		1963	601	601	91.06	8.11	0.16	0.32	0.35	<-------NO FEATURES------->				
M/Fe(original)					605		1.00E+00	8.44E-02	1.68E-03	3.73E-03	4.19E-03					
M/Fe(surface) or Mi/Mf(feature)							1.00E+00	8.91E-02	1.78E-03	3.51E-03	3.95E-03					
L-33ID	3040	422.2		1963	701	701	90.96	8.08	0.32	0.45	0.21	<-------NO FEATURES------->				
M/Fe(original)					705		1.00E+00	9.38E-02	3.73E-03	5.24E-03	2.44E-03					
M/Fe(surface) or Mi/Mf(feature)							1.00E+00	8.86E-02	3.52E-03	4.95E-03	2.31E-03					
L-35ID	3040	433.6		1963	801	801	93.51	6.20	0.06	0.14	0.15	<-------NO FEATURES------->				
M/Fe(original)					805		1.00E+00	7.22E-02	0.00E+00	1.63E-03	1.75E-03					
M/Fe(surface) or Mi/Mf(feature)							1.00E+00	6.83E-02	0.00E+00	1.58E-03	1.66E-03					
L-37ID	3040	445.1		1963	901	901	92.40	7.14	0.02	0.31	0.13	<-------NO FEATURES------->				
M/Fe(original)					905		1.00E+00	8.31E-02	2.33E-04	3.61E-03	1.86E-03					
M/Fe(surface) or Mi/Mf(feature)							1.00E+00	7.73E-02	2.16E-04	3.35E-03	1.73E-03					
L-39ID	3040	457.3		1963	1001	1001	93.85	5.73	0.17	0.20	0.00	58.00	29.00	0.73	1.01	1.17
M/Fe(original)					1010		1.00E+00	6.07E-02	1.98E-03	2.33E-03	0.00E+00					
M/Fe(surface) or Mi/Mf(feature)							1.00E+00	5.11E-02	1.81E-03	2.13E-03	0.00E+00	6.61E-01	2.90E-01	7.31E-03	1.01E-02	1.17E-02
L-41ID	3040	470.3		1963	1101	1101	91.28	8.26	0.03	0.21	0.21	58.38	38.83	0.67	0.61	1.42
M/Fe(original)					1110		1.00E+00	9.62E-02	3.49E-04	2.44E-03	2.44E-03					
M/Fe(surface) or Mi/Mf(feature)							1.00E+00	9.05E-02	3.29E-04	2.30E-03	2.30E-03	5.84E-01	3.89E-01	6.70E-03	6.10E-03	1.42E-02
L-43ID	3040	482		1963	1201	1201	92.97	6.85	0.03	0.11	0.05	58.19	39.29	1.10	0.89	1.52
M/Fe(original)					1210		1.00E+00	7.97E-02	3.49E-04	1.28E-03	5.82E-04					
M/Fe(surface) or Mi/Mf(feature)							1.00E+00	7.37E-02	3.23E-04	1.18E-03	5.38E-04	3.61E-01	8.03E-01	1.10E-02	8.80E-03	1.62E-02

Table C.3 EDX Data for GEB-1 (continued)

Sample	TIME	T (C)	Photo #	Disks	Spectra	Q-file	Fe	Cr	Mo	Si	Ni	Fe	Cr	Mo	Si	Ni
							SSQ Surface Composition (wt%)					SSQ Feature Composition (wt%)				
STD		0 RT		2107	1801	1801	65.90	11.50	1.10	0.90	0.60	<-------NO FEATURES------->				
M/Fe(original)					1803		1.0E+00	1.3E-01	1.3E-02	1.0E-02	7.0E-03					
M/Fe(surface) or M/M(feature)							1.0E+00	1.3E-01	1.3E-02	1.0E-02	7.0E-03					
H-01	ID	2510	526.6	27285	1961	3401	3401	90.20	0.80	0.20	0.90	0.25	85.14	12.99	0.66	0.48	0.40
M/Fe(original)				27286		3410		1.1E+00	1.0E-01	2.3E-03	7.0E-03	2.9E-03					
M/Fe(surface) or M/M(feature)								1.00E+00	9.76E-02	2.22E-03	6.65E-03	2.77E-03	6.57E-01	1.29E-01	6.94E-03	4.03E-03	4.03E-03
H-03	ID	2510	541.7	27287	1961	3501	3501	89.80	9.65	0.50	0.00	0.00	<-------NO FEATURES------->				
M/Fe(original)				27289		3508		1.0E+00	1.12E-01	5.82E-03	0.00E+00	0.00E+00					
M/Fe(surface) or M/M(feature)								1.00E+00	1.07E-01	5.57E-03	0.00E+00	0.00E+00					
H-05	ID	2510	554.1	27290	1961	3601	3601	93.01	6.80	0.15	0.39	0.12	<-------NO FEATURES------->				
M/Fe(original)				27291		3605		1.0E+00	7.68E-02	1.75E-03	4.54E-03	1.40E-03					
M/Fe(surface) or M/M(feature)								1.00E+00	7.10E-02	1.61E-03	4.19E-03	1.29E-03					
H-07	ID	2510	567.6	27292	1961	3701	3701	92.66	6.22	0.50	0.39	0.14	<-------NO FEATURES------->				
M/Fe(original)				27293		3705		1.0E+00	7.24E-02	6.67E-03	4.54E-03	1.63E-03					
M/Fe(surface) or M/M(feature)								1.00E+00	6.71E-02	6.37E-03	4.21E-03	1.51E-03					
H-09	ID	2510	580.7	27344	1961	3801	3801	93.20	5.65	0.39	0.48	0.08	<-------NO FEATURES------->				
M/Fe(original)				27345		3808		1.0E+00	5.81E-02	4.54E-03	5.36E-03	9.31E-04					
M/Fe(surface) or M/M(feature)								1.00E+00	6.23E-02	4.16E-03	4.94E-03	8.56E-04					
H-11	ID	2510	584.5	27346	1961	3901	3901	93.46	5.29	0.75	0.39	0.10	<-------NO FEATURES------->				
M/Fe(original)				27347		3905		1.0E+00	6.16E-02	8.73E-03	4.54E-03	1.16E-03					
M/Fe(surface) or M/M(feature)								1.00E+00	5.58E-02	8.02E-03	4.17E-03	1.07E-03					
H-13	ID	2510	607.3	27348	1961	4001	4001	93.61	4.94	0.84	0.40	0.02	<-------NO FEATURES------->				
M/Fe(original)				27349		4005		1.0E+00	5.75E-02	9.78E-03	4.66E-03	2.33E-04					
M/Fe(surface) or M/M(feature)								1.00E+00	5.27E-02	8.95E-03	4.29E-03	2.13E-04					
H-15	ID	2510	619.2	27350	1961	101	101	93.98	4.58	0.83	0.51	0.10	<-------NO FEATURES------->				
M/Fe(original)				27351		105		1.0E+00	5.33E-02	9.66E-03	5.94E-03	1.18E-03					
M/Fe(surface) or M/M(feature)								1.00E+00	4.87E-02	8.83E-03	5.43E-03	1.08E-03					
H-17	ID	2510	625.8	27352	1961	201	201	94.73	4.26	0.48	0.47	0.04	<-------NO FEATURES------->				
M/Fe(original)				27353		205		1.1E+00	4.96E-02	5.70E-03	5.47E-03	4.89E-04					
M/Fe(surface) or M/M(feature)								1.00E+00	4.50E-02	5.17E-03	4.96E-03	4.22E-04					
H-19	ID	1220	639.0	28454	1959	201	201	85.40	10.23	1.50	1.90	0.80	<-------NO FEATURES------->				
M/Fe(original)				28455		206		9.0E-01	1.19E-01	1.66E-02	2.21E-02	9.31E-03					
M/Fe(surface) or M/M(feature)								1.00E+00	1.20E-01	1.67E-02	2.22E-02	9.37E-03					
H-19	ID	2510	645.5		1961	301	301	94.31	4.18	0.66	0.55	0.18	<-------NO FEATURES------->				
M/Fe(original)						305		1.1E+00	4.87E-02	8.31E-03	6.40E-03	1.86E-03					
M/Fe(surface) or M/M(feature)								1.00E+00	4.43E-02	8.48E-03	5.83E-03	1.70E-03					
H-21	ID	2510	530	27378	1961	401	401	81.47	17.70	0.16	0.41	0.26	19.04	78.66	0.04	0.46	1.55
M/Fe(original)				27379		415		9.4E-01	2.06E-01	1.88E-03	4.77E-03	3.03E-03					
M/Fe(surface) or M/M(feature)								1.00E+00	2.17E-01	1.99E-03	5.03E-03	3.19E-03	1.90E-01	7.97E-01	4.00E-04	9.80E-03	1.53E-02
H-23	ID	1210	535		1959	401	401	87.90	10.80	0.50	0.50	0.50	22.48	72.30	1.30	1.20	0.00
M/Fe(original)						413		1.0E+00	1.26E-01	5.82E-03	5.82E-03	5.82E-03					
M/Fe(surface) or M/M(feature)								1.00E+00	1.23E-01	5.69E-03	5.69E-03	5.69E-03	2.30E-01	7.44E-01	1.34E-02	1.23E-02	0.00E+00
H-25	ID	2510	549.3	27360	1961	501	501	88.99	10.01	0.68	0.16	0.13	18.89	78.79	0.06	0.75	1.15
M/Fe(original)				27361		512		1.0E+00	1.51E-01	8.31E-04	2.10E-03	1.51E-03					
M/Fe(surface) or M/M(feature)								1.00E+00	1.50E-01	8.24E-04	2.08E-03	1.50E-03	1.90E-01	7.91E-01	8.02E-04	7.53E-03	1.15E-02
H-27	ID	2510	550.2	27362	1961	601	601	88.51	10.69	0.13	0.28	0.18	18.87	78.84	0.11	0.93	0.15
M/Fe(original)				27363		609		1.0E+00	1.27E-01	1.51E-03	3.36E-03	2.10E-03					
M/Fe(surface) or M/M(feature)								1.00E+00	1.23E-01	1.47E-03	3.28E-03	2.03E-03	1.91E-01	7.97E-01	1.11E-03	9.42E-03	1.52E-03
H-27	ID	2510	560.1	27443	1961	901	901	87.12	12.87	0.00	0.00	0.01	20.72	78.40	0.43	1.21	1.25
M/Fe(original)				27444		906		1.0E+00	1.50E-01	0.00E+00	0.00E+00	1.15E-04					
M/Fe(surface) or M/M(feature)								1.00E+00	1.48E-01	0.00E+00	0.00E+00	1.15E-04	2.07E-01	7.64E-01	4.30E-03	1.21E-02	1.25E-02
H-29	ID	2510	570.1	27445	1961	1001	1001	88.04	1058.00	0.09	0.11	0.18	25.77	68.88	2.30	1.98	1.06
M/Fe(original)				27446		1008		1.0E+00	1.23E+01	1.05E-03	1.28E-03	2.10E-03					
M/Fe(surface) or M/M(feature)								1.00E+00	1.19E+01	1.01E-03	1.24E-03	2.02E-03	2.58E-01	6.89E-01	2.30E-02	1.98E-02	1.06E-02
H-31	ID	2510	580	27364	1961	801	810	89.49	8.40	0.43	0.50	0.18	25.32	67.78	3.18	2.50	1.25
M/Fe(original)				27367		810		1.0E+00	9.78E-02	5.01E-03	5.82E-03	2.10E-03					
M/Fe(surface) or M/M(feature)								1.00E+00	9.29E-02	4.75E-03	5.53E-03	1.99E-03	2.53E-01	6.78E-01	3.18E-02	2.50E-02	1.25E-02
H-33	ID	2510	590.1	27384	1961	701	701	92.61	7.14	0.09	0.10	0.06					
M/Fe(original)				27385		705		1.0E+00	8.31E-02	9.31E-04	1.10E-03	6.98E-04	<-------NO FEATURES------->				
M/Fe(surface) or M/M(feature)								1.00E+00	7.71E-02	8.64E-04	1.08E-03	6.48E-04					
H-35	ID	2510	599.6		1963	101	101	93.20	5.43	0.10	0.22	0.40					
M/Fe(original)						105		1.0E+00	7.48E-02	1.14E-03	2.58E-03	4.66E-03	<-------NO FEATURES------->				
M/Fe(surface) or M/M(feature)								1.00E+00	6.90E-02	1.07E-03	2.38E-03	4.29E-03					
H-37	ID	2510	609.9		1963	201	201	982.95	6.20	0.55	0.42	0.20					
M/Fe(original)						205		1.1E+01	7.22E-02	6.40E-03	4.89E-03	2.33E-03	<-------NO FEATURES------->				
M/Fe(surface) or M/M(feature)								1.0E+00	6.31E-03	5.60E-04	4.27E-04	2.04E-04					
H-39	ID	2510	614.9		1963	301	301	93.80	5.48	0.39	0.25	0.08					
M/Fe(original)						305		1.0E+00	6.36E-02	4.54E-03	2.91E-03	8.98E-04	<-------NO FEATURES------->				
M/Fe(surface) or M/M(feature)								1.00E+00	5.84E-02	4.16E-03	2.67E-03	8.40E-04					
H-41	ID	2510	630		1963	401	401	93.96	5.17	0.41	0.38	0.08					
M/Fe(original)						405		1.0E+00	6.02E-02	4.77E-03	4.54E-03	8.31E-04	<-------NO FEATURES------->				
M/Fe(surface) or M/M(feature)								1.0E+00	5.50E-02	4.36E-03	4.15E-03	9.31E-04					

Table C.4 EDX Data for GEB-2